Lotta Jokiniemi

Probing Neutrinoless Double-Beta Decay by Charge-Exchange Reactions and Muon Capture

Esitetään Jyväskylän yliopiston matemaattis-luonnontieteellisen tiedekunnan
suostumuksella julkisesti tarkastettavaksi yliopiston Ylistönrinteen salissa FYS1
lokakuun 9. päivänä 2020 kello 12.

Academic dissertation to be publicly discussed, by permission of
the Faculty of Mathematics and Science of the University of Jyväskylä,
in building Ylistönrinne, auditorium FYS1 on October 9, 2020 at 12 o'clock noon.

JYVÄSKYLÄN YLIOPISTO
UNIVERSITY OF JYVÄSKYLÄ

JYVÄSKYLÄ 2020

Preface

The work presented in this thesis has been carried out at University of Jyväskylä between 2016 and 2020. I gratefully acknowledge the financial support from the Doctoral school of University of Jyväskylä and Academy of Finland under the Project No. 318043.

First and foremost I would like to express my gratitude to my supervisor, Prof. Jouni Suhonen, for his excellent guidance on this journey. His supervision has definitely helped me grow up as a scientist. He has guided me to exciting research topics - not to mention all the academic adventures around the globe.

I owe big thanks to Prof. Hiro Ejiri, who has collaborated with me since I was commencing my Master's thesis, for initiating many of my projects and for many valuable discussions in different occasions. I would also like to thank Prof. Dieter Frekers, Dr. Izyan H. Hashim and Dr. Jenni Kotila for collaboration. I would like to thank Prof. Nils Paar and Dr. Javier Menéndez for reviewing the manuscript of this thesis and providing useful comments and Prof. Theocharis Kosmas for promising to be my opponent.

I would like to thank all my friends and colleagues at the Department of Physics for the open atmosphere to do physics. Huge thanks are in order to the staff of the department and faculty for always knowing the answers. Special thanks go to the Holvi Lunchtime Collaboration (HLC) for taking care of the daily nutritional requirement as well as the daily amount of bad jokes.

I also have to thank Dr. Elina Jokinen for organizing, despite the unconventional conditions, a wonderful thesis retreat, which helped me kick off the writing process.

Last but not least I would like to thank my family, my mom for always supporting me in no matter what I decided to do, my sisters for always being there, and my dad for transmitting me his adventurous mind. Thank you, Mikko, I can't describe how lucky I am to have you in my life.

Jyväskylä, September 2020
Lotta Jokiniemi

Abstract

In this thesis, it is shown how charge-exchange reactions and nuclear muon capture can be utilised to probe neutrinoless double-beta ($0\nu\beta\beta$) decay, a beyond-Standard-Model process that, for the time being, has not been observed despite massive experimental efforts. If detected, $0\nu\beta\beta$ decay would not only prove the existence of physics beyond the Standard Model but also provide precious information on the yet unknown nature and mass-scale of neutrinos. Hence, improving the theoretical description of the related nuclear-structure physics is a crucial aid in planning the future experiments.

The $0\nu\beta\beta$ decay proceeds through virtual states of an intermediate nucleus to the ground or excited states of the decay daughter. The decaying, the intermediate and daughter nuclei form a so-called double-beta-decay triplet. One way to improve the description of the related nuclear structure is fine-tuning the nuclear-model parameters by exploiting available data on relevant measured processes. To that end, one can study complementary nuclear processes for which experimental data exist or are being or will be measured. In this thesis, it is proposed that one can probe the $0\nu\beta\beta$ decay by studying the strength distributions of charge-exchange reactions and ordinary muon capture in the double-beta-decay triplets. By studying these nuclear processes one can not only probe the intermediate states of the double-beta decay, but also eventually shed light on the highly debated effective values of the weak couplings in wide excitation-energy and momentum-exchange regions relevant for $0\nu\beta\beta$ decay.

All the computations presented in the thesis were performed in the proton-neutron quasiparticle random-phase approximation (pnQRPA) framework. pnQRPA allows accommodating large no-core single-particle bases including all the relevant spin-orbit-partner orbitals, hence providing access to wide excitation-energy regions. Since pnQRPA has shown to be capable of describing the gross features of the distributions of nuclear states, it is an excellent tool for simultaneous consistent description of double beta decay, charge-exchange reactions and muon capture.

The thesis consists of five publications and an introductory part. Articles

[**I**, **II**] cover probing the $0\nu\beta\beta$ matrix elements by isovector spin-multipole transitions in the key double-beta-decay triplets, and articles [**III**, **IV**, **V**] probing the $0\nu\beta\beta$ decay in various ways by ordinary muon capture. In the introductory part, the study of this thesis is set in the wider frame of weak-interaction processes, and the theoretical formalism and results of all five publications are twined together.

Tiivistelmä

Tässä väitöskirjassa esitetään, kuinka varauksenvaihtoreaktioita ja myonisieppausta voidaan hyödyntää neutriinottoman kaksoisbeetahajoamisen ($0\nu\beta\beta$), erään hiukkasfysiikan standardimallin ulkopuolisen prosessin, tutkimuksessa. Tähän mennessä $0\nu\beta\beta$-hajoamista ei olla onnistuttu havaitsemaan mittavista kokeellisista yrityksistä huolimatta, mutta löydyttyään se paitsi todistaisi standardimallin ulkopuolisen fysiikan olemassaolon, myös tarjoaisi arvokasta tietoa toistaiseksi tuntemattomista neutriinon luonteesta ja massaluokasta. Tämän vuoksi prosessiin liittyvän ydinrakennefysiikan teoreettisen kuvauksen kehittäminen on tulevien kokeiden suunnittelun kannalta elintärkeää.

$0\nu\beta\beta$-hajoaminen etenee välitimen virtuaalisten tilojen tytärytimen perus- tai virITystiloille. Hajoava ydin, väliydin ja tytärydin muodostavat niinsanotun kaksoisbeetahajoamistripletin. Yksi keino kehittää triplettiin liittyvän ydinrakenteen kuvausta on hienosäätää ydinmallin parametreja hyödyntämällä saatavilla olevaa tietoa olennaisista mitatuista prosesseista. Tätä ajatellen voidaan tutkia vastaavanlaisia prosesseja, joista on olemassa kokeellista tietoa tai joita mitataan parhaillaan tai tullaan mittaamaan tulevaisuudessa. Tässä väitöskirjassa esitetään, että $0\nu\beta\beta$-hajoamista voidaan ennustaa tutkimalla varauksenvaihtoreaktioiden ja myonisieppauksen voimakkuusjakaumia kaksoisbeetahajoamistripleteissä. Tutkimalla näitä ydinprosesseja pystytään paitsi tutkimaan kaksoisbeetahajoamisen välitiloja, mutta lopulta myös valottamaan kiisteltyjä heikon vuorovaikutuksen kytkentävakioiden efektiivisiä arvoja laajoissa virITysenergia- ja liikemääränvaihtoalueissa, jotka ovat olennaisia $0\nu\beta\beta$-hajoamiselle.

Kaikki tässä väitöskirjassa esitetyt laskut on tehty pnQRPA (*engl.* protonneutron quasiparticle random-phase approximation) -mallin avulla. Sen ansiosta laskuissa voidaan käyttää suuria yksihiukkaskantoja, joissa kaikki orbitaalit ovat aktiivisia ja jotka sisältävät kaikki tarpeelliset spin-rata -pariorbitaalit, mikä mahdollistaa laskujen ulottamisen laajoille virITysenergia-alueille. Koska pnQRPA on osoittautunut kykeneväksi kuvaamaan ytimien tilojen jakaumien yleisiä ominaisuuksia, on se erinomainen työkalu kaksoisbeetahajoamisen, varauksenvaihtoreaktioiden ja myonisieppauksen yhtäaikaiseen yhtenevään

kuvaamiseen.

Väitöskirja koostuu viidestä artikkelista sekä yhteenvedosta. Artikkeleissa [**I**, **II**] käsitellään $0\nu\beta\beta$-hajoamisen matriisielementtien tutkimista isovektori-spin-multipoli -siirtymien avulla tärkeimmissä kaksoisbeetahajoamistripleteissä, ja artikkeleissa [**III**, **IV**, **V**] käsitellään $0\nu\beta\beta$-hajoamisen ennustamista monin eri tavoin myonisieppauksen avulla. Yhteenveto-osiossa väitöskirjassa tehty tutkimus kytketään laajempaan heikon vuorovaikutuksen prosessien tutkimusalaan, sekä kaikkien viiden artikkelin laskujen teoreettinen muotoilu ja tulokset liitetään yhteen.

Author   Lotta Jokiniemi
               Department of Physics
               University of Jyväskylä
               Finland

Supervisor Prof. Jouni Suhonen
               Department of Physics
               University of Jyväskylä
               Finland

Reviewers   Prof. Nils Paar
               Department of Physics
               University of Zagreb
               Croatia

               Dr. Javier Menéndez
               Department of Quantum Physics and Astrophysics, Faculty of Physics
               University of Barcelona
               Spain

Opponent   Prof. Theocharis Kosmas
               Department of Physics
               University of Ioannina
               Greece

List of Publications

This thesis consists of an introductory part and of the following publications:

[I] **Isovector spin-multipole strength distributions in double-β-decay triplets**
L. Jokiniemi and J. Suhonen, *Phys. Rev. C* 96 (2017) 034308.

[II] **Neutrinoless $\beta\beta$ nuclear matrix elements using isovector spin-dipole $J^\pi = 2^-$ data**
L. Jokiniemi, H. Ejiri, D. Frekers and J. Suhonen, *Phys. Rev. C* 98 (2018) 024608.

[III] **Pinning down the strength function for ordinary muon capture on ^{100}Mo**
L. Jokiniemi, J. Suhonen, H. Ejiri and I. H. Hashim, *Phys. Lett. B* 794 (2019) 143–147.

[IV] **Muon-capture strength functions in intermediate nuclei of $0\nu\beta\beta$ decays**
L. Jokiniemi and J. Suhonen, *Phys. Rev. C* 100 (2019) 014619.

[V] **Comparative analysis of muon capture and $0\nu\beta\beta$ decay matrix elements**
L. Jokiniemi and J. Suhonen, *Phys. Rev. C* 102 (2020) 024303.

The author performed all numerical computations and wrote the original draft of all articles [**I**, **II**, **III**, **IV**, **V**]. The author updated the muon capture theory and developed the computer code used in the muon capture calculations accordingly.

x

Contents

Chapter 1

Introduction

The present knowledge of particle physics is based on the Standard Model, which is extremely successful theory of fundamental interactions and of all known elementary particles. However, the solar-neutrino experiments [1–3] have proven that neutrinos have a non-zero mass, which conflicts with the Standard Model as we know it. This signifies that the Standard Model's perception of neutrinos is not accurate making the search of new physics beyond the Standard Model most intriguing [4–6]. At present, the most practical way to access not only the absolute mass-scale of neutrinos but also the yet-to-be-determined character of the neutrino, whether it is Dirac or Majorana, is measuring neutrinoless double-beta ($0\nu\beta\beta$) decay of atomic nuclei [7, 8].

Double-beta ($\beta\beta$) decay is a weak interaction process in which two neutrons of the mother nucleus are transformed into protons (or vice versa), while two electrons (or positrons) are emitted [1]. There are two modes of this process: two-neutrino double-beta ($2\nu\beta\beta$) decay and neutrinoless double-beta ($0\nu\beta\beta$) decay. In the $2\nu\beta\beta$ decay the lepton number is conserved, hence two (anti)neutrinos are emitted during the process, whereas in $0\nu\beta\beta$ decay no neutrinos are emitted and the Standard Model's lepton-number conservation law is violated. This also means that neutrino has to be its own antiparticle, or *Majorana particle*, which is not predicted by the Standard Model. These circumstances emphasize why observing neutrinoless double-beta decay would make a groundbreaking discovery [9].

There are numerous completed, ongoing and planned large-scale experiments searching for $0\nu\beta\beta$ decay [10–19]. Despite the tremendous experimental effort the $0\nu\beta\beta$ decay is yet to be observed. Since planning the experiments is a formidable and high-cost task, it is of utmost importance to refine the

---

[1]The latter decay mode can be accompanied by β^+/electron-capture or double electron-capture processes.

theoretical predictions of $0\nu\beta\beta$ decay. At present, there are lots of discrepancies in the calculated values of the nuclear matrix elements involved in the determination of the half-life of the of $0\nu\beta\beta$ decay [20] partly related to the fact that the reaction mechanism is not entirely known [21, 22], partly due to the shortcomings of different theoretical approaches. The discrepancies are also subject to the model dependence due to different nuclear effective interactions and theoretical frameworks applied. These dependences are related to the systematic model dependence when describing any quantity of interest. In addition, calculated quantities including the the $0\nu\beta\beta$ matrix elements are often subject to statistical model uncertainties due to the methods often employed in constraining the effective interaction parameters from the experimental data. Nevertheless, one of the largest uncertainties are the half-lives of $0\nu\beta\beta$ decay being proportional to the fourth power of the debated effective value of the weak axial-vector coupling constant g_A. Many studies indicate that the experimental values of observables related to this weak coupling are systematically smaller than the theory predictions, which has lead to the long-standing puzzle of g_A *quenching* [23].

One approach to improve the theoretical predictions of $0\nu\beta\beta$ decay is fine-tuning the model parameters by exploiting available data on relevant measured processes such as β decay, $2\nu\beta\beta$ decay, charge-exchange reactions and charged-lepton capture. To that end, in this work we studied the strength distributions of charge-exchange reactions and ordinary muon capture in the isobaric triplets corresponding to the $\beta\beta$ decay of the key $0\nu\beta\beta$-candidates ^{76}Ge, ^{82}Se, ^{96}Zr, ^{100}Mo, ^{116}Cd, ^{128}Te, ^{130}Te and ^{136}Xe. The computations were performed in the framework of the proton-neutron quasiparticle random-phase approximation (pnQRPA) with large no-core single-particle bases in order to describe the strength distributions in wide-excitation regions up to about 50 MeV. By studying these strength distributions we can not only probe the intermediate states of the double-beta decay (See Fig. 1.1), but also eventually shed light on the unknown effective values of the weak couplings in wide excitation-energy and momentum-exchange regions relevant for $0\nu\beta\beta$ decay.

Where $2\nu\beta\beta$ decay proceeds only via the 1^+ virtual states of the intermediate nucleus, $0\nu\beta\beta$ decay can access states of every possible multipolarity J^π [24]. The virtual Gamow-Teller (GT) transitions trough 1^+ states have typically been probed by β^- or β^+ type $L = 0$ [2] charge-exchange reactions [25–27]. Recently data on the location of the isovector spin-dipole ($L = 1$) giant resonances became available from charge-exchange reactions performed at the Research Center for Nuclear Physics (RCNP), Osaka, Japan, enabling us

---

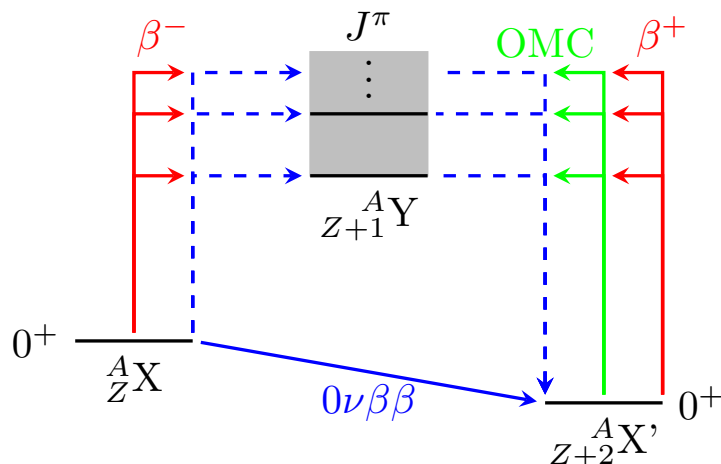[2]L refers to the orbital angular momentum of the transition operator.

Figure 1.1. Schematic figure of a $\beta\beta$-decay triplet with the corresponding β^- type (p,n) and β^+ type (n,p) charge-exchange reactions and ordinary muon captures to the intermediate states. The dashed blue arrows refer to the virtual transitions of the $0\nu\beta\beta$ decay trough different J^π states.

to probe the higher-multipole virtual transitions. In article [**I**], we studied the β^- (β^+) -type of isovector spin-dipole ($L = 1$) and spin-quadrupole ($L = 2$) transitions from the 0^+ ground states of the initial (final) even-even nuclei of the $0\nu\beta\beta$-decay triplets to the excited states of the intermediate odd-odd nuclei, and in article [**II**], we computed the $0\nu\beta\beta$ matrix elements exploiting the newly available data on isovector spin-dipole $J^\pi = 2^-$ transitions for the first time.

Inspired by the newly discovered muon capture giant resonance in ^{100}Nb [28], we computed the ordinary muon capture (OMC) strength function in ^{100}Nb and compared it against the measured strength function in article [**III**] for the first time. The computations were performed using the Morita-Fujii formalism of OMC [29] by extending the original formalism beyond the leading order. In articles [**IV, V**] of the thesis, we extended the study of article [**III**] by computing the ordinary muon capture rates on the daughter nuclei of the key $0\nu\beta\beta$ decay triplets, and finally by comparing the average muon capture matrix elements with the corresponding $0\nu\beta\beta$-decay matrix elements. In all cases, we compared the obtained total muon capture rates with the Primakoff estimates in order to shed light on the g_A quenching.

The introductory part is organized as follows. In Chapter 2, we introduce the nuclear theory tools for solving the nuclear many-body problem. In Chapter 3, we briefly review the concept of double-beta decay. In Chapter 4,

we outline the charge-exchange-reaction formalism and discuss the results of articles [**I**] and [**II**]. In Chapter 5, we outline the muon-capture formalism, discuss the results of articles [**III**, **IV**, **V**], and speculate on some future prospects. Quite some emphasis is given to the theory part, not only due to the author's genuine interest in the subject, but also due to the updates made to the theory developed in 1960's. In Chapter 6, the main results of the thesis are summarized.

Chapter 2

Nuclear Models

We begin with the very heart of the theoretical nuclear physics: the nuclear many-body problem and different nuclear models aiming to solve the problem. The focus is mainly in the nuclear mean field approaches, especially in the proton-neutron version of the quasiparticle random-phase approximation (QRPA) being the nuclear-structure approach of our choice in the thesis.

2.1 The Nuclear Many-Body Problem

A nucleus $^{A}_{Z}X_{N}$ consists of A nucleons, Z protons and N neutrons, interacting through strong (along with weak and electromagnetic) interaction. Solving the resulting *nuclear many-body problem* is one of the main goals of nuclear physics. Accomplishing the goal is a formidable task due to the extremely complex nature of the nuclear strong force. At low energies, such as the nuclear excitations, the underlying theory of *quantum chromodynamics* (QCD) is non-perturbative, and hence extremely difficult to solve. Nuclei are built of nucleons that are, in turn, complex structures made of quarks, antiquarks and gluons - hence not fundamental particles. Consequently, the strong nuclear force is only an 'effective' force arising from QCD and at present our knowledge of it is restricted to models [30].

The *ab initio* methods are aiming at solving the non-relativistic Schrödinger equation

$$H \ket{\Psi} = E \ket{\Psi}$$

for all constituent nucleons and all forces between them from first principles, or *ab initio*. In this framework the modeling of nuclear physics phenomena is based on the implementation of nucleon-nucleon and three-nucleon interactions derived from more fundamental theories, e.g. chiral effective field theory (EFT). The Schrödinger equation is then solved either by solving the equation

exactly for the lightest nuclei with $A \leq 5$ [31], or by using new methods and well-constrained approximations for the heavier nuclei [32]. While some ten years ago the ab initio theories were able to reach only the very lightest nuclei of the nuclear chart [33–35], the theories are developing in accelerating pace, and nuclei as heavy as tin [36] have already been reached.

However, since in this study we are interested in medium-heavy to heavy open-shell nuclei, we need to do some simplifying approximations on the nuclear interactions. A certain widely used method is the *nuclear mean field approximation*, which is discussed in the following subsection.

2.2   Nuclear Mean Field

Instead of solving the nuclear many-body problem of A strongly interacting nucleons, we can treat the nucleus as system of weakly interacting nucleons independently moving in an average potential created by the nucleons themselves, hence disregarding the mesonic or quark degrees of freedom. This is a justified choice due to the fact that the nucleons are, on average, relatively far apart, and thus the strong character of the nucleon-nucleon force is remarkably reduced. There is also experimental evidence supporting the idea of such an average potential, such as the existence of the so-called magic numbers. At these proton and neutron numbers shell effects analogous to the shell closure of electron shells of atoms take place, which leads to the idea of neutrons and protons in the nucleus having a similar kind of shell structure as electrons in an atom [37].

In the *mean field approximation* the nucleons in the nucleus are converted into a system of A weakly-interacting particles. In this approximation, the nuclear many-body Hamiltonian can be written in the form

$$ H = \left[T + \sum_{i=1}^{A} v(\mathbf{r}_i) \right] + \left[V - \sum_{i=1}^{A} v(\mathbf{r}_i) \right] := H_{\mathrm{MF}} + V_{\mathrm{RES}} \, , \qquad (2.1) $$

where H_{MF} is the nuclear *mean-field Hamiltonian* and V_{RES} the *residual interaction* [38]. Hence, the system of strongly interacting fermions becomes a system of non-interacting particles in an external potential $v(\mathbf{r})$.

The Schrödinger equation corresponding to the mean-field Hamiltonian of Eq. (2.1) is easily solved, since it can be separated to A identical one-particle Schrödinger equations. However, the problem lies on determining the optimal mean-field that would minimize the residual interaction between the particles so that it could be treated as a small perturbation. The residual interaction can be numerically solved from a Rayleigh-Ritz variational problem [39] by
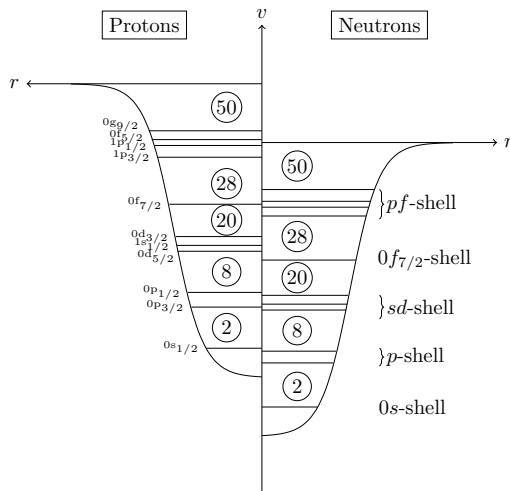
Figure 2.1. Schematic figure of Woods-Saxon -based mean field potentials for protons and neutrons. The different orbitals and shells are labeled. The magic numbers are indicated as circled numbers.

Hartree(-Fock) method, or by using a suitable phenomenological potential [38].

Throughout this study, we use the Woods-Saxon potential with Bohr-Mottelson [40] parametrization, which is optimized for nuclei close to the β-stability line. However, the central potential alone does not suffice to reproduce the experimentally observed behavior of the single-particle states. In order to reproduce the observed shell structure and the magic numbers of the nucleus, one has to add supplementary terms resulting from the Coulomb force and from the *spin-orbit interaction* to the mean-field potential. The origin of the spin-orbit effect is not well understood, and hence one has to resort to a phenomenological description of it [40]. After all the needed terms have been added to the mean-field potential, the resulting Woods-Saxon Hamiltonian can be diagonalized by direct numerical methods, or in terms of linear combinations of harmonic oscillator wave functions as described in detail in [38]. In Fig. 2.1 the Woods-Saxon potentials with magic numbers, orbitals and shells labeled are presented schematically for both protons and neutrons. Note that the potential well is shallower for protons than for neutrons due to the Coulomb force.

After diagonalizing the mean-field Hamiltonian, we are left with looking for the residual interaction V_{RES}, and diagonalizing the full Hamiltonian of Eq. (2.1). To do this, we must first choose a suitable valence space, where the interactions can take place. In order to reduce the computational burden, the complete set of nuclear orbitals is often divided in three parts:

an inert core consisting of filled orbitals of non-interacting nucleons, the valence space, and the external space, where the orbitals remain empty. Then, the residual interaction is defined as an effective interaction in the valence space. This valence-space interaction is often found by using perturbative methods starting from the nuclear-matter G-matrix interaction. In this thesis we start from the Bonn one-boson-exchange G-matrix [41] and obtain the two-nucleon interaction in finite nuclei by phenomenological adjustments of a few key parameters defining the magnitudes of the corresponding two-body interaction matrix elements.

Many nuclear theories, such as Hartree-Fock methods, *nuclear shell model*, Tamm-Dancoff approximation and *quasiparticle random-phase approximation* (QRPA), rely on the mean-field approximation [42]. Of these theories, especially the nuclear shell model and proton-neutron QRPA have been commonly used in the double-beta-decay calculations. The nuclear shell model has been used already for decades in the nuclear-structure calculations of light nuclei [37, 38, 43]. However, the method is ineffective for medium-heavy or heavy nuclei since the configuration spaces are usually too large to handle without truncations in them. Hence, from now on we will focus on the QRPA method, especially on the proton-neutron version of it, which is applicable for the purposes of our study.

2.3 Proton-Neutron Quasiparticle Random-Phase Approximation

The proton-neutron quasiparticle random-phase approximation (pnQRPA) describes nuclear excitations in open-shell odd-odd nuclei in terms of proton-neutron quasiparticle pairs. These excitations are particularly useful for studying charge-changing reactions such as β decays and captures of charged leptons. Even though pnQRPA often fails to reproduce the energy-level structure of the nuclei in detail, it manages to reach high excitation energies with reasonable computational effort and it is shown to describe the gross features of reaction strength functions in a satisfactory way [44]. The downside of pnQRPA theory is that it has some adjustable parameters, for example the particle-particle interaction parameter g_{pp}, which have a strong influence on theoretical predictions of nuclear structure [45, 46]. The values of these parameters are somewhat uncertain, and they need to be constrained by experimental data.

Forming the pnQRPA states begins with the choice of proton and neutron single-particle bases. We choose large no-core Woods-Saxon single-particle

bases containing the orbitals up to a couple of shells above the corresponding Fermi surfaces (the highest occupied single-particle states) for both protons and neutrons. The large bases are needed in order to reach the giant-resonance regions we are interested in at high energies up to 50 MeV.

In order to form the proton and neutron quasiparticle spectra needed in the pnQRPA procedure, we follow the *Bardeen-Cooper-Schrieffer (BCS) method* [38] that was originally developed by J. Bardeen, L. Cooper, and J. R. Schrieffer [47] for the microscopic description of the superconductivity of metals in terms of correlated electron pairs. Having noticed similar pairing effect in nuclei, A. Bohr, B. R. Mottelson and D. Pines [48], and S. T. Belyaev [49] come up with an idea to apply the same method to nuclei, which has later become a standard part of the nuclear-structure calculations.

The BCS ground state of an even-even nucleus can be written in terms of paired protons and paired neutrons in the form

$$|\text{BCS}\rangle = \prod_{\alpha>0} (u_a - v_a A_\alpha^\dagger) \, , \tag{2.2}$$

where α and a denote the quantum numbers of the orbitals as $\alpha = (a, m_\alpha)$ and $a = (n_a, l_a, j_a)$, following the Baranger notation, and v_a and u_a are the *occupation and vacancy amplitudes* of orbital α, respectively.

$$A_\alpha^\dagger = c_\alpha^\dagger \tilde{c}_\alpha^\dagger \tag{2.3}$$

is the pair creation operator, where $c_\alpha^\dagger$ is the particle creation operator and $\tilde{c}_\alpha = (-1)^{j_a+m_a} c_{-\alpha}$.

The BCS ground state defined in Eq. (2.2) is the vacuum for BCS quasiparticles that are created and annihilated by the operators $a_\alpha^\dagger$ and a_α defined by the *Bogoliubov-Valatin transformation*

$$\begin{aligned} a_\alpha^\dagger &= u_a c_\alpha^\dagger + v_a \tilde{c}_\alpha \, , \\ \tilde{a}_\alpha &= u_a \tilde{c}_\alpha - v_a c_\alpha^\dagger \end{aligned} \tag{2.4}$$

introduced first by N. N. Bogoliuv [50], and later by J. G. Valatin [51]. Here $\tilde{\alpha} = (-1)^{j_a+m_a} a_{-\alpha}$ similarly as in the case of particle operators.

The energy of the BCS ground state of Eq. (2.2) is then minimized by varying the parameters u_a and v_a using the Rayleigh-Ritz method [39]. The BCS ground state does not possess good particle number. This lack can be mitigated by constraining the average number of nucleons in the BCS state by the number of valence nucleons in a given even-even nucleus of interest. This even-even nucleus can be called *reference nucleus*, and it is the starting point of the pnQRPA procedure to create the states of the adjacent odd-odd

9

nucleus by quasiproton-quasineutron excitations on the pnQRPA ground state of the reference nucleus. As a result of the constrained variational problem, one obtains the single-quasiparticle energies and the occupation amplitudes of the BCS states as explained in detail in [38]. The lowest quasiparticle energies of the protons and neutrons are adjusted to the empirical pairing gaps by scaling the pairing strength parameters $g_{\text{pair}}^{(\text{p})}$ and $g_{\text{pair}}^{(\text{n})}$.

Finally we find the wave functions and excitation energies for the complete set of J^π excitations in the odd-odd nuclei by performing a pnQRPA diagonalization in the unperturbed basis of quasiproton-quasineutron pairs coupled to J^π [38, 52]. The resulting pnQRPA states in odd-odd nuclei are of the form

$$|J_k^\pi M\rangle = \sum_{pn} [X_{pn}^{J_k^\pi} A_{pn}^\dagger(JM) - Y_{pn}^{J_k^\pi} \tilde{A}_{pn}(JM)]|\text{pnQRPA}\rangle , \qquad (2.5)$$

where k labels the states of spin-parity J^π, the quantities X and Y are the forward- and backward-going pnQRPA-amplitudes, $A^\dagger$ and $\tilde{A}$ are the quasiproton-quasineutron creation and annihilation operators, M is the z projection of J and $|\text{pnQRPA}\rangle$ is the pnQRPA vacuum. The transition densities corresponding to transitions between the 0_{gs}^+ ground state of the even-even reference nucleus and a J_k^π excited state of the corresponding odd-odd nucleus, can then be written as

$$(0_{\text{gs}}^+||[c_p^\dagger \tilde{c}_n]_J||J_k^\pi) = \sqrt{2J+1} \left[v_p u_n X_{pn}^{J_k^\pi} + u_p v_n Y_{pn}^{J_k^\pi} \right] , \qquad (2.6)$$

$$(J_k^\pi||[c_p^\dagger \tilde{c}_n]_J||0_{\text{gs}}^+) = \sqrt{2J+1} \left[u_p v_n X_{pn}^{J_k^\pi} + v_p u_n Y_{pn}^{J_k^\pi} \right] , \qquad (2.7)$$

where v (u) is the BCS occupation (vacancy) amplitude in the even-even nucleus. The formalism is explained in more detail in Refs. [38, 52]. These transition densities can be used as inputs in computations of many kinds of nuclear processes.

The pnQRPA Hamiltonian includes particle-hole and particle-particle channels. The particle-hole contribution is proportional to the particle-hole matrix elements $g_{\text{ph}}\langle pn^{-1}; J^\pi|V|p'n'^{-1}; J^\pi\rangle$, where J^π is the spin-multipolarity of the states in the intermediate odd-odd nucleus, and the particle-particle contribution is proportional to the particle-particle matrix elements $g_{\text{pp}}\langle pn; J^\pi|V|p'n'; J^\pi\rangle$. Here g_{ph} and g_{pp} are the particle-hole and particle-particle renormalization factors correspondingly.

The values of the particle-particle and particle-hole parameters are, however, somewhat uncertain. Especially the value g_{pp} has been under debate since the mid 80's. One idea was to probe the virtual transitions of $0\nu\beta\beta$ decay by adjusting the parameter to the β^- decays or electron capture (EC) data [53, 54]. Unfortunately, the EC or β^- measurements can only probe the
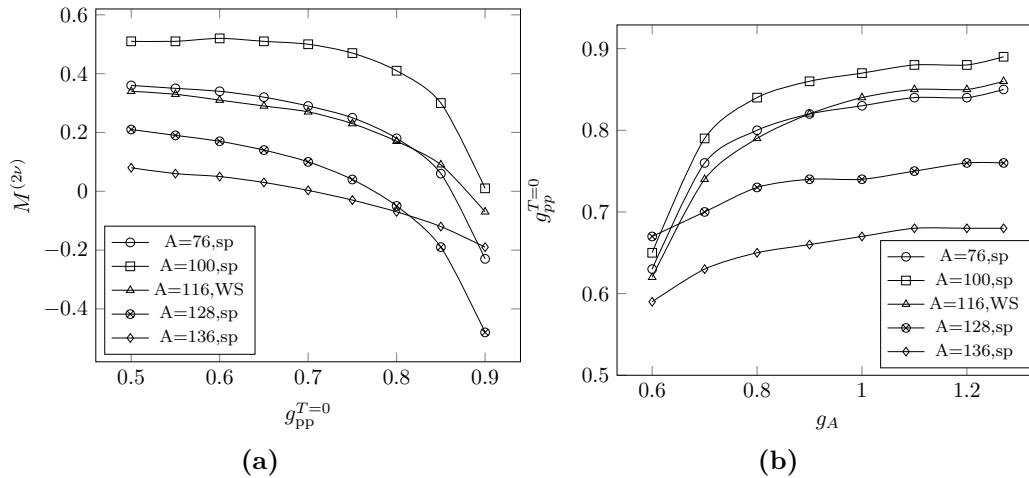
Figure 2.2. Panel (a): Dependence of $M^{(2\nu)}$ on g_{pp}, Panel (b): Dependence of g_{pp} on g_{A}, for different mass numbers. Figures: [**II**].

virtual transitions trought the lowest intermediate J^π states. However, it has turned out that the two-neutrino double-beta ($2\nu\beta\beta$) decay matrix elements are particularly sensitive to this parameter [55–57]. An illustration of this is shown in Fig. 2.2a, which is taken from article [**II**]. This phenomenon has lead to the idea of deducing the value of the NME of the neutrino-mass mode of $0\nu\beta\beta$ decay by fitting the g_{pp} to the half-lives of $2\nu\beta\beta$ decay [46, 58]. This method has been widely used in the $0\nu\beta\beta$ decay studies, see, e.g., [59, 60].

Throughout the studies of this thesis, we have used a more sophisticated method, the so-called *partial isospin restoration scheme* first introduced in [61], for fitting the particle-particle parameters of the pnQRPA: The particle-particle parts of the pnQRPA matrices are divided into isoscalar ($T = 0$) and isovector ($T = 1$) parts by the decomposition

$$
\begin{aligned}
g_{\text{pp}}\langle pn; J^\pi|V|p'n'; J^\pi\rangle \to \ & g_{\text{pp}}^{T=1}\langle pn; J^\pi; T = 1|V|p'n'; J^\pi; T = 1\rangle \\
& + g_{\text{pp}}^{T=0}\langle pn; J^\pi; T = 0|V|p'n'; J^\pi; T = 0\rangle \, .
\end{aligned}
\tag{2.8}
$$

The isovector parameter $g_{\text{pp}}^{T=1}$ is then adjusted so that the Fermi part of the $2\nu\beta\beta$ NME vanishes, and thus the isospin symmetry is partially restored. This is a justified choice, since isospin is known to be a quite well conserved quantum number of nuclear states. Then, we independently vary the isoscalar parameter $g_{\text{pp}}^{T=0}$ such that the calculated NME reproduces the measured $2\nu\beta\beta$ half-life. However, the value of g_{pp} also depends on the chosen value of g_{A} (see Fig. 2.2b taken from article [**II**]), so the fitting has to be done for each g_{A} value separately.

The particle-hole parameter g_{ph}, in turn, has traditionally been adjusted to reproduce the phenomenological energetics of the "left-hand-side" Gamow-Teller giant resonance (GTGR) in the 1^+ channel of the calculations [24, 52, 55, 56]. This parameter value is then applied to each multipole. However, in the article [**II**] we experiment also with different adjusting methods for this parameter by utilising the newly available data on isovector spin-dipole excitations.

Chapter 3

Double-Beta Decay

The search for a process known as double-beta decay was first motivated by the postulation of neutrino by W. Pauli in 1930 [62]. He proposed an electron neutrino to explain how the energy, momentum and angular momentum in beta decay could be conserved. Soon after that, in 1933, E. Fermi developed the theory of $\beta^-(\beta^+)$ decay mediated by weak interaction:

$$
\begin{aligned}
(A, Z) &\rightarrow (A, Z + 1) + e^- + \bar{\nu}_e \ , \\
(A, Z) &\rightarrow (A, Z - 1) + e^+ + \nu_e \ ,
\end{aligned}
\tag{3.1}
$$

where A and Z are the mass and atomic numbers of the decaying nucleus, $e^-(e^+)$ the electron (positron), and $\nu_e(\bar{\nu}_e)$ the electron (anti-)neutrino.

In 1935 M. Goeppert-Mayer [63] came up with the idea of double-beta decay, in which two electrons and two electron antineutrinos are emitted simultaneously:

$$
(A, Z) \rightarrow (A, Z + 2) + 2e^- + 2\bar{\nu}_e \ .
\tag{3.2}
$$

This process is nowadays known as *two-neutrino double-beta (2νββ) decay*, or *ordinary double-beta decay*. The process could take place in even-even nuclei, where single-beta decay is energetically forbidden, but decaying by emitting two electrons simultaneously is energetically possible (see Fig. 3.1 for explanation).

In 1937 E. Majorana proposed that if neutrino was its own antiparticle, later known as *Majorana-particle*, the theory of β decay would remain unchanged [64]. A couple of years later, in 1939, W. F. Furry [65] invented the concept of *neutrinoless double-beta decay*

$$
(A, Z) \rightarrow (A, Z + 2) + 2e^- \ ,
\tag{3.3}
$$

which would require that the neutrino is a Majorana-particle. The process would occur in two stages: first a neutron in the initial nucleus (A, Z) emits
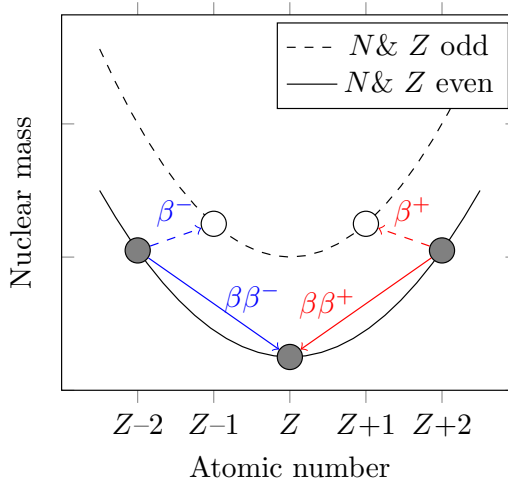
Figure 3.1. Schematic figure illustrating a circumstance, in which single-beta decay is energetically forbidden, but double-beta decay is allowed.

an electron and a virtual antineutrino and turns into a proton. This leads to virtual states in the intermediate nucleus $(A, Z + 1)$ of the $0\nu\beta\beta$ decay. Then, the virtual neutrino (which is also antineutrino, $\nu_e = \bar{\nu}_e$, since neutrino is a Majorana-particle) is absorbed by a neutron of the intermediate nucleus, thus turning into proton and simultaneously emitting an electron in an inverse β-decay process. As a result, the final nucleus $(A, Z + 2)$ of $0\nu\beta\beta$ decay is reached and two electrons have been emitted, without any antineutrinos in the final state (see Fig. 3.2, where the two decay modes are presented). This process would also be a lepton-number violating process, since the lepton numbers of the initial and final states differ by two. These are the features that make neutrinoless double-beta decay, even today, a particularly interesting probe for physics beyond the *Standard Model*. However, at this point it should be remarked that Standard Model, as we know it today, was invented well after these developments, in mid-1970s.

First experiments aiming for detecting double-beta decay were set up in 1948, even before neutrino was observed in 1956 [66], and first $2\nu\beta\beta$ decays were observed in 1950. A lot of effort has been directed to observing (neutrinoless) double-beta decay ever since, and two-neutrino double-beta decay has been observed in about ten nuclei (see, e.g., Refs.[67–70]) the half-lives ranging from 10^{19} years upwards. The existence of neutrinoless double-beta decay, in turn, remains a mystery. For those, who are interested, the history of the investigation of double-beta-decay is thouroghly reviewed e.g. in Refs. [71, 72].

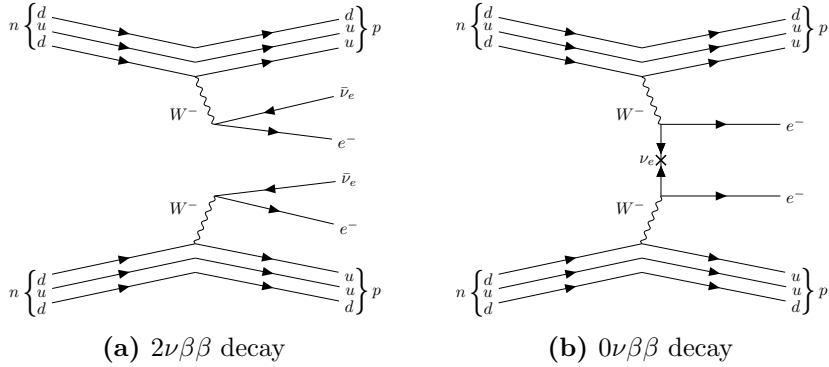Although there are some tens of $\beta\beta$-unstable nuclides, there are only a

(a) $2\nu\beta\beta$ decay **(b)** $0\nu\beta\beta$ decay

Figure 3.2. The two modes of double-beta decay.

handful of candidates of any practical interest for the study of $0\nu\beta\beta$ decay. A suitable candidate needs to have a sufficiently high $\beta\beta$-decay Q-value to have high decay probability, and in order to distinguish $0\nu\beta\beta$ decay from the dominating two-neutrino channel, the two-neutrino half-life should be as long as possible in order to reduce the number of $2\nu\beta\beta$ counts at the $\beta\beta$ end-point energy where the $0\nu\beta\beta$ signal is to be detected. A good candidate also has large natural isotopic abundance and compatibility with a well-established detection technique. The most promising candidates from the experimental point of view are ^{48}Ca, ^{76}Ge, ^{82}Se, ^{96}Zr, ^{100}Mo, ^{116}Cd, ^{128}Te, ^{130}Te, ^{136}Xe and ^{150}Nd [73]. There have been some claims of detecting $0\nu\beta\beta$ decay [74], however, the results are controversial, and only lower limits for the $0\nu\beta\beta$ decay half-life have been approved.

Where two-neutrino double-beta decay runs only trough the $J^{\pi} = 1^{+}$ states, Fermi transitions being suppressed by the isospin selection rules, the neutrinoless version runs trough all possible J^{π} states [75]. Furthermore, the momentum exchange involved in $0\nu\beta\beta$ decay is of the order of 100 MeV, which allows it to run trough high-lying excited states. This has lead to the idea of using weak-decay processes, such as charge-exchange reactions and muon capture, being able to access highly excited J^{π} states, to probe the intermediate states of $0\nu\beta\beta$ decay [45, 76, 77].

In the following subsections the underlying theoretical apparatus behind $2\nu\beta\beta$ and $2\nu\beta\beta$ decays is briefly introduced. We follow the theoretical framework introduced in, e.g., [24, 78].

3.1 Two-Neutrino Double-Beta Decay

The half-life of a ground-state-to-ground-state two-neutrino double-beta decay can be written in the form

$$\left[t_{1/2}^{(2\nu)}(0_i^+ \to 0_f^+)\right]^{-1} = (g_A^{\text{eff}})^4 G_{2\nu} \left|M^{(2\nu)}\right|^2 , \qquad (3.4)$$

where g_A^{eff} is the effective value of the weak axial-vector coupling strength. The factor $G_{2\nu}$ is a leptonic phase-space factor (in units of inverse years) defined in [79]. The ground states of the initial and final nuclei are denoted by 0_i^+ and 0_f^+, correspondingly.

The Gamow-Teller NME involved in Eq. (3.4) can be written as

$$M^{(2\nu)} = \sum_{m,n} \frac{(0_f^+ \| \sum_k t_k^- \boldsymbol{\sigma}_k \| 1_m^+)\langle 1_m^+ | 1_n^+ \rangle (1_n^+ \| \sum_k t_k^- \boldsymbol{\sigma}_k \| 0_i^+)}{D_m + 1} \qquad (3.5)$$

with the energy denominator

$$D_m = \left(\tfrac{1}{2}\Delta + \tfrac{1}{2}[E(1_m^+) + \tilde{E}(1_m^+)] - M_i\right)/m_e , \qquad (3.6)$$

where Δ is the nuclear mass difference between the initial and final 0^+ ground states, M_i the mass of the initial nucleus, and m_e the electron rest mass. $\tilde{E}(1_m^+)$ and $E(1_m^+)$ are the (absolute) energies of the mth 1^+ state in a pnQRPA calculation based on the left- and right-side ground states.

To do the calculations as precisely as possible, the difference $[E(1_m^+) + \tilde{E}(1_m^+)]/2 - M_i$ is adjusted to the measured energy difference between the first 1^+ state in the intermediate nucleus and the ground state of the initial nucleus. The same procedure is followed in the calculations of the $0\nu\beta\beta$ NMEs, as will be stated in the following subsection. The quantity $\langle 1_m^+ | 1_n^+ \rangle$ in Eq. (3.5) is the overlap between the two sets of 1^+ states and it can be written as

$$\langle 1_m^+ | 1_n^+ \rangle = \sum_{pn} \left[X_{pn}^{1_m^+} \bar{X}_{pn}^{1_n^+} - Y_{pn}^{1_m^+} \bar{Y}_{pn}^{1_n^+} \right] , \qquad (3.7)$$

where the quantities X and Y ($\bar{X}$ and $\bar{Y}$) denote the pnQRPA amplitudes originating from the calculation based on the left-side (right-side) nucleus. The overlap factor matches the corresponding states in the two sets of states based on the left- and right-side even-even reference nuclei and makes the computed NMEs more stable. For deformed nuclei, especially when the deformations of the initial and final nuclei are considerably different, the role of the overlap factor becomes of great importance [80, 81].

In principle, the expression in Eq. (3.5) should also contain a Fermi part but our choice for the $g_{\text{pp}}^{T=1}$ parameter forces this contribution to zero, as was

explained in Sec. 2.3. This is justified since the ground states of the mother and daughter nuclei belong to different isospin multiplets, and due to the isospin symmetry, the Fermi contribution to the $2\nu\beta\beta$ NME should vanish, leaving the Gamow-Teller NME in Eq. (3.5) as the sole contributor to the $2\nu\beta\beta$ decay rate. However, recent studies [23, 82] of β decays have shown that various terms going beyond Gamow-Teller transitions have non-negligible contributions to the β-decay rates. Consequently, the role of forbidden transitions is expected to be of relevance also in modeling double beta decays in general.

3.2   Neutrinoless Double-Beta Decay

In this section it is assumed that $0\nu\beta\beta$ decay is dominated by the light-Majorana neutrino-exchange mechanism, and other possible mechanisms are neglected. Here we are only interested in the ground-state-to-ground-state transitions between initial and final even-even nuclei of the double-beta-decay isobaric triplet. The half-life for such a $0\nu\beta\beta$ transition can be written as

$$\left[t_{1/2}^{(0\nu)}(0_i^+ \to 0_f^+) \right]^{-1} = (g_A^{\text{eff}})^4 G_{0\nu} \left| M^{(0\nu)} \right|^2 \left| \frac{\langle m_\nu \rangle}{m_e} \right|^2 , \qquad (3.8)$$

where $G_{0\nu}$ is a phase-space factor for the final-state leptons in units of inverse years (see [79]). The effective light-neutrino mass, $\langle m_\nu \rangle$, of Eq. (3.8) is defined as

$$\langle m_\nu \rangle = \sum_j (U_{ej})^2 m_j \qquad (3.9)$$

with m_j being the mass eigenstates of light neutrinos. The amplitudes U_{ej} are the components of the electron row of the light-neutrino-mass mixing matrix [83].

The $0\nu\beta\beta$-decay NME $M^{(0\nu)}$ in Eq. (3.8) is defined as

$$M^{(0\nu)} = M_{\text{GT}}^{(0\nu)} - \left(\frac{g_V}{g_A^{\text{eff}}} \right)^2 M_{\text{F}}^{(0\nu)} + M_{\text{T}}^{(0\nu)} , \qquad (3.10)$$

where we have adopted the conserved-vector-current (CVC) value $g_V = 1.0$ for the weak vector coupling strength. The double Fermi, Gamow-Teller, and

tensor nuclear matrix elements in Eq. (3.10) are defined as

$$M_{\text{F}}^{(0\nu)} = \sum_k (0_f^+ || \sum_{mn} h_{\text{F}}(r_{mn}, E_k) t_m^- t_n^- || 0_i^+) \, , \tag{3.11}$$

$$M_{\text{GT}}^{(0\nu)} = \sum_k (0_f^+ || \sum_{mn} h_{\text{GT}}(r_{mn}, E_k)(\boldsymbol{\sigma}_m \cdot \boldsymbol{\sigma}_n) t_m^- t_n^- || 0_i^+) \, , \tag{3.12}$$

$$M_{\text{T}}^{(0\nu)} = \sum_k (0_f^+ || \sum_{mn} h_{\text{T}}(r_{mn}, E_k) S_{mn}^{\text{T}} t_m^- t_n^- || 0_i^+) \, , \tag{3.13}$$

where t_m^- is the isospin lowering operator (that changes a neutron into a proton) for the nucleon m. The operator

$$S_{mn}^{\text{T}} = 3[(\boldsymbol{\sigma}_m \cdot \hat{\mathbf{r}}_{mn})(\boldsymbol{\sigma}_n \cdot \hat{\mathbf{r}}_{mn})] - \boldsymbol{\sigma}_m \cdot \boldsymbol{\sigma}_n \tag{3.14}$$

is the spin tensor operator. The summation over k in Eqs. (3.11)–(3.13) runs over all the states of the intermediate odd-odd nucleus, and E_k is the excitation energy of a given state. 0_i^+ (0_f^+) denote the ground state of the initial (final) even-even nucleus. Here $r_{mn} = |\mathbf{r}_m - \mathbf{r}_n|$ denotes the relative distance between the two decaying neutrons, labeled m and n, and $\hat{\mathbf{r}}_{mn} = (\mathbf{r}_m - \mathbf{r}_n)/r_{mn}$. The terms $h_K(r_{mn}, E_k)$, $K = \text{F}, \text{GT}, \text{T}$ are the neutrino potentials defined in [78].

In the pnQRPA framework the nuclear matrix elements of Eqs. (3.11)–(3.13) can be written as

$$
\begin{aligned}
M_K^{(0\nu)} = & \sum_{J^\pi, k_1, k_2, J'} \sum_{pp'nn'} (-1)^{j_n + j_{p'} + J + J'} \sqrt{2J'+1} \\
& \times \left\{ \begin{matrix} j_p & j_n & J \\ j_{n'} & j_{p'} & J' \end{matrix} \right\} (pp'; J' || \mathcal{O}_K || nn'; J') \\
& \times (0_f^+ || \left[c_{p'}^\dagger \tilde{c}_{n'} \right]_J || J_{k_1}^\pi) \langle J_{k_1}^\pi | J_{k_2}^\pi \rangle (J_{k_2}^\pi || \left[c_p^\dagger \tilde{c}_n \right]_J || 0_i^+) \, ,
\end{aligned}
\tag{3.15}
$$

where the summations over k_1 and k_2 run over the different left- and right-hand pnQRPA solutions for a given multipole J^π. Here the 2×3 quantity inside the curly brackets is the Wigner $6j$-symbol. The operators $\mathcal{O}_K$ inside the two-particle matrix element can be written as

$$
\begin{aligned}
\mathcal{O}_{\text{F}} &= h_{\text{F}}(r, E_k)[f_{\text{CD}}(r)]^2 \, , & (3.16) \\
\mathcal{O}_{\text{GT}} &= h_{\text{GT}}(r, E_k)[f_{\text{CD}}(r)]^2 \boldsymbol{\sigma}_1 \cdot \boldsymbol{\sigma}_2 \, , & (3.17) \\
\mathcal{O}_{\text{T}} &= h_{\text{T}}(r, E_k)[f_{\text{CD}}(r)]^2 S_{12}^{\text{T}} \, , & (3.18)
\end{aligned}
$$

where S_{12}^{T} is the tensor operator of Eq. (3.14) and $r = |\mathbf{r}_1 - \mathbf{r}_2|$ is the distance between the involved nucleons. The energy E_k is the average of the kth left- and right-hand-side pnQRPA-computed eigenvalues, corresponding to a given

multipole J^π. The term $\langle J^\pi_{k_1} | J^\pi_{k_2} \rangle$ is the overlap between the two sets of J^π states that, similarly as in Eq. (3.7), can be written as

$$\langle J^\pi_{k_1} | J^\pi_{k_2} \rangle = \sum_{pn} \left[X^{J^\pi_{k_1}}_{pn} \bar{X}^{J^\pi_{k_2}}_{pn} - Y^{J^\pi_{k_1}}_{pn} \bar{Y}^{J^\pi_{k_2}}_{pn} \right] , \qquad (3.19)$$

where X and Y ($\bar{X}$ and $\bar{Y}$) are the pnQRPA amplitudes of the final (initial) nucleus.

The factor $f_{\mathrm{CD}}(r)$ in Eqs. (3.16)–(3.18) involves the nucleon-nucleon short-range correlations (SRC) [84, 85]. We use the CD-Bonn form [86] for it, with the parametrization

$$f_{\mathrm{CD}}(r) = 1 - 0.46 \mathrm{e}^{-(1.52/\mathrm{fm}^2) r^2} [1 - (1.88/\mathrm{fm}^2) r^2] . \qquad (3.20)$$

Chapter 4

Charge-Exchange Reactions

Charge-exchange reactions (CXRs) of nuclei are strong-interaction reactions

$$\,_z^a a +\,_Z^A \mathrm{X} \rightarrow\,_{z\pm1}^a b +\,_{Z\mp1}^A \mathrm{Y}\,, \tag{4.1}$$

where a particle a with charge z interacts with the nucleus X with atomic number Z by changing the atomic number of the nucleus by one. At the same time a particle b with charge $z \mp 1$ is emitted. The charged particles (a, b) can be e.g. (p, n) or $(^3\mathrm{He}, t)$ for the β^--type reactions, or (n, p), $(d,^2\mathrm{He})$, or $(t,^3\mathrm{He})$ for the β^+-type reactions. In Refs. [87, 88] it was manifested that the virtual states and the corresponding charge-exchanging virtual transitions of $0\nu\beta\beta$ decay could be probed by the charge-exchange reactions starting from the initial/final nucleus of the $\beta\beta$ decay.

The virtual Gamow-Teller (GT) type transitions from 0^+ ground states of the initial and final even-even nuclei of the double-beta-decay triplet, which constitute the $2\nu\beta\beta$ decay NME, have traditionally been probed by the partial-wave $L = 0$ CXRs by using the β^- type of (p, n) or $(^3\mathrm{He},t)$ reactions and β^+ type of (n, p), $(d,^2\mathrm{He})$, or $(t,^3\mathrm{He})$ reactions [25, 27, 89]. Results of these studies can be compared with theoretical calculations of the Gamow-Teller and isovector spin-monopole (IVSM) strength distributions computed in, e.g., Refs. [90–92]. Recently, especially the partial-wave $L = 1$ CXRs to 2^- states have become popular by the improved experimental methods and facilities, e.g., the RCNP in Osaka, Japan [93]. These studies are considered to be relevant for the $0\nu\beta\beta$ decays, since a considerable part of the corresponding NME is built from virtual transitions via the $J^\pi = 2^-$ multipole states [78]. Inspired by this, we studied the $L = 1$ and $L = 2$ spin-multipole strength distributions in this thesis.

In Section 4.1 we will introduce the theoretical aspects of the spin-multipole transition strengths briefly, and in Section 4.2 we will summarize articles [**I**] and [**II**] of the thesis.

4.1 Spin-Multipole Operators and Transition Strengths

Here we are interested in the spin-dipole ($L = 1$) and spin-quadrupole ($L = 2$) type of transition strengths from 0_i^+ (0_f^+) ground state of the even-even initial (final) nucleus of the double-beta-decay triplet to J^π excited states of the intermediate odd-odd nucleus. The transition strength to ith J^π state can be written in the form [38]

$$S_{L,J}^\pm(i) = |(J_i^\pi||\mathcal{O}_{L,J}^\pm||0^+)|^2 \ , \tag{4.2}$$

where the reduced nuclear matrix element is written with the help of Wigner-Eckart theorem in the usual way as

$$(J^\pi||\mathcal{O}_{L,J}^\pm||0^+) = \sum_{a,b} \frac{(a||\mathcal{O}_{L,J}^\pm||b)}{\sqrt{2J+1}} (J^\pi||[c_a^\dagger \tilde{c}_b]_J||0^+) \ , \tag{4.3}$$

where a (b) denotes the initial (final) state quantum numbers, $(a||\mathcal{O}_{L,J}^\pm||b)$ is the reduced one-body transition matrix element, and $(J^\pi||[c_a^\dagger \tilde{c}_b]_J||0^+)$ is the one-body transition density introduced in Chapter 2.

For the spin-multipole transitions the transition operators are of the form

$$\mathcal{O}_{L,J}^\pm = r^L[\mathbf{Y}_L\boldsymbol{\sigma}]_J i^L t_\pm \ , \tag{4.4}$$

where $\mathbf{Y}_L$ is a spherical harmonic with the rank L, $\boldsymbol{\sigma}$ the Pauli spin vector, and t_+ (t_-) the isospin raising (lowering) operator [94]. Hence, the one-body transition matrix element in Eq. (4.3) becomes

$$\begin{aligned}
(a||\mathcal{O}_{L,J}^\pm||b) =& (n_f l_f \tfrac{1}{2} j_f ||r^L[\mathbf{Y}_L\boldsymbol{\sigma}]_J i^L||n_i l_i \tfrac{1}{2} j_i) \\
=& \sqrt{6}\hat{j}_f \hat{J}\hat{j}_i \frac{(-1)^{l_f}}{\sqrt{4\pi}}\hat{l}_f \hat{L}\hat{l}_i \begin{pmatrix} l_f & L & l_i \\ 0 & 0 & 0 \end{pmatrix} \begin{Bmatrix} l_f & \tfrac{1}{2} & j_f \\ l_i & \tfrac{1}{2} & j_i \\ L & 1 & J \end{Bmatrix} \\
& \times \mathcal{R}_{fi}^{(L)} (-1)^{\frac{1}{2}(l_i - l_f + L)} \ .
\end{aligned} \tag{4.5}$$

Here n denotes the principal quantum number, l the orbital angular momentum, and j the total angular momentum. The effect of the isospin operator is taken into account by the fact that the initial and final single-particle states have different isospin projections. The 2×3 quantity in the parenthesis is the Wigner 3j-symbol, and the 3×3 quantity inside the curly brackets is the Wigner 9j-symbol. $\mathcal{R}_{fi}^{(L)}$ is the radial integral defined in [38] as

$$\mathcal{R}_{fi}^{(L)} = \int_0^\infty g_{n_i l_i}(r) r^L g_{n_f l_f}(r) r^2 \mathrm{d}r \ , \tag{4.6}$$

where $g_{nl}(r)$ is the harmonic oscillator wave function corresponding to quantum numbers n and l.

4.2 Results

In Ref. [94] the authors studied isovector spin-dipole ($L = 1$) and spin-quadrupole ($L = 2$) transitions in a few closed-shell nuclei using the proton-neutron random-phase approximation (pnRPA) framework. In article [**I**] we have extended these studies by computing the isovector spin-dipole ($L = 1$) and spin-quadrupole ($L = 2$) transition-strength distributions in open-shell nuclei in the proton-neutron quasiparticle random-phase approximation (pnQRPA) framework with large no-core single-particle bases.

We investigated $L = 1$ transitions leading to excited states with spin-parities $J^\pi = 0^-, 1^-, 2^-$, and $L = 2$ transitions leading to the states with $J^\pi = 1^+, 2^+, 3^+$, in the key $\beta\beta$-decay triplets. The transitions from the 0^+ even-even nuclei (^{76}Ge,^{76}Se), (^{82}Se,^{82}Kr), (^{96}Zr,^{96}Mo), (^{100}Mo,^{100}Ru), (^{116}Cd,^{116}Sn), (^{128}Te,^{128}Xe), (^{130}Te,^{130}Xe), and (^{136}Xe,^{136}Ba) to the excited states of the intermediate odd-odd nuclei ^{76}As, ^{82}Br, ^{96}Nb, ^{100}Tc, ^{116}In, ^{128}I, ^{130}I, and ^{136}Cs are computed in the pnQRPA framework introduced in Sec. 2.3. Since we were interested in the giant-resonance regions of the spectra, we used large no-core single-particle bases in order to describe the spectra reliably at high energies up to $E = 50$ MeV.

We decomposed each isobaric $\beta\beta$-decay triplet with mass number A to "left-hand-side" even-even (A, N, Z), "right-hand-side" even-even ($A, N-2, Z+2$), and "intermediate" odd-odd ($A, N-1, Z+1$) nuclei, where N refers to the neutron number and Z to the atomic number of the nucleus. We formed the spectra of J^π excitations in the intermediate odd-odd nuclei applying the pnQRPA formalism to the left-hand-side and right-hand-side even-even nuclei. In this way we obtain two sets of energies and wave functions for each J^π state.

With the help of the pnQRPA wave functions we then formed the strength distributions of the isovector spin-dipole (IVSD) and isovector spin-quadrupole (IVSQ) excitations for the left-hand-side (IVSD- and IVSQ-) and right-hand-side (IVSD+ and IVSQ+) initial ground states. The corresponding strength functions to the ith J^π state of the odd-odd nucleus are

$$S(\text{IVSD}^-)(i) = |(J_i^\pi||\mathcal{O}_{1,J}^-||0_L^+)|^2 \tag{4.7}$$

$$S(\text{IVSD}^+)(i) = |(J_i^\pi||\mathcal{O}_{1,J}^+||0_R^+)|^2 \tag{4.8}$$

$$S(\text{IVSQ}^-)(i) = |(J_i^\pi||\mathcal{O}_{2,J}^-||0_L^+)|^2 \tag{4.9}$$

$$S(\text{IVSQ}^+)(i) = |(J_i^\pi||\mathcal{O}_{2,J}^+||0_R^+)|^2 \, , \tag{4.10}$$

where the operators $\mathcal{O}_{1,J}^\pm$ and $\mathcal{O}_{2,J}^\pm$ are the operators defined in Eq. (4.4).

Since the pnQRPA bases where we performed our calculations are discrete, the resulting strength distributions are also discrete, and not easily comparable with experiments. Therefore we folded them with a Lorentzian folding function [95]. The resulting Lorentzian folded strength distributions for two example cases: $A = 136$ and $A = 82$ are shown in Figs. 4.1 and 4.2. In the panels (a) we show the IVSD$^-$ distributions, corresponding to β^- transitions with $L = 1$ from the left-side even-even nucleus, for different multipoles J^π, in the panels (b) the analogous IVSD$^+$ distributions, corresponding to β^+ transitions from the right-side even-even nucleus, in the panels (c) the IVSQ$^-$ distributions, corresponding to β^- transitions with $L = 2$ from the left-side even-even nucleus, and in the panels (d) the analogous IVSQ$^+$ distributions, corresponding to β^+ transitions from the right-side even-even nucleus. The solid line represents the sum of the distributions with different multipolarities. The energies are given in MeV with respect to the ground state of the intermediate odd-odd nucleus.

Fig. 4.1 represents a typical case in our study: for the $L = 1$ β^- transitions the average energy is highest for the 0^- excitations and lowest for the 2^- excitations (for a few exceptions the average energy was lowest for the 1^- excitations, like in the example case shown in Fig. 4.2). This kind of behavior was also noticed in earlier studies of Refs. [94, 96, 97]. It can also be seen that the strength for $J^\pi = 0^-, 1^-$ is concentrated in a few peaks, whereas the strength for $J^\pi = 2^-$ is more spread, which was also noted in Ref. [94]. On the other hand, similar effects can be seen in the case of $L = 2$ β^- transitions: The 1^+ excitations are the highest in energy, whereas the 3^+ excitations are the lowest. $J^\pi = 1^+$ strength is concentrated on a few peaks, whereas for the $J^\pi = 2^+, 3^+$ excitations the strength distributions are much more fragmented. This was also seen in Ref. [94].

We also deduced the total transition strengths from the original pnQRPA spectra. It was seen that in the case of $L = 1$ transitions for both the IVSD$^-$ and IVSD$^+$ total strengths the largest fraction of the strength comes from 0^- transitions and smallest from 2^- transitions, except for the $A = 82$ system shown in Fig. 4.2, for which the 1^- excitations dominate the total transition strength. This kind of trend was also noted in Ref. [94] for closed-shell nuclei. However, in Ref. [94] it was concluded that for $L = 2$ transitions the largest fraction of the strengths comes from 1^+ excitations and smallest from 3^+ transitions, whereas in our study this was only true for the $A = 116$ and $A = 100$ cases. This is most likely due to the fact that we were dealing with open-shell nuclei whereas in [94] the nuclei are magic. The results of this study are summarized in more detail in Table III of article [**I**].

To conclude the results of article [**I**], we saw that there is a considerable difference in the giant-resonance energy centroids of the various J^π states
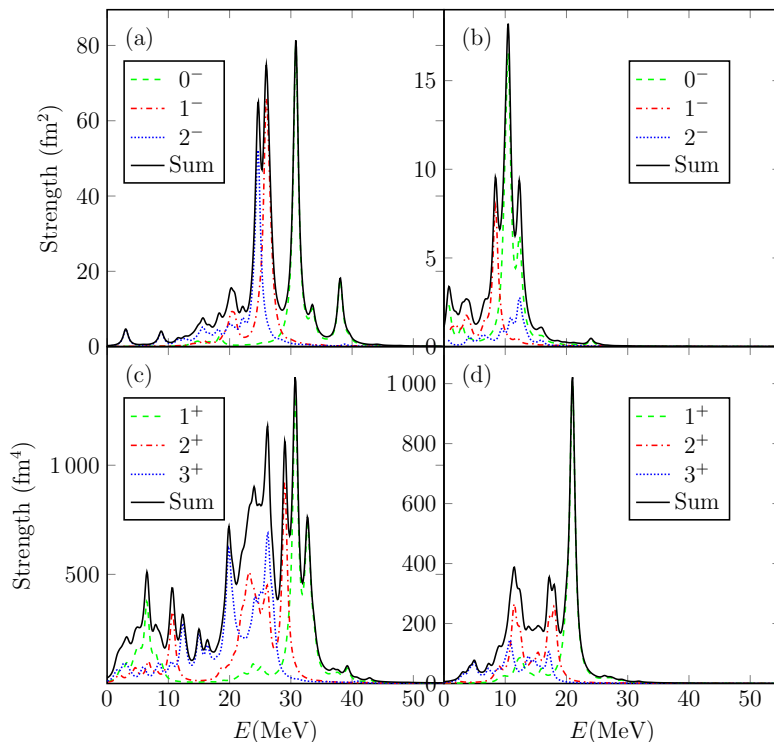
Figure 4.1. Isovector spin-multipole strength distributions for the $A = 136$ system. (a) $L = 1$ β^- (b) $L = 1$ β^+ (c) $L = 2$ β^- (d) $L = 2$ β^+. The solid line represents the sum of the dashed, dotted and dash-dotted individual contributions. Energies are measured relative to the ground state of the odd-odd final nucleus. The strengths are given in units of fm^2 for $J^\pi = 0^-, 1^-, 2^-$ and in fm^4 for $J^\pi = 1^+, 2^+, 3^+$. Figure: [**I**].

corresponding to a given L. For $L = 1$ transitions the transition strengths were highest for the lowest-J transitions and lowest for the highest-J transitions, except for the $A = 82$ system. For $L = 2$ transitions there was no clear ordering for the transition strengths.

The observations made in article [**I**] led to the idea of making comparisons between the calculated strength functions with available experimental data. This was done in article [**II**], where we compared the computed isovector spin-dipole ($L = 1$) $J^\pi = 2^-$ strength distributions in the $\beta\beta$-decay triplets against the experimental data that recently became available from (^{3}He,t) charge-exchange reactions performed at the Research Center for Nuclear Physics (RCNP), Osaka, Japan [25, 26, 89, 98–100]. We then computed the $0\nu\beta\beta$ NMEs based on the values of the 2^- particle-hole parameter $g_{\mathrm{ph}}(2^-)$, fixed for the first time by the observed locations of the IVSD giant resonances.

The particle-hole parameter g_{ph}, a key parameter of pnQRPA as stated
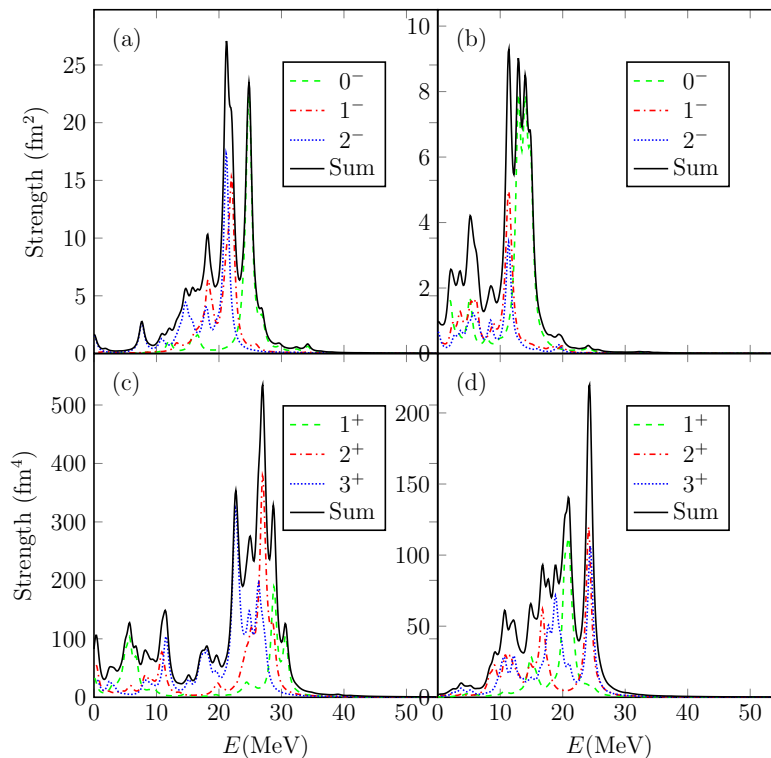
Figure 4.2. The same as in Fig. 4.1 for $A = 82$. Figure: [**I**].

in Sec. 2.3, is associated to the spin-isospin correlations and the locations of giant resonances [38]. Traditionally it has been adjusted to the location of Gamow-Teller giant resonance, and the fitted value $g_{\rm ph}(1^+)$ then together with the $g_{\rm pp}$ fixes the contribution of the 1^+ channel to the $0\nu\beta\beta$ NME. However, the 1^+ contributions are in many cases smaller than the contributions coming from the 2^- isovector spin-dipole excitations (see Fig. 4.3). This observation led to the idea of fixing the contribution of the 2^- channel separately to the observed locations of IVSD giant resonances. We used the traditional Gamow-Teller method as a starting point (we call this **Model 1**), but explore how the particle-hole parameter $g_{\rm ph}(2^-)$ changes the values of the $0\nu\beta\beta$ NMEs by fitting the $J^\pi = 2^-$ channel separately (**Model 2**) and by using the $g_{\rm ph}(2^-)$ parameter for all channels excluding the 1^+ channel (**Model 3**).

Based on these data reported in Refs. [25, 26, 89, 98–100], the experimental GT and IVSD centroid energies for the double-beta-decay nuclei of current interest can be expressed approximately as

$$
\begin{aligned}
E({\rm GT}) &\approx 9 + 0.4 T_Z \quad {\rm MeV} \\
E({\rm SD}) &\approx 16.5 + 0.4 T_Z \quad {\rm MeV} ,
\end{aligned}
\tag{4.11}
$$

Figure 4.3. Multipole decomposition of the total $0\nu\beta\beta$ nuclear matrix element $M^{(0\nu)}$ of (a) ^{76}Ge and (b) ^{128}Te. Figures: [**II**].
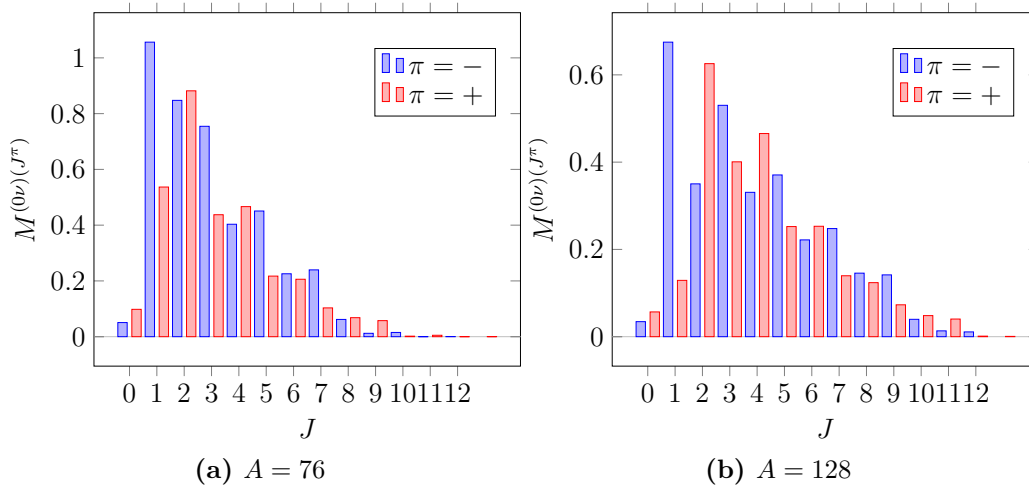
where $T_Z = \frac{1}{2}(N - Z)$. The uncertainties of the GT and IVSD energies are $\approx \pm 0.5$ MeV and $\approx \pm 1$ MeV, respectively. In article [**II**] we adjusted the $g_{\mathrm{ph}}(1^+)$ and $g_{\mathrm{ph}}(2^-)$ into these values, respectively. For $A = 96$ we used the measured centroid, as the linear fits of Eq. (4.11) did not reproduce the measured values well. The resulting particle-hole parameter values are introduced in Table 4.1. The 'WS' and 'sp' bases refer to the bare Woods-Saxon bases and their slightly modified versions, to better reproduce the experimental quasiparticle spectra of relevance to this study. In the cases of mass numbers $A = 96, 100$ the use of the bare Woods-Saxon bases resulted in a nonphysical g_{pp} behavior of the $2\nu\beta\beta$ results, and we used therefore only the sp bases. On the other hand, for $A = 116$ the use of the bare Woods-Saxon bases results in a good correspondence between the calculated and experimental quasiparticle spectra, so no modifications in the single-particle energies were necessary.

A couple of examples of the distributions corresponding to the different g_{ph} values listed in Table 4.1 are shown in Fig. 4.4. In the $A = 76$ case (panel (a)) the large, about 30%, deviation between the values of $g_{\mathrm{ph}}(1^+)$ and $g_{\mathrm{ph}}(2^-)$ (see Table 4.1) results in large deviations between the strength functions calculated using the WS basis. The same kind of observation can be seen in the $A = 116$ case (panel (b)). On the other hand, in the $A = 76$ case for the sp basis the difference between the different g_{ph} values is smaller, which leads to smaller deviations between the strength functions. The conclusion that can be drawn from these observations is that the strength functions are,

Table 4.1. Particle-hole parameters of the pnQRPA calculations for the key $0\nu\beta\beta$ decaying nuclei. Column two indicates the basis that was used in the calculations. Columns three and four list the experimental centroid energies of the IVSD $J^\pi = 2^-$ resonances and the GT $J^\pi = 1^+$ resonances. The last two columns list the values of the particle-hole parameters adjusted to the locations of the IVSD resonance and the GTGR. Table: [**II**].

Nucleus	Basis	$E(\text{SD2}^-)$ (MeV)	$E(\text{GT})$ (MeV	$g_{\text{ph}}(2^-)$	$g_{\text{ph}}(\text{GT})$
^{76}Ge	WS	18.9 ± 1.0	11.4 ± 0.5	0.9 ± 0.2	1.24 ± 0.13
	sp			1.2 ± 0.3	1.03 ± 0.13
^{96}Zr	sp	22 ± 1.0	12.7 ± 0.5	0.8 ± 0.2	0.84 ± 0.09
^{100}Mo	sp	19.7 ± 1.0	12.2 ± 0.5	1.0 ± 0.2	1.19 ± 0.08
^{116}Cd	WS	20.5 ± 1.0	13.0 ± 0.5	1.07 ± 0.09	0.85 ± 0.13
^{128}Te	WS	21.3 ± 1.0	13.8 ± 0.5	1.7 ± 0.2	1.64 ± 0.08
	sp			1.9 ± 0.2	1.40 ± 0.09
^{130}Te	WS	21.7 ± 1.0	14.2 ± 0.5	1.7 ± 0.2	1.58 ± 0.08
	sp			1.9 ± 0.2	1.36 ± 0.09
^{136}Xe	WS	22.1 ± 1.0	14.6 ± 0.5	1.0 ± 0.2	1.36 ± 0.07
	sp			0.9 ± 0.2	1.18 ± 0.08

indeed, quite sensitive to the value of g_{ph}.

The values of the total $0\nu\beta\beta$ matrix elements computed using the different models for the g_{ph} value are presented in Table 4.2. Here we only show the main results, and more comprehensive analysis is made in article [**II**]. The main point to notice on Table 4.2 is that the adoption of the IVSD $J^\pi = 2^-$-fitted value of g_{ph} for the 2^- channel of the $0\nu\beta\beta$ NMEs (Model 2) affects the NMEs negligibly for all of the cases but adoption of $g_{\text{ph}}(2^-)$ for all multipoles $J^\pi \neq 1^+$ (Model 3), however, causes larger deviations in all cases. All in all, the effect of $g_{\text{ph}}(\text{SD2}^-)$ is in most cases moderate even though in some cases there are notable differences between the different g_{ph} values in Table 4.1. On the other hand, the use of large no-core single-particle bases accounts for most of the deviations between the present NMEs and the ones of Ref. [78] computed in much smaller single-particle bases without access to the data on IVSD strength functions.

Altogether, the obtained results deviate from the results of Hyvärinen *et al* [78] by less than 4% for $A = 76$ and 136, and about $10 - 18$ % for the rest. The differences are mostly arising from the extension of the single-particle valence spaces, and the effect of variations in the value of g_{ph} is relatively smaller.

Table 4.2. Values of the $0\nu\beta\beta$ NMEs for $g_A^{\text{eff}} = 1.00$. The first column indicates the transition, the second column the basis used in the calculation, and the third one the model adopted for the g_{ph} values: Model-1: $g_{\text{ph}}(\text{GT})$ used for all J^π, Model-2: $g_{\text{ph}}(\text{SD2}^-)$ used for $J^\pi = 2^-$, for the rest $g_{\text{ph}}(\text{GT})$ is used, Model-3: $g_{\text{ph}}(\text{GT})$ used for $J^\pi = 1^+$, for the rest $g_{\text{ph}}(\text{SD2}^-)$ is used. The last row for each transition corresponds to the earlier calculations performed in Ref. [78]. The quoted errors only take into account uncertainties due to the strength of the particle-hole interaction. The table is a summary of Table V of [**II**].

Nuclear transition	Basis	Model	$M^{(0\nu)}$
$^{76}\text{Ge} \longrightarrow {}^{76}\text{Se}$	sp	1	6.9 ± 0.3
	sp	2	6.8 ± 0.3
	sp	3	6.6 ± 0.4
	sp, small [78]	1	6.54
$^{96}\text{Zr} \longrightarrow {}^{96}\text{Mo}$	sp	1	5.3 ± 0.2
	sp	2	5.3 ± 0.2
	sp	3	5.5 ± 0.4
	sp, small [78]	1	4.47
$^{100}\text{Mo} \longrightarrow {}^{100}\text{Ru}$	sp	1	5.54 ± 0.10
	sp	2	5.55 ± 0.11
	sp	3	5.9 ± 0.4
	sp, small [78]	1	4.98
$^{116}\text{Cd} \longrightarrow {}^{116}\text{Sn}$	WS	1	5.7 ± 0.2
	WS	2	5.7 ± 0.2
	WS	3	5.39 ± 0.13
	WS, small [78]	1	4.93
$^{128}\text{Te} \longrightarrow {}^{128}\text{Xe}$	sp	1	5.52 ± 0.15
	sp	2	5.47 ± 0.15
	sp	3	4.9 ± 0.3
	sp, small [78]	1	5.74
$^{130}\text{Te} \longrightarrow {}^{130}\text{Xe}$	sp	1	4.77 ± 0.12
	sp	2	4.72 ± 0.12
	sp	3	4.1 ± 0.2
	sp, small [78]	1	5.27
$^{136}\text{Xe} \longrightarrow {}^{136}\text{Ba}$	sp	1	3.72 ± 0.09
	sp	2	3.76 ± 0.10
	sp	3	4.1 ± 0.3
	sp, small [78]	1	3.50

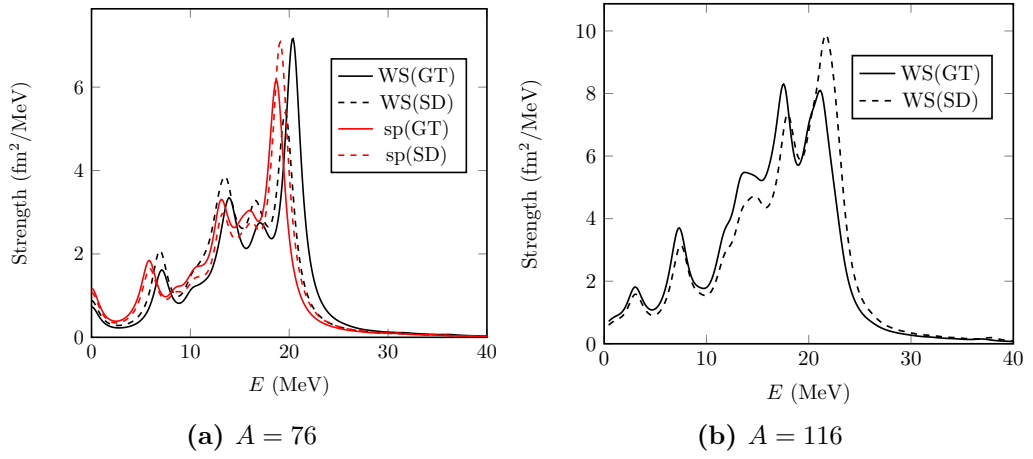**(a)** $A = 76$

(b) $A = 116$

Figure 4.4. Isovector spin-dipole $J^\pi = 2^-$ strength functions for (a)$A = 76$ and (b) $A = 116$ calculated using either a Woods-Saxon (WS) or a modified Woods-Saxon (sp) single-particle basis, and g_{ph} values obtained by fitting to the location of either the Gamow-Teller (GT) or the IVSD $J^\pi = 2^-$ giant resonance. Figures: [**II**].

30

Chapter 5

Ordinary Muon Capture

Ordinary muon capture (OMC) is a semileptonic weak interaction process quite like electron capture (EC). The OMC process we are interested in here can be written as

$$\mu^- + {}_Z^A X(0^+) \rightarrow \nu_\mu + {}_{Z-1}^A Y(J^\pi) \,, \tag{5.1}$$

where the negative muon (μ^-) is captured by the 0^+ ground state of the even-even nucleus X of mass number A and atomic number Z (see Fig. 5.1). The process leads to the J^π multipole states of Y, the odd-odd isobar of the mother nucleus, of atomic number $Z - 1$; here J is the angular momentum and π the parity of the final state. At the same time a muon neutrino ν_μ is emitted. In muon capture process also a gamma photon may be emitted. This kind of a reaction is called radiative muon capture (RMC). However, we will only consider the ordinary, non-radiative, version of muon capture.

The large mass of the captured muon, which is about 200 times the electron rest mass, makes the difference between OMC and EC. The momentum exchange involved in OMC, $Q \approx 50 - 100$ MeV, is remarkably larger than the momentum exchange taking place in EC or β decay. This induces highly forbidden transitions leading to final states with large angular momenta and high excitation energies. However, the large mass of the captured muon also leads to a more complex theoretical treatment of the process in contrast to EC or β decay. The muon recoil activates also induced parts of the nucleonic weak current, especially the pseudoscalar current [101–103], which means that the theoretical expression for the partial OMC rates gets complicated.

In Ref. [104], Kortelainen and Suhonen proposed that these features make OMC a particularly interesting probe for gaining information on the matrix elements of $0\nu\beta\beta$ decay. Since the large mass of the muon allows OMC to excite various J^π states in wide excitation-energy region, it could be used in investigations of the intermediate virtual states of $0\nu\beta\beta$ decay at
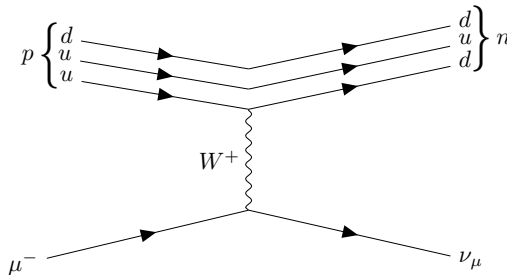
Figure 5.1. Ordinary muon capture.

high energies, where the EC or β decay -type of transitions can only probe the virtual transition through the lowest J^π state. Also the available data concerning the charge-exchange reactions introduced in Section 4 is, for the time being, restricted to certain multipoles, especially the data concerning higher multipoles being out of reach. In turn, partial OMC rates to states even with high multipolarities can be extracted [105]. That being said, it is not straightforward to extract the partial rates between definite nuclear states, since the high energy release excites numerous levels of the final nucleus.

On the other hand, testing g_A at high momentum transfer relevant for $0\nu\beta\beta$ decay is of utmost importance [106], and to that end OMC is an ideal probe. Since the induced terms of the effective weak current are activated in OMC, it can also be used as a test laboratory for the proton's induced pseudoscalar form factor g_P, which was already noticed in 1965 by Gillet and Jenkins [107].

Most of the basic concepts of muon physics are from 1950s and 1960s, the era of remarkable progress in the study of weak processes [108–110]. In 1953, Godfrey proposed the first partial muon capture rate measurement on ^{16}O [111]. Godfrey also established an approximate theoretical relation between muon-capture and β-decay matrix elements. In 1959, H. Primakoff published a comprehensive review of the theory of muon capture [112]. He introduced a phenomenological formula, nowadays known as the *Primakoff formula*, for the total muon capture rate

$$W_{\mathrm{Pr.}}(A, Z) = Z_{\mathrm{eff}}^4 X_1 \left[1 - X_2 \left(\frac{A - Z}{2A} \right) \right] . \tag{5.2}$$

Here A, Z and Z_{eff} are the mass number, atomic number and effective atomic number of the nucleus, X_1 the reduced muon-capture rate for OMC on hydrogen, and X_2 a parameter that takes into account the Pauli exclusion principle. The typical X factor values are

$$X_1 = 170 \ 1/\mathrm{s} \ \text{and} \ X_2 = 3.125 \ .$$

We will utilize this formula later on to estimate the total muon capture rates in the absence of experimental data.

The paper of Primakoff was soon followed by the paper of theory of allowed and forbidden muon capture by M. Morita and A. Fujii [29] in 1960. The robust formalism developed in the paper has been widely used [76, 77, 101, 102, 104, 107, 113–115], and it is also our choice in this thesis. Slightly different muon capture formalism, presented in the paper by Walecka [108], has also been employed in many studies, e.g. in [116–119]. It should be noted that the total capture rates obtained by this formalism seem to deviate from those obtained by the Morita-Fujii formalism. The origin of the discrepancy is yet not understood.

It is perhaps worth elaborating the Morita-Fujii formalism, since when performing the computations for this thesis it soon emerged that some improvements to the original formalism were in order. The formalism is quite involved, and those, who are not interested in all the details on the way, may proceed to Section 5.1.5, where the resulting muon capture rate formula is presented.

5.1 Ordinary Muon Capture Formalism

In this section, we will mainly follow the steps made in the paper of Morita and Fujii [29] and add some clarification and/or update, where needed. We will start by introducing some necessary Dirac algebra and notations that we will face in the ordinary muon capture theory of Morita and Fujii [29]. Then, we will go trough the involved effective Hamiltonian, lepton wave functions, nuclear matrix elements, and finally the capture rate. In the end, some future prospects to develop the muon capture theory are discussed.

5.1.1 Preparation: Dirac algebra and Notations

In the mathematical formulation of muon capture, we will use the Dirac algebra familiar in the particle and neutrino physics fields. Since there are numerous different representations for the Dirac gamma matrices, we will start by introducing the representation adopted in the Morita-Fujii theory. Here the Dirac gamma matrices, which are the generators of the Euclidean Clifford algebra, satisfy the anticommutation relations

$$\{\gamma_\mu, \gamma_\nu\} = \gamma_\mu\gamma_\nu + \gamma_\nu\gamma_\mu = 2\delta_{\mu\nu}\mathbf{1_4} \, , \tag{5.3}$$

where $\delta_{\mu\nu}$ is the Kronecker delta, and $\mathbf{1}$ the 4-by-4 identity matrix. Morita and Fujii chose the non-relativistic representation for the gamma matrices,

33

with the sign convention traditionally used in the β-decay theory [120, 121]. In this representation, the gamma matrices are written as

$$\boldsymbol{\gamma} = \begin{pmatrix} 0 & -i\boldsymbol{\sigma} \\ i\boldsymbol{\sigma} & 0 \end{pmatrix} , \quad \gamma_4 = \begin{pmatrix} -\mathbf{1_2} & 0 \\ 0 & \mathbf{1_2} \end{pmatrix} , \quad \gamma_5 = \gamma_1\gamma_2\gamma_3\gamma_4 = \begin{pmatrix} 0 & \mathbf{1_2} \\ \mathbf{1_2} & 0 \end{pmatrix} , \quad (5.4)$$

where $\boldsymbol{\sigma}$ is the Pauli vector defined as

$$\boldsymbol{\sigma} = (\sigma_1, \sigma_2, \sigma_3) ,$$

whose components are the familiar 2x2 Pauli matrices.

Since the lepton spinors we are operating at are four-vectors, we need 4x4 Pauli matrices traditionally called Σ_i. They are defined (in the vector form) as

$$\boldsymbol{\Sigma} = \begin{pmatrix} \boldsymbol{\sigma} & 0 \\ 0 & \boldsymbol{\sigma} \end{pmatrix} . \quad (5.5)$$

Furthermore, we will need the α_i and β matrices familiar from the Dirac theory. They are all Hermitian and unitary, and they are defined as

$$\boldsymbol{\alpha} = \begin{pmatrix} 0 & \boldsymbol{\sigma} \\ \boldsymbol{\sigma} & 0 \end{pmatrix} , \quad \beta = \begin{pmatrix} \mathbf{1_2} & 0 \\ 0 & -\mathbf{1_2} \end{pmatrix} . \quad (5.6)$$

Trough the muon-capture theory we adopt the units $\hbar = c = m_e = 1$, and use the shorthand notation κ for the total and orbital angular momentum, j and l, of the neutrino. κ is defined such that

$$\boxed{\begin{aligned} &l = \kappa \ \ \text{and} \ \ j = l - \tfrac{1}{2} \ \ \text{for} \ \ \kappa > 0 \\ &l = -\kappa - 1 \ \ \text{and} \ \ j = l + \tfrac{1}{2} \ \ \text{for} \ \ \kappa < 0 . \end{aligned}} \quad (5.7)$$

Hence, summation over κ means summation over all possible values of j and l. The orbital angular momenta corresponding to κ and $-\kappa$ are distinguished by denoting them as l and $\bar{l}$, respectively.

We will change the notation of the coupling constants in the Morita-Fujii paper by making the replacements

$$C_{\mathrm{V}} \rightarrow g_{\mathrm{V}} \ , \ C_{\mathrm{A}} \rightarrow -g_{\mathrm{A}} \ \text{and} \ C_{\mathrm{P}} \rightarrow -g_{\mathrm{P}}$$

in order to be consistent with the convention used in the earlier papers of the Jyväskylä group [76, 77, 101, 102, 104].

5.1.2 Effective Hamiltonian

Before jumping into the definition of the muon capture matrix elements we need to introduce the underlying interaction Hamiltonian. If the lepton bare-nucleon coupling is assumed to be via vector and axial vector interactions of the Fermi type, the interaction Hamiltonian density for ordinary muon capture by a proton, $\mu^- + p \to \nu_\mu + n$, can be written as [29, 122]

$$H = \bar{\psi}_n \mathcal{H} \psi_p$$

with

$$
\begin{aligned}
\sqrt{2}\mathcal{H} =& \gamma_\lambda[g_V(\bar{\psi}_\nu \gamma_\lambda \psi_\mu) + g_V'(\bar{\psi}_\nu \gamma_\lambda \gamma_5 \psi_\mu)] \\
& - i\gamma_\lambda \gamma_5 [g_A(\bar{\psi}_\nu i\gamma_\lambda \gamma_5 \psi_\mu) + g_A'(\bar{\psi}_\nu i\gamma_\lambda \psi_\mu)] \\
& - \gamma_5[g_P(\bar{\psi}_\nu \gamma_5 \psi_\mu) - g_P'(\bar{\psi}_\nu \psi_\mu)] \\
& + \sigma_{\lambda\rho}[g_M p_\rho(\bar{\psi}_\nu i\gamma_\lambda \psi_\mu) + g_M' p_\rho(\bar{\psi}_\nu i\gamma_\lambda \gamma_5 \psi_\mu)] \,,
\end{aligned}
\tag{5.8}
$$

where

$$\bar{\psi} = \psi^\dagger \gamma_4$$

and

$$\sigma_{\lambda\rho} = \frac{1}{2}[\gamma_\lambda \gamma_\rho - \gamma_\rho \gamma_\lambda] \,.$$

The subscripts n, p, ν and μ refer to the neutron, proton, neutrino, and muon, respectively. The gammas $\gamma_{\lambda,\rho,5}$ are the gamma matrices defined in Sec. 5.1.1 and p_ρ the four-momentum $p_\rho = (-i\nabla, -\partial/\partial t)$, which acts on the lepton covariants, but not on ψ_p.

The first three terms in Eq. (5.8) represent the vector, axial vector and induced pseudoscalar interactions, respectively. The last term is the interaction that is added by the conserved vector current (CVC) hypothesis. Assuming time reversal invariance of the Hamiltonian, all the coupling constants g and g' can be chosen to be real. Furthermore, assuming that the neutrino is (almost) left-handed we can conclude that $g_i = g_i'$. Comparing then the weak current with the electromagnetic current gives

$$g_M = g_V(\mu_p - \mu_n)/(2M) \,,$$

where $\mu_p(\mu_n)$ is the magnetic moment of proton(neutron) in nuclear magnetons, for which $\mu_p - \mu_n = 3.706$, and M is the average nucleon mass. The partially conserved axial-vector current (PCAC) hypothesis suggests a Goldberger-Treiman value for the ratio $g_P/g_A = 6.8$ [123] (note that this value is different from the one suggested in Ref. [29]) for free nucleons, but the value of g_P may need to be renormalized in the nuclear medium.

Using the above-mentioned couplings, the Hamiltonian density can be written as

$$H = \psi_n^\dagger \mathbf{H} \psi_p$$

with

$$\begin{aligned}
\mathbf{H} =& g_V[\mathbf{1_4} \cdot L(\mathbf{1_4}) - \boldsymbol{\alpha} \cdot L(\boldsymbol{\alpha})] \\
& - g_A[\boldsymbol{\Sigma} \cdot L(\boldsymbol{\Sigma}) - \gamma_5 \cdot L(\gamma_5)] - g_P \beta \gamma_5 \cdot L(\beta \gamma_5) \\
& + (g_V/(2M))(\mu_p - \mu_n)[-i\beta \boldsymbol{\Sigma} \cdot \mathbf{p} \times L(\boldsymbol{\alpha}) + \beta \boldsymbol{\alpha} \cdot \mathbf{p} L(\mathbf{1_4}) - i\beta \boldsymbol{\alpha} \cdot p_4 L(\boldsymbol{\alpha})] \,,
\end{aligned}$$
(5.9)

where p_4 is the fourth component of the momentum four-vector, corresponding to energy. Furthermore, the lepton covariants are abbreviated as

$$L(\sigma) = \psi_\nu^\dagger[(1 + \gamma_5)/\sqrt{2}]\sigma\psi_\mu \,.$$
(5.10)

Contrary to the β decay theory we cannot leave the nuclear matrix elements as phenomenological parameters, since we only know the transition rate of the muon capture reaction but not the shape of the neutrino spectrum. Therefore, we have to reduce all the relativistic nuclear matrix elements (i.e. the momentum-type matrix elements) into nonrelativistic forms. This in done in [29] by transforming the nuclear part of the interaction Hamiltonian (5.9) into nonrelativistic form by the Foldy-Wouthuysen transformation modified by Rose and Osborn [124]. The relativistic nucleon wave function

$$\psi = \begin{pmatrix} v \\ u \end{pmatrix}$$

is replaced by

$$\psi = \begin{pmatrix} -\frac{1}{2M}\boldsymbol{\sigma} \cdot \mathbf{p} u \\ u \end{pmatrix} \,,$$
(5.11)

where u and v are the large and small components of the Dirac spinor, corresponding to the eigenvalues -1 and $+1$ of the β matrix of Eq. (5.6), correspondingly.

The transformed interaction Hamiltonian becomes

$$H = u_n^\dagger \mathbf{H} u_p$$

with

$$\begin{aligned}
\mathbf{H} =& g_V \mathbf{1} \cdot L(\mathbf{1}) - g_A \boldsymbol{\sigma} \cdot L(\boldsymbol{\sigma}) \\
& + (g_V/2M)[2L(\alpha) \cdot \mathbf{p} + \mathbf{p} \cdot L(\alpha) + i\boldsymbol{\sigma} \cdot \mathbf{p} \times L(\alpha)] \\
& - (g_A/2M)[2L(\gamma_5)\boldsymbol{\sigma} \cdot \mathbf{p} + \boldsymbol{\sigma} \cdot \mathbf{p} L(\gamma_5)] \\
& + (g_P/2M)\boldsymbol{\sigma} \cdot \mathbf{p} L(\beta\gamma_5) + (\mu_p - \mu_n)(g_V/2M)[i\boldsymbol{\sigma} \cdot \mathbf{p} \times L(\alpha)] \,,
\end{aligned}$$
(5.12)

where all terms of the order $1/M^2$ are omitted. The differential operators only act on the lepton covariants but not on u_p.

5.1.3 Lepton Wave functions

In order to form the matrix elements for the muon capture process we need to describe the involved leptons, i.e. the muon and the muon neutrino, in terms of wave functions. We will begin with introducing the wave function of the emitted neutrino.

The spherical wave function for the free neutrino with linear momentum $\mathbf{q}$ and spin $m = \pm\frac{1}{2}$ can be written as an expansion in terms of the normalized spherical spinors $\chi_{\kappa\mu}$

$$\psi_\nu(\mathbf{q}, m; \mathbf{r}) = \sum_{\kappa\mu} i^l (l\ \mu - m\ \tfrac{1}{2}\ m | j\mu) Y_l^{\mu-m}(\hat{q}) \psi_{\kappa\mu}^{(\nu)} , \qquad (5.13)$$

where

$$\psi_{\kappa\mu}^{(\nu)} = \begin{pmatrix} -if_\kappa \chi_{-\kappa\mu} \\ g_\kappa \chi_{-\kappa\mu} \end{pmatrix} , \qquad (5.14)$$

and

$$g_\kappa = \pi^{-1/2} j_l(qr) , \quad f_\kappa = \pi^{-1/2} S_\kappa j_{\bar{l}}(qr) ,$$
$$\chi_{\kappa\mu} = \sum_{m'} (l\ \mu - m'\ \tfrac{1}{2}\ m' | j\mu) Y_{l,\mu-m'}(\hat{r}) \psi_{1/2}^{m'} . \qquad (5.15)$$

Here $j_l(qr)$ is the spherical Bessel function, S_κ the sign of κ, $Y_{l,\mu-m'}$ the Laplace's spherical harmonics and $\psi_{1/2}^{m'}$ the spin wave functions in two dimensions. The quantities $(j_1\ m_1\ j_2\ m_2 | j_3\ m_3)$ in Eqs. (5.13) and (5.15) are the Glebsch-Gordan coefficients. The angular momenta l and $\bar{l}$ correspond to κ and $-\kappa$, respectively. The neutrino wave function of Eq. (5.13) is normalized such that

$$\int \psi_\nu^\dagger(\mathbf{q}', m'; \mathbf{r}) \psi_\nu(\mathbf{q}, m; \mathbf{r}) d\mathbf{r} = \delta_{mm'} \delta(\mathbf{q}' - \mathbf{q}) . \qquad (5.16)$$

The wave function of the captured muon can be expressed in a similar way as the free neutrino wave function. However, since the muon is initially bound on an atomic orbit of the initial nucleus, the wave function corresponds to a definite orbit. That is, the bound state muon wave function can be written as

$$\psi_\mu(\kappa, \mu; \mathbf{r}) = \psi_{\kappa\mu}^{(\mu)} = \begin{pmatrix} -iF_\kappa \chi_{-\kappa\mu} \\ G_\kappa \chi_{\kappa\mu} \end{pmatrix} , \qquad (5.17)$$

where G_κ and F_κ are the radial wave functions of the bound state [29].

After being stopped in the outer shells of an atom, the negative muon undergoes multiple transitions to lower atomic orbitals, leaving it finally on the lowest, K atomic orbit. Hence, the captured muon can be assumed to be initially bound in the lowest state $0s_{1/2}$ corresponding to $\kappa = -1$ and

$\mu = \pm\frac{1}{2}$. In Ref. [29] the authors adopt the explicit form for the muon bound on the $0s_{1/2}$ orbit given by Bethe and Salpeter [125], where point-like nucleus is assumed. Using this approximation, the radial wave functions are

$$G_{-1} = (2Z/a_0)^{\frac{3}{2}} \sqrt{\frac{1+\gamma}{2\Gamma(2\gamma+1)}} \left(\frac{2Zr}{a_0}\right)^{\gamma-1} e^{-Zr/a_0} \,,$$
$$F_{-1} = -\sqrt{\frac{1-\gamma}{1+\gamma}} G_{-1} \,, \tag{5.18}$$

where α is the fine structure constant, Z the atomic number of the initial nucleus,

$$\gamma = \sqrt{1-(\alpha Z)^2} \,,$$

and

$$a_0 = \frac{\hbar}{m'_\mu c\alpha} = \frac{1}{m'_\mu}$$

is the Bohr radius of the μ-mesonic atom [126], where

$$m'_\mu = \frac{m_\mu}{1 + \frac{m_\mu}{AM}} \tag{5.19}$$

is the reduced muon mass in the μ-mesonic atom. If we assume that αZ is very small, $\gamma \approx 1$, and therefore

$$G_{-1} = 2(\alpha Z m'_\mu)^{\frac{3}{2}} e^{-\alpha Z m'_\mu r} \,,$$
$$F_{-1} = 0 \,. \tag{5.20}$$

The muon wave function of Eq. (5.17) is normalized such that

$$\int \psi_\mu^\dagger(\kappa', \mu'; \mathbf{r}) \psi_\mu(\kappa, \mu; \mathbf{r}) d\mathbf{r} = \delta_{\kappa\kappa'}\delta_{\mu\mu'} \,. \tag{5.21}$$

5.1.4   Nuclear Matrix Elements

Using the wave functions of Sec. 5.1.3 one can then evaluate the spherical components of the interaction Hamiltonian introduced in Sec. 5.1.2 defined by

$$(\kappa\mu|\mathbf{H}|\kappa'\mu') \equiv (\psi_{\kappa\mu}^{(\nu)}, \mathbf{H}\psi_{\kappa'\mu'}^{(\mu)}) \,. \tag{5.22}$$

The spherical components of each term in the Hamiltonian (5.12) are listed in Ref. [29], and we will not list those in here.

The reduced transition matrix elements were then defined by using the Wigner-Eckart theorem as

$$\int \Psi_{J_f M_f} \sum_{s=1}^{A} \Xi_{vu}^{s(i)} \tau_-^s \Psi_{J_i M_i} d\mathbf{r}_1 ... d\mathbf{r}_A$$
$$= (J_i \ M_i \ u \ M_f - M_i | J_f \ M_f) \mathcal{M}_{vu}^{(i)} \ , \tag{5.23}$$

where $J_i \ M_i \ u \ M_f - M_i | J_f \ M_f)$ is a Glebsch-Gordan coefficient, and $C^{(i)}$ and $\Xi_{vu}^{s(i)}$ are as defined in Table 5.1. The S-factors showing up in the operators $\Xi_{vu}^{s(i)}$ are defined as

$$S_{k\nu u}(\kappa, \kappa') = \sqrt{2(2l+1)(2l'+1)(2j+1)(2j'+1)}(l \ 0 \ l' \ 0 | \nu \ 0) \begin{Bmatrix} l & l' & \nu \\ j & j' & u \\ \frac{1}{2} & \frac{1}{2} & k \end{Bmatrix} \tag{5.24}$$

for $k = 0$ and 1. Here the 3×3 quantity inside the curly brackets is the Wigner $9j$-symbol. The (vector) spherical harmonics $\mathcal{Y}_{kwu}^M$ in the equations of Table 5.1 are defined as

$$\mathcal{Y}_{0wu}^M(\hat{\mathbf{r}}) \equiv (4\pi)^{-1/2} Y_{w,M}(\hat{\mathbf{r}}) \ ,$$
$$\mathcal{Y}_{1wu}^M(\hat{\mathbf{r}}, \boldsymbol{\sigma}) \equiv \sum_m (1 \ - m \ w \ m + M | u \ M)$$
$$\times Y_{w,m+M}(\hat{\mathbf{r}}) \sqrt{\frac{3}{4\pi}} \sigma_{-m} \ , \tag{5.25}$$

where $\boldsymbol{\sigma}$ is the Pauli spin vector, $Y_{w,M}(\hat{\mathbf{r}})$ are the spherical harmonics and $\hat{\mathbf{r}}$ is the unit coordinate vector for the angles in spherical coordinates. The quantity $j_w(qr_s)$ is the spherical Bessel function.

Finally, the matrix elements with the bound muon wave function obtained form the Bethe-Salepeter formula of Eq. (5.20) are defined in the following manner:

$$\int \Psi_{J_f M_f} \sum_{s=1}^{A} e^{-\alpha Z m'_\mu r_s} \mathcal{O}_s \tau_-^s \Psi_{J_i M_i} d\mathbf{r}_1 ... d\mathbf{r}_A$$
$$= \mathcal{M}[k \ w \ u \begin{pmatrix} \pm \\ p \end{pmatrix}] (J_i \ M_i \ u \ M_f - M_i | J_f \ M_f) \ , \tag{5.26}$$

where $\Psi_{J_f M_f}$ ($\Psi_{J_i M_i}$) is the final (initial) nuclear wave function. The definition for the operator $\mathcal{O}_s$ can be found in Table 5.2.

In our calculations, we write the matrix elements of Eq. (5.26) in terms

Table 5.1. $C^{(i)}$ and $\Xi^{s(i)}_{vu}$ in Eq. (5.23). The differential operators $D_{\pm}$ are given by $D_+ = \frac{\mathrm{d}}{\mathrm{d}r} - \frac{1}{r}$ and $D_- = \frac{\mathrm{d}}{\mathrm{d}r} + \frac{v+1}{r}$. The f_κ, g_κ, $F_{\kappa'}$ and $G_{\kappa'}$ are the components of the neutrino and muon wave functions of Eqs. (5.14) and (5.17). The factors $S_{k\nu u}(\kappa, \kappa')$ are defined in Eq. (5.24), and the spherical harmonics $\mathcal{Y}^M_{k\nu u}$ in Eqs. (5.25). In the last line, $+$ and $-$ signs refer to $i = 7$ and 8, respectively.

i	$C^{(i)}$	$\Xi^{s(i)}_{vu}$
1	g_{V}	$\mathcal{Y}^{M_f - M_i}_{0vu}(\hat{\mathbf{r}}_s)[g_\kappa G_{\kappa'} S_{0vu}(\kappa, \kappa') - f_\kappa F_{\kappa'} S_{0vu}(-\kappa, -\kappa')]\delta_{vu}$
2	g_{A}	$\mathcal{Y}^{M_f - M_i}_{1vu}(\hat{\mathbf{r}}_s, \boldsymbol{\sigma}_s)[g_\kappa G_{\kappa'} S_{1vu}(\kappa, \kappa') - f_\kappa F_{\kappa'} S_{1vu}(-\kappa, -\kappa')]$
3	$-\frac{g_{\mathrm{M}}}{M}$	$i[f_\kappa G_{\kappa'} S_{1vu}(-\kappa, \kappa') + g_\kappa F_{\kappa'} S_{1vu}(\kappa, -\kappa')]\mathcal{Y}^{M_f - M_i}_{1vu}(\hat{\mathbf{r}}_s, \mathbf{p}_s)$
4	$-\frac{\sqrt{3}g_{\mathrm{V}}}{2M}$	$\left(\sqrt{\frac{v+1}{2v+3}}\mathcal{Y}^{M_f - M_i}_{0v+1u}(\hat{r}_s)\delta_{v+1u}D_+ - \sqrt{\frac{v}{2v-1}}\mathcal{Y}^{M_f - M_i}_{0v-1u}(\hat{r}_s)\delta_{v-1u}D_-\right)$
		$\times[f_\kappa G_{\kappa'} S_{1vu}(-\kappa, \kappa') + g_\kappa F_{\kappa'} S_{1vu}(\kappa, -\kappa')]$
5	$-\sqrt{\frac{3}{2}}\frac{g_{\mathrm{V}}(1+\mu_p-\mu_n)}{M}$	$(\sqrt{v+1}W(11uv, 1v+1) \times \mathcal{Y}^{M_f - M_i}_{1v+1u}(\hat{r}_s, \boldsymbol{\sigma}_s)D_+$
		$-\sqrt{v}W(11uv, 1v-1)\mathcal{Y}^{M_f - M_i}_{1v-1u}(\hat{r}_s, \boldsymbol{\sigma}_s)D_-)$
		$\times[f_\kappa G_{\kappa'} S_{1vu}(-\kappa, \kappa') + g_\kappa F_{\kappa'} S_{1vu}(\kappa, -\kappa')]$
6	$-\frac{g_{\mathrm{A}}}{M}$	$i\mathcal{Y}^{M_f - M_i}_{0vu}(\hat{r}_s)[f_\kappa G_{\kappa'} S_{0vu}(-\kappa, \kappa') + g_\kappa F_{\kappa'} S_{0vu}(\kappa, -\kappa')]\boldsymbol{\sigma}_s \cdot \mathbf{p}_s$
7	$\frac{g_{\mathrm{A}}}{2\sqrt{3}M}$	$\left(\sqrt{\frac{v+1}{2v+1}}\mathcal{Y}^{M_f - M_i}_{1v+1u}(\hat{r}_s, \boldsymbol{\sigma}_s)D_+ - \sqrt{\frac{v}{2v+1}}\mathcal{Y}^{M_f - M_i}_{1v-1u}(\hat{r}_s, \boldsymbol{\sigma}_s)D_-\right)$
8	$-\frac{g_{\mathrm{P}}}{2\sqrt{3}M}$	$\times[f_\kappa G_{\kappa'} S_{0vu}(-\kappa, \kappa') \pm g_\kappa F_{\kappa'} S_{0vu}(\kappa, -\kappa')]\delta_{vu}$

of reduced matrix elements as

$$
\begin{aligned}
\mathcal{M}\left[kwu\binom{\pm}{p}\right] &= \hat{J}^{-1}\sum_{pn}(n||\mathcal{O}_{[kwu\binom{\pm}{p}]}||p)u^{-1}(J_f||[c_n^\dagger \tilde{c}_p]||J_i) \\
&= \hat{J}^{-1}\sum_{pn}(n||\mathcal{O}_{[kwu\binom{\pm}{p}]}||p)\mathrm{OBTD} ,
\end{aligned}
\tag{5.27}
$$

where OBTD is the reduced one-body transition density having the expressions (2.6)-(2.7) in the case of the pnQRPA wave functions. The quantities $(n||\mathcal{O}_{[kwu\binom{\pm}{p}]}||p)$ are the one-body matrix elements corresponding to the operators defined in Table 5.2 and evaluated in the harmonic-oscillator basis. Through the OBTDs it is straightforward to implement the initial and final nuclear wave functions, computed in any nuclear model, in our calculations.

Table 5.2. Definition of $\mathcal{O}_s$ in Eq. (5.26) for different nuclear matrix elements (NMEs).

NME	$\mathcal{O}_s$
$\mathcal{M}[0\,w\,u]$	$j_w(qr_s)\mathcal{Y}_{0wu}^{M_f-M_i}(\hat{\mathbf{r}}_s)\delta_{wu}$
$\mathcal{M}[1\,w\,u]$	$j_w(qr_s)\mathcal{Y}_{1wu}^{M_f-M_i}(\hat{\mathbf{r}}_s,\boldsymbol{\sigma}_s)$
$\mathcal{M}[0\,w\,u\pm]$	$[j_w(qr_s)\pm\alpha Z(m'_\mu/p_\nu)j_{w\mp1}(qr_s)]\mathcal{Y}_{0wu}^{M_f-M_i}(\hat{\mathbf{r}}_s)\delta_{wu}$
$\mathcal{M}[1\,w\,u\pm]$	$[j_w(qr_s)\pm\alpha Z(m'_\mu/p_\nu)j_{w\mp1}(qr_s)]\mathcal{Y}_{1wu}^{M_f-M_i}(\hat{\mathbf{r}}_s,\boldsymbol{\sigma}_s)$
$\mathcal{M}[0\,w\,u\,p]$	$ij_w(qr_s)\mathcal{Y}_{0wu}^{M_f-M_i}(\hat{\mathbf{r}}_s)\boldsymbol{\sigma}_s\cdot\mathbf{p}_s\delta_{wu}$
$\mathcal{M}[1\,w\,u\,p]$	$ij_w(qr_s)\mathcal{Y}_{1wu}^{M_f-M_i}(\hat{\mathbf{r}}_s,\mathbf{p}_s)$

5.1.5 Capture Rate

The muon-capture transition rate from an initial state J_i to a final state J_f can, following the formalism of Ref. [29], be written as

$$W = 2\pi\langle|M.E.|^2\rangle_{\text{av}}q^2\frac{\mathrm{d}q}{\mathrm{d}E_f} \tag{5.28}$$

with the phase-space factor

$$\frac{\mathrm{d}q}{\mathrm{d}E_f} = 1 - \frac{q}{m_\mu + AM} \ , \tag{5.29}$$

where A and M are the mass number of the nucleus and the average nucleon mass, and the Q value of the OMC process is defined as

$$q = (m_\mu - W_0)\left(1 - \frac{m_\mu - W_0}{2(M_f + m_\mu)}\right) \ , \tag{5.30}$$

where $W_0 = M_f - M_i + m_e + E_X$. Here M_f and M_i are the nuclear masses of the final and initial nuclei, m_e the rest mass of an electron and E_X the excitation energy of the final-state nucleus.

The $\langle|M.E.|^2\rangle_{\text{av}}$ in Eq. (5.28) is the absolute square of the OMC matrix element summed over all magnetic quantum numbers, integrated over $\mathbf{q}$, and

averaged over the initial substates resulting in

$$\langle |M.E.|^2 \rangle_{\text{av}} = \frac{2J_f + 1}{(2j' + 1)(2J_i + 1)} \times \sum_{ij} \sum_{\kappa u} \left[C^{(i)} \sum_{\nu} \mathcal{M}_{\nu u}^{(i)} \right]^* \left[C^{(j)} \sum_{\nu'} \mathcal{M}_{\nu' u}^{(j)} \right] ,$$

(5.31)

where j' is the angular momentum of the captured muon (here $j' = 1/2$, since we assumed that the muon is bound on the $0s_{1/2}$ orbit) and $C^{(i)}$ and $\mathcal{M}_{\nu u}^{(i)}$ are defined in Table 5.1.

Using the above mentioned interaction Hamiltonian and bound muon wave functions, the muon capture rate to a J^π final state is written as

$$W = 8 \left(\frac{Z_{\text{eff}}}{Z} \right)^4 P(\alpha Z m'_\mu)^3 \frac{2J_f + 1}{2J_i + 1} \left(1 - \frac{q}{m_\mu + AM} \right) q^2 ,$$

(5.32)

where A indicates the mass number of the initial and final nuclei, Z the atomic number of the initial nucleus, J_i (J_f) the angular momentum of the initial (final) nucleus, M the average nucleon rest mass, m_μ the bound muon mass, m'_μ the reduced mass of the muon in the parent μ-mesonic atom, α the fine-structure constant and q the exchanged momentum between the captured muon and the nucleus [29], i.e. the Q value of the OMC.

For heavy nuclei the atomic orbit of the muon penetrates the nucleus and therefore the capture rate has to be corrected for the muonic screening. Here we followed the Primakoff method [112] correcting the capture rate by the factor $(Z_{\text{eff}}/Z)^4$, where the effective atomic number Z_{eff} for different nuclei is obtained from the work of Ford and Wills [127].

The term P in Eq. (5.32) can be written as

$$
\begin{aligned}
P = \frac{1}{2}\sum_{\kappa u} \Big| & g_{\mathrm{V}}\mathcal{M}[0\,l\,u]S_{0u}(\kappa)\delta_{lu} \\
& + g_{\mathrm{A}}\mathcal{M}[1\,l\,u]S_{1u}(\kappa) - \frac{g_{\mathrm{V}}}{M}\mathcal{M}[1\,\bar{l}\,u\,p]S'_{1u}(-\kappa) \\
& + \sqrt{3}\frac{g_{\mathrm{V}}q}{2M}\Big(\sqrt{\frac{\bar{l}+1}{2\bar{l}+3}}\mathcal{M}[0\,\bar{l}+1\,u\,+]\delta_{\bar{l}+1,u} \\
& + \sqrt{\frac{\bar{l}}{2\bar{l}-1}}\mathcal{M}[0\,\bar{l}-1\,u\,-]\delta_{\bar{l}-1,u}\Big)S'_{1u}(-\kappa) \\
& + \sqrt{\frac{3}{2}}\left(\frac{g_{\mathrm{V}}q}{M}\right)(1+\mu_p-\mu_n) \\
& \times \Big(\sqrt{\bar{l}+1}\,W(1\,1\,u\,\bar{l};1\,\bar{l}+1)\mathcal{M}[1\,\bar{l}+1\,u\,+] \\
& + \sqrt{\bar{l}}\,W(1\,1\,u\,\bar{l};1\,\bar{l}-1)\mathcal{M}[1\,\bar{l}-1\,u\,-]\Big)S'_{1u}(-\kappa) \\
& - \left(\frac{g_{\mathrm{A}}}{M}\right)\mathcal{M}[0\,\bar{l}\,u\,p]S'_{0u}(-\kappa)\delta_{\bar{l}u} + \sqrt{\frac{1}{3}}(g_{\mathrm{P}}-g_{\mathrm{A}})\left(\frac{q}{2M}\right) \\
& \times \Big(\sqrt{\frac{\bar{l}+1}{2\bar{l}+1}}\mathcal{M}[1\,\bar{l}+1\,u\,+] + \sqrt{\frac{\bar{l}}{2\bar{l}+1}}\mathcal{M}[1\,\bar{l}-1\,u\,-]\Big) \\
& \times S'_{0u}(-\kappa)\delta_{\bar{l}u}\Big|^2 ,
\end{aligned}
$$

(5.33)

where $W(...)$ are the usual Racah coefficients and $\mathcal{M}[k\,w\,u\,\left(\begin{smallmatrix}\pm\\p\end{smallmatrix}\right)]$ nuclear matrix elements of the OMC. Furthermore,

$$
\begin{aligned}
S_{ku}(\kappa) &= \sqrt{2(2j+1)}W(\tfrac{1}{2}1jl,\tfrac{1}{2}u)\delta_{l\nu} \text{ for } k=1, \\
&= \sqrt{(2j+1)/(2l+1)}\delta_{l\nu} \text{ for } k=0, \text{ and} \\
S'_{ku}(-\kappa) &= S_{\kappa}S_{ku}(-\kappa) ,
\end{aligned}
$$

(5.34)

where S_{κ} is the sign of κ.

In Ref. [29] the authors give the explicit form for the P-term (5.33) for nth forbidden transition. However, they have omitted all terms of the order $1/M^2$ from the explicit form. In the absence of the computational limitations of the 1960's, we have derived the explicit form containing all the next-to-leading-order terms of the order $1/M^2$ and included it into our formalism in order to improve the accuracy of the results. The explicit next-to-leading-order form for the P-term can be found in article [**IV**].

In Ref. [29] beta decay was addressed as the inverse process of muon capture, and information on the beta-decay transition rates was used to scale down the values of the muon-capture rates. There are numerous reasons we did not want to do that: First of all, we are interested in the muon capture rate distributions in wide energy regions, where there are no data on the corresponding beta decays. Secondly, beta decay and muon capture operate in very different momentum exchange regions, and we have no reason to believe that the correspondence between computed and measured muon capture rates would be similar to that of the beta decay. Furthermore, using this kind of scaling we would not access the g_A quenching problem unambiguously.

Over the years the Morita-Fujii formalism introduced in this section has been widely used, and several improvements to the theory have been suggested. In Ref. [107] the authors included the higher-order terms in the P-term (5.33) in the capture rate equation like we did. In Refs. [113, 114] the authors added higher-order terms to the effective Hamiltonian of Eq. (5.9), and in Ref. [115] the authors replaced the point-like-nucleus approximation of the muon wave function by a more realistic one. While adding the higher-order terms into the Hamiltonian resulted in a few-percent correction of the capture rate, the effect of the realistic muon wave function is much less clear.

In the following subsection we will discuss replacing the approximate bound-muon wave function by a more realistic wave function obtained by solving the Dirac equations of the muon by taking into account the finite size of the nucleus.

5.1.6 Improvements to the Theory: Realistic Bound-Muon Wave Function

This part concerns the author's future plans of extending and improving the muon-capture calculations beyond the scope of the publications presented in this thesis.

The Primakoff method introduced in Eq. (5.32) is of course not the most sophisticated method to take into account the finite-size effects in the muon capture. We also can take into account the relativistic effects and finite size of the nucleus in the bound-muon wave function itself. This was already done in Ref. [115], and more recently in Ref. [117].

If we express the bound-muon wave function in the same way as in Eq. (5.17), and assume that the muon is in the lowest state $0s_{1/2}$ ($\kappa = -1$), we can reconstruct a realistic bound-muon wave function by solving the large, G_{-1}, and small, F_{-1}, parts of the wave function in the Coulomb field created by the nucleus. The components satisfy the coupled differential equations
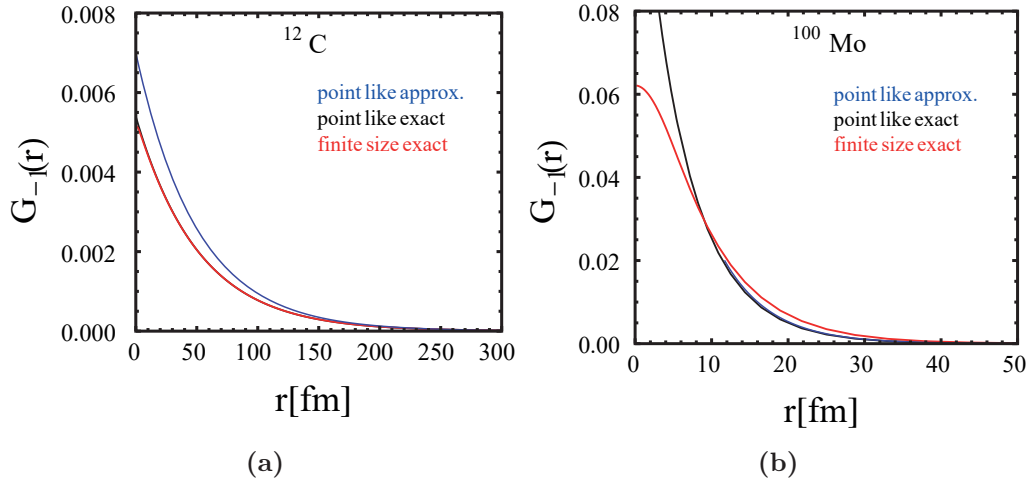
44

Figure 5.2. Large part of the realistic bound-muon wave function (red line) compared with the point-like-nucleus approximation (blue line) in the cases of (a)^{12}C and (b)^{100}Mo. Black line shows the numerical solution of the radial Dirac functions when the nucleus was assumed point-like. Figures: Jenni Kotila.

(see, e.g., [128], but note that they use different notations for the large and small parts)

$$\begin{cases} \frac{\mathrm{d}}{\mathrm{d}r}G_{-1} + \frac{1}{r}G_{-1} = \frac{1}{\hbar c}(mc^2 - E + V(r))F_{-1} \,, \\ \frac{\mathrm{d}}{\mathrm{d}r}F_{-1} - \frac{1}{r}F_{-1} = \frac{1}{\hbar c}(mc^2 + E - V(r))G_{-1} \,. \end{cases} \tag{5.35}$$

If we assume finite nuclear size and uniform charge distribution of the nuclear charge within the charge radius $R_c = r_0 A^{1/3}$, the potential energy $V(r)$ in Eqs. (5.35) can be written in the form

$$V(r) = \begin{cases} \frac{(Z-1)e^2}{2R_c}\left[3 - \left(\frac{r}{R_c}\right)^2\right] \,, & \text{if } r \leq R_c \\ \frac{(Z-1)e^2}{r} \,, & \text{if } r > R_c \end{cases} \tag{5.36}$$

similarly as in Ref. [79] in the case of bound-electron wave functions in the context of double-beta decay. Eqs. (5.35) can then be solved by means of package RADIAL [129] by solving the radial equations by using a piecewise-exact power-series expansion of the radial functions, which then are summed up to the prescribed accuracy. In Fig. 5.2 we compare the large parts of the bound-muon wave functions, computed using this method by our collaborator Jenni Kotila, with the approximate wave function of Eq. (5.20).

To introduce the realistic wave function, we have to modify the muon capture matrix elements and the capture rate equation correspondingly. Since

45

Table 5.3. Definition of $\mathcal{O}'_s$ in Eq. (5.37) for different nuclear matrix elements (NMEs) assuming the realistic bound-muon wave function.

NME	$\mathcal{O}'_s$
$\mathcal{M}[0\,w\,u]$	$j_w(qr_s)G_{-1}(r_s)\mathcal{Y}_{0wu}^{M_f-M_i}(\hat{\mathbf{r}}_s)\delta_{wu}$
$\mathcal{M}[1\,w\,u]$	$j_w(qr_s)G_{-1}(r_s)\mathcal{Y}_{1wu}^{M_f-M_i}(\hat{\mathbf{r}}_s,\boldsymbol{\sigma}_s)$
$\mathcal{M}[0\,w\,u\,\pm]$	$[j_w(qr_s)G_{-1}(r_s)\mp\frac{1}{q}j_{w\mp1}(qr_s)\frac{d}{dr_s}G_{-1}(r_s)]\mathcal{Y}_{0wu}^{M_f-M_i}(\hat{\mathbf{r}}_s)\delta_{wu}$
$\mathcal{M}[1\,w\,u\,\pm]$	$[j_w(qr_s)G_{-1}(r_s)\mp\frac{1}{q}j_{w\mp1}(qr_s)\frac{d}{dr_s}G_{-1}(r_s)]\mathcal{Y}_{1wu}^{M_f-M_i}(\hat{\mathbf{r}}_s,\boldsymbol{\sigma}_s)$
$\mathcal{M}[0\,w\,u\,p]$	$ij_w(qr_s)G_{-1}(r_s)\mathcal{Y}_{0wu}^{M_f-M_i}(\hat{\mathbf{r}}_s)\boldsymbol{\sigma}_s\cdot\mathbf{p}_s\delta_{wu}$
$\mathcal{M}[1\,w\,u\,p]$	$ij_w(qr_s)G_{-1}(r_s)\mathcal{Y}_{1wu}^{M_f-M_i}(\hat{\mathbf{r}}_s,\mathbf{p}_s)$

the wave functions are no more of exponential form, we have to replace the $\mp\alpha Z m'_\mu$ terms by the derivative $\frac{d}{\mathrm{d}r}G_{-1}$. In the Morita-Fujii formalism the coefficient $2(\alpha Z m'_\mu)^{3/2}$ coming from the point-like approximation was taken out of the definition of the matrix elements as a common factor, and hence the square of it appears in the formula of the capture rate (5.32). For general muon wave function we cannot do that, instead we have to keep the parts of the muon wave function as they are in the definition of the matrix elements. Accordingly, the matrix elements can be defined as

$$\int \Psi_{J_f M_f} G_{-1}(r)\sum_{s=1}^{A}\mathcal{O}'_s\tau^s_-\Psi_{J_i M_i}d\mathbf{r}_1...d\mathbf{r}_A$$
$$= \mathcal{M}[k\,w\,u\begin{pmatrix}\pm\\p\end{pmatrix}](J_i\,M_i\,u\,M_f-M_i|J_f\,M_f)\,, \tag{5.37}$$

where the operators $\mathcal{O}'_s$ are now defined as in Table 5.3.

The ordinary muon capture rate of Eq. (5.32) can now be written as

$$W = 2\frac{2J_f+1}{2J_i+1}\left[1-\frac{q}{m_\mu+AM}\right]q^2P \tag{5.38}$$

without the Primakoff term, which should not be needed when having access to the realistic bound-muon wave functions. The capture rates obtained from this equation could then be compared with the values obtained from Eq. (5.32) with the pointlike-nucleus approximation.

Here we assumed that $F_{-1}(r) = 0$, which is a reasonable approximation, since $F_{-1}(r)$ is an order of magnitude smaller than $G_{-1}(r)$. The next step would then be adding also the non-zero $F_{-1}(r)$ into the computations. However, this is much less straightforward, since it activates all the terms in the operators of Table 5.1 making the formulation of the matrix elements and capture rate drastically more complex.

5.2   Results

Here we present the main results of different OMC studies we have performed in articles [**III**, **IV**, **V**].

5.2.1   Muon Capture on ^{100}Mo

Inspired by the first observation of the OMC giant resonance in ^{100}Nb at around 12 MeV [28, 130, 131], in article [**III**] we study both theoretically and experimentally the OMC on ^{100}Mo populating states in ^{100}Nb in a wide excitation region, up to some 50 MeV. The strength function consists of muon capture rates to individual final states, resembling the Gamow-Teller strength function in the case of (n,p) charge-exchange reactions to the final states. The OMC strength function analogously to the Gamow-Teller strength function, or the isovector spin-multipole strength functions introduced in Sec. 4.2, contains giant resonances and in the article we studied the structure of these resonances. The aim was to access the effective values of the weak couplings g_{A} and g_{P} in wide energy and momentum regions by comparing the associated OMC strength function against experimental data. ^{100}Mo is a particularly interesting case, since it is one of the $\beta\beta$-decaying nuclei, and it is also used for solar- and supernova-neutrino studies [9].

The muon capture reaction we studied can be written as

$$\mu^{-} + {}^{100}_{42}\mathrm{Mo}(0^{+}) \rightarrow \nu_{\mu} + {}^{100}_{41}\mathrm{Nb}(J^{\pi}) \ .$$
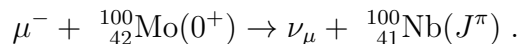
The excited states of $^{100}_{41}$Nb then de-excite either by emitting γ rays to the ground state of $^{100}_{41}$Nb or by emitting a neutron to the neighboring isotope $^{99}_{41}$Nb, depending on whether the excitation energy is below or above the first neutron-emission threshold energy. The residual nucleus $^{99}_{41}$Nb then de-excites either to its ground state by emitting γ rays, or to the neighboring isotope by emitting a second neutron, depending on whether the excitation energy was above or below the second neutron-emission threshold energy, and so on. One finally ends up with the residual isotope of $^{100-x}_{41}$Nb with

$x = 0, 1, 2, 3, ...$, depending on the excitation energy E and the number x of the emitted neutrons.

The OMC strength distribution in ^{100}Nb was studied at the MuSIC beam channel at RCNP and the D2 beam channel in J-PARC MLF as reported in Refs. [28, 132]. The delayed γ-ray characteristics of the residual radioactive isotopes of $^{100-x}$Nb were measured, and the number of the residual isotopes produced by the OMC on ^{100}Mo was then evaluated from the observed γ-ray yields. Finally the strength distribution was derived from the OMC residual-isotope distributions using the neutron equilibrium-emission and pre-equilibrium-emission models [28].

The capture rates for the transitions $\mu^- +^{100} \mathrm{Mo}(0^+_{\mathrm{g.s.}}) \to \nu_\mu +^{100} \mathrm{Nb}(J^\pi_f)$ were computed for all possible multipole states J^π_f reachable with our choice of single-particle basis, while the experimental data applies to multipole states $J^\pi_f = 0^+, 1^\pm, 2^\pm$. We independently varied the values of the axial-vector coupling $g_{\mathrm{A}}(0)$ and the induced pseudoscalar coupling $g_{\mathrm{P}}(0)$ in the ranges of $g_{\mathrm{A}}(0) = 0.6 - 1.27$ (this is considered a sensible range as discussed in the review [133]) and $g_{\mathrm{P}} = 0 - 10$ in order to see how they affect the total capture rate and the OMC strength function. For the vector coupling we kept the well-established conserved-vector-current (CVC) value $g_{\mathrm{V}}(0) = 1.0$ throughout the calculations.

In Fig. 5.3a we present a multipole decomposition of the obtained theoretical OMC rate distribution (OMC strength function) of transitions to the $J^\pi_f = 0^+, 1^\pm, 2^\pm$ states, which presumably form the experimental strength distribution. In Fig. 5.3b we decompose the total capture rate into parts containing these lowest multipoles, and the rest of the multipoles, separately. It quickly becomes clear that the theoretical distribution is mainly built of the transitions to the lowest-multipole $J^\pi_f = 0^+, 1^\pm, 2^\pm$ states, as we could suppose. Furthermore, it is notable that transitions to $J^\pi_f = 1^-, 2^-$ states not only form most of the strength but also are mainly responsible for the giant resonance peak at around 12 MeV. Transitions to the $J^\pi_f = 1^+, 2^+$ states, in turn, form a satellite resonance at around 7 MeV. All in all, the OMC strength distribution is quite broad, since OMC is an (n, p)-type of charge-exchange reaction where for medium-heavy nucleus like ^{100}Nb the $0\hbar\omega$ excitations are hindered by the relative locations of the proton and neutron Fermi surfaces.

The Lorentzian foldings of the experimental relative OMC strength distribution together with the theoretical relative OMC distribution obtained with $g_{\mathrm{A}}(0) = 0.8$ and $g_{\mathrm{P}} = 7.0$ are shown in Fig. 5.4. The theoretical distribution containing only the $J^\pi = 0^+, 1^\pm, 2^\pm$ multipoles is shown separately. The overall features of all the relative rate distributions are strikingly similar: there is a strong peak around 10-12.5 MeV and tails on both sides. However, the experimental distribution is slightly more spread to higher energies than
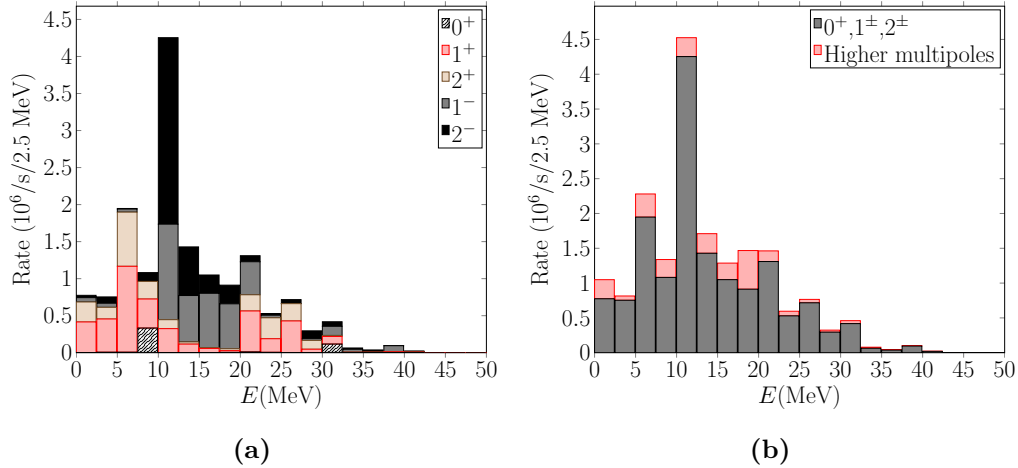
Figure 5.3. Panel (a): Muon-capture-rate distribution including transitions to $J^\pi = 0^+, 1^\pm, 2^\pm$ states. Panel (b): The same but transitions to the rest of the possible multipole final J_f^π states added. The horizontal axes show the excitation energy in the ^{100}Nb nucleus. Here a 2.5 MeV binning in energy is used in order to match the energy binning used in the experimental data analysis. Parameter values $g_A(0) = 0.8$ and $g_P(0) = 7.0$ were adopted in the calculations. Figures: [**III**].

the theoretical distributions, containing also a second giant-resonance-like bump at around 30 MeV. This bump, however, contains some experimental uncertainties and the confirmation of it needs further studies. There are no notable differences between the two theoretical spectra, stemming from the fact that multipoles $J^\pi = 0^,1^\pm, 2^\pm$ are the main responsibles for the total OMC strength function.

We list the total OMC rates obtained with different parameter values in Table 5.4. The computed values are notably higher than the Primakoff approximation $W_{\text{Pr.}} = 7.7 \times 10^6$ 1/s obtained from Eq. (5.2). We noticed that increasing the value of $g_P(0)$ or decreasing the value of $g_A(0)$ decreases the theoretical total capture rate. However, the total capture rate is relatively insensitive to the value of $g_P(0)$, leaving $g_A(0)$ the main responsible for the total capture rate. The differences between the computed and Primakoff total OMC rates are presumably not only due to the possible quenching of the effective weak couplings but also related to the higher average energy of the experimental OMC strength function. Comparison of the computed and Primakoff total capture rates suggests a strongly quenched effective value of $g_A(0)$, in accordance with the results of many earlier β-decay studies [23, 134–137].
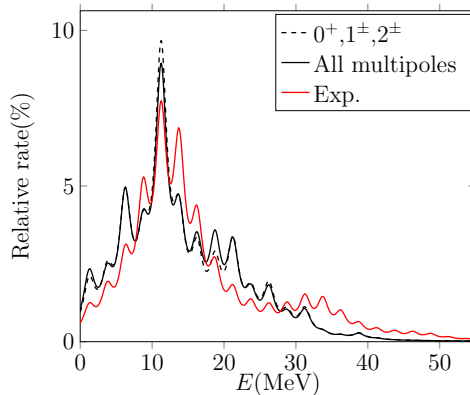
49

Figure 5.4. Theoretical (black lines) and experimental (red line) relative OMC rates on ^{100}Mo in per cents. The theoretical distribution containing only the $J^\pi = 0^+, 1^\pm, 2^\pm$ multipoles is shown as the dashed line, and the distribution containing all multipoles as the solid line. Parameters $g_V(0) = 1.0$, $g_A(0) = 0.8$ and $g_P(0) = 7.0$ were adopted. Figure: [**III**].

Table 5.4. Total rates of muon capture by ^{100}Mo for different values of the pseudoscalar and axial-vector strengths $g_P(0)$ and $g_A(0)$. The rates are expressed in units of 10^6/s. Table: [**III**].

	$g_P(0) = 0$		$g_P(0) = 7$		$g_P(0) = 10$	
$g_A(0)$	$W_{(0^+,1^\pm,2^\pm)}$	W_{tot}	$W_{(0^+,1^\pm,2^\pm)}$	W_{tot}	$W_{(0^+,1^\pm,2^\pm)}$	W_{tot}
0.6	11.8	13.8	10.8	12.4	10.7	12.2
0.8	17.0	20.2	15.7	18.3	15.3	17.7
1.0	23.9	28.4	28.0	31.9	21.2	24.8
1.27	34.8	41.7	32.2	38.2	31.3	37.0

There are two main conclusions arising from this study: our muon-capture formalism is capable of reproducing the observed muon-capture giant resonance in ^{100}Mo at around 12 MeV, however, the obtained total capture rate overestimates the Primakoff value suggesting a strongly quenched $g_A \approx 0.5$.

5.2.2 OMC on the Daughter Nuclei of the Key $0\nu\beta\beta$ Triplets

Inspired by the findings in article [**III**], in article [**IV**] we extended the muon-capture studies on the daughter nuclei of the key $\beta\beta$-decay triplets. Extending the calculations, and eventually the experiments, on these nuclei could help theories better evaluate the β^+ NMEs associated with the $0\nu\beta\beta$ decays and
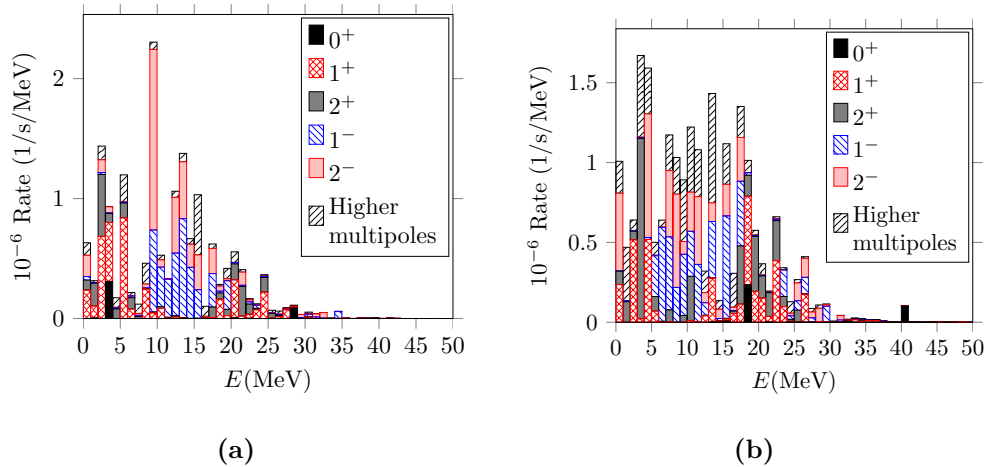
Figure 5.5. Multipole decompositions of the muon-capture-rate distributions in the (a) ^{76}As (b) ^{136}I. Figures: [**IV**].

the NMEs related to astro-(anti)neutrino interactions.

We evaluated the OMC rates on the daughter nuclei of the key $\beta\beta$ triplets listed in Sec. 4.2 leading to the excited states of the intermediate odd-odd nuclei of the $\beta\beta$ triplets. The corresponding OMC (capture-rate) strength functions were then analyzed in terms of multipole decompositions. In Fig. 5.5 we show a couple of examples of the multipole decompositions of the distributions with 1-MeV energy binning. The energy-binning was chosen in order to enable comparison against experimental data in the future. Also from these figures, similarly as in the case of ^{100}Nb, one can observe structures of the OMC strength functions, which would correspond to an OMC giant resonance. For some nuclei, like the example case ^{76}As in 5.5a, the resonance-bump around 12 MeV is relatively clear, but for a few cases, like the ^{136}I case in 5.5b there is no clear resonance peak, but rather a wide flat region of strong captures below ≈ 20 MeV.

In Table 5.5 we compare the Primakoff estimates of Eq. 5.2 with the obtained total muon-capture rates computed with couplings $g_A(0) = 0.8$ and $g_P(0) = 7.0$ for different nuclei. From the table it is obvious that the computed values are systematically higher than the corresponding Primakoff estimates. This refers to the need of strongly quenched $g_A(0) \approx 0.5$, in keeping with OMC computations on ^{100}Mo and the earlier β-decay studies. However, we cannot make any strong conclusions of the quenched value of g_A, since the Primakoff values are only estimates for the total capture rate. For further conclusions we would need to have experimental data in order to compare with the computed total capture rates.

Table 5.5. pnQRPA-computed and Primakoff-formula based total rates for OMC on different parent nuclei (Parent), as well as the effective Z values [127]. Couplings $g_A(0) = 0.8$ and $g_P(0) = 7.0$ were adopted in the calculations. Table: [**IV**].

Parent	Z_{eff}	$W_{\text{pnQRPA}}(10^6/\text{s})$	$W_{\text{Pr.}}(10^6/\text{s})$
^{76}Se	24.47	16.4	8.3
^{82}Kr	24.47	16.5	7.5
^{96}Mo	26.37	20.4	10.0
^{100}Ru	26.37	16.7	10.3
^{116}Sn	28.64	15.7	12.7
^{128}Xe	29.99	21.2	13.3
^{130}Xe	29.99	23.6	11.9
^{136}Ba	29.99	21.1	11.1

In Ref. [105] the lifetime of negative muon and partial OMC rates on a few daughter isotopes of $\beta\beta$-decay were deduced at μE4 and the μE1 beam lines of the Paul Scherrer Institute (PSI) in Switzerland. The results serve as possibility to compare our computed capture rates to the lowest states in ^{76}As against experimental data. We present the "most probable" experimental multipole-by-multipole OMC strength distribution below 1.1 MeV deduced from the results of Ref. [105] against the computed distribution in Table 5.6. The "most probable" here refers to the educated guesses that were produced in order to determine the uncertain spin-parity assignments of the experimental data. The details of the procedure can be found in article [**IV**]. The correspondence between the experimental and pnQRPA-computed OMC strength distributions presented in the table is strikingly good. Only the pnQRPA-computed rate to the 0^+ states is an order of magnitude smaller than the corresponding experimental rate, which might be due to the small deformation of ^{76}Se that is not taken into account in the spherical pnQRPA formalism. These results point to reliability of the present calculations of the OMC strength functions at low energies.

To summarize the results of article [**IV**]; the computed OMC strength distributions in the intermediate nuclei of $\beta\beta$-decay triplets contain giant-resonance-like structures that could be further studied against experimental data in the future. The computed low-energy transition rates are in line with the data of Zinatulina *et al.* [105]. However, the comparison between the total OMC rates and the Primakoff estimates points to a strongly quenched g_A, in keeping with the results of article [**III**].

Table 5.6. Comparison of the "most probable" experimental multipole-by-multipole OMC strength distribution to the excited states of ^{76}As below 1.1 MeV obtained from Ref. [105] with the corresponding pnQRPA-computed distribution deduced from the results of article [**IV**]. The OMC strength to the 2^- ground state has not been measured and this is indicated by '+ g.s.' in the corresponding row. Table: [**IV**].

	OMC rate (1/s)	
J^π	Exp.	pnQRPA
0^+	5120	414
1^+	218 240	236 595
1^-	31 360	28 991
2^+	120 960	114 016
2^-	145 920 + g.s.	177 802
3^+	60 160	55 355
3^-	53 120	34 836
4^+	-	2797
4^-	30 080	23 897

5.2.3 Comparing OMC Rates with $0\nu\beta\beta$ Matrix Elements

Article [**V**] nicely concludes the main emphasis of this thesis. There we compare the $0\nu\beta\beta$-decay matrix elements with the corresponding average muon-capture matrix elements. Earlier the OMC rates have been compared against the $2\nu\beta\beta$ NMEs for light nuclei using the nuclear shell model by Kortelainen *et al.* [77]. There was found a clear correlation between the energy distributions of the OMC rates to 1^+ states and the energy decomposition of the $2\nu\beta\beta$ NMEs for the $2\nu\beta\beta$ decays of the sd-shell nuclei ^{36}Ar, ^{46}Ca, and ^{48}Ca. In article [**V**] we extended these studies to $0\nu\beta\beta$ decays of medium-heavy and heavy nuclei by computing the average OMC matrix elements in the intermediate nuclei of $0\nu\beta\beta$ decays multipole by multipole up to some 50 MeV using the pnQRPA formalism and compared them with the energy-multipole decompositions of the NMEs of $0\nu\beta\beta$ decays computed using the same formalism and model spaces.

Using the notation of Eq. (5.32) we can write Eq. (5.31) in the form

$$\langle |\text{M.E.}|^2 \rangle_{\text{av}} = \frac{8(2J_f + 1)}{2J_i + 1} (\alpha Z m'_\mu)^3 P \ . \tag{5.39}$$

53

In article [**V**] we then defined an average OMC matrix element as

$$|M_{\text{av}}^{(\mu)}| = \sqrt{\langle |\text{M.E.}|^2 \rangle_{\text{av}}} = \sqrt{\frac{8(2J_f + 1)}{2J_i + 1}} (\alpha Z m'_\mu)^3 P \ . \qquad (5.40)$$

We compared this quantity, instead of the OMC rate, with the $0\nu\beta\beta$-decay nuclear matrix element in order to reduce the phase-space effects in the comparison.

In Fig. 5.6, we show an example of the comparison of relative OMC matrix-element distribution with the corresponding multipole decompositions of the $0\nu\beta\beta$-decay NME. The $0\nu\beta\beta$-decay and OMC distributions correspond to $0\nu\beta\beta$ decay of ^{76}Ge and OMC on the daughter nucleus ^{76}Se, correspondingly. We chose to plot the absolute values of the matrix elements, since they carry the essential information needed in the comparison of the OMC and $0\nu\beta\beta$ decay. We concentrated only on the positive $J^\pi = 0^+, 1^+, 2^+, 3^+, 4^+$ and negative $J^\pi = 1^-, 2^-, 3^-, 4^-$ multipolarities of both the average OMC matrix-element distributions and the $0\nu\beta\beta$ NME distributions. These multipoles are by far the most important ones for the OMC rates, as was seen in article[**IV**], and the leading ones for the $0\nu\beta\beta$ NMEs, which was noted in article[**II**] and Ref. [78]. Here we chose the slightly quenched values of $g_\text{A}(0) = 0.8$ and $g_\text{P}(0) = 7.0$ and keep the CVC value $g_\text{V}(0) = 1.00$ for all the studied cases similarly as in article [**IV**], but the (qualitative) results of the present study are not very sensitive to the values of these couplings.

Fig. 5.6 shows that the correspondence between the relative OMC matrix-element and $0\nu\beta\beta$-NME distributions for the multipole $J^\pi = 0^+$ is weak. However, for the rest of the multipoles one can see clear correspondences: in the cases of $J^\pi = 1^+ - 3^+$ there are two bumps at similar energies. The $J^\pi = 1^-$ distributions both are peaked at $E \approx 10$ MeV, and the $J^\pi = 3^-, 4^-$ distributions at $E \approx 15$ MeV. On the other hand, in the case of $J^\pi = 2^-$ the $0\nu\beta\beta$ transition through the 2^- ground state of ^{76}As seems to be enhanced relative to the OMC. Among all the nuclei, the best overall correspondence was found for the $J^\pi = 3^\pm$ and $4^\pm$ multipoles, while the correspondence between the $J^\pi = 0^+$ $0\nu\beta\beta$-NME and OMC-matrix-element distributions was a bit vaque. The distributions and their correspondences varied quite much between the different $0\nu\beta\beta$ triplets indicating variations in the nuclear structure of the different nuclei.

In article [**V**], we discuss also the cumulative average OMC matrix elements and $0\nu\beta\beta$ NMEs that nicely illustrate the build-up of the quantities as functions of the excitation energy of the intermediate nuclei of $0\nu\beta\beta$ decay.

Table 5.7. Contributions (in percentages) from different multipoles to $0\nu\beta\beta$-decay NMEs and average OMC matrix elements for different $0\nu\beta\beta$-decay triplets. The presented values are normalized ratios abbreviated as $R\nu = |M^{(0\nu)}|(J^\pi)/|M^{(0\nu)}|$ and $R\mu = |M^{(\mu)}|_{\mathrm{av}}(J^\pi)/|M^{(\mu)}|_{\mathrm{av}}$. Table: [**V**].

J^π	$A=76$		$A=82$		$A=96$		$A=100$		$A=116$		$A=128$		$A=130$		$A=136$	
	$R\nu$	$R\mu$	$R\nu$	$R\mu$	$R\nu$	$R\mu$	$R\nu$	$R\mu$	$R\nu$	$R\mu$	$R\nu$	$R\mu$	$R\nu$	$R\mu$	$R\nu$	$R\mu$
0^+	2	3	2	2	0	3	1	2	1	2	1	3	1	2	1	2
1^+	7	18	6	17	6	17	6	17	9	16	2	16	2	14	7	14
1^-	16	21	16	21	18	18	20	19	23	18	13	17	13	17	9	17
2^+	13	16	14	17	13	16	12	16	9	16	12	17	12	15	14	15
2^-	10	18	9	17	7	17	3	17	7	17	5	16	5	17	6	16
3^+	5	11	5	11	6	12	5	12	6	11	6	12	6	12	7	12
3^-	11	6	11	6	10	7	9	8	9	8	10	8	10	9	9	9
4^+	7	2	7	2	8	2	8	2	7	3	9	3	9	4	9	4
4^-	5	5	5	5	4	5	4	5	4	5	5	5	5	6	5	6
$\sum$	76	100	75	98	72	97	68	98	75	96	63	97	63	96	67	95

In Fig. 5.7 we show the normalized cumulative matrix elements

$$\sum_{J^\pi} |M^{(0\nu)}(J^\pi)|(E) \Big/ \sum_{J^\pi,E} |M^{(0\nu)}(J^\pi)|(E)$$

and

$$\sum_{J^\pi} |M^{(\mu)}|_{av}(J^\pi)(E) \Big/ \sum_{J^\pi,E} |M^{(\mu)}|_{av}(J^\pi)(E)$$

as functions of energy in the intermediate nuclei ^{76}As and ^{136}Cs of the $A = 76$ and $A = 136$ $0\nu\beta\beta$ triplets. It was demonstrated that the running sums of the quantities are quite similar, but both cases show that $0\nu\beta\beta$ decay NME is a little bit more concentrated in lower energies than the corresponding OMC matrix element.

The relative multipole contributions to the $0\nu\beta\beta$ NMEs and average OMC matrix elements for the discussed $0\nu\beta\beta$-decay triplets are presented in Table 5.7. The multipole $J^\pi = 0^-$ is omitted from the table, since its contribution to both $0\nu\beta\beta$ NME and OMC matrix element is negligible. It is worth noticing that basically all the OMC strength is coming from the multipoles with $J \leq 4$, while the $0\nu\beta\beta$ NME is more distributed to higher multipoles, only about $60 - 75$ % coming the from multipoles with $J \leq 4$. However, the $J^\pi = 1^+, 1^-, 2^+$ and 2^- multipoles are among the leading multipoles for both the $0\nu\beta\beta$ decay and OMC for all the nuclei, and the contributions coming from $J^\pi = 1^-$ and 2^+ are practically the same for both processes.

We can summarize the results of article [**V**] by concluding that the overall behavior of the OMC and $0\nu\beta\beta$ matrix elements in the $\beta\beta$-decay triplets is pretty similar. Therefore, we are hopeful that future measurements of the OMC strength functions in the intermediate nuclei of $\beta\beta$ triplets could help

improve the accuracy of evaluating the $0\nu\beta\beta$ NMEs by serving information on the effective values of the weak couplings.

(a) $J^\pi = 0^+$ **(b)** $J^\pi = 1^+$ **(c)** $J^\pi = 2^+$

(d) $J^\pi = 3^+$ **(e)** $J^\pi = 4^+$ **(f)** $J^\pi = 1^-$

(g) $J^\pi = 2^-$ **(h)** $J^\pi = 3^-$ **(i)** $J^\pi = 4^-$
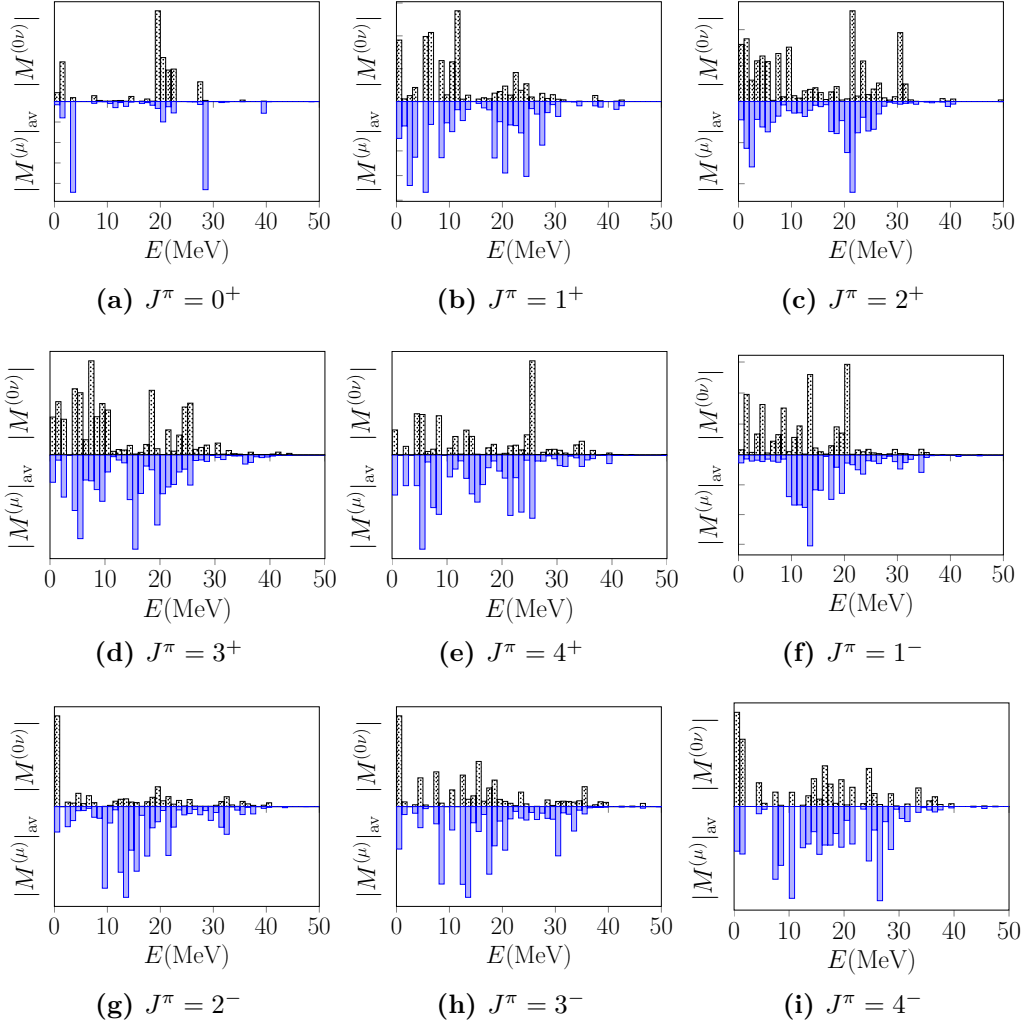
Figure 5.6. Multipole decompositions in terms of relative $0\nu\beta\beta$-decay matrix elements (positive y axes) and average matrix elements of the OMC on ^{76}Se (negative y axes) as functions of the excitation energy E in the intermediate nucleus ^{76}As of the $0\nu\beta\beta$ decay of ^{76}Ge. Here J^π refer to the angular momenta and parities of the virtual states in ^{76}As and all quantities have been summed within 1 MeV energy bins. Figures: [**V**].

Figure 5.7. Normalized cumulative average OMC matrix elements and normalized $0\nu\beta\beta$ NMEs as functions of energy in the intermediate nuclei ^{76}As [panel (a)] and ^{136}Cs [panel (b)] of the $A = 76$ and $A = 136$ $0\nu\beta\beta$ triplets. Figures: [**V**].

Chapter 6

Conclusions and outlook

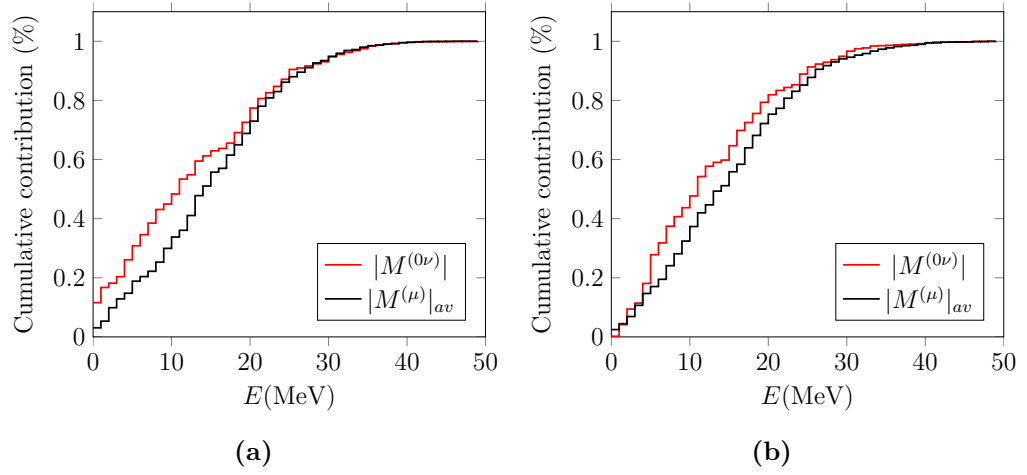The main emphasis of this thesis is probing the yet hypothetical nuclear process called neutrinoless double-beta decay by charge-exchange reactions and nuclear muon capture. These reactions could help analyze the intermediate virtual states of the double-beta decay and shed light on the highly debated value of weak couplings, most importantly the axial-vector coupling constant g_{A} entering the double-beta-decay matrix elements in the fourth power.

In article [**I**], we examine the energetics and strength distributions of the isovector spin-dipole ($L = 1$) and spin-quadrupole ($L = 2$) excitations in odd-odd nuclei belonging to double-β-decay triplets with $A = 76$, $A = 82$, $A = 96$, $A = 100$, $A = 116$, $A = 128$, $A = 130$, and $A = 136$ in the pnQRPA framework. We noticed that there is a considerable difference in the giant-resonance energy centroids of the various J^π states corresponding to a given L. We also found correlation between angular momenta and the transition strengths of $L = 1$ transitions: the strengths were highest for the lowest-J transitions and lowest for the highest-J transitions. These findings suggest that in the future, having access to experimental data, one could fine-tune the model Hamiltonian by comparing the computed isovector spin-multipole distributions against the data.

In article [**II**], we extend the studies of article [**I**] by computing the $0\nu\beta\beta$ nuclear matrix elements exploiting the newly available data on isovector spin-dipole (IVSD) $J^\pi = 2^-$ giant resonances. We computed the IVSD transition strength spectra in the intermediate nuclei of the key $0\nu\beta\beta$-decay triplets using the pnQRPA formalism. We adjusted the particle-hole parameter g_{ph} to the available data on the locations of the IVSD $J^\pi = 2^-$ giant resonances measured at RCNP, Osaka. Traditionally the particle-hole parameter has been adjusted to the location of Gamow-Teller ($J^\pi = 1^+$) giant resonances. We studied the effects of different parameter-adjusting schemes on the values of $0\nu\beta\beta$ NMEs, and found that most of the deviations from earlier results are

due to the extension of the single-particle space of pnQRPA, while the effect of adjusting the particle-hole interaction to data on spin-dipole resonances is relatively smaller.

In article [**III**], we study the ordinary muon capture (OMC) on ^{100}Mo both experimentally and theoretically in order to access the weak responses in wide energy and momentum regions. For the first time, the associated OMC strength function was computed and compared with the obtained data. The computations were performed in the no-core pnQRPA framework using the Morita-Fujii formalism of OMC by extending the original formalism beyond the leading order. The computed and experimental OMC strength distributions consistently showed a giant resonance at around 12 MeV, while comparing the computed total capture rate with the Primakoff estimate suggested a strongly quenched g_A in keeping with earlier β-decay studies.

In article [**IV**], we extend the studies of article [**III**] to the daughter nuclei of $\beta\beta$-decay triplets in order to access the OMC strength functions in the intermediate nuclei of $\beta\beta$ decay. We analyzed the strength functions in terms of energy and multipole decompositions. We also compared the OMC rates to the low-energy states in ^{76}As with the available data and found that the correspondence is pretty good. The comparison of the total capture rates with the Primakoff estimates, however, suggested a quenched g_A in accordance with the ^{100}Mo case.

In article [**V**], we compare the average matrix elements of OMC with the corresponding $0\nu\beta\beta$ decay matrix elements in terms of energy and multipole decompositions in the intermediate nuclei of $\beta\beta$-decay triplets. We found that there are correspondences especially between the $J^\pi = 3^+$ and 4^+ $0\nu\beta\beta$ NMEs and average OMC matrix elements, and also for other multipoles there can be seen similarities for all the studied $\beta\beta$-decay triplets. It was also noted that $0\nu\beta\beta$ strength is distributed to higher multipoles than OMC, while the cumulative behavior of these two quantities is almost identical. These findings support the idea of using OMC as a probe of $0\nu\beta\beta$ decay.

Further experimental and theoretical studies on the muon-capture strengths are called for in order to access the effective values of the weak couplings g_A and g_P. There are experimental studies in progress e.g. at RCNP Osaka and PSI Villigen for the nuclei of interest in studies of nuclear double beta decay and astro-neutrino interactions. From the theory side, to enhance the reliability of the capture-rate values, some improvements to the theoretical formalism are in order.

References

[1] **SNO** collaboration: B. Aharmim et al., *Phys. Rev. Lett.* 101 (2008) 111301.

[2] **Super-Kamiokande** collaboration: K. Abe et al., *Phys. Rev. D* 94 (2016) 052010.

[3] **T2K** collaboration: K. Abe et al., *Phys. Rev. Lett.* 118 (2018) 151801.

[4] S. Rappoccio, *Rev. Phys.* 4 (2019) 100027.

[5] J. Ellis, *Int. J. Mod. Phys. A* 33 (2018) 1830003.

[6] H. M. Lee, *Lectures on Physics Beyond the Standard Model,* arXiv:1907.12409v3 [hep-ph], 2019.

[7] F. T. Avignone III, S. R. Elliot and J. Engel, *Rev. Mod. Phys.* 80 (2008) 481.

[8] M. Hirsch, R. Srivastava and J. W. F. Valle, *Phys. Lett. B* 781 (2018) 302–305.

[9] J. D. Vergados, H. Ejiri and F. Šimkovic, *Rep. Prog. Phys.* 75 (2012) 106301.

[10] **NEMO-3** collaboration: R. Arnold et al., *JETP Letters* 80 (2004) 377–381.

[11] **NEMO-3** collaboration: R. Arnold et al., *Phys. Rev. D* 92 (2015) 072011.

[12] **Majorana** collaboration: C. E. Aalseth et al., *Phys. Rev. Lett.* 120 (2018) 132502.

[13] **CUORE** collaboration: C. Alduino et al., *Eur. Phys. J. C* 79 (2019) 795.

[14] **GERDA** collaboration: M. Agostini et al., *Nature* 544 (2017) 47–52.

[15] **GERDA** collaboration: M. Agostini et al., *Phys. Rev. Lett.* 120 (2018) 132503.

[16] **EXO-200** collaboration: J. B. Albert et al., *Phys. Rev. Lett.* 120 (2018) 072701.

[17] **CUPID-0** collaboration: O. Azzolini et al., *Phys. Rev. Lett.* 120 (2018) 232502.

[18] **KamLAND-Zen** collaboration: A. Gando et al., *Phys. Rev. Lett.* 117 (2016) 082503.

[19] **NEXT** collaboration: J. Martín-Albo et al., *J. High Energ. Phys.* 2016 (2016) 159.

[20] J. Engel and J. Menéndez, *Rep. Prog. Phys.* 80 (2017) 046301.

[21] F. Šimkovic and A. Faessler, *Prog. Part. Nucl. Phys.* 48 (2002) 201.

[22] V. Cirigliano et al., *Phys. Rev. Lett.* 120 (2018) 202001.

[23] J. Suhonen and J. Kostensalo, *Front. Phys.* 7 (2019) 29.

[24] J. Suhonen and O. Civitarese, *Phys. Rep.* 300 (1998) 123.

[25] P. Puppe et al., *Phys. Rev. C* 84 (2011) 051305.

[26] J. H. Thies et al., *Phys. Rev. C* 86 (2012) 014304.

[27] D. Frekers, P. Puppe, J. H. Thies and H. Ejiri, *Nucl. Phys. A* 916 (2013) 219.

[28] I.H. Hashim et al., *Phys. Rev. C* 97 (2018) 014617.

[29] M. Morita and A. Fujii, *Phys. Rev.* 118 (1960) 606.

[30] P. Navrátil, S. Quaglioni, G. Hupin, C. Romero-Redondo and A. Calci, *Physica Scripta* 91 (2016) 053002.

[31] R. Lazauskas, *Few-Body Syst.* 59 (2018) 13.

[32] K. Hebeler, S. K. Bogner, R. J. Furnstahl, A. Nogga and A. Schwenk, *Phys. Rev. C* 83 (2011) 031301(R).

[33] S. C. Pieper, R. B. Wiringa and J. Carlson, *Phys. Rev. C* 70 (2004) 054325.

[34] P. Navrátil, S. Quaglioni, I. Stetcu and B. R. Barrett, *J. Phys. G: Nucl. Part. Phys.* 36 (2009) 083101.

[35] B. R. Barrett, P. Navrátil and J. P. Vary, *Prog. Part. Nucl. Phys.* 69 (2013) 131–181.

[36] T. D. Morris et al., *Phys. Rev. Lett.* 120 (2018) 152503.

[37] P. Ring and P. Schuck, *The Nuclear Many-Body Problem*, 1st edition, Berlin Heidelberg: Springer-Verlag, 1980.

[38] J. Suhonen, *From Nucleons to Nucleus: Concepts of Microscopic Nuclear Theory*, 1st edition, Berlin Heidelberg: Springer-Verlag, 2007.

[39] E. T. Whittaker and G. Robinson, *Mathematical Methods for Physicists*, 3rd edition, Orlando, FL: Academic Press, 1967.

[40] A. Bohr and B. R. Mottelson, *Nuclear Structure*, New York: Benjamin, 1969.

[41] R. Machleidt, K. Holinde and Ch. Elster, *Phys. Rep.* 149 (1 1987) 1–89.

[42] D. J. Rowe, *Nuclear Collective Motion: Models and Theory*, Revised, World Scientific Publishing Co Pte Ltd, 2010.

[43] B.A. Brown and W.D.M. Rae, *Nucl. Data Sheets* 120 (2014) 115.

[44] O. Civitarese, H. Müther, L. D. Skouras and A. Faessler, *J. Phys. G* 17 (1991) 1363.

[45] J. Suhonen, *Czech, J. Phys.* 56 (2006) 511.

[46] V. A. Rodin, A. Faessler, F. Šimkovic and P. Vogel, *Phys. Rev. C* 68 (2003) 044302.

[47] J. Bardeen, L. Cooper and J. R. Schrieffer, *Phys. Rev.* 108 (1957) 1175.

[48] A. Bohr, B.R. Mottelson and D. Pines, *Phys. Rev.* 110 (1958) 936.

[49] S. T. Belyaev, *Mat. Fys. Medd. Dan. Vid. Selsk.* 31, no.11 (1959) 1.

[50] N. N. Bogoliubov, *Sov. Phys. JETP* 7 (1958) 41.

[51] J. G. Valatin, *Phys. Rev.* 122 (1961) 1012.

[52] J. Suhonen, T. Taigel and A. Faessler, *Nucl. Phys A* 486 (1988) 91.

[53] J. Suhonen, *Phys. Lett. B* 607 (2005) 87–95.

[54] J. Suhonen, *Nucl. Phys. A* 864 (2011) 63–90.

[55] P. Vogel and M. R. Zirnbauer, *Phys. Rev. Lett.* 57 (1986) 3148.

[56] O. Civitarese, A. Faessler and T. Tomoda, *Phys. Lett. B* 194 (1987) 11.

[57] K. Muto, E. Bender and H. V. Klapdor, *Z. Phys. A* 334 (1989) 177.

[58] S. Stoica and H. V. Klapdor-Kleingrothaus, *Phys. Rev. C* 63 (2001) 064304.

[59] V. A. Rodin, A. Faessler, F. Šimkovic and P. Vogel, *Nucl. Phys. A* 766 (2006) 107–131.

[60] M. Kortelainen and J. Suhonen, *Phys. Rev. C* 76 (2007) 024315.

[61] F. Šimkovic, V. Rodin, A. Faessler and P. Vogel, *Phys. Rev. C* 87 (2013) 045501.

[62] L. M. Brown, *Phys. Today* 31, no.9 (1978) 23.

[63] M. Goeppert-Mayer, *Phys. Rev.* 48 (1935) 512.

[64] E. Majorana, *Nuovo Cimento* 14 (1937) 171.

[65] W. H. Furry, *Phys. Rev.* 56 (1939) 1184.

[66] C. L. Cowan, Jr., F. Reines, F. B. Harrison, H. W. Kruse and A. D. McCuire, *Science* 124, no.3212 (1956) 103–104.

[67] **NEMO-3** collaboration: R. Arnold et al., *Phys. Rev. D* 93 (2016) 112008.

[68] **CUORE** collaboration: C. Alduino et al., *Eur. Phys. J. C* 77 (2017) 13.

[69] **XENON** collaboration: E. Aprile et al., *Nature* 568 (2019) 532–535.

[70] A. P. Meshik, C. M. Hohenberg, O. V. Pravdivtseva and Ya. S. Kapusta, *Phys. Rev. C* 64 (2001) 035205.

[71] H. V. Klapdor-Kleingrothaus, *Seventy Years Of Double Beta Decay: From Nuclear Physics To Beyond-standard-model Particle Physics*, Singapore: World Scientific Publishing Co. Pte. Ltd., 2010.

[72] A. S. Barabash, *Phys. Atom. Nuclei* 74 (2011) 603–613.

[73] C. Brofferio, O. Cremonesi and S. Dell'Oro, *Front. Phys.* 7 (2019) 86.

[74] H. V. Klapdor-Kleingrothaus, *Found. Phys.* 33 (2003) 813–829.

[75] J. Suhonen, *Nucl. Phys. A* 752 (2005) 53c–66c.

[76] M. Kortelainen and J. Suhonen, *Europhys. Lett.* 58, no.5 (2002) 666–672.

[77] M. Kortelainen and J. Suhonen, *J. Phys. G* 30 (2004) 2003–2018.

[78] J. Hyvärinen and J. Suhonen, *Phys. Rev. C* 91 (2015) 024613.

[79] J. Kotila and F. Iachello, *Phys. Rev. C* 85 (2012) 034316.

[80] D.-L. Fang, A. Faessler, V. Rodin and F. Šimkovic, *Phys. Rev. C* 82 (2010) 051301.

[81] J. Terasaki, *Phys. Rev. C* 91 (2015) 034318.

[82] T. Marketin, L. Huther and G. Martínez-Pinedo, *Phys. Rev. C* 93 (2016) 025805.

[83] B. Kayser, *Neutrino Mass, Mixing, and Flavor Change*, arXiv:0804.1497v2 [hep-ph], 2008.

[84] G. A. Miller and J. E. Spencer, *Ann. Phys. (NY)* 100 (1976) 562.

[85] M. Kortelainen, O. Civitarese, J. Suhonen and J. Toivanen, *Phys. Lett. B* 647 (2007) 128.

[86] F. Šimkovic, A. Faessler, H. Müther, V. Rodin and M. Stauf, *Phys. Rev. C* 79 (2009) 055501.

[87] H. Ejiri, *Phys. Rep.* 338 (2000) 265–351.

[88] S. Rakers et al., *Phys. Rev. C* 71 (2005) 054313.

[89] P. Puppe et al., *Phys. Rev. C* 86 (2012) 044603.

[90] I. Hamamoto and H. Sagawa, *Phys. Rev. C* 62 (2000) 024319.

[91] D. R. Bes, O. Civitarese and J. Suhonen, *Phys. Rev. C* 86 (2012) 024314.

[92] O. Civitarese and J. Suhonen, *Phys. Rev. C* 89 (2014) 044319.

[93] D Frekers et al., *Phys. Rev. C* 95 (2017) 034619.

[94] N. Auerbach and A. Klein, *Phys. Rev. C* 30 (1984) 1032.

[95] B. Frois and I. Sick, *Modern Topics in Electron Scattering*, Singapore: World Scientific, 1991.

[96] G. F. Bertsch, D. Cha and H. Toki, *Phys. Rev. C* 24 (1981) 533.

[97] F. Krmpotic, K. Ebert and W. Wild, *Nucl. Phys. A* 342 (1980) 497.

[98] J. H. Thies et al., *Phys. Rev. C* 86 (2012) 054323.

[99] J. H. Thies et al., *Phys. Rev. C* 86 (2012) 044309.

[100] H. Akimune et al., *Phys. Lett. B* 394 (1997) 23.

[101] T. Siiskonen, J. Suhonen, V. A. Kuz'min and T. V. Tetereva, *Nucl. Phys. A* 635 (1998) 446–469.

[102] T. Siiskonen, J. Suhonen and M. Hjorth-Jensen, *J. Phys. G: Nucl. Part. Phys.* 25 (1999) L55.

[103] P. Kammel, *Muon Capture and Muon Lifetime*, arXiv:0304019v2 [nucl-ex], 2003.

[104] M. Kortelainen and J. Suhonen, *Nucl. Phys. A* 713 (2003) 501–521.

[105] D. Zinatulina et al., *Phys. Rev. C* 99 (2019) 024327.

[106] J. Menéndez, D. Gazit and A. Schwenk, *Phys. Rev. Lett.* 107 (2011) 062501.

[107] V. Gillet and D. A. Jenkins, *Phys. Rev.* 140, no.1B (1965) B32–B41.

[108]   J. D. Walecka, Semileptonic Weak Interactions in Nuclei, *Muon Physics: Weak Interactions*, edited by V. W. Hughes and C. S. Wu, volume 2, New York: Academic Press, 1975, chapter 4 113–211.

[109]   N. C. Mukhopadhyay, *Phys. Rep.* 335 (1977) 111–135.

[110]   D.F. Measday, *Phys. Rep.* 354 (2001) 243–409.

[111]   T. N. K. Godfrey, *Phys. Rev.* 92 (1953) 512.

[112]   H. Primakoff, *Rev. Mod. Phys.* 31 (1959) 802.

[113]   H. Ohtsubo, *Phys. Lett.* 22 (1966) 480–482.

[114]   J. L. Friar, *Nucl. Phys.* 87 (1966) 407–413.

[115]   H. Hiro-Oka et al., *Prog. Theor. Phys.* 40 (1968) 808.

[116]   E. Kolbe, K. Langanke and P. Vogel, *Phys. Rev. C* 62 (2000) 055502.

[117]   N. T. Zinner, K. Langanke and P. Vogel, *Phys. Rev. C* 74 (2006) 024326.

[118]   T. Marketin, N. Paar, T. Nikšić and D. Vretenar, *Phys. Rev. C* 79 (2009) 054323.

[119]   P. G. Giannaka and T. S. Kosmas, *Phys. Rev. C* 92 (2015) 014606.

[120]   E. J. Konopinski and G. E. Uhlenbeck, *Phys. Rev.* 60 (1941) 308.

[121]   M. Yamada and M. Morita, *Progr. Theoret. Phys. (Kyoto)* 8 (1952) 431.

[122]   M.L. Goldberger and S.B. Treiman, *Phys. Rev.* 111 (1958) 354.

[123]   E. D. Commmins and P. H. Bucksbaum, *Weak Interactions of Leptons and Quarks*, Cambridge: Cambridge University Press, 1983.

[124]   M. E. Rose and R. K. Osborn, *Phys. Rev.* 93 (1954) 1315.

[125]   H. A. Bethe and E. E. Salpeter, *Quantum Mechanics of One- and Two-Electron Atoms*, New York: Academic Press Inc., 1959.

[126]   D. J. Griffiths, *Introduction to Quantum Mechanics*, 2nd edition, Prentice Hall: Pearson, 1995.

[127]   K.W. Ford and J.G. Wills, *Nucl. Phys.* 35 (1962) 295.

[128]   I. G. Tsoulos, O. T. Kosmas and V. N. Stavrou, *DiracSolver: a tool for solving the Dirac Equation*, arXiv:1810.13042 [physics.comp-ph], 2018.

[129]   F. Salvat, J. Fernández-Varea and W. Williamson Jr., *Comput. Phys. Commun.* 90 (1995) 151–168.

[130]   H. Ejiri, J. Suhonen and K. Zuber, *Phys. Rep.* 797 (2019) 1.

[131] H. Ejiri, *Proc. CNNP2017*, volume 1056, J. Phys. Conf. Ser. 012019.

[132] H. Ejiri et al., *J. Phys. Soc. Jpn.* 82 (2013) 044202.

[133] J. Suhonen, *Front. Phys.* 5 (2017) 55.

[134] H. Ejiri, N. Soukouti and J. Suhonen, *Phys. Lett. B* 729 (2014) 27.

[135] J. Suhonen H. Ejiri, *J. Phys. G, Nucl. Part. Phys.* 42 (2015) 055201.

[136] P. Pirinen and J. Suhonen, *Phys. Rev. C* 91 (2015) 054309.

[137] F. F. Deppisch and J. Suhonen, *Phys. Rev. C* 94 (2016) 055501.

Article I

Isovector spin-multipole strength distributions in double-β-decay triplets
L. Jokiniemi and J. Suhonen,
Phys. Rev. C **96** (2017) 034308.

Isovector spin-multipole strength distributions in double-β-decay triplets

Lotta Jokiniemi[*] and Jouni Suhonen[†]

Department of Physics, University of Jyvaskyla, P.O. Box 35 (YFL), FI-40014 Jyvaskyla, Finland

In this work the energetics and strength distributions of isovector spin-dipole and spin-quadrupole transitions from the ground states of the pairs (^{76}Ge, ^{76}Se), (^{82}Se, ^{82}Kr), (^{96}Zr, ^{96}Mo), (^{100}Mo, ^{100}Ru), (^{116}Cd, ^{116}Sn), (^{128}Te, ^{128}Xe), (^{130}Te, ^{130}Xe), and (^{136}Xe, ^{136}Ba), of double-β-decay initial and final nuclei, to the $J^\pi = 0^-, 1^-, 2^-, 1^+, 2^+$, and 3^+ excited states of the intermediate odd-odd nuclei ^{76}As, ^{82}Br, ^{96}Nb, ^{100}Tc, ^{116}In, ^{128,130}I, and ^{136}Cs are investigated. The calculations are performed using a proton-neutron quasiparticle random-phase approximation (pnQRPA) theory framework with the Bonn-A two-body interaction in no-core single-particle valence spaces.

I. INTRODUCTION

At present, the properties of neutrinos attract a lot of interest in the particle-physics and nuclear-physics communities. These properties can be studied in many ways, among others by the neutrino-oscillation experiments, the neutrino-nucleus scattering, and the neutrinoless double-β ($0\nu\beta\beta$) decay [1–5]. The latter two processes require knowledge about nuclear properties in the form of the nuclear matrix elements (NMEs). The NMEs of these processes are built from real or virtual transitions between the ground state of an initial nucleus and the ground and excited states of a daughter nucleus. In particular, the transitions in the charged-current neutrino-nucleus scattering [6–8] and $0\nu\beta\beta$ share many common features, like the possibility to feed (highly) excited $J^\pi = 0^+, 0^-, 1^+, 1^-, 2^+, 2^-, 3^+, \ldots$ states of an odd-odd nucleus starting from the 0^+ ground state of the neighboring even-even isobar. A suitable framework for studying these real or virtual transitions is the proton-neutron random-phase approximation (pnRPA) at closed nuclear major shells [9] and the corresponding theory for quasiparticles (pnQRPA) in the case of superfluid open-shell systems [10,11].

In the case of two-neutrino double-β ($2\nu\beta\beta$) decay the NME consists of virtual Gamow-Teller (GT) transitions from the 0^+ ground states of the initial and final even-even nuclei to the 1^+ states of the intermediate nucleus. These transitions have typically been probed by the partial-wave $L = 0$ charge-exchange reactions (CXRs) by using the β^- type of (p,n) or (^{3}He,t) reactions and β^+ type of (n,p), (d,^{2}He), or (t,^{3}He) reactions [12–14]. Results of these reaction studies can be compared with theoretical calculations of the Gamow-Teller and isovector spin-monopole (IVSM) strength distributions [15–17]. Lately, the partial-wave $L = 1$ CXRs to 2^- states have gained momentum by the improved experimental methods and facilities, e.g., the RCNP in Osaka, Japan [18]. These studies could be relevant for the $0\nu\beta\beta$ decays because a considerable portion of the corresponding NME can be built from virtual transitions via the $J^\pi = 2^-$ multipole states [19,20]. The experimental considerations can also be extended to the other $L = 1$ CXRs by studying the β^- and

β^+ types of feedings of the 0^- and 1^- states involved in the NMEs of the $0\nu\beta\beta$ decays.

In the present work we extend the study of [9] to open-shell superfluid nuclei relevant for the $0\nu\beta\beta$ decays. In [9] the pnRPA model was used for closed-shell nuclei to study the isovector spin-dipole (IVSD, $L = 1$) and spin-quadrupole (IVSQ, $L = 2$) β^- and β^+ types of feeding of the $J^\pi = 0^-, 1^-, 2^-$ ($L = 1$) and $J^\pi = 1^+, 2^+, 3^+$ ($L = 2$) nuclear states in a few cases of odd-odd nuclei. Instead of the pnRPA, we adopt the pnQRPA (proton-neutron quasiparticle random-phase approximation) with partial restoration of the isospin symmetry [21] for our studies of the isovector spin-multipole $L = 1, 2$ feeding of the nuclei ^{76}As, ^{82}Br, ^{96}Nb, ^{100}Tc, ^{116}In, ^{128,130}I, and ^{136}Cs from the 0^+ ground states of ^{76}Ge, ^{82}Se, ^{96}Zr, ^{100}Mo, ^{116}Cd, ^{128,130}Te, and ^{136}Xe (β^- type of feeding) and from the 0^+ ground states of ^{76}Se, ^{82}Kr, ^{96}Mo, ^{100}Ru, ^{116}Sn, ^{128,130}Xe, and ^{136}Ba (β^+ type of feeding). The feasibility of probing experimentally the IVSD $L = 1$ strength distributions to $J^\pi = 1^-, 2^-$ states was demonstrated and experimental results are to be expected in the near future [18]. The feasibility of probing the IVSQ $L = 2$ strengths to $J^\pi = 1^+, 2^+, 3^+$ states is still an open question but could probably be done in the not so distant future. When and if available, the measured $L = 1$ and $L = 2$ strength distributions can be compared to the presently computed ones to learn more about the ability of the pnQRPA to describe the feeding of the important intermediate $J^\pi = 0^+, 0^-, 1^+, 1^-, 2^+, 2^-, 3^+$ multipole states in $0\nu\beta\beta$ processes.

The outline of this article is as follows: In Sec. II we introduce the used formalism, including the pnQRPA framework and transition amplitudes, in Sec. III we present and discuss the obtained results, and finally in Sec. IV we draw the final conclusions of the study.

II. SHORT REVIEW OF THE FORMALISM

The formalism developed in [16], for the GT and isovector spin-monopole (IVSM) excitation modes, is now extended to the IVSD and IVSQ modes. At the same time we extend the corresponding studies of [9] to open-shell superfluid nuclei. The calculations start from the ground states of a number of selected even-even nuclei. In the present study we investigate the double-beta emitters in the triplets of isobars with $A = 76, A = 82, A = 96, A = 100, A = 116, A = 128, A = 130,$

---

[*]lotta.m.jokiniemi@student.jyu.fi
[†]jouni.suhonen@phys.jyu.fi

and $A = 136$. In the following subsections the stages of this step-by-step study are explained briefly.

A. Single-particle bases

The single-particle energies for both protons and neutrons, for each even-even nucleus involved, are obtained by solving the radial Schrödinger equation for a Coulomb-corrected Woods-Saxon potential. The Woods-Saxon parameters are obtained from [22]. We include in our calculations only the bound and quasibound single-particle states.

In this work, the calculations are performed in large no-core single-particle bases, which means that all the states starting from $nl_j = 0s_{1/2}$ up to two oscillator major shells above the proton Fermi surface of each nucleus are taken into account. The same single-particle space is adopted also for neutrons.

B. Quasiparticle spectra

The two-body interaction used in the BCS calculations is derived from the Bonn-A one-boson-exchange potential introduced in [23]. The BCS pairing gaps are fitted to the observed ones [24–26] using the three-point formulas,

$$\Delta_n(A,Z) = \tfrac{1}{4}(-1)^{A-Z+1}[S_n(A+1,Z) - 2S_n(A,Z) + S_n(A-1,Z)],$$

$$\Delta_p(A,Z) = \tfrac{1}{4}(-1)^{Z+1}[S_p(A+1,Z+1) - 2S_p(A,Z) + S_p(A-1,Z-1)],$$ (1)

where S_p and S_n are the separation energies for protons and neutrons, respectively. This is achieved by adjusting the pairing strength parameters $g_{\text{pair}}^{(n)}$ and $g_{\text{pair}}^{(p)}$ which multiply the monopole G-matrix elements. The resulting pairing strength constants and pairing gaps are discussed in the next section.

C. Spectra of the J^π excitations in odd-odd nuclei

The wave functions and excitation energies for the complete set of J^π excitations in the odd-odd nuclei are obtained by performing a pnQRPA diagonalization in the basis of unperturbed quasiproton-quasineutron pairs coupled to J^π. The pnQRPA states in odd-odd nuclei are then of the form,

$$|\omega\rangle = Q_\omega^\dagger |\text{pnQRPA}\rangle$$
$$= \sum_{pn} \left[X_{pn}^\omega A_{pn}^\dagger(JM) - Y_{pn}^\omega \tilde{A}_{pn}(JM) \right] |\text{pnQRPA}\rangle,$$ (2)

where $\omega = nJ^\pi M$, X and Y are the forward- and backward-going amplitudes, $A^\dagger$ and $\tilde{A}$ the quasiproton-quasineutron creation and annihilation operators, and $|\text{pnQRPA}\rangle$ is the pnQRPA vacuum. M denotes the z projection of J. The formalism is explained in detail in, e.g., [24,26].

The X and Y amplitudes of (2) are calculated by diagonalizing the pnQRPA matrix separately for each multipole J^π. The isoscalar ($T = 0$) and isovector ($T = 1$) parts of the particle-particle G-matrix elements are multiplied by common factors $g_{pp}^{T=0}$ and $g_{pp}^{T=1}$, respectively, for all the multipoles according to a method proposed in [21]. In addition, the particle-hole part was scaled by a common factor g_{ph} for all

the multipoles. These renormalization factors are listed in the following section for each mass number separately.

D. Transition operators and strength distributions

The transition operators for the spin-dipole ($L = 1$) and spin-quadrupole ($L = 2$) transitions are of the form,

$$Q_{L,J}^\pm = r^L [\boldsymbol{Y}_L \boldsymbol{\sigma}]_J i^L t_\pm,$$ (3)

where Y_L is the spherical harmonic of rank L, $\boldsymbol{\sigma}$ the Pauli spin tensor operator, and t_+ and t_- are the isospin raising and lowering operators. The reduced single-particle NMEs of this operator are of the form [22,24],

$$(j_f || \mathcal{O}_{L,J}^\pm || j_i) = (n_f l_f \tfrac{1}{2} j_f || r^L [\boldsymbol{Y}_L \boldsymbol{\sigma}]_J i^L || n_i l_i \tfrac{1}{2} j_i)$$

$$= \sqrt{6} \hat{j}_f \hat{J} \hat{j}_i \frac{(-1)^{l_f}}{\sqrt{4\pi}} \hat{l}_f \hat{L} \hat{l}_i \begin{pmatrix} l_f & L & l_i \\ 0 & 0 & 0 \end{pmatrix}$$

$$\times \begin{Bmatrix} l_f & \tfrac{1}{2} & j_f \\ l_i & \tfrac{1}{2} & j_i \\ L & 1 & J \end{Bmatrix} \mathcal{R}_{fi}^{(L)} (-1)^{\frac{1}{2}(l_i - l_f + L)},$$ (4)

where $\mathcal{R}_{fi}^{(L)}$ is a radial integral [24] and the effect of the isospin ladder operators is taken into account by the fact that the initial $j_i = (n_i l_i \tfrac{1}{2} j_i)$ and final $j_f = (n_f l_f \tfrac{1}{2} j_f)$ single-particle states have different isospin projections. Here n denotes the principal quantum number, l the orbital angular momentum, and j the total angular momentum. Now the reduced NMEs can be calculated from [24]

$$(J^\pi || \mathcal{O}_{L,J}^\pm || 0^+) = \sum_{ab} \frac{(a || \mathcal{O}_{L,J}^\pm || b)}{\sqrt{2J+1}} (J^\pi || [c_a^\dagger \tilde{c}_b]_J || 0^+),$$ (5)

where b and a denote the initial and final single-particle quantum numbers.

The transition strength for a transition from a 0^+ ground state to the ith J^π state can be calculated from

$$S_{LJ}^\pm(i) = |(J_i^\pi || \mathcal{O}_{L,J}^\pm || 0^+)|^2.$$ (6)

III. RESULTS AND DISCUSSION

In this chapter we present and discuss the results and the methods used in the calculations.

A. Single-particle bases and energies

We created the single-particle bases by solving the eigenstates of the Woods-Saxon potential for protons and neutrons, separately (for protons we corrected the potential with the Coulomb force). The values for the central, orbital, and spin-orbit parameters, and the radius and the surface thickness parameters needed in the calculations were taken from [22]. Small adjustments to the proton and neutron single-particle energies were done for the orbitals close to the Fermi surfaces to better reproduce the low-lying spectra of the neighboring odd-mass nuclei. Because we are dealing with no-core calculations, we take all the orbits from the $N = 0$ oscillator major shell up to about two oscillator major shells above the respective Fermi surfaces for protons and neutrons.

TABLE I. Pairing scaling factors and the resulting pairing gaps for the nuclei relevant for this work.

Nucleus	$g_{\text{pair}}^{(n)}$	$g_{\text{pair}}^{(p)}$	Δ_n(MeV)	Δ_p(MeV)
^{76}Ge	0.97	0.89	1.57	1.52
^{76}Se	1.01	0.91	1.72	1.71
^{82}Se	0.94	0.84	1.51	1.43
^{82}Kr	1.01	0.86	1.65	1.63
^{96}Zr	0.77	0.85	0.92	1.48
^{96}Mo	0.90	0.93	1.03	1.52
^{100}Mo	0.88	0.96	1.31	1.63
^{100}Ru	0.85	0.93	1.27	1.60
^{116}Cd	0.89	0.93	1.37	1.43
^{116}Sn	0.82	0.89	1.16	1.84
^{128}Te	0.86	0.81	1.30	1.09
^{128}Xe	0.86	0.88	1.27	1.30
^{130}Te	0.86	0.78	1.21	1.02
^{130}Xe	0.85	0.86	1.25	1.26
^{136}Xe	0.84	0.76	1.44	0.98
^{136}Ba	0.87	0.83	1.08	1.22

An example of the single-particle orbitals and energies for the $A = 76$ system is shown in Table I in [17].

B. Pairing gaps, quasiparticle spectra, and BCS occupation factors

The two-body matrix elements obtained from the Bonn-A interaction were applied to the "left-hand-side" and "right-hand-side" even-even nuclei by renormalizing the monopole neutron and proton channels, separately. The scaling factors $g_{\text{pair}}^{(n)}$ and $g_{\text{pair}}^{(p)}$ were adjusted to reproduce the phenomenological pairing gaps given in Eq. (1). The needed neutron (proton) separation energies S_n (S_p) were taken from [27] and [28]. The scaling factors and the resulting pairing gaps for the nuclei of interest are listed in Table I. Using these scaling factors we performed the BCS calculations and obtained the one-quasiparticle spectra and occupation factors v and vacancy factors u needed in the subsequent pnQRPA calculations of the energies and wave functions. These factors, along with the pnQRPA amplitudes of (2), are used to construct the one-body transition densities of (5) in the form [24],

$$(J^\pi||[c_p^\dagger \tilde{c}_n]_J||0^+) = \hat{J}\left(u_p v_n X_{pn}^\omega + v_p u_n Y_{pn}^\omega\right), \quad (7)$$

$$(J^\pi||[c_n^\dagger \tilde{c}_p]_J||0^+) = \hat{J}(-1)^J\left(v_p u_n X_{pn}^\omega + u_p v_n Y_{pn}^\omega\right). \quad (8)$$

C. Energy spectra and IVSD and IVSQ strength distributions

We decompose each isobaric triplet with mass number A to "left-hand-side" even-even (A, N, Z), "right-hand-side" even-even $(A, N-2, Z+2)$, and "intermediate" odd-odd $(A, N-1, Z+1)$ nuclei. We construct the spectra of J^π excitations in the intermediate odd-odd nuclei applying the pnQRPA formalism [25,26,29], including particle-hole and particle-particle channels, to the left- and right-hand-side even-even nuclei. In this way we obtain two sets of energies and wave functions for each J^π state.

TABLE II. Renormalization factors for the particle-hole and particle-particle interactions in different nuclei.

A	g_{ph}	$g_{\text{pp}}^{T=0}$	$g_{\text{pp}}^{T=1}$
76	1.156	0.83	0.96
82	0.997	0.82	0.95
96	1.415	0.89	0.94
100	1.224	0.875	0.91
116	1.518	0.82	0.81
128	1.267	0.745	0.87
130	1.228	0.73	0.86
136	1.262	0.67	0.87

The values of the particle-hole (particle-particle) renormalization factors g_{ph} ($g_{\text{pp}}^{T=0,1}$) are listed in Table II. The g_{ph} values were fitted to reproduce the energetics of the "left-hand-side" GT$^-$ giant resonance (GTGR). The g_{pp} values have usually been fixed by the half-lives of $2\nu\beta\beta$ decays [30–34], by the $\log ft$ values of β decays [35,36], or by both β and $2\nu\beta\beta$ decays [37,38]. In this work, we adopt an improved method, quasiparticle random phase approximation with partial restoration of the isospin symmetry, introduced in [19], and first proposed in [21]: We decompose the pnQRPA NMEs into isoscalar $(T = 0)$ and isovector $(T = 1)$ parts and then adjust the parameters $g_{\text{pp}}^{T=0}$ and $g_{\text{pp}}^{T=1}$ independently. The isovector parameter $g_{\text{pp}}^{T=1}$ is adjusted so that the Fermi NME of $2\nu\beta\beta$ matrix element vanishes, and thus the isospin symmetry is restored. Then we independently vary the isoscalar parameter $g_{\text{pp}}^{T=0}$ such that it reproduces the calculated matrix element corresponding to the measured $2\nu\beta\beta$ half-life and a slightly quenched value $g_A = 1.0$ of the axial vector coupling constant. These values are determined for each mass number separately, and the obtained parameters are adopted for all the multipoles in both left- and right-hand-side even-even nuclei. The bare value $g_A = 1.27$ was also tested in the determination of the $g_{\text{pp}}^{T=0}$ parameters, but the parameter values obtained this way differed only by 0.01–0.03 from those obtained with $g_A = 1.0$, resulting in less than 0.3-MeV differences in the obtained energy centroids of the spin-multipole giant resonances. Because the changes in the energy centroids were so minor, we do not list separately the results for $g_A = 1.27$.

D. Energy centroids and strength functions for the spin-dipole and spin-quadrupole excitations

In this section we discuss the strength distributions of the IVSD and IVSQ excitations for the left-hand-side (IVSD$^-$ and IVSQ$^-$) and right-hand-side (IVSD$^+$ and IVSQ$^+$) initial ground states. The corresponding strength functions are

$$S(\text{IVSD}^-)(i) = |(J_i^\pi||\mathcal{O}_{1,J}^-||0_L^+)|^2, \quad (9)$$

$$S(\text{IVSD}^+)(i) = |(J_i^\pi||\mathcal{O}_{1,J}^+||0_R^+)|^2, \quad (10)$$

$$S(\text{IVSQ}^-)(i) = |(J_i^\pi||\mathcal{O}_{2,J}^-||0_L^+)|^2, \quad (11)$$

$$S(\text{IVSQ}^+)(i) = |(J_i^\pi||\mathcal{O}_{2,J}^+||0_R^+)|^2, \quad (12)$$
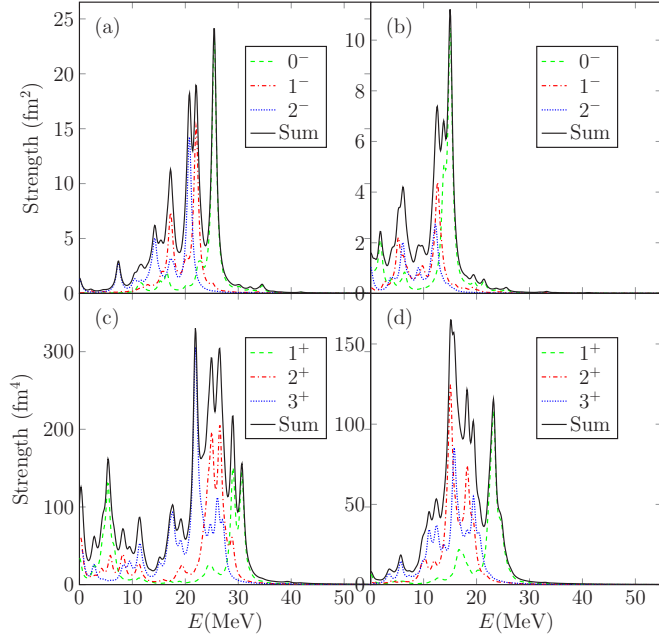
FIG. 1. Strength distributions for $A = 76$. (a) $L = 1, \beta^-$, (b) $L = 1, \beta^+$, (c) $L = 2, \beta^-$, (d) $L = 2, \beta^+$. The solid line denotes the sum of the dashed, dotted, and dash-dotted individual contributions. Energies are measured relative to the ground state of the odd-odd final nucleus. The strengths are given in units of fm^2 for $J^\pi = 0^-, 1^-, 2^-$ and in fm^4 for $J^\pi = 1^+, 2^+, 3^+$.

where the transition operator is given in (3), 0_L^+ (0_R^+) is the ground state of the left-hand-side (right-hand-side) even-even nucleus, and J_i^π is the ith J^π state in the intermediate odd-odd nucleus.

The resulting strength distribution is discrete because of the discrete basis used in the calculation. To make it better comparable with the experimental distribution we fold it with the Lorentzian folding function [39],

$$F_L(E - E_0) = \frac{W}{\pi} \frac{1}{W^2 + (E - E_0)^2}, \qquad (13)$$

where E is the excitation energy in the odd-odd final nucleus, E_0 the energy of the pnQRPA phonon corresponding to a peak, and W the width of this Lorentz peak. For the width we have chosen the value $W = 0.5$ MeV. The folded strength distributions are shown in Figs. 1–8 for different mass numbers. In the (a) panels the strength distributions of IVSD$^-$ transitions to different multipoles are shown, in the (b) panels the corresponding strength distributions of IVSD$^+$ transitions are shown, and in the (c) and (d) panels the IVSQ$^-$ and IVSQ$^+$ transitions to different multipoles are shown. The energies are given in MeV with respect to the ground state of the odd-odd final nucleus and the solid line gives the sum distribution by adding the dashed, dotted, and dash-dotted individual contributions. The strengths are given in units of fm^2 for the $L = 1$ ($J^\pi = 0^-, 1^-, 2^-$) transitions and in fm^4 for the $L = 2$ ($J^\pi = 1^+, 2^+, 3^+$) transitions.

We note that for $L = 1$ β^- transitions the average energy is highest for 0^- excitations, except for a few exceptions, lowest for 2^- excitations. This effect was also noted in the earlier
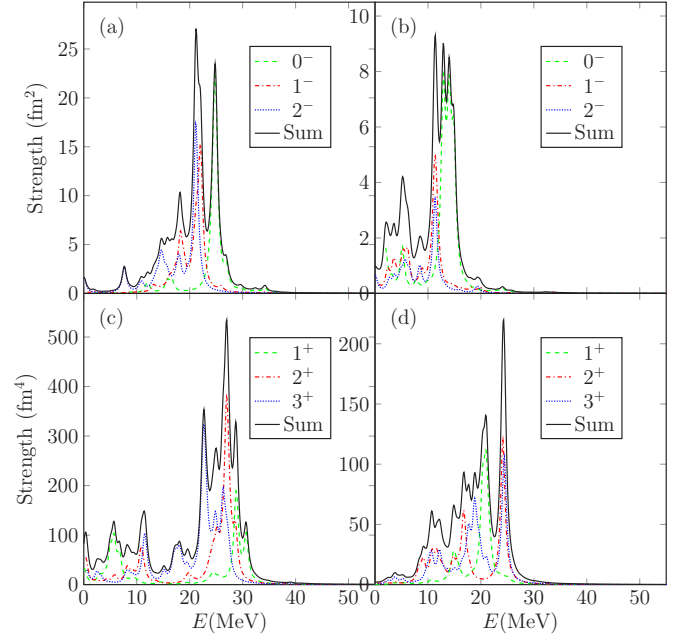
FIG. 2. The same as in Fig. 1 for $A = 82$.

calculations [9,40,41]. It can also be noted that the strength for $J^\pi = 0^-, 1^-$ is concentrated in a few peaks, whereas the strength for $J^\pi = 2^-$ is more spread. This was noted also in [9].

Similar effects can be seen in the case of $L = 2$ β^- transitions: The 1^+ excitations are the highest in energy, whereas the 3^+ excitations are the lowest. As noted in [9], most of the strength of $J^\pi = 1^+$ resonances is carried by a few peaks, whereas for the $J^\pi = 2^+, 3^+$ excitations the strength distributions are much more fragmented. This effect becomes more visible for the heavier masses.
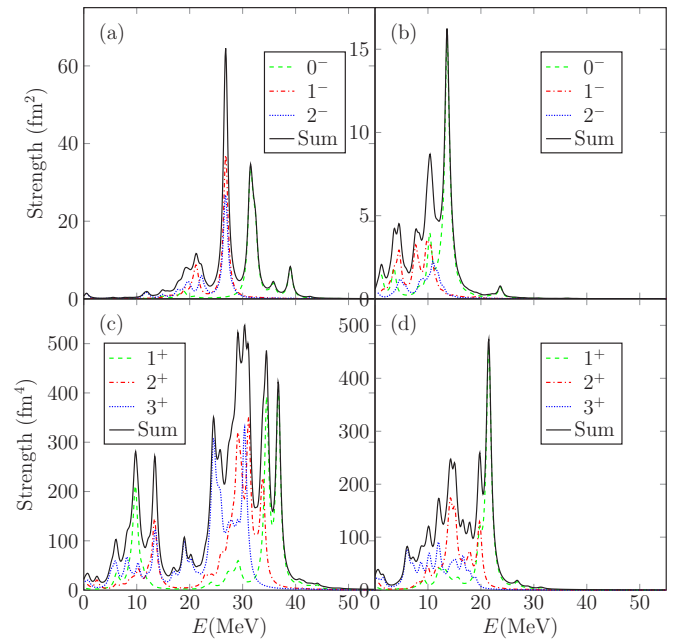
FIG. 3. The same as in Fig. 1 for $A = 96$.

FIG. 4. The same as in Fig. 1 for $A = 100$.

In Table III we present the calculated energy centroids for IVSD$^\pm$ and IVSQ$^\pm$ transitions for different multipoles and mass numbers. The energies are again given with respect to the odd-odd final nucleus. For the β^- type of strength the spin-multipole giant resonance (SMGR) region forms a more or less isolated island so that the total strength of the GR region can be separated from the low-energy one. This is why in Table III the spin-multipole strength of the SMGR is only part of the total β^- strength S_{tot}^-. For the β^+ type of transitions such a separation is not easy and hence only the total strength S_{tot}^+ is given.
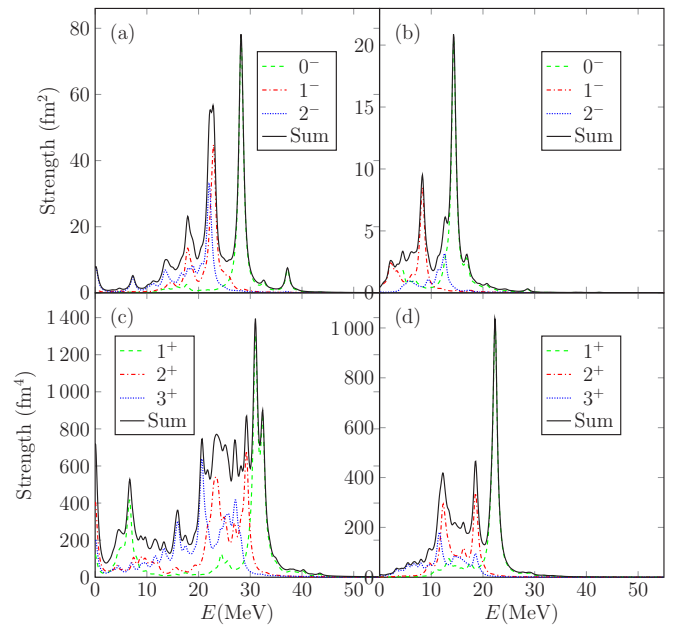
From Table III we see that for $L = 1$ transitions the strengths S_{tot}^- and S_{tot}^+ are largest for 0^- transitions and smallest for 2^- transitions, except for the $A = 82$ system. This kind of trend was also noted in [9] for closed-shell nuclei. In [9] it was seen that for $L = 2$ transitions the strengths S_{tot}^- and S_{tot}^+ are largest for 1^+ transitions and smallest for 3^+ transitions. Our results for S_{tot}^- and S_{tot}^+ differ from [9] for mass numbers $A = 76$ and 82, and S_{tot}^- for mass numbers $A = 96, 128, 130$, and 136. Only for $A = 116$ and 100 our results agree with [9]. The deviations from the IVSD results of [9] are most likely related to the fact that in the present work we discuss open-shell nuclei, not magic nuclei as in [9].
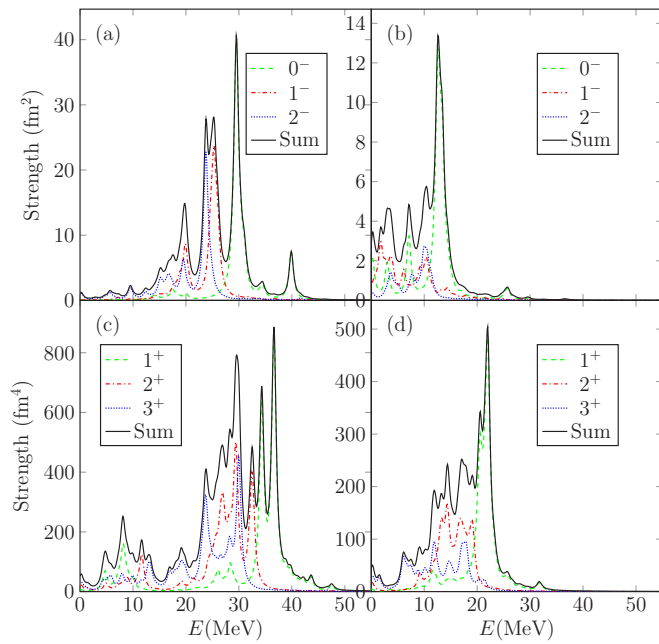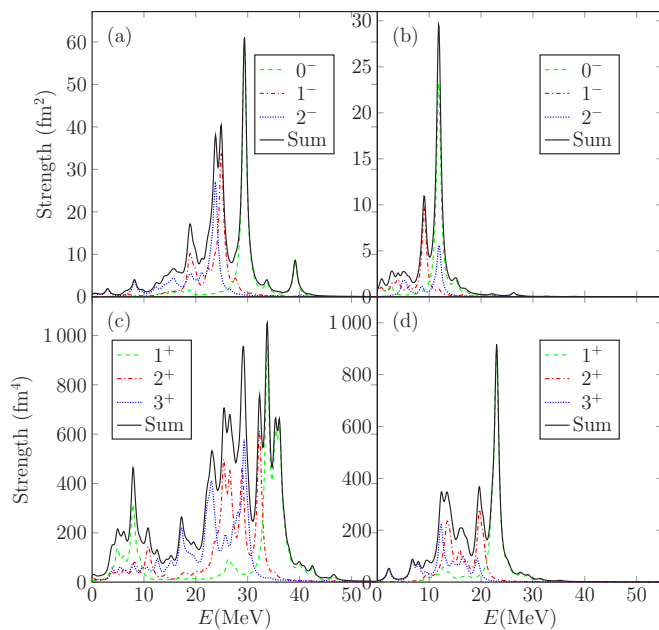

FIG. 6. The same as in Fig. 1 for $A = 128$.
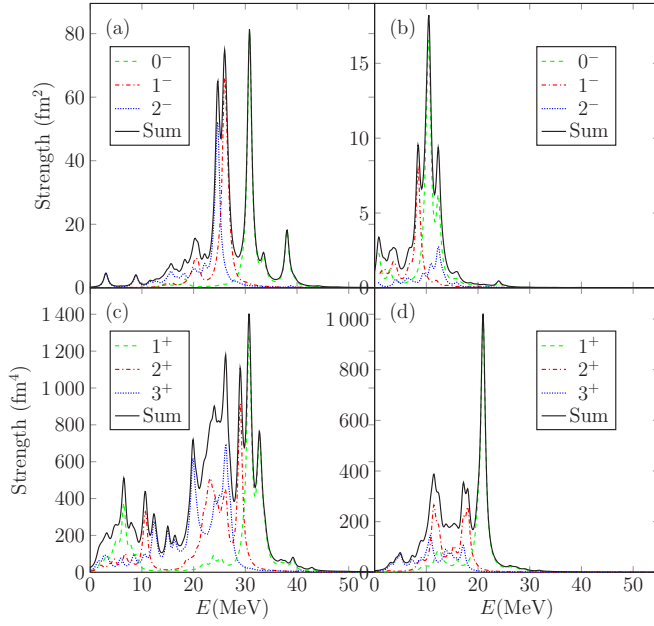

FIG. 5. The same as in Fig. 1 for $A = 116$.
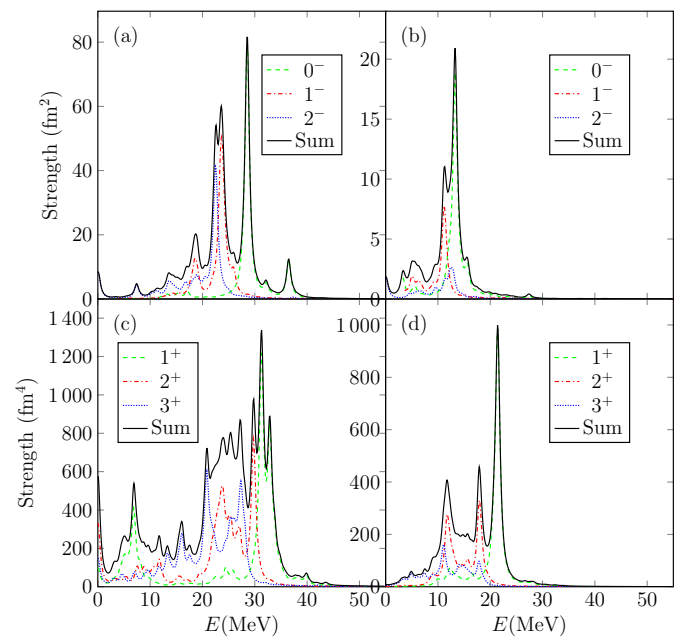
FIG. 7. The same as in Fig. 1 for $A = 130$.

FIG. 8. The same as in Fig. 1 for $A = 136$.

IV. CONCLUSIONS

In this work we have performed realistic pnQRPA calculations of the isovector spin-dipole and spin-quadrupole excitations in odd-odd nuclei belonging to double-β-decay triplets with $A = 76$, $A = 82$, $A = 96$, $A = 100$, $A = 116$, $A = 128$, $A = 130$, and $A = 136$. The calculations were performed in large no-core single-particle bases with realistic Bonn-A-type two-body interactions. The couplings of the pairing monopole channels were adjusted to reproduce the experimental odd-even mass differences separately for protons and neutrons. Furthermore, the proton-neutron particle-hole renormalization factor was fitted to the energy of the GTGR centroids of the left-hand-side even-even nuclei. The isovector and isoscalar particle-particle strengths were fitted to reproduce the observed $2\nu\beta\beta$ half-lives and to restore the isospin symmetry of the $2\nu\beta\beta$ transitions, as proposed in [21].

The resulting strength distributions of orbital angular momentum $L = 1,2$ transitions were computed and plotted for the multipole $J^\pi = 0^-,1^+,1^-,2^+,2^-,3^+$ states in the odd-odd intermediate nuclei. From these distributions we can see that there is a considerable difference in the giant-resonance energy centroids of the various J states corresponding to a given L. For $L = 1$ transitions the transition strengths were highest for the lowest-J transitions and lowest for the highest-J transitions, except for $A = 82$. For $L = 2$ transitions there was no clear ordering for the transition strengths.

In the future, having access to experimental data on the $L = 1$ (and possibly $L = 2$) strength functions, one could make comparisons with the present and future theoretical calculations and access the validity of, e.g., the model Hamiltonians and their predicted isovector spin-multipole distributions and giant resonance properties.

TABLE III. Energy centroids of SMGRs and transition strengths $S^\pm(\text{GR})$ of the corresponding β^- and β^+ transitions for different mass numbers. Also the total strengths $S_{\text{tot}}^\pm$ are given. The strengths are given in units of fm^2 for $J^\pi = 0^-,1^-,2^-$ and in fm^4 for $J^\pi = 1^+,2^+,3^+$.

A	J^π	$E(\text{GR})_-$ (MeV)	$S^-(\text{GR})$	S_{tot}^-	$E(\text{GR})_+$ (MeV)	$S_{\text{tot}}^+ = S^+(\text{GR})$
76	0^-	18.752	48.168	50.360	11.623	30.945
	1^-	14.751	47.910	48.785	6.871	21.143
	2^-	16.639	39.080	45.333	10.225	12.391
	1^+	26.502	529.73	834.15	20.199	370.39
	2^+	22.406	1017.3	1220.3	16.455	485.92
	3^+	19.285	1295.8	1496.2	13.101	550.41
82	0^-	17.339	47.873	50.305	10.388	32.835
	1^-	14.300	52.503	53.505	7.197	22.323
	2^-	15.798	47.021	52.472	10.218	12.758
	1^+	25.493	512.94	847.96	19.542	383.65
	2^+	23.201	1080.6	1441.6	19.395	511.23
	3^+	19.387	1385.8	1815.7	18.018	604.18
96	0^-	31.703	99.535	99.695	11.914	41.175
	1^-	24.954	82.338	82.990	7.810	23.343
	2^-	22.720	66.923	71.897	8.325	12.496
	1^+	33.900	1485.8	1987.0	19.959	1128.7
	2^+	27.214	2137.8	2306.3	14.967	963.80
	3^+	24.002	2108.2	2440.8	10.803	816.56
100	0^-	25.639	104.54	105.21	11.532	46.076
	1^-	19.847	86.159	87.810	7.356	27.033
	2^-	18.487	69.902	74.454	8.673	13.785
	1^+	31.196	2946.2	3447.2	20.938	1629.2
	2^+	24.227	2644.2	3088.6	15.122	1212.2
	3^+	21.248	2405.9	2842.4	11.063	925.65
116	0^-	29.069	123.49	124.29	11.537	42.862
	1^-	22.780	107.91	108.56	7.215	24.937
	2^-	21.002	89.649	100.83	9.278	15.684
	1^+	34.214	3541.6	4450.9	22.103	1920.6
	2^+	27.367	3559.4	4084.1	16.253	1411.7
	3^+	24.327	3567.6	4021.4	12.840	1140.8
128	0^-	22.888	156.98	160.33	10.189	47.981
	1^-	16.943	135.86	138.30	6.841	26.435
	2^-	17.069	108.12	121.01	9.774	14.658
	1^+	28.038	3733.4	4771.9	21.330	2204.5
	2^+	22.628	3749.4	4613.8	16.018	1595.0
	3^+	19.087	4166.9	4861.7	12.939	1153.4
130	0^-	25.108	165.89	169.18	11.614	46.475
	1^-	19.342	143.27	147.54	8.517	25.007
	2^-	17.058	116.69	130.18	9.369	13.620
	1^+	27.796	3842.5	4973.5	20.950	2201.8
	2^+	22.648	3918.9	4870.3	16.058	1574.0
	3^+	19.252	4443.6	5207.7	12.798	1103.3
136	0^-	29.610	180.57	180.63	9.858	44.987
	1^-	23.886	158.95	159.29	6.812	23.770
	2^-	21.631	132.88	149.85	9.146	13.265
	1^+	28.709	3897.1	5163.8	20.268	2220.1
	2^+	23.065	4627.8	5112.8	15.707	1584.7
	3^+	20.234	5004.4	5498.7	12.231	1094.8

ACKNOWLEDGMENTS

This work was partially supported by the Academy of Finland under the Finnish Centre of Excellence Programme 2012-2017 (Nuclear and Accelerator Based Programme at JYFL).

[1] H. Ejiri, Phys. Rep. **338**, 265 (2000).

[2] F. T. Avignone, S. R. Elliot, and J. Engel, Rev. Mod. Phys. **80**, 481 (2008).

[3] J. D. Vergados, H. Ejiri, and F. Šimkovic, Rep. Prog. Phys. **75**, 106301 (2012).

[4] J. Suhonen and O. Civitarese, Phys. Rep. **300**, 123 (1998).

[5] J. Maalampi and J. Suhonen, Adv. High Energy Phys. **2013**, 505874 (2013).

[6] E. Ydrefors and J. Suhonen, Phys. Rev. C **87**, 034314 (2013).

[7] W. Almosly, B. G. Carlsson, J. Dobaczewski, J. Suhonen, J. Toivanen, P. Vesely, and E. Ydrefors, Phys. Rev. C **89**, 024308 (2014).

[8] W. Almosly, B. G. Carlsson, J. Suhonen, J. Toivanen, and E. Ydrefors, Phys. Rev. C **94**, 044614 (2016).

[9] N. Auerbach and A. Klein, Phys. Rev. C **30**, 1032 (1984).

[10] J. Suhonen and O. Civitarese, J. Phys. G **39**, 085105 (2012).

[11] J. Suhonen and O. Civitarese, J. Phys. G **39**, 124005 (2012).

[12] P. Puppe, D. Frekers, T. Adachi, H. Akimune, N. Aoi, B. Bilgier, H. Ejiri, H. Fujita, Y. Fujita, M. Fujiwara, E. Ganioğlu, M. N. Harakeh, K. Hatanaka, M. Holl, H. C. Kozer, J. Lee, A. Lennarz, H. Matsubara, K. Miki, S. E. A. Orrigo, T. Suzuki, A. Tamii, and J. H. Thies, Phys. Rev. C **84**, 051305(R) (2011).

[13] J. H. Thies, D. Frekers, T. Adachi, M. Dozono, H. Ejiri, H. Fujita, Y. Fujita, M. Fujiwara, E.-W. Grewe, K. Hatanaka, P. Heinrichs, D. Ishikawa, N. T. Khai, A. Lennarz, H. Matsubara, H. Okamura, Y. Y. Oo, P. Puppe, T. Ruhe, K. Suda, A. Tamii, H. P. Yoshida, and R. G. T. Zegers, Phys. Rev. C **86**, 014304 (2012).

[14] D. Frekers, P. Puppe, J. H. Thies, and H. Ejiri, Nucl. Phys. A **916**, 219 (2013).

[15] I. Hamamoto and H. Sagawa, Phys. Rev. C **62**, 024319 (2000).

[16] D. R. Bes, O. Civitarese, and J. Suhonen, Phys. Rev. C **86**, 024314 (2012).

[17] O. Civitarese and J. Suhonen, Phys. Rev. C **89**, 044319 (2014).

[18] D. Frekers, M. Alanssari, H. Ejiri, M. Holl, A. Poves, and J. Suhonen, Phys. Rev. C **95**, 034619 (2017).

[19] J. Hyvärinen and J. Suhonen, Phys. Rev. C **91**, 024613 (2015).

[20] J. Hyvärinen and J. Suhonen, Adv. High Energy Phys. **2016**, 4714829 (2016).

[21] F. Šimkovic, V. Rodin, A. Faessler, and P. Vogel, Phys. Rev. C **87**, 045501 (2013).

[22] A. Bohr and B. R. Mottelson, *Nuclear Structure*, Vol. 1 (Benjamin, New York, 1969).

[23] K. Holinde, Phys. Rep. **68**, 121 (1981).

[24] J. Suhonen, *From Nucleons to Nucleus: Concepts of Microscopic Nuclear Theory* (Springer, Berlin, 2007).

[25] J. Suhonen, Nucl. Phys. A **563**, 205 (1993).

[26] J. Suhonen, T. Taigel, and A. Faessler, Nucl. Phys. A **486**, 91 (1988).

[27] Computer code NUDAT 2.6, Brookhaven National Laboratory, online [http://www.nndc.bnl.gov/nudat2/].

[28] M. Wang, G. Audi, A. H. Wapstra, F. G. Kondev, M. MacCormick, X. Xu, and B. Pfeiffer, Chin. Phys. C **36**, 1157 (2012).

[29] O. Civitarese, A. Faessler, and T. Tomoda, Phys. Lett. B **194**, 11 (1987).

[30] F. Šimkovic, A. Faessler, V. Rodin, P. Vogel, and J. Engel, Phys. Rev. C **77**, 045503 (2008).

[31] M. Kortelainen, O. Civitarese, J. Suhonen, and J. Toivanen, Phys. Lett. B **647**, 128 (2007).

[32] M. Kortelainen and J. Suhonen, Phys. Rev. C **75**, 051303(R) (2007).

[33] M. Kortelainen and J. Suhonen, Phys. Rev. C **76**, 024315 (2007).

[34] J. Suhonen and M. Kortelainen, Int. J. Mod. Phys. E **17**, 1 (2008).

[35] M. Aunola and J. Suhonen, Nucl. Phys. A **602**, 133 (1996).

[36] J. Suhonen, Phys. Lett. B **607**, 87 (2005).

[37] J. Suhonen and O. Civitarese, Phys. Lett. B **725**, 153 (2013).

[38] J. Suhonen and O. Civitarese, Nucl. Phys. A **924**, 1 (2014).

[39] B. Frois and I. Sick, *Modern Topics in Electron Scattering* (World Scientific, Singapore, 1991).

[40] G. F. Bertsch, D. Cha, and H. Toki, Phys. Rev. C **24**, 533 (1981).

[41] F. Krmpotic, K. Ebert, and W. Wild, Nucl. Phys. A **342**, 497 (1980).

Article II

Neutrinoless $\beta\beta$ nuclear matrix elements using isovector spin-dipole $J^\pi = 2^-$ data

L. Jokiniemi,[1] H. Ejiri,[2,3] D. Frekers,[4] and J. Suhonen[1]

[1]*Department of Physics, University of Jyväskylä, P.O. Box 35 (YFL), FI-40014 Jyväskylä, Finland*
[2]*Research Center for Nuclear Physics, Osaka University, Ibaraki, Osaka 567-0047, Japan*
[3]*Nuclear Physics, Czech Technical University, Prague, Czech Republic*
[4]*Institut für Kernphysik, Westfälische Wilhelms-Universität, D-48149 Münster, Germany*

Ground-state-to-ground-state neutrinoless double-beta ($0\nu\beta\beta$) decays in nuclei of current experimental interest are revisited. In order to improve the reliability of the nuclear matrix element (NME) calculations for the light Majorana-neutrino mode, the NMEs are calculated by exploiting the newly available data on isovector spin-dipole (IVSD) $J^\pi = 2^-$ giant resonances. In order to correctly describe the IVSD up to and beyond the giant-resonance region, the present computations are performed in extended no-core single-particle model spaces using the spherical version of the proton-neutron quasiparticle random-phase approximation (pnQRPA) with two-nucleon interactions based on the Bonn one-boson-exchange G matrix. The appropriate short-range correlations, nucleon form factors, higher-order nucleonic weak currents, and partial restoration of the isospin symmetry are included in the calculations. The results are compared with earlier calculations of Hyvärinen and Suhonen [Phys. Rev. C **91**, 024613 (2015)] performed in much smaller single-particle bases without access to the IVSD $J^\pi = 2^-$ giant-resonance data reported here.

I. INTRODUCTION

The neutrinoless double-beta ($0\nu\beta\beta$) decay of atomic nuclei is a promising way to access the physics beyond the standard model [1–5], as witnessed by the ever growing experimental interest in this decay mode. At the same time half-lives of the two-neutrino $\beta\beta$ ($2\nu\beta\beta$) decays of several nuclei have been measured with increased precision [6,7]. Important nuclei for the present $0\nu\beta\beta$ experiments are ^{76}Ge, ^{82}Se, ^{96}Zr, ^{100}Mo, ^{116}Cd, ^{130}Te, and ^{136}Xe [8].

There are many models which have recently been used to compute the $0\nu\beta\beta$ nuclear matrix elements (NMEs): the quasiparticle random-phase approximation (QRPA), as well as its proton-neutron version (pnQRPA) (see, e.g., [9]) and its renormalized extensions [10,11], the interacting shell model (ISM) [12,13], the microscopic interacting boson model (IBA-2) [14], the Gogny-based energy-density functional (EDF) [15] and its variation [16], and the projected Hartree-Fock-Bogoliubov mean-field scheme (PHFB) [17]. Very recently also the beyond-mean-field covariant density functional theory [18,19] and advanced shell-model frameworks [20–23] have been used to describe the $0\nu\beta\beta$ NMEs of nuclei. For more details see the reviews [5,24].

The pnQRPA has several advantages in calculating the $2\nu\beta\beta$ and $0\nu\beta\beta$ NMEs:

(i) In the pnQRPA calculations one avoids the use of the closure approximation,

(ii) pnQRPA can accommodate large single-particle bases, including all the relevant spin-orbit-partner orbitals [25,26], and

(iii) the gross features of the distribution of nuclear states can be reliably accounted for by the pnQRPA [27]

although the model may fail to predict properties of individual states.

The features (i)–(iii) of the pnQRPA make it an ideal nuclear model to combine the $2\nu\beta\beta$ and $0\nu\beta\beta$ calculations in a consistent way. The relation of the pnQRPA Hamiltonian and the $2\nu\beta\beta$ decay was further deepened in the work of Ref. [28] where a partial isospin-restoration scheme for the pnQRPA was proposed. This same method was later used by Hyvärinen *et al.* [29] for pnQRPA-based and in Barea *et al.* [30] for IBM-2 based $0\nu\beta\beta$-decay calculations.

A key parameter of the pnQRPA is the particle-hole parameter g_{ph} associated with the spin-isospin correlations and the location [31] of the giant resonances. So far in the calculations the value of this parameter has been fixed by fitting the location of the Gamow-Teller giant resonance (GTR). The fitted value, $g_{ph}(1^+)$, together with the value of the particle-particle parameter g_{pp} of the pnQRPA, fixes the contribution of the 1^+ channel to the $0\nu\beta\beta$ NME. However, the 1^+ contributions to the $0\nu\beta\beta$ NME are in many cases (much) smaller than the contributions from the 2^- isovector spin-dipole (IVSD) states which play an important role in this NME, in particular for the medium-heavy nuclei (see Fig. 7). Recently data on the location of the IVSD giant resonances became available from charge-exchange reactions performed at the Research Center for Nuclear Physics (RCNP), Osaka, Japan. Here we report for the first time on the values of the $0\nu\beta\beta$ NMEs based on g_{ph} values $g_{ph}(2^-)$, fixed by the observed location of the IVSD giant resonances.

In the present work we compute the $0\nu\beta\beta$ NMEs using the spherical version of pnQRPA framework and the partial isospin-restoration scheme of Ref. [28]. The value of g_{ph}

is determined by the empirical locations of the $J^\pi = 1^+$ GTR and the $J^\pi = 2^-$ IVSD giant resonance. The isoscalar part of the particle-particle parameter, $g_{pp}^{T=0}$, is fitted to the values of the $2\nu\beta\beta$ matrix elements. The value of the isovector part of the particle-particle parameter, $g_{pp}^{T=1}$, on the other hand, is determined by the isospin-restoration scheme. We extend the studies of [29,32–34] by using large no-core single-particle bases in order to reliably describe the IVSD $J^\pi = 2^-$ giant-resonance region and to see how the extension of the valence space affects the magnitudes of the $0\nu\beta\beta$ NMEs for the nuclei of interest. We also extend our previous work [35] by studying the impact of the value of the parameter $g_{ph}(2^-)$ on the magnitude of the $0\nu\beta\beta$ NME, when adjusted to describe the energy of the measured IVSD $J^\pi = 2^-$ giant resonance separately. All this is done to test the reliability of the $0\nu\beta\beta$ NMEs computed in Ref. [29] and to produce an improved set of NMEs for further use in, e.g., analyses related to the experimental $0\nu\beta\beta$ data.

This article is organized as follows: In Sec. II we briefly introduce the underlying formalism of the $2\nu\beta\beta$ and $0\nu\beta\beta$ decays as well as the IVSD $J^\pi = 2^-$ strength. In Sec. III we discuss the determination of the model parameters, and display and discuss the obtained results for the $0\nu\beta\beta$ NMEs calculated using different single-particle bases and model parameters. The final conclusions are drawn in Sec. IV.

II. COMPUTATIONAL SCHEME

In this section we introduce a brief theoretical outline of our computational scheme. Both the IVSD $J^\pi = 2^-$ and $0\nu\beta\beta$ calculations are based on the spherical version of pnQRPA theory, which is reviewed briefly in the first subsection. In the following subsections we introduce the theoretical aspects of the IVSD $J^\pi = 2^-$ strength, two-neutrino double-beta decay, and neutrinoless double-beta decay, correspondingly.

A. pnQRPA and the Hamiltonian parameters

In this section we explain the spherical version of the pn-QRPA procedure briefly, starting from the single-particle bases for protons and neutrons: The single-particle energies for both protons and neutrons, for each even-even nucleus involved, are obtained by solving the radial Schrödinger equation for a Coulomb-corrected Woods-Saxon (WS) potential optimized for nuclei close to the β stability line [36]. This choice is justified since the $\beta\beta$-decaying nuclei lie always rather close to the bottom of the valley of beta stability. We adopt the single-particle bases used in the isovector spin-multipole calculations of [35], i.e., no-core bases with all the orbits from the $N = 0$ oscillator major shell up to at least two oscillator major shells above the respective Fermi surfaces for protons and neutrons. We include in our calculations both the bound and quasibound single-particle states. The same orbitals are used for both neutrons and protons. We perform our calculations, whenever possible, in both the bare Woods-Saxon bases, abbreviated as "WS", and in the slightly modified bases that we used in [35], where the proton/neutron single-particle energies of the orbitals close to the Fermi surfaces were adjusted to better

TABLE I. Pairing scaling factors and the resulting pairing gaps for the nuclei relevant for this work. "WS" denotes the Woods-Saxon and "sp" the modified basis.

Nucleus	Basis	$g_{pair}^{(n)}$	$g_{pair}^{(p)}$	Δ_n (MeV)	Δ_p (MeV)
^{76}Ge	WS	1.05	0.89	1.57	1.52
	sp	0.97	0.89		
^{76}Se	WS	1.06	0.91	1.72	1.71
	sp	1.01	0.91		
^{96}Zr	sp	0.73	0.86	0.92	1.48
^{96}Mo	sp	0.90	0.91	1.03	1.52
^{100}Mo	WS	0.85	0.95	1.31	1.63
	sp	0.88	0.96		
^{100}Ru	WS	0.89	0.96	1.27	1.60
	sp	0.85	0.93		
^{116}Cd	WS	0.89	0.93	1.37	1.43
^{116}Sn	WS	0.82	0.89	1.16	1.84
^{128}Te	WS	0.96	0.81	1.30	1.09
	sp	0.86	0.81		
^{128}Xe	WS	0.94	0.88	1.27	1.30
	sp	0.86	0.88		
^{130}Te	WS	0.94	0.78	1.21	1.02
	sp	0.86	0.78		
^{130}Xe	WS	0.95	0.86	1.25	1.26
	sp	0.85	0.86		
^{136}Xe	WS	0.85	0.76	1.44	0.98
	sp	0.84	0.76		
^{136}Ba	WS	0.90	0.83	1.08	1.22
	sp	0.87	0.83		

reproduce the low-lying spectra of the neighboring odd-mass nuclei. These bases are abbreviated as "sp" (see Table I). In the cases of mass numbers $A = 96, 100$ the use of the bare Woods-Saxon bases results in a nonphysical g_{pp} behavior of the $2\nu\beta\beta$ results, and we use therefore only the sp bases. On the other hand, for $A = 116$ the use of the bare Woods-Saxon bases results in a good correspondence between the calculated and experimental spectra, so no modifications in the single-particle energies were necessary.

The quasiparticle spectra for protons and neutrons, needed in the pnQRPA diagonalization, are obtained by solving the BCS equations for protons and neutrons, separately. In our calculations the two-body interaction is derived from the Bonn-A one-boson-exchange potential introduced in [37]. The calculated BCS pairing gaps are fitted (see [31,38–40]) to the phenomenological ones, Δ_n for neutrons and Δ_p for protons, by using adjustable pairing strengths, $g_{pair}^{(n)}$ for neutrons and $g_{pair}^{(p)}$ for protons, in a way described in detail in Ref. [35]. The needed separation energies were taken from [41]. The values of the resulting pairing scaling factors are presented in Table I.

The wave functions and excitation energies for the complete set of J^π excitations in an odd-odd nucleus are obtained by performing a pnQRPA diagonalization in the basis of unperturbed quasiproton-quasineutron pairs coupled to J^π. The spherical pnQRPA states in odd-odd nuclei are then of

the form

$$\left| J_k^\pi M \right\rangle = \sum_{pn} \left[X_{pn}^{J_k^\pi} A_{pn}^\dagger (JM) - Y_{pn}^{J_k^\pi} \tilde{A}_{pn}(JM) \right] | \text{pnQRPA} \rangle, \tag{1}$$

where k numbers the states of the same spin-parity J^π, the amplitudes X and Y are the forward- and backward-going amplitudes, $A^\dagger$ and $\tilde{A}$ the quasiproton-quasineutron creation and annihilation operators, and $| \text{pnQRPA} \rangle$ is the pnQRPA vacuum. M denotes the z projection of J. The formalism is explained in detail in Refs. [31,38].

The X and Y amplitudes in Eq. (1) are calculated by diagonalizing the pnQRPA matrix separately for each multipole J^π. The isoscalar ($T = 0$) and isovector ($T = 1$) parts of the particle-particle G-matrix elements are multiplied by common factors $g_{pp}^{T=0}$ and $g_{pp}^{T=1}$, respectively, for all the multipoles. In addition, the particle-hole part was scaled by a common factor g_{ph} for each multipole. These renormalization factors are listed in the following section for each mass number A separately.

B. Isovector spin-dipole $J^\pi = 2^-$ strength

The transition operator for the IVSD ($L = 1$) $J^\pi = 2^-$ transitions is of the form

$$\mathcal{O}_{1,2}^\pm = ir[Y_1 \boldsymbol{\sigma}]_2 t_\pm, \tag{2}$$

where Y_1 is the spherical harmonic of rank 1, $\boldsymbol{\sigma}$ the Pauli spin operator, r the radial coordinate, and t_+ and t_- are the isospin raising and lowering operators. The reduced single-particle NMEs of this operator are of the form [31,36]

$$
(j_f \| \mathcal{O}_{1,2}^\pm \| j_i) = \left(n_f l_f \tfrac{1}{2} j_f \left\| ir[Y_1 \boldsymbol{\sigma}]_2 \right\| n_i l_i \tfrac{1}{2} j_i \right)
$$
$$
= \sqrt{6} \hat{j}_f \sqrt{5} \hat{j}_i \frac{(-1)^{l_f}}{\sqrt{4\pi}} \hat{l}_f \sqrt{3} \hat{l}_i \begin{pmatrix} l_f & 1 & l_i \\ 0 & 0 & 0 \end{pmatrix}
$$
$$
\times \begin{Bmatrix} l_f & \tfrac{1}{2} & j_f \\ l_i & \tfrac{1}{2} & j_i \\ 1 & 1 & 2 \end{Bmatrix} \mathcal{R}_{fi}^{(1)} (-1)^{\frac{1}{2}(l_i - l_f + 1)}, \tag{3}
$$

where $\hat{j} = \sqrt{2j+1}$, $\mathcal{R}_{fi}^{(1)}$ is a radial integral [31] and n denotes the principal quantum number, l the orbital angular momentum, and j the total angular momentum. The reduced NMEs of (2) can now be calculated from [31]

$$(2_f^- \| \mathcal{O}_{1,2}^\pm \| 0_i^+) = \sum_{ab} \frac{(a \| \mathcal{O}_{1,2}^\pm \| b)}{\sqrt{5}} (2_f^- \| [c_a^\dagger \tilde{c}_b]_2 \| 0_i^+), \tag{4}$$

where b and a denote the initial and final single-particle quantum numbers, 0_i^+ is the initial ground state in an even-even nucleus, and 2_f^- is a final 2^- state in an odd-odd nucleus.

The transition strength for a transition from the initial 0_i^+ ground state to the 2_f^- final state can be calculated from

$$S_{1,2}^\pm (f) = |(2_f^- \| \mathcal{O}_{1,2}^\pm \| 0_i^+)|^2. \tag{5}$$

In the present work 0_i^+ corresponds to the ground state of a mother nucleus of $0\nu\beta\beta$ decay, and we need the (p,n) type strength $S_{1,2}^-(f)$ for the whole range of final states f, up to and

beyond the IVSD $J^\pi = 2^-$ giant-resonance region, in order to be able to compare with the corresponding experimental data.

C. Two-neutrino double-beta decays

The half-life of the $2\nu\beta\beta$ decay can be written in the form

$$\left[t_{1/2}^{(2\nu)} (0_i^+ \to 0_f^+) \right]^{-1} = \left(g_A^{\text{eff}} \right)^4 G_{2\nu} |M^{(2\nu)}|^2, \tag{6}$$

where g_A^{eff} is the effective value of the weak axial-vector coupling strength and $G_{2\nu}$ is a leptonic phase-space factor (in units of inverse years) as defined in Ref. [42] without the axial-vector coupling strength g_A. The initial and final ground states are denoted by 0_i^+ and 0_f^+, correspondingly. The Gamow-Teller NME involved in the equation is written in the pnQRPA formalism as

$$M^{(2\nu)} = \sum_{m,n} \frac{(0_f^+ \| \sum_k t_k^- \sigma_k \| 1_m^+) \langle 1_m^+ | 1_n^+ \rangle (1_n^+ \| \sum_k t_k^- \sigma_k \| 0_i^+)}{D_m + 1} \tag{7}$$

for the $2\nu\beta^-\beta^-$ decays, with D_m being the energy denominator

$$D_m = \left(\tfrac{1}{2} \Delta + \tfrac{1}{2}[E(1_m^+) + \tilde{E}(1_m^+)] - M_i \right) / m_e, \tag{8}$$

where Δ is the nuclear mass difference between the initial and final 0^+ ground states, M_i the mass of the initial nucleus, m_e the electron rest mass, $\tilde{E}(1_m^+)$ is the (absolute) energy of the mth 1^+ state in a pnQRPA calculation based on the left-side ground state, and $E(1_m^+)$ the same for a calculation based on the right-side ground state. To do the calculations as accurately as possible, the difference $[E(1_m^+) + \tilde{E}(1_m^+)]/2 - M_i$ is adjusted to the experimental energy difference between the first 1^+ state in the intermediate nucleus and the ground state of the initial nucleus. The same is done in the calculations of the $0\nu\beta\beta$ NMEs. The quantity $\langle 1_m^+ | 1_n^+ \rangle$ is the overlap between the two sets of 1^+ states and it can be written as

$$\langle 1_m^+ | 1_n^+ \rangle = \sum_{pn} \left[X_{pn}^{1_m^+} \bar{X}_{pn}^{1_n^+} - Y_{pn}^{1_m^+} \bar{Y}_{pn}^{1_n^+} \right]. \tag{9}$$

The overlap factor matches the corresponding states in the two sets of states based on the left- and right-side even-even reference nuclei and makes the computed NMEs more stable. For deformed nuclei, and especially when the deformations of the mother and daughter nuclei are considerably different, the role of the overlap factor is important [43,44]. The quantities X and Y ($\bar{X}$ and $\bar{Y}$) denote the pnQRPA amplitudes which stem from the calculation based on the left-side (right-side) nucleus.

In principle, the expression in Eq. (7) should also contain a Fermi part, but our choice for the $g_{pp}^{T=1}$ parameter forces this contribution to zero, as will be explained in Sec. III A. This is justified since in the case of isospin symmetry, which is obeyed by the nuclear forces to a high degree, the ground states of the mother and daughter nuclei belong to different isospin multiplets and the Fermi contribution to the $2\nu\beta\beta$ NME should vanish, leaving the Gamow-Teller NME in Eq. (7) as the sole contributor to the $2\nu\beta\beta$ decay rate.

D. Neutrinoless double-beta decays

Assuming that the exchange of light Majorana neutrino dominates the $0\nu\beta\beta$ mechanisms, the half-life for a

ground-state-to-ground-state $0\nu\beta\beta$ transition can be written as

$$
\left[t_{1/2}^{(0\nu)}(0_i^+ \to 0_f^+)\right]^{-1} = (g_A^{\text{eff}})^4 G_{0\nu}|M^{(0\nu)}|^2 \left|\frac{\langle m_\nu \rangle}{m_e}\right|^2, \quad (10)
$$

where $G_{0\nu}$ is a phase-space factor, cited in Ref. [42] in units of inverse years, for the final-state leptons defined here without the axial-vector coupling strength g_A [42] and $\langle m_\nu \rangle$ is the effective light-neutrino mass

$$
\langle m_\nu \rangle = \sum_{j=\text{light}} \left(U_{ej}^l\right)^2 m_j \quad (11)
$$

with m_j being the individual light-neutrino masses. Here the amplitudes U_{ej}^l are the components of the electron row of the neutrino-mixing matrix corresponding to the light sector.

The nuclear matrix element $M^{(0\nu)}$ in Eq. (10) is defined as

$$
M^{(0\nu)} = M_{\text{GT}}^{(0\nu)} - \left(\frac{g_V}{g_A^{\text{eff}}}\right)^2 M_F^{(0\nu)} + M_T^{(0\nu)}, \quad (12)
$$

where we adopt the CVC value $g_V = 1.0$ for the weak vector coupling strength and the double Fermi, Gamow-Teller, and tensor nuclear matrix elements are defined for the $0\nu\beta^-\beta^-$ decays as

$$
M_F^{(0\nu)} = \sum_k (0_f^+ \| \sum_{mn} h_F(r_{mn}, E_k) t_m^- t_n^- \| 0_i^+), \quad (13)
$$

$$
M_{\text{GT}}^{(0\nu)} = \sum_k (0_f^+ \| \sum_{mn} h_{\text{GT}}(r_{mn}, E_k)(\sigma_m \cdot \sigma_n) t_m^- t_n^- \| 0_i^+), \quad (14)
$$

$$
M_T^{(0\nu)} = \sum_k (0_f^+ \| \sum_{mn} h_T(r_{mn}, E_k) S_{mn}^T t_m^- t_n^- \| 0_i^+), \quad (15)
$$

where the operator t_m^- is the isospin lowering operator (neutron to proton) for the nucleon m and the spin tensor operator is defined as

$$
S_{mn}^T = 3[(\sigma_m \cdot \hat{\mathbf{r}}_{mn})(\sigma_n \cdot \hat{\mathbf{r}}_{mn})] - \sigma_m \cdot \sigma_n. \quad (16)
$$

The summation over k in Eqs. (13)–(15) runs over all the states of the intermediate odd-odd nucleus, $r_{mn} = |\mathbf{r}_m - \mathbf{r}_n|$ is the relative distance between the two decaying neutrons, labeled m and n, and $\hat{\mathbf{r}}_{mn} = (\mathbf{r}_m - \mathbf{r}_n)/r_{mn}$. As in the two-neutrino case the ground state of the initial even-even nucleus is denoted by 0_i^+ and the ground state of the final even-even nucleus is denoted by 0_f^+. Expressions for the neutrino potentials $h_K(r_{mn}, E_k)$, $K =$ F, GT, T are given in Ref. [29].

The nuclear matrix elements can be written in the pnQRPA framework as

$$
M_K^{(0\nu)} = \sum_{J^\pi, k_1, k_2, J'} \sum_{pp'nn'} (-1)^{j_n + j_{p'} + J + J'} \sqrt{2J' + 1}
$$

$$
\times \begin{Bmatrix} j_p & j_n & J \\ j_{n'} & j_{p'} & J' \end{Bmatrix} (pp' : J' \| \mathcal{O}_K \| nn' : J')
$$

$$
\times (0_f^+ \| [c_{p'}^\dagger \tilde{c}_{n'}]_J \| J_{k_1}^\pi) \langle J_{k_1}^\pi | J_{k_2}^\pi \rangle (J_{k_2}^\pi \| [c_p^\dagger \tilde{c}_n]_J \| 0_i^+), \quad (17)
$$

where k_1 and k_2 label the different pnQRPA solutions for a given multipole J^π. The operators $\mathcal{O}_K$ inside the two-particle

matrix element correspond to the ones of Eqs. (13), (14), and (15), and they can be written as

$$
\mathcal{O}_F = h_F(r, E_k)[f_{\text{CD}}(r)]^2, \quad (18)
$$

$$
\mathcal{O}_{\text{GT}} = h_{\text{GT}}(r, E_k)[f_{\text{CD}}(r)]^2 \sigma_1 \cdot \sigma_2, \quad (19)
$$

$$
\mathcal{O}_T = h_T(r, E_k)[f_{\text{CD}}(r)]^2 S_{12}^T, \quad (20)
$$

where S_{12}^T is the tensor operator of Eq. (16) and $r = |\mathbf{r}_1 - \mathbf{r}_2|$ is the distance between the participating nucleons. The energy E_k is the average of the kth eigenvalues of the pnQRPA calculations based on the initial and final nuclei of the decay, and the overlap factor $\langle J_{k_1}^\pi | J_{k_2}^\pi \rangle$ in Eq. (17) is the one of Eq. (9). It has an important role for deformed nuclei, especially when the deformations of the mother and daughter nuclei are considerably different. The factor $f_{\text{CD}}(r)$ takes into account the nucleon-nucleon short-range correlations (SRC) [32,45] and here we use the CD-Bonn form [46] with the parametrization

$$
f_{\text{CD}}(r) = 1 - 0.46 e^{-(1.52/\text{fm}^2)r^2}[1 - (1.88/\text{fm}^2)r^2]. \quad (21)
$$

In the pnQRPA the state of Eq. (1) leads to the transition densities

$$
(0_f^+ \| [c_{p'}^\dagger \tilde{c}_{n'}]_J \| J_{k_1}^\pi) = \hat{J}[\bar{v}_{p'} \bar{u}_{n'} \bar{X}_{p'n'}^{J^\pi k_1} + \bar{u}_{p'} \bar{v}_{n'} \bar{Y}_{p'n'}^{J^\pi k_1}], \quad (22)
$$

$$
(J_{k_2}^\pi \| [c_p^\dagger \tilde{c}_n]_J \| 0_i^+) = \hat{J}[u_p v_n X_{pn}^{J^\pi k_2} + v_p u_n Y_{pn}^{J^\pi k_2}], \quad (23)
$$

where v ($\bar{v}$) and u ($\bar{u}$) correspond to the BCS occupation and vacancy amplitudes of the initial (final) even-even nucleus. The amplitudes X and Y ($\bar{X}$ and $\bar{Y}$) emerge from the pnQRPA calculation based on the initial (final) nucleus of the double-beta decay. Equation (17) does not include the overlap between the initial and final BCS states that can be rather important, according to the recent study by Fang *et al.* based on the deformed QRPA formalism [47]. In this work it was found that the $0\nu\beta\beta$ NMEs were reduced by as much as 30–60% in comparison with the spherical formalism, mainly due to the BCS overlap factors and partly due to the deformation. According to the discussion in Ref. [47], the BCS factors could cause a large (as large as 60%) decrease to the calculated NMEs, if the neutron or proton number is close to a magic number (as for ^{116}Cd and ^{136}Xe), and a milder ($\approx$20–30%) decrease in the other cases. In a purely spherical pnQRPA approach it is expected that these changes in the NMEs constitute an upper limit. In particular one has to be careful in using the BCS overlap for the semimagic nuclei where the BCS approach does not produce a pairing gap, and some higher-order approach, like the Lipkin-Nogami approach [31], would be better.

III. RESULTS AND DISCUSSION

In this section we present and discuss the results of our studies. In the calculations we use two slightly different sets of single-particle bases, and we also compare our results with the numbers obtained in an earlier study of Hyvärinen *et al.* [29] of the same $0\nu\beta\beta$ transitions.

A. Determination of model parameters

Here we adopt the single-particle bases used in the isovector spin-multipole calculations of [35] discussed already in

Sec. II A. We decompose each isobaric triplet with mass number A to "left-side" even-even (A, N, Z), "right-side" even-even $(A, N-2, Z+2)$ and "intermediate" odd-odd $(A, N-1, Z+1)$ nuclei and construct the spectra of J^π excitations in the intermediate odd-odd nuclei, applying the pnQRPA formalism [31,38,39] to the left- and right-side even-even nuclei. In this way one obtains two sets of energies and wave functions for each J^π state. The residual Hamiltonian for the pnQRPA includes particle-hole and particle-particle components. The particle-hole contribution is proportional to the particle-hole matrix elements $g_{ph}\langle pn^{-1}; J^\pi|V|p'n'^{-1}; J^\pi\rangle$, where J^π is the multipole of the states in the intermediate odd-odd nucleus, and the particle-particle contribution is proportional to the two-body matrix elements $g_{pp}\langle pn; J^\pi|V|p'n'; J^\pi\rangle$. Here g_{ph} and g_{pp} are the particle-hole and particle-particle renormalization factors correspondingly.

Traditionally the g_{ph} parameter is fixed by fitting the centroid of the Gamow-Teller resonance (GTR) in the 1^+ channel of the calculations [1,38,39,48,49]. This same g_{ph} is then used for all multipoles J^π. We use this method as a starting point (we call this Model 1), but explore how the particle-hole parameter $g_{ph}(2^-)$ changes the values of the $0\nu\beta\beta$ NMEs by fitting the $J^\pi = 2^-$ channel separately (Model 2) and by using the $g_{ph}(2^-)$ parameter for all channels excluding the 1^+ channel (Model 3). We adjust the $g_{ph}(1^+)$ and $g_{ph}(2^-)$ parameters to the available data on Gamow-Teller [50–53] and isovector spin-dipole giant-resonance energies [53–58].

The GT and IVSD strength distributions were studied at RCNP, Osaka University, through high-resolution $(^3\mathrm{He},t)$ charge-exchange reactions. Significant GT and IVSD strengths are found as broad giant resonances around 12 and 20 MeV, and the widths are around 5 and 10 MeV, respectively. In fact, the IVSD resonance was first discussed in Ref. [59] to account for the reduction of the low-lying SD β NMEs. We adjust the $g_{ph}(2^-)$ parameter to the available data on the giant resonance energies. The data for different nuclei are: ^{76}Ge [53], ^{96}Zr [54], ^{100}Mo [55], ^{116}Cd [56], ^{128}Te [57], ^{130}Te [57], and ^{136}Xe [58]. The GTR and IVSD energies for the DBD nuclei of current interest are expressed approximately as

$$E(\mathrm{GT}) \approx 9 + 0.4T_Z \text{ MeV},$$
$$E(\mathrm{SD}) \approx 16.5 + 0.4T_Z \text{ MeV}, \quad (24)$$

where $T_Z = \frac{1}{2}(N - Z)$. The uncertainties of the GT and IVSD energies are around ± 0.5 and 1 MeV, respectively. The g_{ph} values adjusted in this way are presented in Table II, together with the values of the GTR and IVSD giant-resonance centroids obtained from Eq. (24). For $A = 96$ we use the measured centroid, as the linear fits of (24) do not reproduce the measured values well. It is seen in Table II that the g_{ph} values vary by 20–30% depending on the basis (WS/sp) and the type of GR (GT/SD).

The g_{pp} parameter has usually been adjusted by fitting this value to the measured $2\nu\beta\beta$-decay half-life [32–34,60,61], to the log ft values of β decays [62,63], or to both β and $2\nu\beta\beta$ decays [64,65]. In this work, we adopt an improved method introduced in Ref. [28] and later used in Ref. [29], where we decompose the pnQRPA NMEs into isoscalar $(T = 0)$ and isovector $(T = 1)$ parts and then adjust the parameters

TABLE II. Parameters of the pnQRPA calculations for various $0\nu\beta\beta$ decaying nuclei. Column 2 indicates the basis that was used in the calculations. Columns 3 and 4 list the experimental centroid energies of the IVSD $J^\pi = 2^-$ and GTR $J^\pi = 1^+$ resonances. The last two columns list the values of the particle-hole parameters adjusted to the locations of the IVSD resonance and the GTR.

Nucleus	Basis	$E(\mathrm{SD}2^-)$ (MeV)	$E(\mathrm{GT})$ (MeV)	$g_{ph}(2^-)$	$g_{ph}(1^+)$
^{76}Ge	WS	18.9 ± 1.0	11.4 ± 0.5	0.9 ± 0.2	1.24 ± 0.13
	sp			1.2 ± 0.3	1.03 ± 0.13
^{96}Zr	sp	22 ± 1.0	12.7 ± 0.5	0.8 ± 0.2	0.84 ± 0.09
^{100}Mo	sp	19.7 ± 1.0	12.2 ± 0.5	1.0 ± 0.2	1.19 ± 0.08
^{116}Cd	WS	20.5 ± 1.0	13.0 ± 0.5	1.07 ± 0.09	0.85 ± 0.13
^{128}Te	WS	21.3 ± 1.0	13.8 ± 0.5	1.7 ± 0.2	1.64 ± 0.08
	sp			1.9 ± 0.2	1.40 ± 0.09
^{130}Te	WS	21.7 ± 1.0	14.2 ± 0.5	1.7 ± 0.2	1.58 ± 0.08
	sp			1.9 ± 0.2	1.36 ± 0.09
^{136}Xe	WS	22.1 ± 1.0	14.6 ± 0.5	1.0 ± 0.2	1.36 ± 0.07
	sp			0.9 ± 0.2	1.18 ± 0.08

$g_{pp}^{T=0}$ and $g_{pp}^{T=1}$ independently. The particle-particle parts of the pnQRPA matrices are divided into isoscalar $(T = 0)$ and isovector $(T = 1)$ parts by the decomposition

$$g_{pp}\langle pn; J^\pi|V|p'n'; J^\pi\rangle$$
$$\rightarrow g_{pp}^{T=1}\langle pn; J^\pi; T = 1|V|p'n'; J^\pi; T = 1\rangle$$
$$+ g_{pp}^{T=0}\langle pn; J^\pi; T = 0|V|p'n'; J^\pi; T = 0\rangle. \quad (25)$$

The isovector parameter $g_{pp}^{T=1}$ is adjusted so that the Fermi $2\nu\beta\beta$ NME vanishes, and thus the isospin symmetry is partially restored. Then we independently vary the isoscalar parameter $g_{pp}^{T=0}$ such that it reproduces the calculated matrix element corresponding to the measured $2\nu\beta\beta$ half-life and a (moderately) quenched effective value $g_A^{eff} = 1.0$ of the axial-vector coupling strength. These values are determined for each mass number separately, and the obtained parameters are adopted for all multipoles in both the left- and right-side even-even nuclei. We list the obtained values in Table III. The $g_{pp}^{T=0,1}$ values depend on the g_{ph} value only weakly: The variation in

TABLE III. The g_{pp} parameters used in the present calculations for the isoscalar (column 3) and the isovector (column 4) interaction.

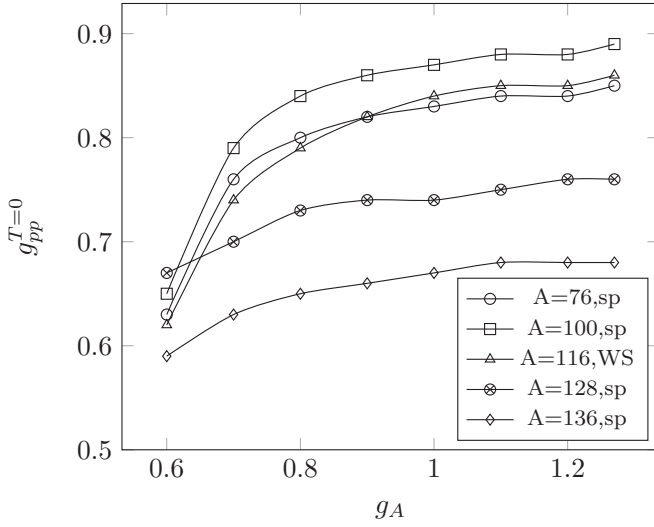| Nucleus	Basis	$g_{pp}^{T=0}(g_A \approx 1.00\text{–}1.27)$	$g_{pp}^{T=1}$
^{76}Ge	WS	0.80	0.99
	sp	0.83	0.96
^{96}Zr	sp	0.83	0.93
^{100}Mo	sp	0.87	0.91
^{116}Cd	WS	0.82	0.82
^{128}Te	WS	0.73	0.94
	sp	0.745	0.87
^{130}Te	WS	0.74	0.95
	sp	0.73	0.86
^{136}Xe	WS	0.64	0.98
	sp	0.67	0.87

FIG. 1. Values of the particle-particle parameter $g_{pp}^{T=0}$ as functions of g_A for a representative set of bases and different nuclei.

the range of the g_{ph} values of Table II is only about 1–5% for each nucleus. Since the impact of the variation on the NME values in negligible, the g_{pp} values obtained with $g_{ph}(1^+)$ were adopted. The bare value $g_A^{bare} = 1.27$ was also tested in the determination of the $g_{pp}^{T=0}$ parameters, but the parameter values obtained this way differed only by 1–3% from those obtained with $g_A^{eff} = 1.0$ (see Fig. 1) so we do not list them separately for $g_A^{bare} = 1.27$. It seems that in the considered large basis sets the behavior of g_{pp} as a function of g_A is rather flat for values larger than 1, and only for the smaller g_A values do the variations in the g_{pp} values set in. Hence, the $2\nu\beta\beta$ nuclear matrix element $M^{(2\nu)}$ is strongly dependent on the $g_{pp}^{T=0}$ value (see Fig. 2). As a result, the values of the NMEs $M_{GT}^{(0\nu)}$, $M_F^{(0\nu)}$, and $M_T^{(0\nu)}$ are altered mildly in the range $g_A \approx 1.00$–1.27, resulting in about 10–20% changes in the total NMEs $M^{(0\nu)}$ as in Ref.
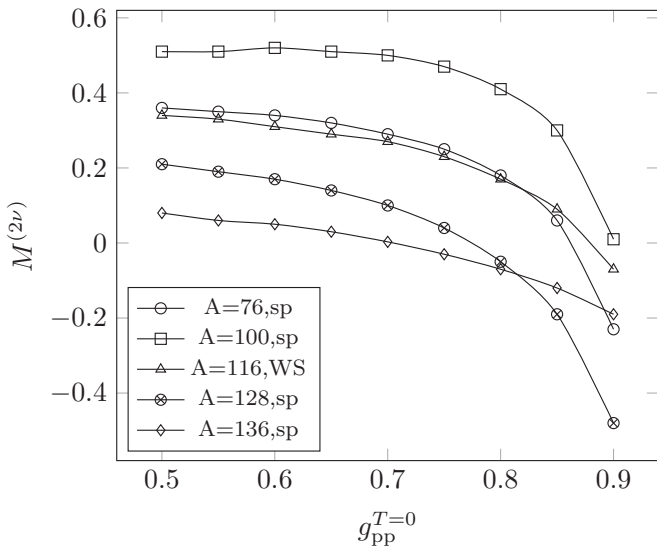

FIG. 2. Values of the $2\nu\beta\beta$ nuclear matrix element as functions of $g_{pp}^{T=0}$ for a representative set of bases and different nuclei.

TABLE IV. IAS energies calculated using $g_{ph}(1^+)$ of Table II and $g_{pp}^{T=0,1}$ of Table III. The corresponding experimental IAS energies are listed in the last column.

Nucleus	$E(IAS)_{sp}$ (MeV)	$E(IAS)_{WS}$ (MeV)	$E_{fit}(IAS)$ (MeV)
^{76}Ge	6.5	7.0	8.6
^{96}Zr	5.8		9.8
^{100}Mo	9.5		9.8
^{116}Cd		9.8	11.0
^{128}Te	11.0	11.9	12.2
^{130}Te	10.6	11.4	12.8
^{136}Xe	10.1	10.5	13.4

[29], and we adopt the effective value $g_A^{eff} = 1.0$ in the present calculations.

The IAS (isobaric analog state) energies calculated using the $g_{ph}(1^+)$ values of Table II and $g_{pp}^{T=0,1}$ values of Table III are presented in Table IV. From the results of [53–59] we can derive the following expression for the experimental IAS locations for the DBD nuclei of current interest:

$$E_{fit}(IAS) = 5 + 0.6T_Z \text{ MeV}, \quad (26)$$

where $T_Z = \frac{1}{2}(N - Z)$. These values are presented in Table IV for comparison. As can be seen in the table the computed locations of the IAS are too low in comparison with the experimental locations. The difference between the computed and the experimental locations varies between 1.2 and 4 MeV, except for the cases $A = 100$ and 128 (sp basis), for which the differences are less than 0.5 MeV. The sum rule $S_- - S_+ = N - Z$, S_- [S_+] being the total Fermi strength in the (p, n) [(n, p)] direction, is exactly fulfilled in our calculations. The discrepancy in the computed IAS energies is typical of pnQRPA calculations which are not self-consistent, i.e., the mean field is not determined by the same Hamiltonian as the excited states. In self-consistent calculations the situation is improved and the discrepancies reach typically a level below 1 MeV, the computed energies of the IAS being still below the measured ones (see, e.g., [66]).

B. IVSD $J^\pi = 2^-$ strength functions

The $J^\pi = 2^-$ strength functions were calculated in the bare Woods-Saxon (WS) bases, as well as in the slightly modified single-particle (sp) bases. Two different g_{ph} values were adopted: one was obtained by adjusting it to the measured location of the Gamow-Teller (GT) giant resonance, and the other was obtained by adjusting it to the measured location of the IVSD $J^\pi = 2^-$ giant resonance (see Sec. III A). The resulting strength functions for mass numbers $A = 76$, 100, 116, and 128 are presented in Figs. 3–6. In the figures we use Lorentzian folding with a peak width of 0.5 MeV [35].

As we can see in Fig. 3, for $A = 76$ the large, about 30%, deviation between the values of $g_{ph}(1^+)$ and $g_{ph}(2^-)$ (see Table II) results in large deviations between the strength functions calculated using the WS basis. On the other hand, for the sp basis the difference between the different g_{ph} values is
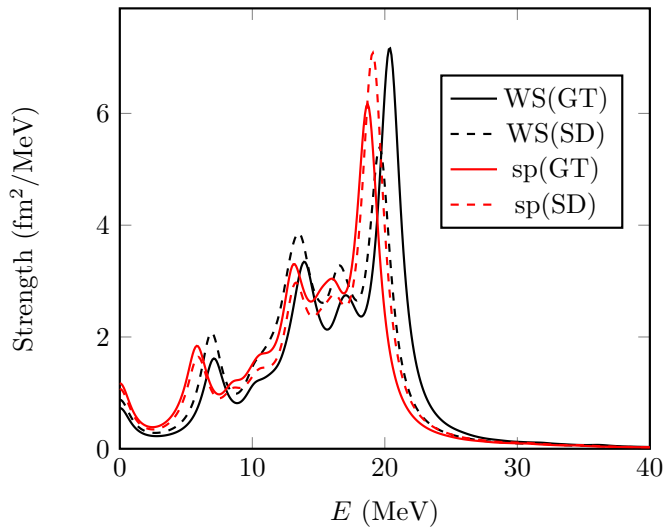
FIG. 3. Isovector spin-dipole $J^\pi = 2^-$ strength functions for $A = 76$ calculated using either a Woods-Saxon (WS) or a modified Woods-Saxon (sp) single-particle basis, and g_{ph} values obtained by fitting to the location of either the Gamow-Teller (GT) or the IVSD $J^\pi = 2^-$ giant resonance.

smaller, which leads to smaller deviations between the strength functions.

From Fig. 4 we see that for $A = 100$ the moderate, about 15%, deviation between the g_{ph} values (see Table II) leads to moderate differences between the calculated strength functions. From Fig. 5, in turn, we see that large deviations between the g_{ph} values lead to large deviations between the strength functions.

As can be seen in Fig. 6, for $A = 128$ the large, about 30%, deviations in g_{ph} values lead to large deviations in the strength functions calculated using the sp basis. The small, about 4%, difference between the g_{ph} values, on the other hand, leads to small differences in the strength functions calculated using the WS basis.

FIG. 5. The same as Fig. 3 for $A = 116$.

For $A = 96$ the strength functions were almost identical, so the corresponding spectra are not presented here. The cases $A = 130$ and 136 were almost identical with $A = 128$, with slightly more moderate deviations between the different spectra, so the figures are omitted here.

C. Matrix elements for neutrinoless $\beta\beta$ decay

We present our final results for the nuclear matrix elements ($M^{(0\nu)}$) of the light-Majorana-mediated neutrinoless $\beta\beta$ decay using the two sets of single-particle bases discussed in Sec. II A. Furthermore, we investigate the impact of using the $g_{ph}(2^-)$ value in the evaluation of the $0\nu\beta\beta$ NME by using three different methods. That is, for both sets of bases we compute $M^{(0\nu)}$ [Eq. (12)] first by using the common parameter $g_{ph} = g_{ph}(1^+)$ for each multipole (Model 1), then change the g_{ph} value into $g_{ph}(2^-)$ for the multipole $J^\pi = 2^-$, and keep $g_{ph} = g_{ph}(1^+)$ for the other multipoles (Model 2). Furthermore, we

FIG. 4. The same as Fig. 3 for $A = 100$.
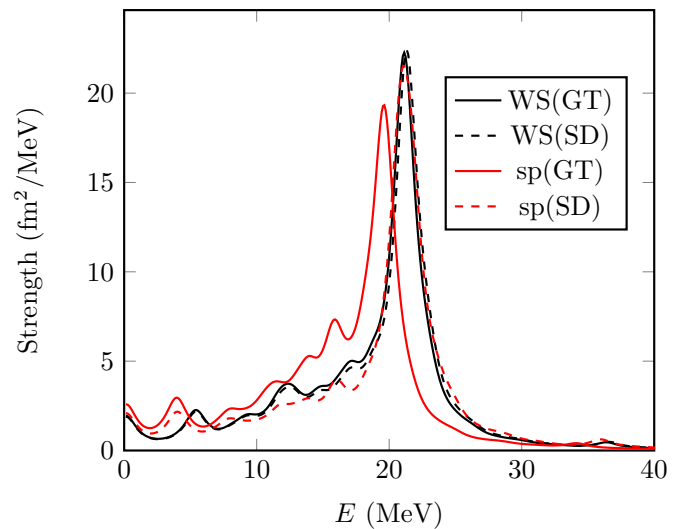
FIG. 6. The same as Fig. 3 for $A = 128$.
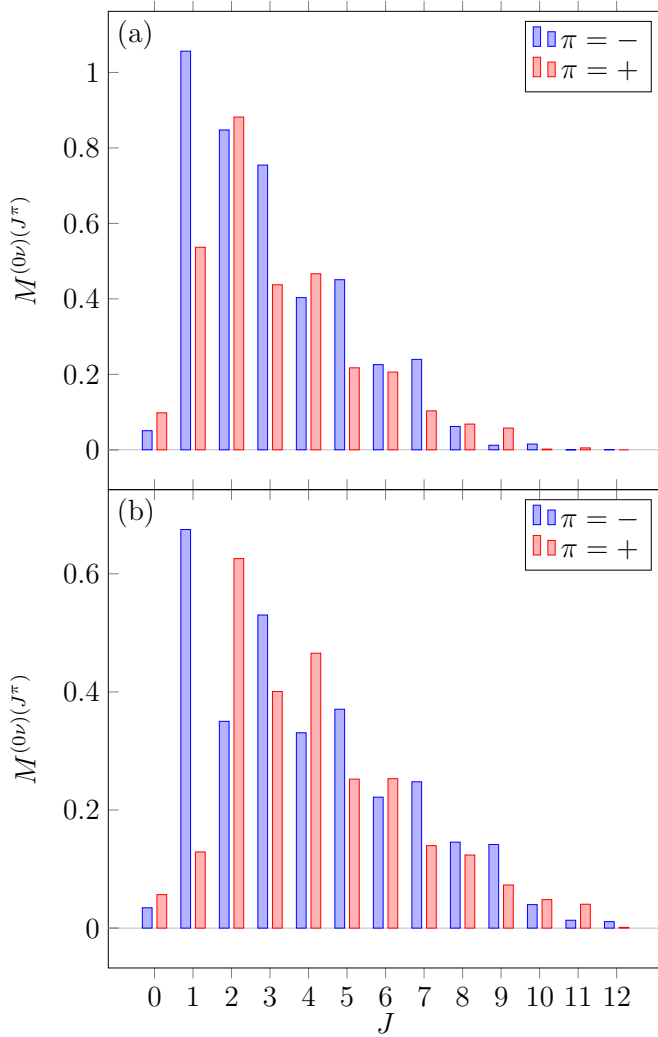
FIG. 7. Multipole decomposition of the total $0\nu\beta\beta$ matrix element $M^{(0\nu)}$ of (a) ^{76}Ge (b) ^{128}Te.

perform the calculations using $g_{ph}(1^+)$ for the 1^+ channel and $g_{ph}(J^\pi) = g_{ph}(2^-)$ for $J^\pi \neq 1^+$ (Model 3). The $g_{pp}^{T=0,1}$ values of Table III are used for each multipole. We adopt the effective axial-vector coupling $g_A^{eff} = 1.00$ for our $0\nu\beta\beta$ NME calculations. We use the effective g_A to incorporate the nuclear medium and non-nucleonic correlations, but we use $g_V = 1.0$ on the basis of the CVC.

The relative importance of the 2^- contributions in the $0\nu\beta\beta$ NMEs has been illustrated in Fig. 7. For a medium-heavy nucleus, like ^{76}Ge [panel (a) of Fig. 7)], the contributions from the 2^- states can be considerable. For a heavier nucleus, like ^{128}Te [panel (b) of Fig. 7], the contribution is not that conspicuous. Nevertheless, it is worth studying the effect of the spin-dipole states on the values of the $0\nu\beta\beta$ NMEs.

We present our final NMEs of Eq. (12) in Tables V and VI, and compare them with the results of Hyvärinen *et al.* [29] for $g_A^{eff} = 1.00$. In Ref. [29] smaller single-particle bases were used, i.e., the orbitals $1p$–$0f$–$2s$–$1d$–$0g$–$0h_{11/2}$ for the $A = 76, 82$ systems, the

orbitals $1p$–$0f$–$2s$–$1d$–$0g$–$0h$ for the $A = 96, 100$ systems, and the orbitals $1p$–$0f$–$2s$–$1d$–$0g$–$2p$–$1f$–$0h$ for the $A = 116, 128, 130, 136$ systems. The same orbitals were used for both neutrons and protons. The $g_{pp}^{T=0,1}$ parameters were determined in the same manner as in the present study, and the g_{ph} parameter was adjusted to the GTR in the traditional way.

If we compare the content of Tables II and V with the differences shown in Fig. 8 and with the IVSD $J^\pi = 2^-$ strength functions in Figs. 3–6, we can draw the following conclusions.

A = 76: There is a large, about 30%, difference between the IVSD- and GT-determined g_{ph} values for the WS basis. This is reflected as a large difference in both the strength functions, Fig. 3, and $0\nu\beta\beta$ NMEs, Table V. Increasing the impact of $g_{ph}(2^-)$ on the NMEs (Model 3) increases the difference even more. For the sp basis the differences are smaller for all quantities and, in particular, the deviations from the NME computed in the smaller single-particle space [29] are on the percent level.

A = 96: The deviations in the g_{ph} values, and $0\nu\beta\beta$ NMEs are small, at the few-percent level. However, there is a notable deviation from the small-basis $0\nu\beta\beta$ NME [29].

A = 100: The adjusted g_{ph} values differ by some 20%, and also the strength functions (cf. Fig. 4) change correspondingly. There is a negligible difference in the values of the $0\nu\beta\beta$ NMEs between Model 1 and Model 2, but a notable difference when going to Model 3. There is also a notable deviation from the NME value obtained in the smaller basis [29].

A = 116: The determined g_{ph} values deviate by some 20%, producing slight differences in the strength functions, as seen in Fig. 5. As a result, the values of the $0\nu\beta\beta$ NMEs do not differ from each other between Model 1 and Model 2, and only slightly when going to Model 3. However, there is a notable deviation from the one computed in the smaller basis [29].

A = 128: There are notable, about 30%, deviations in the g_{ph} values for the sp basis and this is reflected in the deviations in the strength functions, Fig. 6, for the sp-basis based calculations. Deviations in the values of the $0\nu\beta\beta$ NMEs between Model 1 and Model 2 are moderate, less than a percent within a given basis, but there are few-percent deviations when going from the WS-computed to the sp-computed NMEs. The sp-computed NMEs of Model 1 and Model 2 are consistent with the one produced in the smaller basis [29]. However, using Model 3 causes again some 10% deviations from the small-basis NME when using the sp basis.

A = 130: The situation is similar to the $A = 128$ case, except that all the sp-computed $0\nu\beta\beta$ NMEs deviate by 10–20% from that computed in the smaller basis [29].

A = 136: There are 20–30% differences in the g_{ph} values for both bases but the differences in the strength functions are moderate. Except for the NME computed in Model 3 in the sp basis, there are only some 10% differences in the values of the WS-computed and the sp-computed $0\nu\beta\beta$ NMEs, and less than 7% deviations from the NME obtained in the smaller basis [29].

Table V shows that the adoption of the IVSD $J^\pi = 2^-$-fitted value of g_{ph} for the 2^- channel of the $0\nu\beta\beta$ NMEs (Model 2) affects the NMEs negligibly for all of the cases (blue dots

TABLE V. Values of the $0\nu\beta\beta$ NMEs for $g_A^{\mathrm{eff}} = 1.00$. The first column indicates the transition, the second column the basis used in the calculation, and the third one the model adopted for the g_{ph} values. Model 1: $g_{\mathrm{ph}}(1^+)$ used for all J^π; Model 2: $g_{\mathrm{ph}}(2^-)$ used for $J^\pi = 2^-$, for the rest $g_{\mathrm{ph}}(1^+)$ is used; Model 3: $g_{\mathrm{ph}}(1^+)$ used for $J^\pi = 1^+$, for the rest $g_{\mathrm{ph}}(2^-)$ is used. The columns 4 to 6 show the decomposition of the total NMEs (column 7) in terms of the Fermi, Gamow-Teller, and tensor contributions. The last row for each transition corresponds to the earlier calculations performed in Ref. [29]. The quoted errors only take into account uncertainties due to the strength of the particle-hole interaction.

Nuclear transition	Basis	Model	$M_{\mathrm{F}}^{(0\nu)}$	$M_{\mathrm{GT}}^{(0\nu)}$	$M_{\mathrm{T}}^{(0\nu)}$	$M^{(0\nu)}$
$^{76}\mathrm{Ge} \longrightarrow {}^{76}\mathrm{Se}$	WS	1	-1.76 ± 0.06	5.4 ± 0.2	-0.356 ± 0.013	6.8 ± 0.3
	WS	2	-1.76 ± 0.05	5.5 ± 0.2	-0.357 ± 0.012	6.9 ± 0.3
	WS	3	-1.95 ± 0.11	5.8 ± 0.3	-0.31 ± 0.03	7.4 ± 0.4
	sp	1	-1.99 ± 0.08	5.3 ± 0.2	-0.390 ± 0.015	6.9 ± 0.3
	sp	2	-1.99 ± 0.08	5.2 ± 0.2	-0.389 ± 0.014	6.8 ± 0.3
	sp	3	-1.90 ± 0.13	5.1 ± 0.3	-0.41 ± 0.03	6.6 ± 0.4
	sp, small [29]	1	-1.74	5.07	-0.28	6.54
$^{96}\mathrm{Zr} \longrightarrow {}^{96}\mathrm{Mo}$	sp	1	-1.64 ± 0.06	3.95 ± 0.12	-0.254 ± 0.014	5.3 ± 0.2
	sp	2	-1.64 ± 0.06	3.97 ± 0.14	-0.255 ± 0.013	5.3 ± 0.2
	sp	3	-1.68 ± 0.13	4.0 ± 0.3	-0.24 ± 0.04	5.5 ± 0.4
	sp, small [29]	1	-1.44	3.26	-0.23	4.47
$^{100}\mathrm{Mo} \longrightarrow {}^{100}\mathrm{Ru}$	sp	1	-2.30 ± 0.05	3.74 ± 0.04	-0.500 ± 0.010	5.54 ± 0.10
	sp	2	-2.30 ± 0.05	3.76 ± 0.05	-0.503 ± 0.009	5.55 ± 0.11
	sp	3	-2.43 ± 0.15	3.9 ± 0.2	-0.47 ± 0.03	5.9 ± 0.4
	sp, small [29]	1	-1.63	3.62	-0.27	4.98
$^{116}\mathrm{Cd} \longrightarrow {}^{116}\mathrm{Sn}$	WS	1	-1.76 ± 0.07	4.11 ± 0.12	-0.171 ± 0.012	5.7 ± 0.2
	WS	2	-1.76 ± 0.07	4.08 ± 0.11	-0.168 ± 0.013	5.7 ± 0.2
	WS	3	-1.64 ± 0.05	3.94 ± 0.08	-0.191 ± 0.008	5.39 ± 0.13
	WS, small [29]	1	-1.50	3.61	-0.17	4.93
$^{128}\mathrm{Te} \longrightarrow {}^{128}\mathrm{Xe}$	WS	1	-1.65 ± 0.04	4.68 ± 0.08	-0.523 ± 0.010	5.81 ± 0.12
	WS	2	-1.65 ± 0.04	4.67 ± 0.10	-0.523 ± 0.009	5.81 ± 0.14
	WS	3	-1.64 ± 0.08	4.7 ± 0.2	-0.53 ± 0.03	5.8 ± 0.3
	sp	1	-1.77 ± 0.05	4.27 ± 0.09	-0.523 ± 0.011	5.52 ± 0.15
	sp	2	-1.77 ± 0.05	4.22 ± 0.09	-0.519 ± 0.011	5.47 ± 0.15
	sp	3	-1.55 ± 0.08	3.89 ± 0.13	-0.59 ± 0.03	4.9 ± 0.3
	sp, small [29]	1	-1.78	4.40	-0.43	5.74
$^{130}\mathrm{Te} \longrightarrow {}^{130}\mathrm{Xe}$	WS	1	-1.46 ± 0.03	4.04 ± 0.07	-0.468 ± 0.008	5.03 ± 0.10
	WS	2	-1.46 ± 0.03	4.03 ± 0.08	-0.468 ± 0.007	5.02 ± 0.12
	WS	3	-1.42 ± 0.07	3.97 ± 0.15	-0.48 ± 0.03	4.9 ± 0.3
	sp	1	-1.53 ± 0.04	3.70 ± 0.08	-0.460 ± 0.009	4.77 ± 0.12
	sp	2	-1.53 ± 0.04	3.65 ± 0.08	-0.456 ± 0.009	4.72 ± 0.12
	sp	3	-1.30 ± 0.06	3.31 ± 0.09	-0.53 ± 0.02	4.1 ± 0.2
	sp, small [29]	1	-1.52	4.12	-0.38	5.27
$^{136}\mathrm{Xe} \longrightarrow {}^{136}\mathrm{Ba}$	WS	1	-0.683 ± 0.010	2.83 ± 0.06	-0.227 ± 0.004	3.28 ± 0.07
	WS	2	-0.683 ± 0.010	2.90 ± 0.09	-0.229 ± 0.003	3.35 ± 0.10
	WS	3	-0.683 ± 0.010	2.93 ± 0.10	-0.231 ± 0.003	3.38 ± 0.12
	sp	1	-1.01 ± 0.03	2.96 ± 0.06	-0.249 ± 0.005	3.72 ± 0.09
	sp	2	-1.01 ± 0.03	3.01 ± 0.08	-0.251 ± 0.005	3.76 ± 0.10
	sp	3	-1.12 ± 0.06	3.21 ± 0.15	-0.220 ± 0.014	4.1 ± 0.3
	sp, small [29]	1	-0.89	2.82	-0.22	3.50

in Fig. 8). Adoption of $g_{\mathrm{ph}}(2^-)$ for all multipoles $J^\pi \neq 1^+$ (Model 3), however, causes larger deviations in all cases (red squares and open triangles in Fig. 8).

The results obtained in the WS bases deviate from those obtained in the sp bases by about 12% in the case of $A = 136$, and by less than 10% in the other cases for Model 1 and Model 2, as seen in Fig. 9, blue dots and red squares. However, for Model 3 the differences between the different single-particle bases are 15–21% for $A = 128, 130, 136$ and about 11% for $A = 76$. Hence, the features of the single-particle valence spaces affect notably the values of the NMEs.

The present results are summarized in Table VI where we quote the combined no-core $0\nu\beta\beta$ NMEs of Model 2 and Model 3. Comparing the NME values of Table VI with the NMEs of [29] shows that the present results deviate from those obtained in the smaller basis [29] by less than 4% for $A = 76, 136$, and about 10–18% for the rest (see also the black asterisks in Fig. 8). Hence, the numbers of Table VI indicate that the NME results of Hyvärinen et al. [29] deviate by at most 18% from the present results, the differences emerging from variations in the nuclear mean field, size of the single-particle valence space, and variations in the value of g_{ph}.

TABLE VI. Computed no-core nuclear matrix elements for $g_A^{\text{eff}} = 1.00$ (column 2); combined results of Model 2 and Model 3 are adopted. Given are also the single-particle bases (column 3) and the nuclear-structure coefficients of Eq. (27) (column 4). The phase-space factors are taken from [42].

Nuclear transition	$0\nu\beta\beta$ NME	Basis	$C^{(0\nu)}$
$^{76}\text{Ge} \longrightarrow {}^{76}\text{Se}$	6.7 ± 0.3	sp	0.25 ± 0.03
$^{96}\text{Zr} \longrightarrow {}^{96}\text{Mo}$	5.4 ± 0.3	sp	0.044 ± 0.005
$^{100}\text{Mo} \longrightarrow {}^{100}\text{Ru}$	5.7 ± 0.3	sp	0.050 ± 0.006
$^{116}\text{Cd} \longrightarrow {}^{116}\text{Sn}$	5.55 ± 0.12	WS	0.051 ± 0.003
$^{128}\text{Te} \longrightarrow {}^{128}\text{Xe}$	5.2 ± 0.2	sp	1.64 ± 0.13
$^{130}\text{Te} \longrightarrow {}^{130}\text{Xe}$	4.41 ± 0.12	sp	0.094 ± 0.006
$^{136}\text{Xe} \longrightarrow {}^{136}\text{Ba}$	3.9 ± 0.2	sp	0.118 ± 0.013

The expression for the half-life, Eq. (10), can be written in an easily usable form,

$$t_{1/2}^{(0\nu)}(0_i^+ \longrightarrow 0_f^+) = \frac{C^{(0\nu)}}{(|\langle m_\nu \rangle|[\text{eV}])^2} \times 10^{25} \text{ yr}, \qquad (27)$$

where the effective electron neutrino mass is given in eV. From this expression it is easy to derive the values of the half-lives once the value of the neutrino mass is known. We list the nuclear-structure coefficients $C^{(0\nu)}$, together with the adopted NMEs, in Table VI.
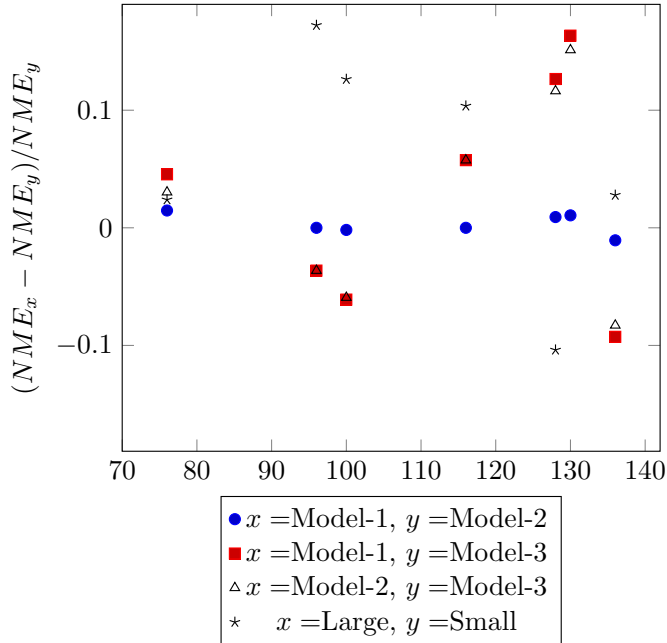

FIG. 8. Relative differences between the $0\nu\beta\beta$ NMEs calculated in the sp bases (except WS for $A = 116$) using different models for g_{ph} values. The asterisk describes differences between the NMEs of Ref. [29] and the combined results of Model 2 and Model 3, displayed in the second column of Table VI.
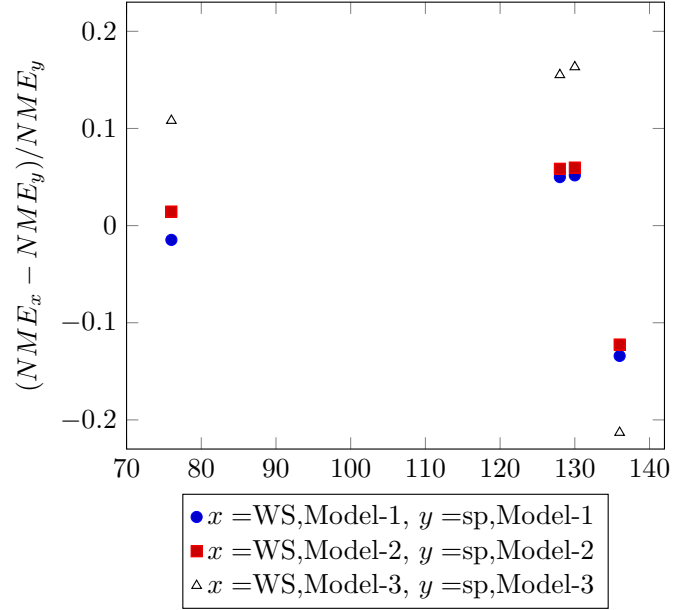

FIG. 9. Relative differences between the $0\nu\beta\beta$ NMEs calculated using different single-particle bases.

IV. CONCLUSIONS

In this work we calculated the nuclear matrix elements of the neutrinoless $\beta\beta$ decays mediated by the light Majorana neutrino. The matrix elements were computed for seven key decays of immediate experimental interest, and for which experimental data on isovector spin-dipole $J^\pi = 2^-$ giant resonances have become available. The calculations were performed using realistic two-body interactions and two different sets of no-core single-particle bases, the bare Woods-Saxon bases and their slightly modified versions, to better reproduce the experimental quasiparticle spectra of relevance to this study. In addition, we include up-to-date nucleon-nucleon short-range correlations, nucleon form factors, induced weak nucleonic currents, and partial restoration of isospin. We adjusted the g_{ph} parameter of the pnQRPA in two different ways: by fitting it to the location of the GT giant resonance (GTR) in the traditional way, and by fitting it to the location of the IVSD $J^\pi = 2^-$ giant resonance as a new method which has become possible because of new experimental data. We calculated the $0\nu\beta\beta$ NMEs using three methods: adopting the g_{ph} adjusted to GTR for each multipole, adjusting the $g_{\text{ph}}(2^-)$ separately to the IVSD $J^\pi = 2^-$ giant resonance, and adopting the $g_{\text{ph}}(2^-)$ for each multipole $J^\pi \neq 1^+$. Finally we compared the obtained results against each other and against a previous study of Hyvärinen *et al.* in which smaller single-particle model spaces were used.

The $0\nu\beta\beta$ NMEs computed in the present no-core modified-WS single-particle bases, using the IVSD $J^\pi = 2^-$ fitted g_{ph} values, deviate from the previously computed NMEs of Hyvärinen *et al.* [29], based on the g_{ph} adjusted by the empirical GT resonance energies, by less than 4% for the decays of ^{76}Ge and ^{136}Xe, and by some 10–18% for the rest of the cases. Most of the deviations are due to the extension of the single-particle space of pnQRPA, while the effect of adjusting

the particle-hole interaction to data on spin-dipole resonances is relatively smaller. Table VI summarizes our results for the nuclear-structure coefficients that reflect the improvements of the $0\nu\beta\beta$ NMEs achieved in the present work. The quoted errors only take into account the uncertainties due to the strength of the particle-hole interaction.

[1] J. Suhonen and O. Civitarese, Phys. Rep. **300**, 123 (1998).
[2] H. Ejiri, J. Phys. Soc. Jpn. **74**, 2101 (2005).
[3] J. D. Vergados, H. Ejiri, and F. Šimkovic, Rep. Prog. Phys. **75**, 106301 (2012).
[4] J. D. Vergados, H. Ejiri, and F. Šimkovic, Int. J. Mod. Phys. E **25**, 1630007 (2016).
[5] J. Engel and J. Menéndez, Rep. Prog. Phys. **80**, 046301 (2017).
[6] A. S. Barabash, Phys. Rev. C **81**, 035501 (2010).
[7] A. S. Barabash, Nucl. Phys. A **935**, 52 (2015).
[8] M. Agostini *et al.* (GERDA Collaboration), Nature (London) **544**, 47 (2017); Phys. Rev. Lett. **120**, 132503 (2018); R. Arnold *et al.* (NEMO-3 Collaboration), JETP Lett. **80**, 377 (2004); J. Argyriades *et al.* (NEMO-3 Collaboration), Nucl. Phys. A **847**, 168 (2010); R. Arnold *et al.* (NEMO-3 Collaboration), Phys. Rev. D **92**, 072011 (2015); **95**, 012007 (2017); K. Alfonso *et al.* (CUORE Collaboration), Phys. Rev. Lett. **115**, 102502 (2015); H. S. Antila and E. Luijten (CUORE Collaboration), *ibid.* **120**, 135501 (2018); J. B. Albert *et al.* (EXO-200 Collaboration), Nature (London) **510**, 229 (2014); Phys. Rev. Lett. **120**, 072701 (2018); A. Gando, Y. Gando, T. Hachiya, A. Hayashi, S. Hayashida, H. Ikeda, K. Inoue, K. Ishidoshiro, Y. Karino, M. Koga, S. Matsuda, T. Mitsui, K. Nakamura, S. Obara, T. Oura, H. Ozaki, I. Shimizu, Y. Shirahata, J. Shirai, A. Suzuki, T. Takai, K. Tamae, Y. Teraoka, K. Ueshima, H. Watanabe, A. Kozlov, Y. Takemoto, S. Yoshida, K. Fushimi, T. I. Banks, B. E. Berger, B. K. Fujikawa, T. ODonnell, L. A. Winslow, Y. Efremenko, H. J. Karwowski, D. M. Markoff, W. Tornow, J. A. Detwiler, S. Enomoto, M. P. Decowski (KamLAND-Zen Collaboration), *ibid.* **117**, 082503 (2016); C. E. Aalseth *et al.* (MAJORANA Collaboration), *ibid.* **120**, 132502 (2018).
[9] J. Suhonen and O. Civitarese, J. Phys. G **39**, 085105 (2012).
[10] J. Toivanen and J. Suhonen, Phys. Rev. Lett. **75**, 410 (1995).
[11] C. M. Raduta and A. A. Raduta, Phys. Rev. C **82**, 068501 (2010).
[12] E. Caurier, J. Menéndez, F. Nowacki, and A. Poves, Phys. Rev. Lett. **100**, 052503 (2008).
[13] J. Menéndez, A. Poves, E. Caurier, and F. Nowacki, Nucl. Phys. A **818**, 139 (2009).
[14] J. Barea and F. Iachello, Phys. Rev. C **79**, 044301 (2009).
[15] T. R. Rodríguez and G. Martínez-Pinedo, Phys. Rev. Lett. **105**, 252503 (2010).
[16] N. L. Vaquero, T. R. Rodriguez, and J. L. Egido, Phys. Rev. Lett. **111**, 142501 (2013).
[17] P. K. Rath, R. Chandra, K. Chaturvedi, P. K. Raina, and J. G. Hirsch, Phys. Rev. C **82**, 064310 (2010).
[18] J. M. Yao, L. S. Song, K. Hagino, P. Ring, and J. Meng, Phys. Rev. C **91**, 024316 (2015).
[19] L. S. Song, J. M. Yao, P. Ring, and J. Meng, Phys. Rev. C **95**, 024305 (2017).
[20] M. Horoi and B. A. Brown, Phys. Rev. Lett. **110**, 222502 (2013).
[21] R. A. Sen'kov and M. Horoi, Phys. Rev. C **90**, 051301(R) (2014).
[22] B. A. Brown, D. L. Fang, and M. Horoi, Phys. Rev. C **92**, 041301(R) (2015).
[23] Y. Iwata, N. Shimizu, T. Otsuka, Y. Utsuno, J. Menéndez, M. Honma, and T. Abe, Phys. Rev. Lett. **116**, 112502 (2016).
[24] J. Suhonen and O. Civitarese, J. Phys. G **39**, 124005 (2012).
[25] J. Suhonen and O. Civitarese, Nucl. Phys. A **847**, 207 (2010).
[26] J. Suhonen, Nucl. Phys. A **853**, 36 (2011).
[27] O. Civitarese, H. Müther, L. D. Skouras, and A. Faessler, J. Phys. G **17**, 1363 (1991).
[28] F. Šimkovic, V. Rodin, A. Faessler, and P. Vogel, Phys. Rev. C **87**, 045501 (2013).
[29] J. Hyvärinen and J. Suhonen, Phys. Rev. C **91**, 024613 (2015).
[30] J. Barea, J. Kotila, and F. Iachello, Phys. Rev. C **91**, 034304 (2015).
[31] J. Suhonen, *From Nucleons to Nucleus: Concepts of Microscopic Nuclear Theory* (Springer, Berlin, 2007).
[32] M. Kortelainen, O. Civitarese, J. Suhonen, and J. Toivanen, Phys. Lett. B **647**, 128 (2007).
[33] M. Kortelainen and J. Suhonen, Phys. Rev. C **75**, 051303(R) (2007).
[34] M. Kortelainen and J. Suhonen, Phys. Rev. C **76**, 024315 (2007).
[35] L. Jokiniemi and J. Suhonen, Phys. Rev. C **96**, 034308 (2017).
[36] A. Bohr and B. R. Mottelson, *Nuclear Structure, Vol. I* (Benjamin, New York, 1969).
[37] K. Holinde, Phys. Rep. **68**, 121 (1981).
[38] J. Suhonen, T. Taigel, and A. Faessler, Nucl. Phys. A **486**, 91 (1988).
[39] J. Suhonen, Nucl. Phys. A **563**, 205 (1993).
[40] J. Suhonen, Nucl. Phys. A **700**, 649 (2002).
[41] NuDat 2.6, Brookhaven National Laboratory, National Nuclear Data Center, http://www.nndc.bnl.gov/nudat2/.
[42] J. Kotila and F. Iachello, Phys. Rev. C **85**, 034316 (2012).
[43] D.-L. Fang, A. Faessler, V. Rodin, and F. Šimkovic, Phys. Rev. C **82**, 051301 (2010).
[44] J. Terasaki, Phys. Rev. C **91**, 034318 (2015).
[45] G. A. Miller and J. E. Spencer, Ann. Phys. (NY) **100**, 562 (1976).
[46] F. Šimkovic, A. Faessler, H. Müther, V. Rodin, and M. Stauf, Phys. Rev. C **79**, 055501 (2009).
[47] D.-L. Fang, A. Faessler, and F. Šimkovic, Phys. Rev. C **97**, 045503 (2017).
[48] P. Vogel and M. R. Zirnbauer, Phys. Rev. Lett. **57**, 3148 (1986).
[49] O. Civitarese, A. Faessler, and T. Tomoda, Phys. Lett. B **194**, 11 (1987).
[50] C. Gaarde, J. S. Larsen, M. N. Harakeh, S. Y. van der Werf, M. Igarashi, and A. Müller-Arnke, Nucl. Phys. A **334**, 248 (1980).
[51] C. D. Goodman, Nucl. Phys. A **374**, 241c (1982).
[52] H. Akimune, I. Daito, Y. Fujita, M. Fujiwara, M. B. Greenfield, M. N. Harakeh, T. Inomata, J. Jänecke, K. Katori, S. Nakayama *et al.*, Phys. Rev. C **52**, 604 (1995).
[53] J. H. Thies, D. Frekers, T. Adachi, M. Dozono, H. Ejiri, H. Fujita, M. Fujiwara, E.-W. Grewe, K. Hatanaka, P. Heinrichs *et al.*, Phys. Rev. C **86**, 014304 (2012).
[54] J. H. Thies, P. Puppe, T. Adachi, M. Dozono, H. Ejiri, D. Frekers, H. Fujita, Y. Fujita, M. Fujiwara, E.-W. Grewe *et al.*, Phys. Rev. C **86**, 054323 (2012).
[55] J. H. Thies, T. Adachi, M. Dozono, H. Ejiri, D. Frekers, H. Fujita, Y. Fujita, M. Fujiwara, E.-W. Grewe, K. Hatanaka *et al.*, Phys. Rev. C **86**, 044309 (2012).

[56] H. Akimune, H. Ejiri, M. Fujiwara, I. Daito, T. Inomata, R. Hazama, A. Tamii, H. Toyokawa, and M. Yosoi, Phys. Lett. B **394**, 23 (1997).

[57] P. Puppe, A. Lennarz, T. Adachi, H. Akimune, H. Ejiri, D. Frekers, H. Fujita, M. Fujiwara, E. Ganioğlu, E.-W. Grewe *et al.*, Phys. Rev. C **86**, 044603 (2012).

[58] P. Puppe, D. Frekers, T. Adachi, H. Akimune, N. Aoi, B. Bilgier, H. Ejiri, H. Fujita, Y. Fujita, M. Fujiwara *et al.*, Phys. Rev. C **84**, 051305 (2011).

[59] H. Ejiri, K. Ikeda, and J. I. Fujita, Phys. Rev. **176**, 1277 (1968).

[60] F. Šimkovic, A. Faessler, V. A. Rodin, P. Vogel, and J. Engel, Phys. Rev. C **77**, 045503 (2008).

[61] J. Suhonen and M. Kortelainen, Int. J. Mod. Phys. E **17**, 1 (2008).

[62] M. Aunola and J. Suhonen, Nucl. Phys. A **602**, 133 (1996).

[63] J. Suhonen, Phys. Lett. B **607**, 87 (2005).

[64] J. Suhonen and O. Civitarese, Phys. Lett. B **725**, 153 (2013).

[65] J. Suhonen and O. Civitarese, Nucl. Phys. A **924**, 1 (2014).

[66] Z. M. Niu, Y. F. Niu, H. Z. Liang, W. H. Long, and J. Meng, Phys. Rev. C **95**, 044301 (2017).

Article III

Pinning down the strength function for ordinary muon capture on ^{100}Mo

L. Jokiniemi, J. Suhonen, H. Ejiri and I. H. Hashim,

Contents lists available at ScienceDirect

Physics Letters B

Pinning down the strength function for ordinary muon capture on ^{100}Mo

L. Jokiniemi [a,*], J. Suhonen [a], H. Ejiri [b], I.H. Hashim [c]

[a] *University of Jyvaskyla, Department of Physics, P.O. Box 35, FI-40014, Finland*
[b] *Research Center for Nuclear Physics, Osaka University, Ibaraki, Osaka 567-0047, Japan*
[c] *Physics Department, Faculty of Science, Universiti Teknologi Malaysia, 81310 Johor Bahru, Malaysia*

ABSTRACT

Ordinary muon capture (OMC) on ^{100}Mo is studied both experimentally and theoretically in order to access the weak responses in wide energy and momentum regions. The OMC populates states in ^{100}Nb up to some 50 MeV in excitation energy. For the first time the associated OMC strength function has been computed and compared with the obtained data. The present computations are performed using the Morita-Fujii formalism of OMC by extending the original formalism beyond the leading order. The participant nuclear wave functions are obtained in extended no-core single-particle model space using the spherical version of proton-neutron quasiparticle random-phase approximation (pnQRPA) with two-nucleon interactions based on the Bonn one-boson-exchange G matrix. Partial restoration of the isospin symmetry is implemented in the calculations by separately fitting the isoscalar and isovector parts of the particle-particle interaction strength of pnQRPA. Both the computed and experimental OMC strength distributions show a giant resonance at around 12 MeV. Further measurements and calculations of the OMC strength functions for double-beta-decay daughter nuclei could enable access to in-medium renormalization of the weak axial couplings and pave the way to improved accuracy of the double-beta-decay nuclear matrix elements.

© 2019 The Author(s). Published by Elsevier B.V. This is an open access article under the CC BY license (http://creativecommons.org/licenses/by/4.0/). Funded by SCOAP³.

In the ordinary muon capture (OMC) a negative muon on an atomic orbit is captured by the atomic nucleus quite like in the ordinary electron capture of a nucleus, except that the rest mass of the muon is some 200 times the rest mass of an electron. Due to the large momentum exchange, $q \sim 50$–100 MeV/c, in the process, the OMC can lead to final states that are both highly excited and of high multipolarity J^π, quite like in the analogous process of the neutrinoless double beta ($0\nu\beta\beta$) decay where the Majorana-neutrino exchange with $q \sim 100$ MeV induces high-excitation and high-multipolarity transitions through the virtual states of the intermediate nucleus. This analogue leads immediately to the idea of using the OMC as probe of the nuclear matrix elements (NMEs) involved in the $0\nu\beta\beta$ decays. This probe corresponds to the right branch (β^+ type of transitions) of the $0\nu\beta\beta$ virtual transitions.

As mentioned above, one of the incentives of the OMC studies is related to the $0\nu\beta\beta$ decays [1,2] and to neutrino-nucleus interactions in general (see the recent review [3]). General aspects of

these relations have been treated also in the reviews [4–9] and the associated $0\nu\beta\beta$ NMEs have been discussed e.g. in [1,10,11]. The muon-capture processes concern β^+ type of transitions from a nucleus ^A_ZX to the states of the residual nucleus $^A_{Z-1}$Y (see the review [12]). Nuclear-structure calculations for the OMC transitions have been performed in a wide range of nuclear masses along the years. In these calculations the muon-capture transitions have been used to probe the right-leg (the β^+ side) virtual transitions of $0\nu\beta\beta$ decays and the value of the particle-particle interaction parameter g_{pp} of the pnQRPA, as discussed in [13–15]. The OMC calculations can also be used to yield information on the in-medium renormalization of the axial current in the form of an effective strength of the weak axial-vector coupling g_A [16–21]. For the experimental aspects of the axial-vector coupling see the reviews [3,4,22,23]. The involved large momentum exchange in the OMC activates the induced weak currents quite like in the case of the $0\nu\beta\beta$ decay [24]. These induced terms include the weak magnetism and pseudoscalar contributions, the magnitude of the induced pseudoscalar term being a very interesting unknown in finite atomic nuclei [16,17,25–31]. A recent review on the renormalization of g_P is given in [32].

---

* Corresponding author.
E-mail address: lotta.m.jokiniemi@jyu.fi (L. Jokiniemi).

Experimentally, it has been shown that mass distributions of residual isotopes from the OMC can be used to study astro-(anti)neutrino β^+ type of strength distribution and the associated giant resonances in the high-excitation regions [3,33,34]. The OMC probe is also used to study nuclear responses for medium-energy astro-(anti)neutrinos (μ and τ (anti)neutrinos from supernovae) [3,4]. Weak $\beta^\pm$ responses and giant resonances have been discussed before in [4,22,23].

In the present work we study both theoretically and experimentally the OMC on ^{100}Mo populating states in ^{100}Nb in a wide excitation region, up to some 50 MeV. The rate of OMC to individual final states forms a strength function quite like in the case of (n,p) charge-exchange reactions for 1^+ final states (the Gamow-Teller strength function). The OMC strength function contains giant resonances analogously to the Gamow-Teller giant resonance [35] or isovector spin-monopole [36,37] and higher isovector spin-multipole resonances [3,4,22,38], and here we study the structure of these resonances. This is the first time such resonances are being studied both theoretically and experimentally, inspired by the first observation of the OMC giant resonance at around 12 MeV [3,39,40]. Eventual extension of the experiments and calculations to other nuclei, involved in $0\nu\beta\beta$ decays, helps theories better evaluate the β^+ NMEs associated with the $0\nu\beta\beta$ decays and the NMEs related to astro-(anti)neutrino interactions. In addition, the effective values of the axial-vector coupling g_A and induced pseudoscalar coupling g_P play essential roles both in $0\nu\beta\beta$ decays and OMC [41].

The OMC process we are interested in here can be written as

$$\mu^- + {}^A_Z X(0^+) \rightarrow \nu_\mu + {}^A_{Z-1} Y(J^\pi), \qquad (1)$$

where the muon (μ^-) is captured by the 0^+ ground state of the even-even nucleus X of mass number A and atomic number Z leading to the J^π states of its odd-odd isobar Y of atomic number $Z-1$; here J is the angular momentum and π the parity of the final state. At the same time a muon neutrino ν_μ is emitted. The OMC on a nucleus ${}^A_Z X$ populates excited states in a wide excitation region of the residual nucleus ${}^A_{Z-1} Y$. They de-excite by emitting γ rays to the ground state of ${}^A_{Z-1} Y$ or by emitting mostly the first neutron to a state in a nucleus ${}^{A-1}_{Z-1} Y'$, depending on whether the excitation energy is below or above the first neutron-emission threshold energy. The residual nucleus ${}^{A-1}_{Z-1} Y'$, after the first neutron emission, de-excites by emitting γ rays to the ground state of ${}^{A-1}_{Z-1} Y'$ or by emitting a second neutron, depending on whether the excitation energy is below or above the second neutron-emission threshold energy, and so on. Then, one finally ends up with the residual isotopes of ${}^{A-x}_{Z-1} Y'$ with $x = 0, 1, 2, 3,...$, depending on the excitation energy E and the number x of the emitted neutrons. Here proton emissions are suppressed by the Coulomb barrier in medium-heavy and heavy nuclei.

The OMC on ^{100}Mo was studied at the MuSIC beam channel at RCNP and the D2 beam channel in J-PARC MLF [40,42]. The nucleus ^{100}Mo is one of DBD nuclei, and is used also for solar- and supernova-neutrino studies [6,34,43,44]. The delayed γ-ray characteristics of the residual radioactive isotopes of $^{100-x}$Nb were measured, and the number of the Nb residual isotopes $^{100-x}$Nb produced by the OMC on ^{100}Mo was evaluated from the observed γ-ray yields. The 1^+ strength can produce the Gamow-Teller component of the OMC giant resonance. The vector 1^- and axial-vector 2^- spin-dipole strengths with $1\hbar\omega$ jump show broad giant-resonance-like distributions similarly to the isovector spin-dipole (p,n)-type of charge-exchange resonance [38]. The Gamow-Teller and spin-dipole resonances have also been discussed in [22, 45]. The corresponding OMC distributions, being of (n,p) charge-exchange type [22], are shown later in this article.

A powerful formalism for the calculation of the OMC rates in muonic atoms was developed by Morita and Fujii in [46]. In the present calculations we use a similar formalism by writing the partial muon capture rate to a J^π final state as

$$W = 8 \left(\frac{Z_{\text{eff}}}{Z} \right)^4 P (\alpha Z m'_\mu)^3 \frac{2J_f + 1}{2J_i + 1} \left(1 - \frac{q}{m_\mu + AM} \right) q^2, \qquad (2)$$

where A denotes the mass number of the initial and final nuclei, J_i (J_f) the angular momentum of the initial (final) nucleus, M the average nucleon rest mass, m_μ the bound muon mass (the rest mass minus the binding energy of the muon in the K orbital of the μ-mesonic atom), m'_μ the muon reduced mass in the parent μ-mesonic atom, Z the atomic number of the initial nucleus, α the fine-structure constant and q the magnitude of the exchanged momentum between the captured muon and the nucleus [46], i.e. the Q value of the OMC (momentum of the emitted muon neutrino). The Q value can be obtained from

$$q = (m_\mu - W_0) \left(1 - \frac{m_\mu - W_0}{2(M_f + m_\mu)} \right), \qquad (3)$$

where $W_0 = M_f - M_i + m_e + E_X$ [46]. Here M_f and M_i are the nuclear masses of the final and initial nuclei, m_e the electron rest mass and E_X is the excitation energy of the final-state nucleus. For the heavy nuclei the atomic orbit of the muon penetrates the nucleus and the capture rate has to be corrected for the muonic screening. Here we follow the Primakoff procedure [47] where the capture rate has been corrected by the factor $(Z_{\text{eff}}/Z)^4$, where the effective atomic number is obtained from the work of Ford and Wills [48], giving $Z_{\text{eff}} = 26.37$ in the present case. The term P in Eq. (2) has a complex structure, containing all the nuclear matrix elements, as well as weak couplings, Racah coefficients and some geometric factors. For the exact form see Eq. (45) in the paper of Morita and Fujii [46].

For nth forbidden OMC transitions the P term in (2) can be expanded in powers of the small quantity $1/M^2$. In this way one ends up with the explicit formula $P = P_0 + P_1$, where P_0 is the part which one obtains by neglecting all terms of order $1/M^2$ (except for terms containing g_P^2, which is large compared with the other coupling constants) and P_1 contains the rest of the $1/M^2$ terms. The P_0 part is the explicit form that can be found in [46], Eq. (58). The next-to-leading-order term P_1 in the expansion is sometimes needed for OMC transitions which are quite weak, usually for captures to high-lying states of high multipolarity J_f^π, where π is the parity of the final state. We derived this part from Eq. (46) of [46] and introduced it into our capture-rate calculations [49].

The P term contains coefficients $g_V \equiv g_V(q)$ and $g_A \equiv g_A(q)$ that are the usual weak vector and axial-vector couplings at finite momentum transfer $q > 0$. The conserved vector current (CVC) and partially conserved axial-vector current (PCAC) hypotheses dictate for a free nucleon the values $g_V(0) = 1.00$ and $g_A(0) = 1.27$ at zero momentum transfer and the dipole approximation can be used for finite momentum transfer [3]. For these couplings deviations from the CVC and PCAC values have been recorded at zero momentum transfer (the situation with the renormalization of the weak couplings has been charted in the recent reviews [23,41]). Then one refers to effective values of these couplings. For the induced pseudoscalar coupling g_P the Goldberger-Treiman PCAC relation [50] gives $g_P/g_A = 7.0$. In order to see how the values of these coupling strengths affect the OMC strength function and the total OMC rate, we vary in this work independently the values of $g_A(0)$ and $g_P(0)$ and keep the CVC value $g_V(0) = 1.00$. Such a procedure is justified by the earlier results from the OMC studies in
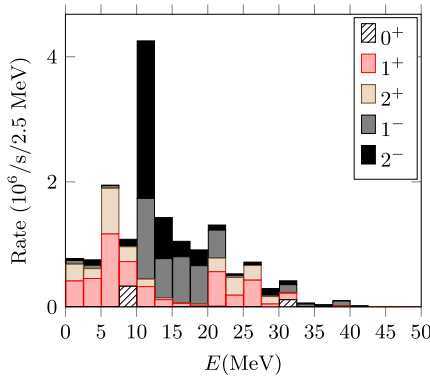
Fig. 1. Muon-capture-rate distribution (OMC strength function) including transitions to $J_f^\pi = 0^+, 1^\pm, 2^\pm$ states. The horizontal axis shows the excitation energy in the ^{100}Nb nucleus. Here a 2.5 MeV binning in energy is used in order to match the energy binning used in the experimental data analysis. Parameter values $g_A(0) = 0.8$ and $g_P(0) = 7.0$ were adopted in the calculations.

Fig. 2. The same as in Fig. 1 but with the transitions to the rest of the possible multipole final states J_f^π added.

Fig. 3. The same as in Fig. 1 but for multipole states $J_f^\pi = 3^\pm, 4^\pm$.

light, medium-heavy and heavy nuclei (see e.g. [19,20,31] and the review [32]) where renormalized values of g_A and g_P, breaking the Goldberger-Treiman PCAC relation, were recorded.

In the numerical computations we used no-core single-particle bases for both protons and neutrons. The bases contained all orbitals up to the $0i - 1g$ oscillator shell, i.e. 7 full oscillator shells (see [38]). This single-particle basis is thus able to catch $n\hbar\omega$ excitations for $n \leq 6$. The corresponding single-particle energies were obtained using the Woods-Saxon (WS) potential with the parametrization of [51], suitable for nuclei which lie close to the β-decay stability line, like ^{100}Mo. Some adjustments of the WS single-particle energies were made near the corresponding Fermi surfaces in order to improve the quality of the one-quasiparticle spectra. These details were addressed in our paper [52] and the reader is referred to it for further information.

The nuclear Hamiltonian was obtained from the Bonn-A one-boson-exchange potential introduced in [53]. The BCS pairing gaps are adjusted to the phenomenological pairing gaps by adjustable pairing strengths for protons and neutrons in a way described in [38] where isovector spin-multipole giant resonances were treated in the same formalism.

The wave functions and energies of the complete set of J_f^π multipole states are obtained by performing a pnQRPA diagonalization in the unperturbed basis of quasiproton-quasineutron pairs coupled to J_f^π (see, e.g., [1,54–56]). All the particle-hole G-matrix elements are multiplied by a factor g_{ph} the value of which is adjusted to the centroid of the Gamow-Teller giant resonance in the nucleus ^{100}Tc. The isoscalar ($T = 0$) and isovector ($T = 1$) parts of the particle-particle G-matrix elements are multiplied by factors $g_{pp}^{T=0}$ and $g_{pp}^{T=1}$ that are adjusted according to isospin-symmetry restoration scheme introduced in [57] as explained in detail in the double-β-decay paper [52].

The capture rates for the transitions $\mu^- + {}^{100}$Mo$(0_{gs}^+) \rightarrow \nu_\mu + {}^{100}Nb(J_f^\pi)$ were computed for all multipole states J_f^π and the data applies to multipole states $J_f^\pi = 0^+, 1^\pm, 2^\pm$. In the present calculations we have varied independently the values of the axial-vector coupling $g_A(0)$ and the induced pseudoscalar coupling $g_P(0)$ and keep the CVC value $g_V(0) = 1.00$ of the vector coupling. Furthermore, we have varied these parameters in the ranges of $g_A(0) = 0.6 - 1.27$ (this is a reasonable range as discussed in the review [41]) and $g_P(0) = 0 - 10$ in order to see how they affect the total capture rate and the structure of the OMC strength function.

In Fig. 1 we present the OMC rate distribution (OMC strength function) of transitions to the lowest multipole states $J_f^\pi =$
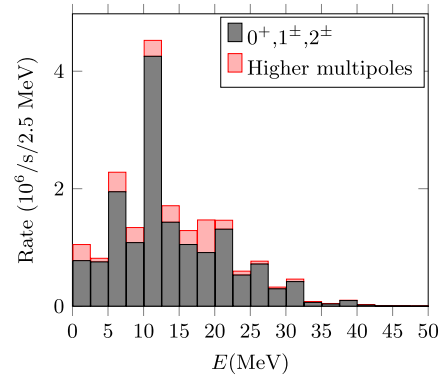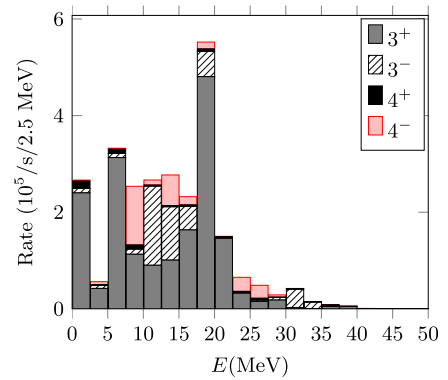
$0^+, 1^+, 2^+, 1^-$ and 2^-. We notice that transitions to $J_f^\pi = 1^-, 2^-$, which are $1\hbar\omega$ excitations, have the highest capture rates and that these multipoles are the ones that are primarily responsible of the OMC giant resonance at around 12 MeV of excitation. The OMC to multipole states 1^+ and 2^+ forms a satellite resonance at around 7 MeV. These are $0\hbar\omega$ excitations, together with the low-lying 0^+ strength. The higher-lying 0^+, 1^+ and 2^+ strength, beyond some 20 MeV, stems from $2\hbar\omega$ excitations and the 1^- and 2^- strength in this high-excitation region stems from $3\hbar\omega$ excitations. It should be noted that the (p,n)-type charge-exchange 1^+ Gamow-Teller giant resonance is quite strong and peaked but here this resonance is diluted since OMC is an (n,p) type of charge-exchange mechanism where for medium-heavy and heavy nuclei the relative locations of the proton and neutron Fermi surfaces hinder $0\hbar\omega$ excitations.

In Fig. 2 we present the total OMC rate to all multipoles. We separate the total capture rates to two parts: strength containing either the lowest-multipole ($J_f^\pi = 0^+, 1^\pm, 2^\pm$) states or the higher-multipole states. We notice that approximately $80 - 90\%$ of the total capture rate consists of transitions to the lowest multipoles, and the rest $10 - 20\%$ comes from the transitions to higher multipoles. The contributions of some of the leading higher multipoles ($J_f^\pi = 3^\pm, 4^\pm$) are presented in Fig. 3. It can be seen that the overwhelming contribution comes from the $0\hbar\omega$ and $2\hbar\omega$ 3^+ multipole, the $1\hbar\omega$ 3^- and 4^- contributions being the sub-leading ones. The 4^+ contribution is negligible.

In Table 1 we show the ratio $W_A(J_f^\pi)/W(J_f^\pi)$, where $W_A(J_f^\pi)$ contains only the axial part of the total capture rate $W(J_f^\pi)$ to the multipole states J_f^π. The OMC rate to 0^+ states is purely vector and is not displayed in the table. From the table one sees that the axial contribution increases with increasing value of $g_A(0)$ and

Table 1

Axial-vector contribution to the total capture rate ($W_A(J_f^\pi)/W(J_f^\pi)$) to final states $J_f^\pi = 1^\pm, 2^\pm$ for different values of $g_A(0)$. The values are calculated using pseudoscalar strength $g_P(0) = 7.0$.

$g_A(0)$	Final-state multipole J_f^π			
	1^+	2^+	1^-	2^-
0.6	0.65	0.22	0.26	0.66
0.8	0.72	0.32	0.36	0.74
1.0	0.77	0.40	0.45	0.79
1.27	0.82	0.49	0.54	0.83

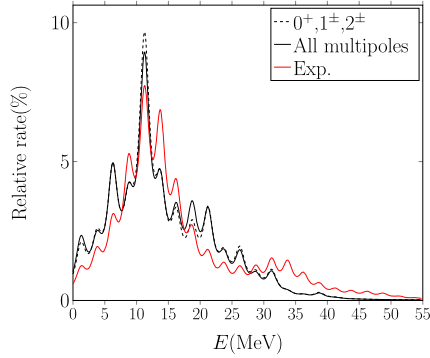**Fig. 4.** Comparison of different relative (in per cents) muon-capture-rate distributions: theoretical capture rates to $J_f^\pi = 0^+, 1^\pm, 2^\pm$ states, and to all possible states, compared with the experimental strength distribution. The theoretical rates were computed with parameter values $g_A(0) = 0.8$ and $g_P(0) = 7.0$. The original energy-binned distributions are smeared by a Lorentzian folding function for clearer presentation.

that the OMC to 1^+ and 2^- states is mostly axial and very similar for both multipoles. The capture rate for the 1^- and 2^+ states is mostly vector with a similar ratio for both multipoles.

In Fig. 4 we plot the theoretical and experimental relative capture-rate distributions against each other. The distributions are smeared by a Lorentzian folding function for easier comparison of the different distributions. Here the experimental giant resonances GR1 at around 12 MeV and GR2 at around 30 MeV were derived from the OMC residual-isotope distributions using the neutron equilibrium-emission and pre-equilibrium-emission models as given in [33,40]. There are two different theoretical capture-rate distributions, one including the transitions to the lowest multipole ($J_f^\pi = 0^+, 1^\pm, 2^\pm$) states and the other containing transitions to all multipole states. We notice that the overall features of all the relative rate distributions are similar: there is a strong peak, GR1, around $10 - 12.5$ MeV and tails on both sides. However, the experimental distribution is a bit more spread to higher energies as compared to the theoretical distributions, containing also the GR2 bump. Here it should be noted that the strength at around 30 MeV, which is analyzed in terms of the second giant resonance GR2, includes some experimental and analysis uncertainties, and thus requires further studies to confirm the amount of the high-energy strength. It is interesting to note that the experimental rates are spread beyond 30 MeV, suggesting some spread of GR strengths with higher multipoles of $J^\pm$ with $J \geq 3$ and n (radial node) ≥ 2. Similar effect was observed beyond the SD GR region (30 MeV) in case of (^{3}He,t) charge exchange reactions [3]. Also, in the theoretical distributions, there is a satellite (consisting mainly of transitions to $J_f^\pi = 1^+, 2^+$ states) that is absent in the experimental distribution or shifted to higher energy. There are no notable differences between the two theoretical distributions.

In Table 2 we present the total OMC rates obtained by using different values for $g_A(0)$ and $g_P(0)$. If we compare the computed values with the total capture rate $W = 7.7 \times 10^6$ 1/s evaluated

Table 2

Total rates of muon capture by ^{100}Mo for different values of the pseudoscalar and axial-vector strengths $g_P(0)$ and $g_A(0)$. The rates are expressed in units of 10^6/s.

$g_A(0)$	$g_P(0) = 0$		$g_P(0) = 7$		$g_P(0) = 10$	
	$W_{(0^+, 1^\pm, 2^\pm)}$	W_{tot}	$W_{(0^+, 1^\pm, 2^\pm)}$	W_{tot}	$W_{(0^+, 1^\pm, 2^\pm)}$	W_{tot}
0.6	11.8	13.8	10.8	12.4	10.7	12.2
0.8	17.0	20.2	15.7	18.3	15.3	17.7
1.0	23.9	28.4	28.0	31.9	21.2	24.8
1.27	34.8	41.7	32.2	38.2	31.3	37.0

Fig. 5. The relative OMC-rate distributions using two different parameter sets: $g_A(0) = 0.6$ and $g_P(0) = 10$, and $g_A(0) = 1.27$ and $g_P(0) = 0$. The distributions are smeared by a Lorentzian folding function.

by using the Primakoff approximation (see Eq. (4.53) of the review article [12]), we notice that the Primakoff value is smaller than the theoretical rates. Increasing the value of $g_P(0)$ or decreasing the value of $g_A(0)$ decreases the theoretical total capture rate, and the closest value to the Primakoff value is achieved by using $g_A(0) = 0.6$ and $g_P(0) = 10$, leading to $g_P(0)/g_A(0) = 16.7$, much larger than the PCAC value of 7.0. It is evident from the table that the total rate is quite insensitive to the value of $g_P(0)$ and not too much can be said about the value of $g_P(0)$ based on the total OMC rates. The differences between the computed and Primakoff total OMC rates are partly related to the higher average energy (smaller phase space) of the experimental OMC strength function and partly to the possible quenching of the effective weak couplings $g_A(0)$ and $g_P(0)$. Comparison of the computed and Primakoff total capture rates suggests a strongly quenched effective value of $g_A(0) \approx 0.5$, which is in accord with the results of many earlier β-decay studies (see e.g. [58–62]). From Table 2 one can also see that a decrease of $g_A(0)$ by a factor of 2 results in reduction of the rate by a factor of 3, not by a factor of 4, due to the vector components, as in the case of $0\nu\beta\beta$ NMEs [3,23,63]. It should also be noted that the considered variation in the values of $g_A(0)$ and $g_P(0)$ does not affect noticeably the shape of the computed capture-rate distribution as visible in Fig. 5 where we plot the Lorentzian folding of the total rate distributions computed for parameter-value pairs of $g_A = 0.6$ and $g_P = 10$, and $g_A = 1.27$ and $g_P = 0$.

In this Letter we show for the first time a direct comparison between the experimental and computed distributions of muon-capture rates to low-multipole J_f^π states in a daughter nucleus. The presently discussed case is the ordinary muon capture (OMC) on the 0^+ ground state of ^{100}Mo leading to $J_f^\pi = 0^+, 1^\pm, 2^\pm$ states in ^{100}Nb. The experimental distribution and the OMC giant resonance are based on the recent measurement of the γ rays in the residual ions produced by the OMC. The computations were performed using the Morita-Fujii formalism of the OMC and treating the involved nuclear matrix elements by using the proton-neutron quasiparticle random-phase approximation with two-nucleon in-

teractions based on the Bonn one-boson-exchange G matrix. The nuclear Hamiltonian was taken from our earlier calculations of the locations of the isovector spin-multipole giant resonances in nuclei involved in double beta decays. Partial restoration of the isospin symmetry was achieved by the method used earlier in the context of double-beta-decay calculations.

The computed OMC strength predicts a giant resonance at around 12 MeV and thus is consistent with the recent experimental observation of the OMC giant resonance GR1 for ^{100}Mo. Calculated decomposition of the OMC strength function in terms of the involved multipoles is shown and the low-multipole strength function is compared with the one containing all multipoles. Integral over the computed complete strength function yields the total OMC rate which can be compared with the Primakoff approximation. Since the axial-vector component dominates the OMC rate, the rate is quite sensitive to the value of the weak axial coupling g_A and thus OMC can be used to study the effective value of weak axial coupling. On the other hand, the rate does not depend much on the value of the pseudoscalar coupling g_P. In our calculations we assumed the CVC value $g_V(0) = 1.00$ for the vector coupling at zero-momentum transfer. Comparison of the computed and Primakoff capture rates suggests a strongly quenched effective value of $g_A(0)$ in keeping with the results of many earlier β-decay studies. The shape of the OMC strength function is practically independent of the values of the weak axial couplings.

Further measurements and computations of the OMC strength functions for final nuclei of double beta decays would enable a systematic scan of the sensitivity of the OMC strength function to the effective in-medium values of the weak axial couplings. This, in turn, could help in improving the accuracy of calculations of the nuclear matrix elements of the neutrinoless double beta decay. Furthermore, the OMC with its large excitation energy and momentum transfer provides a unique opportunity for studying the (anti)neutrino responses for medium-energy astro-neutrino interactions. Further experimental studies are in progress at RCNP Osaka for nuclei of interest in studies of nuclear double beta decay and asto-neutrino interactions.

Acknowledgements

References

[1] J. Suhonen, O. Civitarese, Phys. Rep. 300 (1998) 123.
[2] D. Zinatulina, V. Brudanin, V. Egorov, C. Petitjean, M. Shirchenko, J. Suhonen, I. Yutlandov, Phys. Rev. C 99 (2019) 024327.
[3] H. Ejiri, J. Suhonen, K. Zuber, Phys. Rep. 797 (2019) 1.
[4] H. Ejiri, Phys. Rep. 338 (2000) 265.
[5] H. Ejiri, Prog. Part. Nucl. Phys. 54 (2010) 249.
[6] J. Vergados, H. Ejiri, F. Šimkovic, Rep. Prog. Phys. 75 (2012) 106301.
[7] J. Maalampi, J. Suhonen, Adv. High Energy Phys. 2013 (2013) 505874.
[8] J. Vergados, H. Ejiri, F. Šimkovic, Int. J. Mod. Phys. E 25 (2016) 1630007.
[9] J. Engel, J. Menendez, Rep. Prog. Phys. 60 (2017) 046301.
[10] J. Suhonen, O. Civitarese, J. Phys. G, Nucl. Part. Phys. 39 (2012) 085105.
[11] J. Suhonen, O. Civitarese, J. Phys. G, Nucl. Part. Phys. 39 (2012) 124005.
[12] D.F. Measday, Phys. Rep. 354 (2001) 243.
[13] M. Kortelainen, J. Suhonen, Europhys. Lett. 58 (2002) 666.
[14] M. Kortelainen, J. Suhonen, Nucl. Phys. A 713 (2003) 501.
[15] M. Kortelainen, J. Suhonen, J. Phys. G, Nucl. Part. Phys. 30 (2004) 2003.
[16] E. Kolbe, K. Langanke, P. Vogel, Phys. Rev. C 50 (1994) 2576.
[17] B.L. Johnson, et al., Phys. Rev. C 54 (1996) 2714.
[18] T.P. Gorringe, et al., Phys. Rev. C 60 (1999) 055501.
[19] T. Siiskonen, J. Suhonen, M. Hjorth-Jensen, J. Phys. G, Nucl. Part. Phys. 25 (1999) L55.
[20] T. Siiskonen, M. Hjorth-Jensen, J. Suhonen, Phys. Rev. C 63 (2001) 055501.
[21] N. Auerbach, B.A. Brown, Phys. Rev. C 65 (2002) 024322.
[22] H. Ejiri, Phys. Rep. 38C (1978) 85.
[23] H. Ejiri, Front. Phys. 7 (2019) 30.
[24] F. Šimkovic, G. Pantis, J.D. Vergados, A. Faessler, Phys. Rev. C 60 (1999) 055502.
[25] T.P. Gorringe, et al., Phys. Rev. Lett. 72 (1994) 3472.
[26] G. Jonkmans, et al., Phys. Rev. Lett. 77 (1996) 4512.
[27] D. Gazit, Phys. Lett. B 666 (2008) 472.
[28] L.E. Marcucci, A. Kievsky, S. Rosati, R. Schiavilla, M. Viviani, Phys. Rev. Lett. 108 (2012) 052502.
[29] V. Brudanin, et al., Nucl. Phys. A 587 (1995) 577.
[30] T. Siiskonen, J. Suhonen, V.A. Kuz'min, T.V. Tetereva, Nucl. Phys. A 635 (1998) 446; Erratum: Nucl. Phys. A 651 (1999) 437.
[31] T. Siiskonen, J. Suhonen, M. Hjorth-Jensen, Phys. Rev. C 59 (1999) R1839.
[32] T. Gorringe, H.W. Fearing, Rev. Mod. Phys. 76 (2004) 31.
[33] H. Ejiri, Proc. Int. Conf. Nuclear Structures Studied Using Electron Scattering and Photo Nuclear Reaction, Research Rep. Lab. Nucl. Sci., vol. 5, Tohoku Univ., 1972, p. 261.
[34] H. Ejiri, J. Phys. Soc. Jpn. 74 (2005) 2101.
[35] J. Suhonen, From Nucleons to Nucleus: Concepts of Microscopic Nuclear Theory, Springer, Berlin, 2007.
[36] D.R. Bes, O. Civitarese, J. Suhonen, Phys. Rev. C 86 (2012) 024314.
[37] O. Civitarese, J. Suhonen, Phys. Rev. C 89 (2014) 044319.
[38] L. Jokiniemi, J. Suhonen, Phys. Rev. C 96 (2017) 034308.
[39] H. Ejiri, Proc. CNNP17, J. Phys. Conf. Ser. 1056 (2018) 012019.
[40] I.H. Hashim, H. Ejiri, T. Shima, K. Takahisa, Y. Kuno, A. Sato, K. Ninomiya, N. Kawamura, Y. Miyake, Phys. Rev. C 97 (2018) 014617.
[41] J. Suhonen, Front. Phys. 5 (2017) 55.
[42] H. Ejiri, et al., J. Phys. Soc. Jpn. 82 (2013) 044202.
[43] H. Ejiri, J. Engel, R. Hazama, P. Krasyev, N. Kudomi, R.G.H. Robertson, Phys. Rev. Lett. 85 (2000) 2917.
[44] H. Ejiri, J. Engel, N. Kudomi, Phys. Lett. B 530 (2002) 27.
[45] H. Ejiri, J.I. Fujita, K. Ikeda, Phys. Rev. 176 (1968) 1277.
[46] M. Morita, A. Fujii, Phys. Rev. 118 (1960) 606.
[47] H. Primakoff, Rev. Mod. Phys. 31 (1959) 802.
[48] K.W. Ford, J.G. Wills, Nucl. Phys. 35 (1968) 295.
[49] L. Jokiniemi, J. Suhonen, Phys. Rev. C (2019), submitted for publication.
[50] M.L. Goldberger, S.B. Treiman, Phys. Rev. 111 (1958) 354.
[51] A. Bohr, B.R. Mottelson, Nuclear Structure, vol. I, Benjamin, New York, 1969.
[52] L. Jokiniemi, H. Ejiri, D. Frekers, J. Suhonen, Phys. Rev. C 98 (2018) 024608.
[53] K. Holinde, Phys. Rep. 68 (1981) 121.
[54] J. Suhonen, A. Faessler, T. Taigel, T. Tomoda, Phys. Lett. B 202 (1988) 174.
[55] J. Suhonen, T. Taigel, A. Faessler, Nucl. Phys. A 486 (1988) 91.
[56] J. Suhonen, Nucl. Phys. A 700 (2002) 649.
[57] F. Šimkovic, V. Rodin, A. Faessler, P. Vogel, Phys. Rev. C 87 (2013) 045501.
[58] H. Ejiri, N. Soukouti, J. Suhonen, Phys. Lett. B 729 (2014) 27.
[59] H. Ejiri, J. Suhonen, J. Phys. G, Nucl. Part. Phys. 42 (2015) 055201.
[60] P. Pirinen, J. Suhonen, Phys. Rev. C 91 (2015) 054309.
[61] F.F. Deppisch, J. Suhonen, Phys. Rev. C 94 (2016) 055501.
[62] J. Suhonen, J. Kostensalo, Front. Phys. 7 (2019) 29.
[63] J. Suhonen, Phys. Rev. C 96 (2017) 055501.

Article IV

Muon capture strength functions in intermediate nuclei of $0\nu\beta\beta$ decays
L. Jokiniemi and J. Suhonen,
Phys. Rev. C **100** (2019) 014619.

Muon-capture strength functions in intermediate nuclei of $0\nu\beta\beta$ decays

L. Jokiniemi and J. Suhonen

University of Jyväskylä, Department of Physics, P.O. Box 35 (YFL), FI-40014, Finland

Capture rates of ordinary muon capture (OMC) to the intermediate nuclei of neutrinoless double beta ($0\nu\beta\beta$) decays of current experimental interest are computed. The corresponding OMC (capture-rate) strength functions have been analyzed in terms of multipole decompositions. The computed low-energy OMC-rate distribution to ^{76}As is compared with the available data of Zinatulina *et al.* [Phys. Rev. C **99**, 024327 (2019)]. The present OMC computations are performed using the Morita-Fujii formalism by extending the original formalism beyond the leading order. The participant nuclear wave functions are obtained in extended no-core single-particle model spaces using the spherical version of proton-neutron quasiparticle random-phase approximation (pnQRPA) with two-nucleon interactions based on the Bonn one-boson-exchange G matrix. The Hamiltonian parameters are taken from our earlier work [Jokiniemi *et al.*, Phys. Rev. C **98**, 024608 (2018)], except for $A = 82$ nuclei for which the parameters were determined in this work. Both the OMC and $0\nu\beta\beta$ decays involve momentum exchanges of the order of 100 MeV and thus future measurements of the OMC strength functions for $0\nu\beta\beta$ daughter nuclei help trace the in-medium renormalization of the weak axial couplings with the aim to improve the accuracy of the $0\nu\beta\beta$-decay nuclear matrix elements.

I. INTRODUCTION

Ordinary muon capture (OMC) is a process in which a negative muon implanted in an atomic K orbit is captured by the nucleus of the atom. The large momentum, $q \approx 50$–100 MeV, exchanged in the process leads to final states that are both highly excited and of high multipolarity, quite like in the case of the neutrinoless double beta ($0\nu\beta\beta$) decay. In this way the OMC corresponds to the right branch (β^+ type of transitions) of the $0\nu\beta\beta$ virtual transitions, which makes it a promising tool to study the nuclear matrix elements (NMEs) of the $0\nu\beta\beta$ decay [1,2], as also the neutrino-nucleus interactions in general [3]. In particular, the OMC probes nuclear responses for medium-energy astro-(anti)neutrinos (μ and τ (anti)neutrinos from supernovae) [3,4].

The muon-capture processes concern β^+ type of transitions from a mother nucleus $^A_Z X$ to the states of the residual nucleus $^A_{Z-1} Y$ (see the review [5]). Over years nuclear-structure calculations for the OMC transitions have been performed in a wide range of nuclear masses in order to probe the right-leg (the β^+ side) virtual transitions of $0\nu\beta\beta$ decays and the value of the particle-particle parameter g_{pp} of the proton-neutron quasiparticle random-phase approximation (pnQRPA), as discussed in Refs. [6–8], or the in-medium renormalization of the axial-vector coupling constant g_A [9–14]. The large momentum exchange involved in the OMC activates the induced weak currents, including the weak magnetism and pseudoscalar contributions, quite like in the case of the $0\nu\beta\beta$ decay [15]. The magnitude of the induced pseudoscalar term is largely unknown in finite atomic nuclei [9,10,16–23].

The OMC process we are interested in here can be written as

$$\mu^- + {}^A_Z X(0^+) \rightarrow \nu_\mu + {}^A_{Z-1} Y(J^\pi), \tag{1}$$

where the muon (μ^-) is captured by the 0^+ ground state of the even-even nucleus X of mass number A and atomic number Z leading to the J^π multipole states of its odd-odd isobar Y of atomic number $Z - 1$; here J is the angular momentum and π the parity of the final state. At the same time a muon neutrino ν_μ is emitted. The capture rates to the full set of final states constitutes the OMC strength function.

In this study we compute the OMC strength functions in the intermediate nuclei of $0\nu\beta\beta$ decays up to some 50 MeV using the pnQRPA formalism. The strength function is composed of OMC rates to individual final states of multipolarities J^π, extending the idea of (n,p) charge-exchange reactions, which populate the 1^+ final states, thus producing the Gamow-Teller strength function. The OMC strength function can contain giant resonances analogously to the Gamow-Teller giant resonance [24] or the isovector spin-monopole [25,26] and higher isovector spin-multipole resonances [3,4,27,28]. Here we study the possible existence and structure of these resonances. In our earlier study [29] we computed the strength function for the OMC on ^{100}Mo and compared it with the available data [30]. In this study we extend those calculations by computing the strength functions for the OMCs on ^{76}Se, ^{82}Kr, ^{96}Mo, ^{100}Ru, ^{116}Sn, ^{128}Xe, ^{130}Xe, and ^{136}Ba, leading to states in $0\nu\beta\beta$ intermediate nuclei ^{76}As, ^{82}Br, ^{96}Nb, ^{100}Tc, ^{116}In, ^{128}I, ^{130}I, and ^{136}Cs. In the case of the OMCs on ^{76}Se we compare the low-energy part of our results with the recently available data from Zinatulina *et al.* [2].

Since the nuclei of interest are medium-heavy or heavy open-shell nuclei, the shell-model framework is unfeasible for the calculation of the strength functions due to the excessive computational burden and the very restricted single-particle model spaces allowed by the shell-model treatment. The pnQRPA formalism allows us to study the OMC strength

functions at high energies, since it allows the use of large no-core single-particle bases. Even though the pnQRPA often fails to predict the properties of individual states accurately, it can reproduce the gross features of a distribution of nuclear states quite reasonably. It has been shown that the pnQRPA reproduces the locations of the isovector spin-dipole giant resonances reliably [31], and in our earlier OMC study it was shown that it also reproduces the location of the newly discovered OMC giant resonance correctly in the case of ^{100}Mo [29,30].

Additional OMC experiments and calculations concerning nuclei involved in $0\nu\beta\beta$ decays could help theories better evaluate the NMEs associated with the $0\nu\beta\beta$ decays and also the NMEs related to astro-(anti)neutrino interactions. Furthermore, the effective values of the axial-vector coupling g_A and induced pseudoscalar coupling g_P are involved both in $0\nu\beta\beta$ decays and in the OMC [32].

This paper is organized as follows. In Sec. II we briefly introduce the underlying formalism of the ordinary muon capture. In Sec. III we briefly discuss the determination of the model parameters. There we display and discuss the obtained results for the OMC rates and compare them with the available experimental data. The final conclusions are drawn in Sec. IV.

II. COMPUTATIONAL SCHEME

In this section we introduce briefly our computational scheme. The calculations are based on the pnQRPA theory. In Sec. II A we introduce the theoretical aspects of the OMC rate. The pnQRPA theory is explained briefly in Sec. II B.

A. Formalism of the ordinary muon capture

For the calculation of the OMC rates we use the robust formalism that was developed by Morita and Fujii in Ref. [33].

The muon capture rate to a J^π final state is written as

$$W = 8\left(\frac{Z_{\text{eff}}}{Z}\right)^4 P(\alpha Z m'_\mu)^3 \frac{2J_f+1}{2J_i+1}\left(1 - \frac{q}{m_\mu + AM}\right)q^2, \tag{2}$$

where A indicates the mass number of the initial and final nuclei, J_i (J_f) the angular momentum of the initial (final) nucleus, M the average nucleon rest mass, m_μ the bound muon mass (the rest mass of a muon minus the binding energy of the muon in the K orbital of the μ-mesonic atom), m'_μ the reduced mass of the muon in the parent μ-mesonic atom, Z the atomic number of the initial nucleus, α the fine-structure constant and q the exchanged momentum between the captured muon and the nucleus [33], i.e. the Q value of the OMC.

For heavy nuclei the capture rate has to be corrected for the muonic screening since the atomic orbit of the muon penetrates the nucleus. We follow the Primakoff method [34] correcting the capture rate by the factor $(Z_{\text{eff}}/Z)^4$, where the effective atomic number Z_{eff} is obtained from the work of Ford and Wills [35]. The effective atomic numbers for the nuclei of interest are listed in the following section.

The Q value of the OMC process can be obtained from

$$q = (m_\mu - W_0)\left(1 - \frac{m_\mu - W_0}{2(M_f + m_\mu)}\right), \tag{3}$$

where $W_0 = M_f - M_i + m_e + E_X$ [33]. Here M_f and M_i are the nuclear masses of the final and initial nuclei, m_e the rest mass of an electron and E_X the excitation energy of the final-state nucleus.

The term P in Eq. (2) can be written as

$$P = \frac{1}{2}\sum_{\kappa u}\Bigg| g_V \mathcal{M}[0\,l\,u]S_{0u}(\kappa)\delta_{lu} + g_A \mathcal{M}[1\,l\,u]S_{1u}(\kappa) - \frac{g_V}{M}\mathcal{M}[1\,\bar{l}\,u\,p]S'_{1u}(-\kappa)$$

$$+ \sqrt{3}\frac{g_V q}{2M}\left(\sqrt{\frac{\bar{l}+1}{2\bar{l}+3}}\mathcal{M}[0\,\bar{l}+1\,u+]\delta_{\bar{l}+1,u} + \sqrt{\frac{\bar{l}}{2\bar{l}-1}}\mathcal{M}[0\,\bar{l}-1\,u-]\delta_{\bar{l}-1,u}\right)S'_{1u}(-\kappa)$$

$$+ \sqrt{\frac{3}{2}}\left(\frac{g_V q}{M}\right)(1+\mu_p-\mu_n)(\sqrt{\bar{l}+1}W(1\,1\,u\,\bar{l};1\,\bar{l}+1)\mathcal{M}[1\,\bar{l}+1\,u+]$$

$$+ \sqrt{\bar{l}}W(1\,1\,u\,\bar{l};1\,\bar{l}-1)\mathcal{M}[1\,\bar{l}-1\,u-])S'_{1u}(-\kappa) - \left(\frac{g_A}{M}\right)\mathcal{M}[0\,\bar{l}\,u\,p]S'_{0u}(-\kappa)\delta_{\bar{l}u}$$

$$+ \sqrt{\frac{1}{3}}(g_P - g_A)\left(\frac{q}{2M}\right)\left(\sqrt{\frac{\bar{l}+1}{2\bar{l}+1}}\mathcal{M}[1\,\bar{l}+1\,u+] + \sqrt{\frac{\bar{l}}{2\bar{l}+1}}\mathcal{M}[1\,\bar{l}-1\,u-]\right)S'_{0u}(-\kappa)\delta_{\bar{l}u}\Bigg|^2, \tag{4}$$

where $W(\ldots)$ are the usual Racah coefficients and $\mathcal{M}[k\,w\,u\,(\frac{\pm}{p})]$ nuclear matrix elements of the OMC. The NMEs $\mathcal{M}[k\,w\,u\,(\pm)]$ are dimensionless numbers while the NMEs $\mathcal{M}[k\,w\,u\,p]$ are related to the nucleon momentum and hence are in energy units. The matrix elements are defined in the following manner:

$$\int \Psi_{J_f M_f}\sum_{s=1}^A e^{-\alpha Z m'_\mu r_s}O_s\tau_-^s\Psi_{J_i M_i}d\mathbf{r}_1\ldots d\mathbf{r}_A = \mathcal{M}\left[k\,w\,u\begin{pmatrix}\pm\\p\end{pmatrix}\right](J_i M_i u M_f - M_i | J_f M_f), \tag{5}$$

where $\Psi_{J_f M_f}$ ($\Psi_{J_i M_i}$) is the final (initial) nuclear wave function. The definition for the operator O_s can be found in Table I.

TABLE I. Definition of O_s in Eq. (5) for different nuclear matrix elements (NMEs).

NME	O_s
$\mathcal{M}[0\,w\,u]$	$j_w(qr_s)\mathcal{Y}_{0wu}^{M_f-M_i}(\hat{\mathbf{r}}_s)\delta_{wu}$
$\mathcal{M}[1\,w\,u]$	$j_w(qr_s)\mathcal{Y}_{1wu}^{M_f-M_i}(\hat{\mathbf{r}}_s,\boldsymbol{\sigma}_s)$
$\mathcal{M}[0\,w\,u\pm]$	$[j_w(qr_s)\pm\alpha Z(m'_\mu/p_\nu)j_{w\mp1}(qr_s)]\mathcal{Y}_{0wu}^{M_f-M_i}(\hat{\mathbf{r}}_s)\delta_{wu}$
$\mathcal{M}[1\,w\,u\pm]$	$[j_w(qr_s)\pm\alpha Z(m'_\mu/p_\nu)j_{w\mp1}(qr_s)]\mathcal{Y}_{1wu}^{M_f-M_i}(\hat{\mathbf{r}}_s,\boldsymbol{\sigma}_s)$
$\mathcal{M}[0\,w\,u\,p]$	$ij_w(qr_s)\mathcal{Y}_{0wu}^{M_f-M_i}(\hat{\mathbf{r}}_s)\boldsymbol{\sigma}_s\cdot\mathbf{p}_s\delta_{wu}$
$\mathcal{M}[1\,w\,u\,p]$	$ij_w(qr_s)\mathcal{Y}_{1wu}^{M_f-M_i}(\hat{\mathbf{r}}_s,\mathbf{p}_s)$

The (vector) spherical harmonics $\mathcal{Y}_{kwu}^M$ in the equations of Table I are defined as

$$\mathcal{Y}_{0wu}^M(\hat{\mathbf{r}})\equiv(4\pi)^{-1/2}Y_{w,M}(\hat{\mathbf{r}}),\tag{6}$$

$$\mathcal{Y}_{1wu}^M(\hat{\mathbf{r}},\boldsymbol{\sigma})\equiv\sum_m(1-m\,w\,m+M|u\,M)Y_{w,m+M}(\hat{\mathbf{r}})\sqrt{\frac{3}{4\pi}}\sigma_{-m},\tag{7}$$

where $\boldsymbol{\sigma}$ is the Pauli spin vector, $Y_{w,M}(\hat{\mathbf{r}})$ are the spherical harmonics and $\hat{\mathbf{r}}$ is the unit coordinate vector for the angles in spherical coordinates. The quantity $j_w(qr_s)$ is the spherical Bessel function.

The geometric factors in Eq. (4) are defined as

$$S_{ku}(\kappa)=\begin{cases}\sqrt{2(2j+1)}W\left(\frac{1}{2}\,1\,j\,l\,;\frac{1}{2}\,u\right)\delta_{lw}, & \text{for }k=1\\\sqrt{\frac{2j+1}{2l+1}}\delta_{lw}, & \text{for }k=0\end{cases}\tag{8}$$

and

$$S'_{ku}(-\kappa)=S_\kappa S_{ku}(-\kappa),\tag{9}$$

where S_κ is the sign of κ. Here $\kappa>0$ corresponds to $l=\kappa$ and $j=l-1/2$ and $\kappa<0$ to $l=-\kappa-1$ and $j=l+1/2$. The angular momenta l and $\bar{l}$ correspond to κ and $-\kappa$, respectively.

The coefficients $g_V\equiv g_V(q)$ and $g_A\equiv g_A(q)$ in Eq. (4) are the usual weak vector and axial-vector couplings at finite momentum transfer $q>0$. The conserved vector current (CVC) and partially conserved axial-vector current (PCAC) hypotheses give the values $g_V(0)=1.00$ and $g_A(0)=1.27$ for a free nucleon at zero momentum transfer, and for finite momentum transfer we can use the dipole approximation [3]. For these couplings deviations from the CVC and PCAC values have been recorded at zero momentum transfer [32,36]). For the induced pseudoscalar coupling g_P the Goldberger-Treiman PCAC relation [37] gives $g_P/g_A=7.0$. In this work we choose the slightly quenched values of $g_A(0)=0.8$ and $g_P(0)=7.0$ and keep the CVC value $g_V(0)=1.00$.

The expression (4) can be expanded in powers of the small quantity $1/M^2$. In this way one ends up with the explicit formula $P=P_0+P_1$, where P_0 is the part that one obtains by neglecting all terms of order $1/M^2$ (except for terms containing g_P^2, which is large compared with the other coupling constants) and P_1 contains the rest of the $1/M^2$ terms. For nth forbidden OMC transitions the P_0 term can be written as

$$\begin{aligned}P_0={}&g_V^2[0\,n\,n]^2+\frac{1}{3}g_A^2([1\,n\,n]^2+[1\,n\,n+1]^2+[1\,n+2\,n+1]^2)+\frac{1}{2n+1}g_V^2\frac{q}{M}[0\,n\,n](n[0\,n\,n+]+(n+1)[0\,n\,n-])\\&+\sqrt{\frac{n(n+1)}{3}}\frac{1}{2n+1}g_V^2\frac{q}{M}(1+\mu_p-\mu_n)[0\,n\,n](-[1\,n\,n-]+[1\,n\,n+])-\sqrt{\frac{n(n+1)}{3}}\frac{1}{2n+1}g_Ag_V\frac{q}{M}[1\,n\,n]([0\,n\,n-]\\&-[0\,n\,n+])+\frac{1}{3}g_Ag_V\frac{q}{M}(1+\mu_p-\mu_n)\Bigg\{\frac{1}{2n+1}[1\,n\,n](n[1\,n\,n-]+(n+1)[1\,n\,n+])\\&+\frac{1}{2n+3}(\sqrt{n+2}[1\,n\,n+1]-\sqrt{n+1}[1\,n+2\,n+1])(\sqrt{n+2}[1\,n\,n+1-]-\sqrt{n+1}[1\,n+2\,n+1+])\Bigg\}\\&+\frac{1}{3(2n+3)}g_A(g_A-g_P)\frac{q}{M}(\sqrt{n+1}[1\,n\,n+1]+\sqrt{n+2}[1\,n+2\,n+1])(\sqrt{n+1}[1\,n\,n+1-]\\&+\sqrt{n+2}[1\,n+2\,n+1+])-\frac{2}{\sqrt{3}(2n+1)}g_V^2\frac{1}{M}[0\,n\,n](\sqrt{n}[1\,n-1\,n\,p]+\sqrt{n+1}[1\,n+1\,n\,p])\\&-\frac{2}{3}g_Ag_V\frac{1}{M}\Bigg\{\frac{1}{\sqrt{2n+3}}(-\sqrt{n+2}[1\,n\,n+1]+\sqrt{n+1}[1\,n+2\,n+1])[1\,n+1\,n+1\,p]\\&+\frac{1}{\sqrt{2n+1}}[1\,n\,n](\sqrt{n+1}[1\,n-1\,n\,p]-\sqrt{n}[1\,n+1\,n\,p])\Bigg\}+\frac{2}{\sqrt{3}(2n+3)}g_A^2\frac{1}{M}(\sqrt{n+1}[1\,n\,n+1]\\&+\sqrt{n+2}[1\,n+2\,n+1])[0\,n+1\,n+1\,p]+\frac{1}{12(2n+3)}\left(\frac{g_Pq}{M}\right)^2(\sqrt{n+1}[1\,n\,n+1-]+\sqrt{n+2}[1\,n+2\,n+1+])^2,\end{aligned}\tag{10}$$

which is the explicit form that can be found in Ref. [33]. Here we use the abbreviation $[k\,w\,u\,(\begin{smallmatrix}\pm\\p\end{smallmatrix})]:=\mathcal{M}[k\,w\,u\,(\begin{smallmatrix}\pm\\p\end{smallmatrix})]$.

We introduce in our calculations also the next-to-leading-order term P_1 in the expansion $P=P_0+P_1$, which can be derived from Eq. (4). It is needed for OMC transitions, which are quite weak, usually for captures to high-lying states of high

multipolarity, in order to avoid nonphysical negative OMC rates. The term P_1 for nth forbidden transitions reads as

$$
\begin{aligned}
P_1 &= \left(\frac{g_A}{M}\right)^2 [0\,n+1\,n+1]^2 + g_V^2 \left(\frac{q}{2M}\right)^2 \frac{1}{2n+1}(n[0\,n\,n+]^2 + (n+1)[0\,n\,n-]^2) + \frac{1}{3}\left(\frac{g_V}{M}\right)^2 ([1\,n-1\,n\,p]^2 \\
&+ [1\,n+1\,n\,p]^2 + [1\,n+1\,n+1\,p]^2) + \frac{1}{12}(g_A^2 - 2g_A g_P)\left(\frac{q}{M}\right)^2 \frac{1}{2n+3}(\sqrt{n+2}[1\,n+2\,n+1+] \\
&+ \sqrt{n+1}[1\,n\,n+1-])^2 + \frac{1}{12}\left(\frac{g_V q}{2M}\right)^2 (1+\mu_p-\mu_n)\left\{\frac{1}{2n+1}((n+1)[1\,n\,n+]^2 \right. \\
&+ n[1\,n\,n-]^2) + \frac{1}{2n+3}(\sqrt{n+1}[1\,n+2\,n+1+] - \sqrt{n+2}[1\,n\,n+1-])^2\bigg\} \\
&- \frac{1}{\sqrt{3}(2n+1)}\left(\frac{g_V}{M}\right)^2 q(\sqrt{n}[1\,n-1\,n\,p][0\,n\,n+] + \sqrt{n+1}[1\,n+1\,n\,p][0\,n\,n-]) \\
&+ \frac{1}{3}\left(\frac{g_V}{M}\right)^2 q(1+\mu_p-\mu_n)\left\{\frac{1}{\sqrt{2n+1}}(\sqrt{n}[1\,n+1\,n\,p][1\,n\,n-] - \sqrt{n+1}[1\,n-1\,n\,p][1\,n\,n+]) \right. \\
&+ \frac{1}{\sqrt{2n+3}}(\sqrt{n+2}[1\,n+1\,n+1\,p][1\,n\,n+1-] - \sqrt{n+1}[1\,n+1\,n+1\,p][1\,n+2\,n+1+])\bigg\} \\
&+ \frac{1}{2\sqrt{3}}\left(\frac{g_V q}{M}\right)^2 (1+\mu_p-\mu_n)\frac{\sqrt{n(n+1)}}{2n+1}([0\,n\,n+][1\,n\,n+] - [0\,n\,n-][1\,n\,n-]) \\
&+ \frac{1}{\sqrt{3}}g_A(g_A-g_P)\frac{q}{M^2}\frac{1}{\sqrt{2n+3}}[0\,n+1\,n+1\,p](\sqrt{n+2}[1\,n+2\,n+1+] + \sqrt{n+1}[1\,n\,n+1-]). \quad (11)
\end{aligned}
$$

B. pnQRPA and the Hamiltonian parameters

In this section we introduce the spherical version of the pnQRPA and discuss briefly the determination of the parameter values of its Hamiltonian. The wave functions and excitation energies for the complete set of J^π excitations in the odd-odd daughter nuclei are obtained by performing a pnQRPA diagonalization in the unperturbed basis of quasiproton-quasineutron pairs coupled to J^π. The resulting pnQRPA states in odd-odd nuclei are then of the form

$$
\left|J_k^\pi M\right\rangle = \sum_{pn}\left[X_{pn}^{J_k^\pi} A_{pn}^\dagger(JM) - Y_{pn}^{J_k^\pi}\tilde{A}_{pn}(JM)\right]|\text{pnQRPA}\rangle, \quad (12)
$$

where k numbers the states of spin-parity J^π, the amplitudes X and Y are the forward- and backward-going pnQRPA amplitudes, $A^\dagger$ and $\tilde{A}$ the quasiproton-quasineutron creation and annihilation operators, M the z projection of J and $|\text{pnQRPA}\rangle$ the pnQRPA vacuum. The transition density corresponding to a transition from a 0_{gs}^+ initial state to a J_k^π final state can then be written as

$$
\left(J_k^\pi||[c_p^\dagger\tilde{c}_n]_J||0_{gs}^+\right) = \sqrt{2J+1}\left[u_p v_n X_{pn}^{J_k^\pi} + v_p u_n Y_{pn}^{J_k^\pi}\right]. \quad (13)
$$

The formalism is explained in detail in Refs. [24,38].

The X and Y amplitudes in Eq. (12) are calculated by diagonalizing the pnQRPA matrix separately for each multipole J^π. We follow the partial isospin-restoration scheme introduced in Ref. [39], in which the isoscalar ($T=0$) and isovector ($T=1$) parts of the particle-particle G-matrix elements are multiplied by factors $g_{pp}^{T=0}$ and $g_{pp}^{T=1}$, respectively, for all the multipoles. The isovector parameter $g_{pp}^{T=1}$ is adjusted such that the Fermi part of the corresponding two-neutrino double

β ($2\nu\beta\beta$) NME vanishes. The isoscalar parameter $g_{pp}^{T=0}$ is then independently varied to reproduce the $2\nu\beta\beta$-decay half-life. In addition, the particle-hole part was scaled by a common factor g_{ph}, fixed by fitting the centroid of the Gamow-Teller giant resonance (GTGR) in the 1^+ channel of the calculations in the usual way. These renormalization factors are adopted from Ref. [31] except for the case $A=82$, which was not included in there. For $A=82$ the corresponding parameter values are $g_{pp}^{T=0}=0.82$, $g_{pp}^{T=1}=0.95$, and $g_{ph}=0.997$.

We adopt for each even-even nucleus involved in the computations the single-particle bases used in the isovector spin-multipole calculations of Refs. [28,31], i.e., no-core bases with all the orbitals from the $N=0$ oscillator major shell up to at least two oscillator major shells above the respective Fermi surfaces for both protons and neutrons. The single-particle energies were obtained by solving the radial Schrödinger equation for a Coulomb-corrected Woods-Saxon (WS) potential, optimized for nuclei close to the β-stability line [40]. This choice is justified since the $\beta\beta$-decaying nuclei lie always rather close to the bottom of the valley of β stability. Both the bound and quasibound single-particle states are active in the calculations. The single-particle energies close to the proton and neutron Fermi surfaces were slightly modified in order to better reproduce the low-lying spectra of the neighboring odd-mass nuclei at the BCS quasiparticle level.

The quasiparticle spectra for protons and neutrons, needed in the pnQRPA diagonalization, are obtained by solving the BCS equations for protons and neutrons, separately. In our calculations the two-body interaction is derived from the Bonn-A one-boson-exchange potential introduced in Ref. [41]. The calculated BCS pairing gaps are fitted (see

TABLE II. pnQRPA-computed and Primakoff-formula based total rates for OMC on different parent nuclei (Parent), as well as the effective Z values. Axial couplings $g_A(0) = 0.8$ and $g_P(0) = 7.0$ were adopted in the calculations.

Parent	Z_{eff}	$W_{\text{pnQRPA}}(10^6/\text{s})$	$W_{\text{Pr.}}(10^6/\text{s})$
^{76}Se	24.47 (for $Z = 37$)	16.4	8.3
^{82}Kr	24.47 (for $Z = 37$)	16.5	7.5
^{96}Mo	26.37	20.4	10.0
^{100}Ru	26.37 (for $Z = 42$)	16.7	10.3
^{116}Sn	28.64	15.7	12.7
^{128}Xe	29.99 (for $Z = 56$)	21.2	13.3
^{130}Xe	29.99 (for $Z = 56$)	23.6	11.9
^{136}Ba	29.99	21.1	11.1

Refs. [24,38,42,43]) to the phenomenological proton and neutron pairing gaps in a way described in detail in Ref. [28]. The values of the resulting pairing scaling factors are listed in Refs. [28,31].

III. RESULTS AND DISCUSSION

In this section we present and discuss the results of our studies. The style of presentation of the results serves the purpose of easy comparison with future experimental data.

A. OMC strength functions in intermediate nuclei of $0\nu\beta\beta$ decays

An approximation for the total OMC rate on nucleus $^A_Z X$ can be computed using the Primakoff formula [34]

$$W_{\text{Pr.}}(A, Z) = Z_{\text{eff}}^4 X_1 \left[1 - X_2 \left(\frac{A - Z}{2A} \right) \right], \qquad (14)$$
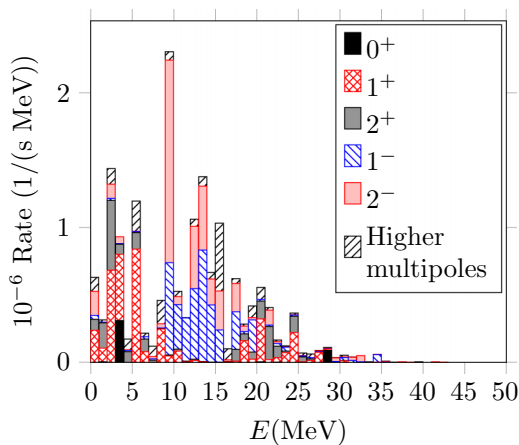
FIG. 1. OMC on ^{76}Se: muon-capture-rate distribution (OMC strength function) in ^{76}As. Transition strengths to $J_f^\pi = 0^+, 1^\pm, 2^\pm$ states and to states of higher multipolarity are separated. The y axis gives the capture rate in millions of captures per second and per MeV. The horizontal axis shows the excitation energy in the ^{76}As nucleus. Here a 1.0 MeV binning in energy is used and coupling strengths $g_A(0) = 0.8$ and $g_P(0) = 7.0$ were adopted in the calculations.
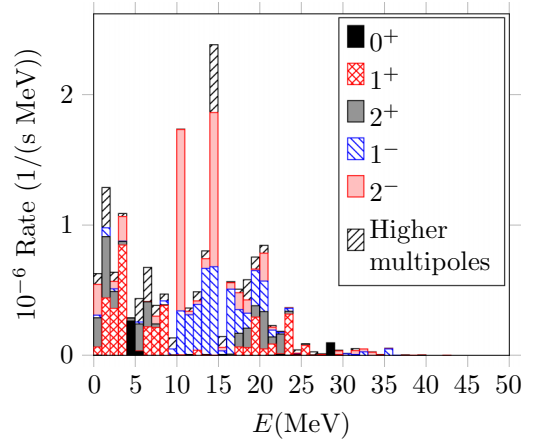
FIG. 2. The same as in Fig. 1 but for captures on ^{82}Kr to states in ^{82}Br.

where A, Z, and Z_{eff} are the mass number, atomic number, and effective atomic number of the nucleus, X_1 the reduced muon-capture rate for OMC on hydrogen, and X_2 a parameter that takes into account the Pauli exclusion principle. We adopt the typical values

$$X_1 = 170 \ 1/\text{s} \quad \text{and} \quad X_2 = 3.125.$$

for the X factors.

In Table II we list for each nucleus of interest the effective Z values Z_{eff} obtained from the work of Ford and Wills [35], and the total muon capture rates obtained from the Primakoff formula (14) as well as the total capture rate of Eq. (2) obtained from the pnQRPA calculations. The pnQRPA results include transition rates to all possible multipole states summed over an energy region of 0–55 MeV. The moderately quenched parameter values $g_A(0) = 0.8$ and $g_P(0) = 7.0$ were adopted in the calculations.

We notice that using the parameter values $g_A(0) = 0.8$ and $g_P(0) = 7.0$ the pnQRPA formalism gives larger capture rates than the corresponding Primakoff estimates. However, it was noticed in Ref. [29] that decreasing the value of g_A or increasing the value of g_P decreases the total capture rate. In terms of

FIG. 3. The same as in Fig. 1 but for captures on ^{96}Mo to states in ^{96}Nb.
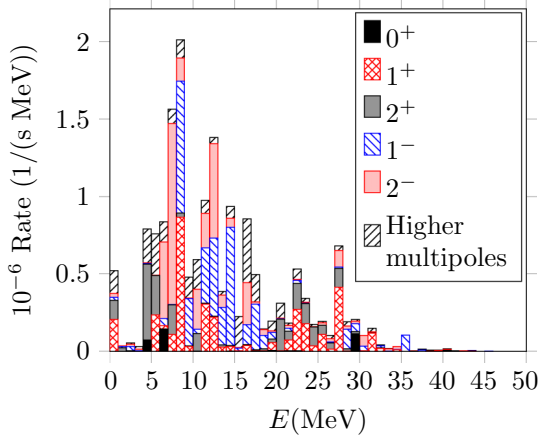
FIG. 4. The same as in Fig. 1 but for captures on ^{100}Ru to states in ^{100}Tc.

FIG. 6. The same as in Fig. 1 but for captures on ^{128}Xe to states in ^{128}I.

the axial coupling, the Primakoff rates can be reproduced by a strongly quenched effective value of $g_A(0) \approx 0.5$.

In Figs. 1–8 we present the OMC strength functions for the captures on ^{76}Se, ^{82}Kr, ^{96}Mo, ^{100}Ru, ^{116}Sn, ^{128}Xe, ^{130}Xe, and ^{136}Ba obtained from Eq. (2) with the parameter values $g_A(0) = 0.8$ and $g_P(0) = 7.0$. We separately indicate the OMC rates to $J^\pi = 0^+, 1^\pm, 2^\pm$ states of the daughter nuclei (the intermediate nuclei of $0\nu\beta\beta$ decays) and also give the total capture rate, which includes transitions to states of all possible multipolarities. The results are presented using a 1.0 MeV binning in energy. One can see that transitions to $J^\pi = 0^+, 1^\pm, 2^\pm$ states form the majority of the total capture rates, transitions to states of higher multipolarity forming only some 10–20% of the total capture rate.

In Tables VI–XIII (see the Appendix) we present the relative capture rates $W(J^\pi)/W_{\text{tot}}$ (%) to states of different multipolarities corresponding to Figs. 1–8. Here the numbers of the bins refer to the different energy bins in the figures: Bin No. 1 refers to the 0–1 MeV energy bin and so on. These tables are handy when one wants to compare the OMC distributions obtained in future muon experiments with the presently calculated ones.

In Ref. [29] the first theoretical evidence of an OMC giant resonance was produced for the OMC on ^{100}Mo. In that work it was seen that the computed location of the resonance agreed well with the experimentally determined one. Also from Figs. 1–8 one can observe structures of the OMC strength functions, which would correspond to an OMC giant resonance. In Figs. 1 (OMC on ^{76}Se) and 3 (OMC on ^{96}Mo) the centroid of a resonancelike structure can be observed at around 12 MeV, in Fig. 2 (OMC on ^{82}Kr) the resonance is around 14 MeV, in Fig. 4 (OMC on ^{100}Ru) the resonance is around 10 MeV, and in Fig. 6 (OMC on ^{128}Xe) a broad resonancelike structure is found around 14 MeV. For the OMC on the heaviest two nuclei, ^{130}Xe and ^{136}Ba, no clear resonance can be identified, but rather a wide flat region of strong captures to states below about 18 MeV. Also for the OMC on ^{116}Sn, Fig. 5, no clear giant resonance can be identified.

The resonancelike structures are dominated by the $1\hbar\omega$ excitations of multipolarities $J^\pi = 1^-, 2^-$. For the OMC on ^{76}Se and ^{82}Kr there is a visible low-energy satellite of the OMC resonance consisting mainly of $0\hbar\omega$ excitations of multipolarities $J^\pi = 1^+, 2^+$. In general, these excitations
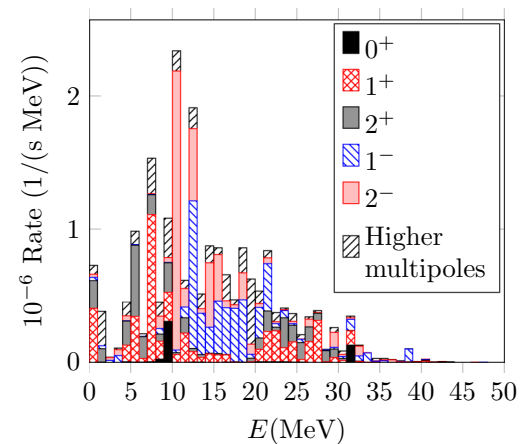

FIG. 5. The same as in Fig. 1 but for captures on ^{116}Sn to states in ^{116}In.
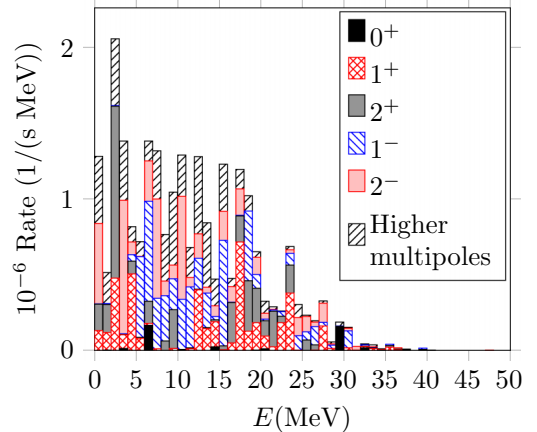
FIG. 7. The same as in Fig. 1 but for captures on ^{130}Xe to states in ^{130}I.
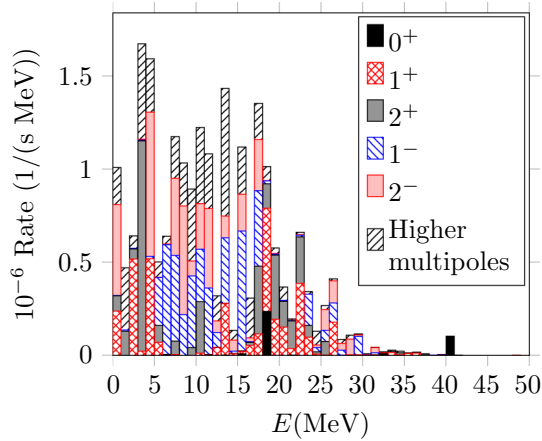
FIG. 8. The same as in Fig. 1 but for captures on ^{136}Ba to states in ^{136}Cs.

play a major role at low energies for all cases. At high energies, 15–28 MeV, the $2\hbar\omega$ excitations of multipolarities $J^\pi = 1^+, 2^+$ dominate forming even a high-energy satellite resonance in the cases of OMC on ^{100}Ru, ^{116}Sn, and ^{128}Xe. At energies of about 28–32 MeV one can see traces of $2\hbar\omega$ $J^\pi = 0^+$ excitations. For the heaviest nuclei these 0^+ contributions can reach up to 40 MeV of excitation. The high-energy tail of the $J^\pi = 1^-, 2^-$ excitations, beyond 24–28 MeV, stems from $3\hbar\omega$ excitations.

B. OMC rates in ^{76}As compared with available data

There is a possibility to compare our pnQRPA-computed rates with data for the OMC on ^{76}Se. In Ref. [2] the OMC

rates to states of low excitation in ^{76}As were measured. In the present calculations we use the coupling strengths $g_A(0) = 0.8$ and $g_P(0) = 7.0$.

The experimental OMC rates to different low-energy states of ^{76}As, deduced from the results of Ref. [2], are presented in Table III. The table has been divided in two, and the excitation energies of the states are listed i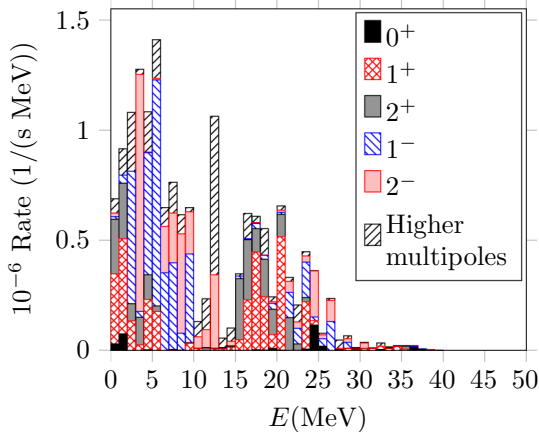n the first columns, the J^π assignments in the second columns and the capture rates in the third columns. The corresponding pnQRPA results are presented in Table IV.

Let us first compare Tables III and IV. Direct comparison of the tables is hampered by the unknown spin-parities in the experimental energy spectrum. Overall, similar spin-parity assignments J^π and OMC rates of the same order of magnitude are recorded by comparing the numbers of the tables. However, there are much fewer states in the low-energy spectrum computed with the pnQRPA. This is a typical feature of the pnQRPA calculations: The pnQRPA calculations predict less states in odd-odd nuclei than is detected experimentally. However, the corresponding transition strength (in this case OMC rates) is there, but concentrated in few strong states. Usually the centroid of the experimental strength is well reproduced but the fine structure is not due to the too small a configuration space of the pnQRPA approach. In many cases, in low momentum-exchange processes, the pnQRPA strength is concentrated in the lowest collective states, usually of the multipolarities $J^\pi = 1^+, 2^-$ (Gamow-Teller and spin-dipole strength). For high momentum-exchange processes, such as the $0\nu\beta\beta$ decay and the OMC, the strength is gathered by the lowest states with multipolarities $J^\pi = 1^+, 2^\pm, 3^\pm$. The realistic nature of the summed OMC strength of pnQRPA is visible in the obtained total capture rate 6.7×10^5 1/s below 1.1 MeV, which is quite close to the corresponding

TABLE III. OMC on ^{76}Se: measured OMC rates (column 3) to low-energy states of ^{76}As as deduced from Ref. [2]. The table has been cut in two and appears as left and right halves. The excitation energies are displayed in columns 1 and the J^π values in column 2. The OMC rate to the ground state of ^{76}As cannot be measured.

E (MeV)	J^π	Rate (1/s)	E (MeV)	J^π	Rate (1/s)
0.0000	2^-	g.s.	0.6401	$(1^-, 2^-)$	11 520
0.1203	1^+	20 480	0.6691	$(1^+, 2^+)$	40 960
0.1222	$(1)^-$	13 440	0.6811	$(1^-, 4)$	21 120
0.165	$(3)^-$	34 560	0.7344	$(\leqslant 4)^-$	5 120
0.2035	$(0,1)^+$	5 120	0.7518	$(0^-, 1, 2)$	23 680
0.2803	$(1,2)^+$	7 040	0.7566	$(0^+, 3^+)$	16 640
0.2926	$(2,3,4)^-$	3 200	0.7744	$(1^+, 3^+)$	14 720
0.3285	$(3,4)^-$	5 760	0.7936	$(1,2,3)^+$	12 800
0.3524	$(3)^-$	3 200	0.8024	$(1^-, 2^-, 3^+)$	10 880
0.4018	$(1,2)^+$	26 240	0.8633	1^+	17 280
0.4368	$(1,2,3)^-$	17 920	0.8932	$(1^-, 2^-, 3^+)$	14 720
0.4472	$(1,2)^+$	29 440	0.9247	$(\leqslant 3)^-$	15 360
0.471	$(2)^-$	3 200	0.9397	$(1,2,3)$	21 120
0.4996	$(1^+, 2^-)$	63 360	0.9584	$\leqslant 3$	8 320
0.5052	$(2,3)^+$	16 000	0.9855	$(1,2,3)^+$	13 440
0.5176	$(1,2^+)$	15 360	1.0262	$(1^+, 3^+)$	61 440
0.544	$(2,3)^-$	24 960	1.0342	$(1,2,3)^+$	8 320
0.61	$(1,2,3^-)$	43 520	1.0645	1^+	14 720
				Tot.	664 960

TABLE IV. OMC on ^{76}Se: pnQRPA-computed OMC rates (column 3) to low-energy states of ^{76}As. Coupling strengths $g_A(0) = 0.8$ and $g_P(0) = 7.0$ were adopted in the calculations.

E (MeV)	J^π	Rate (1/s)
0.0	2$^-$	177 802
0.044	1$^+$	236 595
0.122	1$^-$	28 991
0.165	3$^-$	23 568
0.204	0$^+$	414.27
0.211	4$^-$	19 911
0.265	2$^+$	83 516
0.505	3$^+$	55 355
0.854	3$^-$	9 647
1.0	4$^+$	2 797
1.004	2$^+$	30 500
1.007	4$^-$	3 986
1.075	3$^-$	1 621
	Tot.	670 716

experimental value 6.6×10^5 1/s despite the differences in the rates to the individual states.

The uncertain spin-parity assignments of Table III allow for speculations about the division of the OMC strength between different multipole states. In fact, one can play with the spin-parity assignments of Table III within the limits allowed by the uncertainties. In this way one could try to produce an educated guess of the most probable spin-parity assignments and then sum up the OMC strength multipole by multipole. In this way one creates a kind of most probable experimental OMC strength distribution below about 1.1 MeV. This probable distribution can then be compared with the multipole-by-multipole-summed OMC strength of Table IV for pnQRPA. These two distributions have been gathered into Table V. From the table one immediately sees that

TABLE V. Comparison of the most probable experimental multipole-by-multipole OMC strength distribution obtained from Table III with the corresponding pnQRPA-computed distribution deduced from Table IV. The OMC strength to the 2$^-$ ground state has not been measured and this is indicated by + g.s. in the corresponding row.

J^π	OMC rate (1/s)	
	Expt.	pnQRPA
0$^+$	5120	414
1$^+$	218 240	236 595
1$^-$	31 360	28 991
2$^+$	120 960	114 016
2$^-$	145 920 + g.s.	177 802
3$^+$	60 160	55 355
3$^-$	53 120	34 836
4$^+$	–	2797
4$^-$	30 080	23 897

the correspondence between the experimental and pnQRPA-computed OMC strength distributions is strikingly good. Only the pnQRPA-computed rate to the 0$^+$ states is an order of magnitude smaller than the corresponding experimental rate. The deviation might be due to the small deformation of ^{76}Se [44]. It has to be borne in mind that the OMC strength to the 2$^-$ ground state has not been measured since the corresponding γ rays could not be extracted. This experimental deficit in OMC has been indicated by + g.s. in the corresponding row of Table V. Future spin-assignment sensitive measurements will shed light on the reliability of the presently introduced most probable experimental OMC strength distribution.

IV. CONCLUSIONS

In this work we have calculated the rates of ordinary muon capture on the 0$^+$ ground states of the daughter nuclei of eight $0\nu\beta\beta$-decaying parent nuclei in the Morita-Fujii formalism of the OMC. The calculations have been performed using the proton-neutron quasiparticle RPA with realistic two-body interactions and slightly modified no-core Woods-Saxon bases. The computed OMC strength functions are presented for the OMC on ^{76}Se, ^{82}Kr, ^{96}Mo, ^{100}Ru, ^{116}Sn, ^{128}Xe, ^{130}Xe, and ^{136}Ba. The computed total OMC capture rates are compared with the corresponding Primakoff estimates. The computed total rates are somewhat larger than the Primakoff values, which suggests a rather strongly quenched effective value of $g_A(0) \approx 0.5$.

The pnQRPA-computed rates of OMC on ^{76}Se to the states below 1.1 MeV in ^{76}As were compared with the available data of Ref. [2]. It was found that the correspondence of the experimental and pnQRPA-computed strength, decomposed in multipoles, is quite good. This, in turn, points to reliability of the present calculations of the OMC strength functions.

Further measurements and computations of the OMC strength functions for final nuclei of double β decays could enable a systematic study of the sensitivity of the OMC strength function to the effective values of the weak axial couplings. This could help improve the accuracy of calculations of the nuclear matrix elements of the neutrinoless double β decay. On the other hand, the OMC provides a promising opportunity for studying the (anti)neutrino responses for medium-energy astroneutrino interactions. Further experimental studies are in progress at RCNP Osaka for nuclei of interest in studies of nuclear double β decay and astroneutrino interactions.

APPENDIX: TABLES FOR RELATIVE OMC RATES

Our pnQRPA-computed relative OMC rates for $g_A(0) = 0.8$ and $g_P(0) = 7.0$ are summarized in Tables VI–XIII. Here the quantities $W(J^\pi)/W_{\text{tot}}$ are given in per cents for multipoles $J^\pi = 0^+, 1^\pm, 2^\pm$ separately, and the rest as a lump sum. The energy bins are numbered such that bin No. n corresponds to the energy interval $[n-1, n]$ MeV. These tables enable easy comparison with the strength functions extracted from future OMC experiments.

TABLE VI. Relative pnQRPA-computed rates to states in ^{76}As for the OMC on ^{76}Se. The rates are given in 1 MeV energy bins as percents of the total OMC rate. There are three separate tables side by side listing the bin numbers (columns 1) and the different multipolarities (columns 2–7). The values $g_A(0) = 0.8$ and $g_P(0) = 7.0$ for the weak couplings were adopted in the calculations.

Bin No.	\multicolumn{6}{c	}{$W(J^\pi)/W_{tot}(\%)$}	Bin No.	\multicolumn{6}{c	}{$W(J^\pi)/W_{tot}(\%)$}	Bin No.	\multicolumn{6}{c}{$W(J^\pi)/W_{tot}(\%)$}
	0^+	1^+	2^+	1^-	2^-	Others		0^+	1^+	2^+	1^-	2^-	Others		0^+	1^+	2^+	1^-	2^-	Others
1	0.00	1.44	0.51	0.18	1.08	0.63	16	0.00	0.00	0.01	1.45	1.77	3.05	31	0.00	0.08	0.00	0.14	0.02	0.08
2	0.03	0.61	1.15	0.03	0.00	0.10	17	0.00	0.03	0.01	0.00	0.07	0.51	32	0.00	0.00	0.00	0.08	0.15	0.01
3	0.00	4.17	3.14	0.10	0.65	0.69	18	0.00	0.05	0.53	1.70	1.28	0.22	33	0.00	0.00	0.00	0.02	0.28	0.00
4	1.89	2.99	0.45	0.04	0.30	0.01	19	0.00	0.98	0.31	0.10	0.26	0.08	34	0.00	0.00	0.00	0.00	0.00	0.03
5	0.00	0.00	0.49	0.06	0.03	0.49	20	0.00	0.15	0.31	1.45	0.10	0.53	35	0.00	0.01	0.00	0.34	0.01	0.00
6	0.00	5.11	0.75	0.04	0.01	1.37	21	0.03	1.93	0.81	0.07	0.01	0.53	36	0.00	0.00	0.00	0.01	0.03	0.02
7	0.00	0.49	0.57	0.09	0.00	0.16	22	0.00	0.13	1.50	0.06	0.66	0.12	37	0.00	0.00	0.00	0.00	0.00	0.01
8	0.00	0.00	0.10	0.07	0.10	0.47	23	0.02	0.20	0.52	0.11	0.10	0.06	38	0.00	0.01	0.00	0.00	0.01	0.00
9	0.00	1.50	0.01	0.04	0.19	1.06	24	0.00	0.44	0.07	0.18	0.01	0.05	39	0.00	0.01	0.00	0.00	0.00	0.00
10	0.00	0.29	0.04	4.17	9.16	0.37	25	0.00	1.34	0.74	0.05	0.02	0.07	40	0.01	0.00	0.01	0.00	0.00	0.00
11	0.00	0.51	0.09	2.01	0.36	0.24	26	0.00	0.02	0.23	0.03	0.02	0.12	41	0.00	0.00	0.00	0.00	0.00	0.00
12	0.00	0.02	0.04	1.94	0.01	0.00	27	0.00	0.09	0.06	0.06	0.00	0.16	42	0.00	0.02	0.00	0.00	0.00	0.00
13	0.00	0.08	0.06	3.18	2.82	0.31	28	0.00	0.44	0.01	0.02	0.05	0.02	43	0.00	0.01	0.00	0.00	0.00	0.00
14	0.00	0.02	0.03	5.02	2.89	0.43	29	0.54	0.07	0.00	0.00	0.01	0.05							
15	0.00	0.00	0.01	2.59	1.17	0.29	30	0.00	0.00	0.00	0.03	0.16	0.01							

TABLE VII. The same as in Table VI but for OMC on ^{82}Kr to states in ^{82}Br.

Bin No.	\multicolumn{6}{c	}{$W(J^\pi)/W_{tot}(\%)$}	Bin No.	\multicolumn{6}{c	}{$W(J^\pi)/W_{tot}(\%)$}	Bin No.	\multicolumn{6}{c}{$W(J^\pi)/W_{tot}(\%)$}
	0^+	1^+	2^+	1^-	2^-	Others		0^+	1^+	2^+	1^-	2^-	Others		0^+	1^+	2^+	1^-	2^-	Others
1	0.01	0.38	1.36	0.12	1.43	0.50	16	0.00	0.00	0.05	0.17	0.16	0.49	31	0.00	0.00	0.00	0.07	0.01	0.01
2	0.00	2.67	2.85	0.40	0.00	1.87	17	0.00	0.00	0.05	3.02	0.30	0.05	32	0.00	0.00	0.00	0.04	0.18	0.09
3	0.00	2.19	0.78	0.12	0.35	0.42	18	0.00	0.39	0.63	1.10	0.78	0.17	33	0.00	0.00	0.00	0.16	0.14	0.00
4	0.00	5.13	0.17	0.01	1.16	0.13	19	0.00	0.37	0.89	0.70	0.61	0.94	34	0.00	0.00	0.00	0.00	0.14	0.03
5	1.60	0.00	0.13	0.00	0.01	0.01	20	0.00	1.78	0.53	1.62	0.09	0.55	35	0.00	0.00	0.00	0.00	0.03	0.01
6	0.19	0.02	1.26	0.08	0.00	1.09	21	0.00	0.29	1.75	1.41	1.31	0.35	36	0.00	0.00	0.00	0.30	0.02	0.01
7	0.00	1.32	1.17	0.00	0.02	1.58	22	0.01	0.52	0.34	0.31	0.15	0.07	37	0.00	0.00	0.00	0.01	0.00	0.00
8	0.00	1.29	0.17	0.00	0.37	0.49	23	0.04	0.04	0.91	0.08	0.00	0.04	38	0.00	0.01	0.02	0.00	0.00	0.00
9	0.00	2.32	0.03	0.18	0.00	0.31	24	0.02	1.91	0.13	0.13	0.01	0.02	39	0.00	0.01	0.00	0.00	0.00	0.00
10	0.00	0.01	0.01	0.28	0.00	0.52	25	0.00	0.01	0.04	0.01	0.05	0.14	40	0.01	0.01	0.00	0.00	0.00	0.00
11	0.00	0.03	0.00	2.04	8.45	0.01	26	0.00	0.46	0.06	0.00	0.00	0.01	41	0.00	0.00	0.00	0.00	0.00	0.00
12	0.00	0.00	0.04	1.85	0.17	0.15	27	0.00	0.02	0.01	0.00	0.00	0.14	42	0.00	0.00	0.00	0.00	0.00	0.00
13	0.00	0.24	0.00	2.13	0.16	0.43	28	0.00	0.04	0.00	0.00	0.00	0.02	43	0.00	0.01	0.00	0.00	0.00	0.00
14	0.00	0.01	0.02	4.01	0.45	0.36	29	0.51	0.00	0.02	0.01	0.00	0.05							
15	0.00	0.01	0.00	4.11	7.18	3.15	30	0.00	0.04	0.00	0.01	0.17	0.03							

TABLE VIII. The same as in Table VI but for OMC on ^{96}Mo to states in ^{96}Nb.

Bin No.	$W(J^\pi)/W_{tot}(\%)$						Bin No.	$W(J^\pi)/W_{tot}(\%)$						Bin No.	$W(J^\pi)/W_{tot}(\%)$					
	0^+	1^+	2^+	1^-	2^-	Others		0^+	1^+	2^+	1^-	2^-	Others		0^+	1^+	2^+	1^-	2^-	Others
1	0.00	1.99	1.02	0.12	0.12	0.33	17	0.01	0.27	0.01	1.72	0.25	0.96	33	0.00	0.04	0.00	0.19	0.36	0.04
2	0.01	0.00	0.49	0.11	0.00	1.27	18	0.00	0.01	0.01	1.97	0.13	0.17	34	0.00	0.01	0.00	0.33	0.01	0.00
3	0.00	0.00	0.00	0.08	0.10	0.02	19	0.00	0.00	0.01	2.29	1.00	0.92	35	0.00	0.01	0.00	0.03	0.01	0.09
4	0.00	0.00	0.00	0.25	0.22	0.06	20	0.00	0.03	0.13	0.14	0.38	2.39	36	0.00	0.00	0.00	0.05	0.04	0.05
5	0.02	0.62	0.89	0.01	0.17	0.51	21	0.03	0.45	0.42	1.12	0.15	0.45	37	0.00	0.00	0.00	0.00	0.10	0.00
6	0.01	1.67	2.62	0.03	0.00	0.49	22	0.02	1.12	0.76	1.73	0.22	0.26	38	0.00	0.02	0.01	0.01	0.00	0.02
7	0.01	0.14	0.81	0.00	0.01	0.10	23	0.02	1.14	0.13	0.13	0.07	0.34	39	0.00	0.01	0.01	0.47	0.00	0.02
8	0.03	5.41	0.73	0.00	0.03	1.30	24	0.02	0.52	1.10	0.26	0.04	0.06	40	0.00	0.02	0.01	0.00	0.00	0.00
9	0.12	0.66	0.26	0.21	0.45	0.51	25	0.01	0.74	0.61	0.06	0.09	0.29	41	0.00	0.05	0.03	0.03	0.00	0.00
10	1.50	1.07	1.09	0.00	0.18	1.45	26	0.02	0.09	0.62	0.12	0.01	0.16	42	0.00	0.01	0.01	0.00	0.00	0.00
11	0.00	0.28	0.08	0.09	10.27	0.74	27	0.00	0.77	0.54	0.01	0.28	0.08	43	0.03	0.00	0.00	0.00	0.00	0.00
12	0.00	1.08	0.56	0.39	0.68	0.30	28	0.00	1.55	0.26	0.01	0.02	0.07	44	0.00	0.00	0.02	0.00	0.00	0.00
13	0.01	0.38	0.12	5.44	2.66	0.77	29	0.00	0.02	0.41	0.02	0.00	0.02	45	0.00	0.00	0.00	0.00	0.00	0.00
14	0.00	0.17	0.12	1.52	0.17	0.54	30	0.00	0.18	0.31	0.06	0.55	0.18	46	0.00	0.00	0.00	0.00	0.00	0.00
15	0.00	0.32	0.01	0.97	2.36	0.63	31	0.00	0.07	0.07	0.06	0.09	0.12	47	0.00	0.00	0.00	0.00	0.00	0.00
16	0.00	0.27	0.05	1.93	1.71	0.25	32	0.63	0.53	0.01	0.40	0.06	0.07	48	0.00	0.00	0.00	0.01	0.00	0.00

TABLE IX. The same as in Table VI but for OMC on ^{100}Ru to states in ^{100}Tc.

Bin No.	$W(J^\pi)/W_{tot}(\%)$						Bin No.	$W(J^\pi)/W_{tot}(\%)$						Bin No.	$W(J^\pi)/W_{tot}(\%)$					
	0^+	1^+	2^+	1^-	2^-	Others		0^+	1^+	2^+	1^-	2^-	Others		0^+	1^+	2^+	1^-	2^-	Others
1	0.00	1.23	0.73	0.11	0.16	0.88	16	0.00	0.02	0.00	0.11	0.03	1.19	31	0.00	0.02	0.01	0.18	0.41	0.01
2	0.00	0.00	0.13	0.05	0.02	0.00	17	0.00	0.23	0.03	0.78	1.62	2.47	32	0.00	0.71	0.00	0.00	0.04	0.13
3	0.03	0.00	0.00	0.16	0.09	0.05	18	0.01	0.02	0.03	1.77	0.08	1.07	33	0.00	0.12	0.01	0.08	0.00	0.03
4	0.00	0.00	0.00	0.02	0.06	0.10	19	0.01	0.01	0.08	0.51	0.23	0.03	34	0.00	0.00	0.00	0.00	0.09	0.01
5	0.44	0.00	2.93	0.02	0.02	1.31	20	0.03	0.31	0.13	0.25	0.06	0.39	35	0.00	0.07	0.00	0.00	0.12	0.00
6	0.00	1.40	1.53	0.00	0.01	1.60	21	0.01	0.02	1.22	0.01	0.03	0.57	36	0.00	0.00	0.00	0.62	0.00	0.01
7	0.87	0.13	0.00	0.28	2.95	0.79	22	0.03	0.41	0.34	0.11	0.11	0.09	37	0.01	0.00	0.00	0.01	0.00	0.00
8	0.00	0.65	1.15	0.01	6.99	0.56	23	0.02	1.60	1.01	0.12	0.04	0.40	38	0.00	0.00	0.00	0.05	0.00	0.04
9	0.00	5.19	0.16	5.10	0.89	0.70	24	0.00	1.07	0.79	0.00	0.05	0.14	39	0.00	0.02	0.02	0.00	0.00	0.02
10	0.00	0.19	0.02	1.83	0.02	0.81	25	0.00	0.21	0.73	0.01	0.01	0.08	40	0.00	0.04	0.00	0.00	0.00	0.00
11	0.01	0.00	0.68	0.16	1.55	1.14	26	0.00	0.65	0.35	0.00	0.10	0.05	41	0.03	0.04	0.03	0.00	0.00	0.00
12	0.00	1.83	0.03	2.14	1.34	0.51	27	0.00	0.08	0.24	0.04	0.13	0.13	42	0.00	0.00	0.02	0.00	0.00	0.00
13	0.00	1.32	0.04	3.03	3.64	0.24	28	0.00	2.48	0.73	0.05	0.64	0.17	43	0.00	0.02	0.00	0.00	0.00	0.00
14	0.00	0.16	0.10	1.44	0.48	0.14	29	0.00	0.02	0.08	0.75	0.13	0.16	44	0.00	0.01	0.02	0.01	0.00	0.00
15	0.00	0.18	0.05	4.56	0.35	0.46	30	0.68	0.01	0.09	0.30	0.10	0.06							

TABLE X. The same as in Table VI but for OMC on ^{116}Sn to states in ^{116}In.

Bin No.	0^+	1^+	2^+	1^-	2^-	Others	Bin No.	0^+	1^+	2^+	1^-	2^-	Others	Bin No.	0^+	1^+	2^+	1^-	2^-	Others
1	0.00	2.12	0.95	0.08	0.14	0.41	14	0.00	0.05	0.04	0.00	0.00	0.27	27	0.01	0.00	0.00	0.85	0.61	0.06
2	0.21	2.70	2.39	0.23	0.00	0.76	15	0.01	0.09	0.07	0.01	0.14	0.38	28	0.01	0.00	0.01	0.00	0.04	0.24
3	0.35	0.89	0.37	4.03	0.00	1.71	16	0.00	0.02	1.76	0.09	0.00	0.06	29	0.00	0.03	0.01	0.17	0.11	0.09
4	0.00	0.09	0.72	0.12	6.86	0.15	17	0.00	1.64	1.74	0.01	0.00	0.73	30	0.01	0.03	0.02	0.00	0.02	0.03
5	0.03	1.51	0.81	3.51	0.01	1.17	18	0.01	2.89	0.60	0.19	0.04	0.18	31	0.01	0.05	0.00	0.01	0.16	0.02
6	0.14	1.12	0.12	5.96	0.03	1.11	19	0.04	1.56	1.13	0.06	0.00	0.76	32	0.00	0.06	0.00	0.00	0.00	0.01
7	0.00	0.00	0.00	2.10	1.36	0.55	20	0.03	0.40	0.74	0.16	0.04	0.15	33	0.03	0.09	0.00	0.01	0.00	0.09
8	0.00	0.01	0.01	1.51	1.43	0.90	21	0.00	3.29	0.59	0.07	0.07	0.12	34	0.00	0.06	0.02	0.00	0.00	0.02
9	0.00	0.00	0.00	1.59	2.92	0.56	22	0.00	0.00	1.02	0.73	0.39	0.11	35	0.00	0.11	0.06	0.02	0.00	0.00
10	0.00	0.21	0.00	2.71	1.29	0.13	23	0.00	0.00	0.19	0.45	0.13	0.49	36	0.00	0.04	0.02	0.00	0.01	0.00
11	0.00	0.06	0.03	0.00	0.27	0.44	24	0.01	1.37	0.12	1.01	0.99	0.12	37	0.05	0.00	0.03	0.03	0.02	0.00
12	0.00	0.00	0.07	0.01	1.78	0.89	25	0.71	0.14	0.00	0.10	0.54	0.01	38	0.00	0.00	0.03	0.01	0.00	0.00
13	0.01	0.04	0.01	0.01	0.83	4.59	26	0.18	0.00	0.00	0.19	0.11	0.04	39	0.00	0.02	0.00	0.00	0.00	0.00

TABLE XI. The same as in Table VI but for OMC on ^{128}Xe to states in ^{128}I.

Bin No.	0^+	1^+	2^+	1^-	2^-	Others	Bin No.	0^+	1^+	2^+	1^-	2^-	Others	Bin No.	0^+	1^+	2^+	1^-	2^-	Others
1	0.00	0.29	0.53	0.18	0.09	0.80	17	0.00	0.20	0.05	0.80	0.26	3.82	33	0.00	0.00	0.04	0.35	0.48	0.03
2	0.00	0.00	0.00	0.29	0.48	0.15	18	0.00	0.11	0.10	1.60	0.52	0.46	34	0.11	0.12	0.00	0.42	0.06	0.08
3	0.00	0.00	0.00	0.09	1.15	0.18	19	0.00	0.20	0.07	0.89	0.43	0.91	35	0.00	0.01	0.00	0.04	0.00	0.03
4	0.03	0.79	1.38	0.11	0.25	1.44	20	0.01	0.59	0.95	2.09	0.20	0.30	36	0.02	0.01	0.00	0.07	0.08	0.03
5	0.00	0.83	0.77	0.01	0.00	1.25	21	0.00	2.60	1.03	0.25	1.62	0.66	37	0.00	0.12	0.01	0.00	0.09	0.06
6	0.01	0.83	2.53	0.17	0.37	0.41	22	0.07	0.70	0.72	0.00	0.00	0.28	38	0.00	0.03	0.02	0.00	0.00	0.01
7	0.00	3.00	0.58	0.00	0.00	0.42	23	0.00	1.43	0.45	1.81	0.05	0.05	39	0.00	0.08	0.04	0.52	0.00	0.00
8	1.01	1.28	0.16	0.00	0.03	0.29	24	0.00	0.54	0.86	2.03	0.00	0.09	40	0.00	0.03	0.02	0.00	0.01	0.00
9	0.03	0.30	0.22	0.01	0.00	2.37	25	0.00	0.09	0.94	0.00	0.28	0.34	41	0.07	0.01	0.00	0.04	0.00	0.00
10	0.00	0.42	1.11	0.00	0.00	1.25	26	0.00	0.09	0.38	0.07	0.12	0.07	42	0.00	0.00	0.03	0.00	0.03	0.00
11	0.00	0.06	0.99	0.02	6.46	0.07	27	0.00	2.98	0.37	0.26	0.14	0.07	43	0.00	0.00	0.00	0.00	0.00	0.00
12	0.00	0.27	0.08	0.12	0.11	1.36	28	0.00	0.00	0.38	0.20	0.08	0.22	44	0.00	0.02	0.00	0.03	0.00	0.00
13	0.00	0.00	0.00	4.37	3.60	0.19	29	0.00	0.00	0.38	0.02	0.15	0.10	45	0.00	0.00	0.00	0.00	0.00	0.00
14	0.00	1.63	0.00	0.81	0.33	0.61	30	0.49	0.00	0.06	0.15	0.18	0.11	46	0.00	0.00	0.00	0.00	0.00	0.00
15	0.00	0.00	0.03	1.76	0.37	0.64	31	0.24	0.02	0.00	0.10	0.61	0.03	47	0.00	0.00	0.00	0.00	0.00	0.00
16	0.03	0.14	0.02	0.92	2.62	0.31	32	0.00	0.81	0.00	0.40	0.11	0.09	48	0.00	0.00	0.00	0.03	0.00	0.00

TABLE XII. The same as in Table VI but for OMC on ^{130}Xe to states in ^{130}I.

Bin No.	0^+	1^+	2^+	1^-	2^-	Others	Bin No.	0^+	1^+	2^+	1^-	2^-	Others	Bin No.	0^+	1^+	2^+	1^-	2^-	Others
1	0.00	0.56	0.73	0.01	2.25	1.88	17	0.00	0.21	1.12	0.01	0.44	0.22	33	0.07	0.04	0.00	0.04	0.00	0.03
2	0.01	0.49	0.78	0.03	0.00	0.87	18	0.00	3.03	0.73	0.02	0.74	0.55	34	0.00	0.06	0.01	0.01	0.02	0.06
3	0.00	2.02	4.81	0.02	0.00	1.86	19	0.00	0.53	1.42	1.95	0.00	0.42	35	0.01	0.02	0.02	0.00	0.00	0.00
4	0.05	0.39	0.00	0.02	3.73	1.66	20	0.00	0.77	0.96	0.38	0.48	0.16	36	0.00	0.09	0.05	0.03	0.00	0.01
5	0.00	2.14	0.35	0.18	0.36	0.43	21	0.05	0.35	0.43	0.05	0.16	0.34	37	0.00	0.02	0.02	0.00	0.03	0.00
6	0.00	0.34	0.03	2.25	0.01	0.41	22	0.00	0.10	0.99	0.04	0.01	0.08	38	0.00	0.00	0.02	0.01	0.00	0.00
7	0.70	0.06	0.62	2.80	1.13	0.56	23	0.00	0.77	0.18	0.13	0.00	0.02	39	0.00	0.00	0.00	0.00	0.00	0.00
8	0.00	0.05	0.00	1.41	2.78	1.34	24	0.00	1.60	0.78	0.33	0.10	0.09	40	0.03	0.00	0.00	0.03	0.00	0.00
9	0.00	0.00	0.26	1.27	0.41	1.30	25	0.00	0.01	0.00	0.40	0.51	0.36	41	0.00	0.00	0.00	0.00	0.00	0.00
10	0.00	0.06	1.07	0.87	0.38	2.04	26	0.00	0.00	0.28	0.23	0.43	0.03	42	0.00	0.00	0.00	0.00	0.00	0.00
11	0.00	0.00	0.02	1.40	2.88	1.15	27	0.00	0.01	0.15	0.51	0.13	0.03	43	0.00	0.00	0.00	0.00	0.00	0.00
12	0.00	0.05	0.02	1.70	0.27	0.84	28	0.00	0.68	0.00	0.10	0.54	0.06	44	0.00	0.00	0.00	0.00	0.00	0.00
13	0.00	1.69	0.02	0.86	0.69	2.16	29	0.00	0.05	0.00	0.09	0.03	0.06	45	0.00	0.00	0.00	0.00	0.00	0.00
14	0.00	0.61	0.02	0.97	0.16	1.81	30	0.65	0.00	0.02	0.00	0.00	0.11	46	0.00	0.00	0.00	0.00	0.00	0.00
15	0.10	0.70	0.05	0.09	0.30	0.74	31	0.00	0.07	0.00	0.47	0.07	0.02	47	0.00	0.00	0.00	0.00	0.00	0.00
16	0.00	0.01	0.11	2.95	0.81	1.32	32	0.00	0.01	0.00	0.00	0.10	0.01	48	0.00	0.01	0.00	0.00	0.00	0.00

TABLE XIII. The same as in Table VI but for OMC on ^{136}Ba to states in ^{136}Cs.

Bin No.	$W(J^\pi)/W_{\text{tot}}(\%)$						Bin No.	$W(J^\pi)/W_{\text{tot}}(\%)$						Bin No.	$W(J^\pi)/W_{\text{tot}}(\%)$					
	0^+	1^+	2^+	1^-	2^-	Others		0^+	1^+	2^+	1^-	2^-	Others		0^+	1^+	2^+	1^-	2^-	Others
1	0.00	1.12	0.39	0.00	2.31	0.95	18	0.00	0.54	1.72	1.92	1.30	0.92	35	0.00	0.02	0.04	0.00	0.00	0.05
2	0.00	0.00	0.61	0.03	0.00	1.58	19	1.11	2.62	0.62	0.08	0.00	0.36	36	0.00	0.05	0.01	0.00	0.00	0.00
3	0.00	2.45	0.25	0.02	0.00	0.31	20	0.00	0.91	1.63	0.02	0.02	0.14	37	0.00	0.05	0.02	0.00	0.00	0.00
4	0.00	0.10	5.35	0.02	0.02	2.42	21	0.00	0.72	0.66	0.02	0.00	0.34	38	0.00	0.00	0.03	0.01	0.00	0.00
5	0.00	2.46	0.00	0.06	3.66	1.36	22	0.01	0.17	0.70	0.01	0.00	0.04	39	0.00	0.00	0.00	0.01	0.00	0.00
6	0.00	0.33	0.43	1.21	0.01	0.38	23	0.00	1.83	1.19	0.04	0.01	0.06	40	0.01	0.00	0.00	0.01	0.00	0.00
7	0.00	0.00	0.03	2.78	0.01	0.20	24	0.00	0.46	0.30	0.79	0.00	0.06	41	0.48	0.00	0.00	0.00	0.00	0.00
8	0.00	0.02	0.35	2.17	1.96	1.06	25	0.00	0.03	0.05	0.11	0.07	0.34	42	0.00	0.00	0.00	0.00	0.00	0.00
9	0.00	0.00	0.00	1.03	2.77	1.09	26	0.00	0.01	0.35	0.28	0.53	0.10	43	0.00	0.00	0.00	0.00	0.00	0.00
10	0.00	0.00	0.20	1.81	0.38	1.83	27	0.00	0.84	0.00	0.49	0.56	0.05	44	0.00	0.00	0.00	0.00	0.00	0.00
11	0.00	0.05	1.31	1.33	1.16	1.93	28	0.00	0.00	0.00	0.13	0.17	0.11	45	0.00	0.00	0.00	0.00	0.00	0.00
12	0.00	0.00	0.02	1.69	2.01	1.39	29	0.00	0.01	0.00	0.00	0.40	0.10	46	0.00	0.00	0.00	0.00	0.00	0.00
13	0.00	0.20	0.01	0.37	0.30	0.64	30	0.00	0.02	0.00	0.46	0.05	0.02	47	0.00	0.00	0.00	0.00	0.00	0.00
14	0.01	1.31	0.00	1.67	0.55	3.24	31	0.00	0.00	0.00	0.01	0.00	0.02	48	0.00	0.00	0.00	0.00	0.00	0.00
15	0.00	0.04	0.01	0.06	0.28	0.25	32	0.00	0.01	0.00	0.05	0.13	0.01	49	0.00	0.01	0.00	0.00	0.00	0.00
16	0.04	0.06	0.02	3.04	0.93	1.20	33	0.04	0.01	0.00	0.00	0.02	0.02	50	0.00	0.00	0.00	0.00	0.00	0.00
17	0.00	0.26	0.07	0.01	0.10	1.00	34	0.00	0.08	0.02	0.00	0.00	0.03	51	0.01	0.00	0.00	0.00	0.00	0.00

[1] J. Suhonen and O. Civitarese, Phys. Rep. **300**, 123 (1998).

[2] D. Zinatulina, V. Brudanin, V. Egorov, C. Petitjean, M. Shirchenko, J. Suhonen, and I. Yutlandov, Phys. Rev. C **99**, 024327 (2019).

[3] H. Ejiri, J. Suhonen, and K. Zuber, Phys. Rep. **797**, 1 (2019).

[4] H. Ejiri, Phys. Rep. **338**, 265 (2000).

[5] D. F. Measday, Phys. Rep. **354**, 243 (2001).

[6] M. Kortelainen and J. Suhonen, Europhys. Lett. **58**, 666 (2002).

[7] M. Kortelainen and J. Suhonen, Nucl. Phys. A **713**, 501 (2003).

[8] M. Kortelainen and J. Suhonen, J. Phys. G: Nucl. Part. Phys. **30**, 2003 (2004).

[9] E. Kolbe, K. Langanke, and P. Vogel, Phys. Rev. C **50**, 2576 (1994).

[10] B. L. Johnson *et al.*, Phys. Rev. C **54**, 2714 (1996).

[11] T. P. Gorringe *et al.*, Phys. Rev. C **60**, 055501 (1999).

[12] T. Siiskonen, J. Suhonen, and M. Hjorth-Jensen, J. Phys. G: Nucl. Part. Phys. **25**, L55 (1999).

[13] T. Siiskonen, M. Hjorth-Jensen, and J. Suhonen, Phys. Rev. C **63**, 055501 (2001).

[14] N. Auerbach and B. A. Brown, Phys. Rev. C **65**, 024322 (2002).

[15] F. Šimkovic, G. Pantis, J. D. Vergados, and A. Faessler, Phys. Rev. C **60**, 055502 (1999).

[16] T. P. Gorringe *et al.*, Phys. Rev. Lett. **72**, 3472 (1994).

[17] G. Jonkmans, S. Ahmad, D. S. Armstrong, G. Azuelos, W. Bertl, M. Blecher, C. Q. Chen, P. Depommier, B. C. Doyle *et al.*, Phys. Rev. Lett. **77**, 4512 (1996).

[18] D. Gazit, Phys. Lett. B **666**, 472 (2008).

[19] L. E. Marcucci, A. Kievsky, S. Rosati, R. Schiavilla, and M. Viviani, Phys. Rev. Lett. **108**, 052502 (2012).

[20] V. Brudanin *et al.*, Nucl. Phys. A **587**, 577 (1995).

[21] T. Siiskonen, J. Suhonen, V. A. Kuz'min, and T. V. Tetereva, Nucl. Phys. A **635**, 446 (1998); **651**, 437(E) (1999).

[22] T. Siiskonen, J. Suhonen, and M. Hjorth-Jensen, Phys. Rev. C **59**, R1839 (1999).

[23] T. Gorringe and H. W. Fearing, Rev. Mod. Phys. **76**, 31 (2004).

[24] J. Suhonen, *From Nucleons to Nucleus: Concepts of Microscopic Nuclear Theory* (Springer, Berlin, 2007).

[25] D. R. Bes, O. Civitarese, and J. Suhonen, Phys. Rev. C **86**, 024314 (2012).

[26] O. Civitarese and J. Suhonen, Phys. Rev. C **89**, 044319 (2014).

[27] H. Ejiri, Phys. Rep. **38**, C85 (1978).

[28] L. Jokiniemi and J. Suhonen, Phys. Rev. C **96**, 034308 (2017).

[29] L. Jokiniemi, J. Suhonen, H. Ejiri, and I. H. Hashim, Phys. Lett. B **794**, 143 (2019).

[30] I. H. Hashim, H. Ejiri, T. Shima, K. Takahisa, A. Sato, Y. Kuno, K. Ninomiya, N. Kawamura, and Y. Miyake, Phys. Rev. C **97**, 014617 (2018).

[31] L. Jokiniemi, H. Ejiri, D. Frekers, and J. Suhonen, Phys. Rev. C **98**, 024608 (2018).

[32] J. Suhonen, Front. Phys. **5**, 55 (2017).

[33] M. Morita and A. Fujii, Phys. Rev. **118**, 606 (1960).

[34] H. Primakoff, Rev. Mod. Phys. **31**, 802 (1959).

[35] K. W. Ford and J. G. Wills, Nucl. Phys. **35**, 295 (1962).

[36] H. Ejiri, Front. Phys. **7**, 30 (2019).

[37] M. L. Goldberger and S. B. Treiman, Phys. Rev. **111**, 354 (1958).

[38] J. Suhonen, T. Taigel, and A. Faessler, Nucl. Phys. A **486**, 91 (1988).

[39] F. Šimkovic, V. Rodin, A. Faessler, and P. Vogel, Phys. Rev. C **87**, 045501 (2013).

[40] A. Bohr and B. R. Mottelson, *Nuclear Structure* (Benjamin, New York, 1969), Vol. I.

[41] K. Holinde, Phys. Rep. **68**, 121 (1981).

[42] J. Suhonen, Nucl. Phys. A **563**, 205 (1993).

[43] J. Suhonen, Nucl. Phys. A **700**, 649 (2002).

[44] P. Sarriguren, Phys. Rev. C **86**, 034335 (2012).

Article V

Comparative analysis of muon capture and $0\nu\beta\beta$ decay matrix elements
L. Jokiniemi and J. Suhonen,
Phys. Rev. C **102** (2020) 024303.

Comparative analysis of muon-capture and $0\nu\beta\beta$-decay matrix elements

L. Jokiniemi and J. Suhonen

Department of Physics, University of Jyväskylä, P. O. Box 35 (YFL), FI-40014, Finland

Average matrix elements of ordinary muon capture (OMC) to the intermediate nuclei of neutrinoless double beta ($0\nu\beta\beta$) decays of current experimental interest are computed and compared with the corresponding energy and multipole decompositions of $0\nu\beta\beta$-decay nuclear matrix elements (NMEs). The present OMC computations are performed using the Morita-Fujii formalism by extending the original formalism beyond the leading order. The $0\nu\beta\beta$ NMEs include the appropriate short-range correlations, nuclear form factors, and higher-order nucleonic weak currents. The nuclear wave functions are obtained in extended no-core single-particle model spaces using the spherical version of the proton-neutron quasiparticle random-phase approximation with two-nucleon interactions based on the Bonn one-boson-exchange G matrix. Both the OMC and $0\nu\beta\beta$ processes involve 100-MeV-range momentum exchanges and hence similarities could be expected for both processes in the feeding of the $0\nu\beta\beta$ intermediate states. These similarities may help improve the accuracy of the $0\nu\beta\beta$ NME calculations by using the data from the currently planned OMC experiments.

I. INTRODUCTION

Ordinary muon capture (OMC) is a process in which a negative muon from an atomic K orbit is captured by the nucleus of the atom. The large mass of the captured muon induces large momentum exchange, $q \approx 50$–100 MeV, which leads to final states that are both highly excited and of high multipolarity. These same states are expected to contribute as the intermediate states of neutrinoless double beta ($0\nu\beta\beta$) decay in $0\nu\beta\beta$ decay chains. Here, we discuss cases where the OMC happens on the daughter nucleus of a $0\nu\beta\beta$-decay parent and hence the OMC corresponds to the right virtual branch (β^+ type of transitions) of the $0\nu\beta\beta$ decay. This makes OMC a promising tool to study the nuclear matrix elements (NMEs) of the $0\nu\beta\beta$ decay [1,2].

We are interested in the ground-state–to–ground–state $0\nu\beta\beta$ decay, which can be schematically written as

$$_{Z-2}^{A}X'(0^+) \dashrightarrow {}_{Z-1}^{A}Y(J^\pi) \dashrightarrow 2e^- + {}_{Z}^{A}X(0^+) , \quad (1)$$

where the even-even parent nucleus X' of mass number A and atomic number $Z - 2$ in its 0^+ ground state emits two electrons e^- leading to the 0^+ ground state of its daughter X, an even-even isobar of atomic number Z. The transition goes through the virtual states of multipolarity J^π of the intermediate odd-odd nucleus Y of atomic number $Z - 1$; here, J is the angular momentum and π the parity of the intermediate state. The dashed arrow represents virtual transitions through the intermediate states. Using the notation of Eq. (1) the OMC process, which corresponds to the right branch of the $0\nu\beta\beta$ process of Eq. (1), can be illustrated as

$$\mu^- + {}_{Z}^{A}X(0^+) \to \nu_\mu + {}_{Z-1}^{A}Y(J^\pi) , \quad (2)$$

where the muon (μ^-) is captured by the 0^+ ground state of the even-even nucleus X leading to the J^π multipole states of

its odd-odd isobar Y (see the review by Measday [3]). At the same time a muon neutrino ν_μ is emitted. Comparing Eqs. (1) and (2) one can see how ordinary muon capture is linked with neutrinoless double β decay: OMC feeds the same excited J^π states of Y that are involved as virtual states in the $0\nu\beta\beta$ decay.

Through the years a number of calculations for the OMC transitions in different nuclear-structure formalisms and for various nuclei have been performed in order to probe the right-leg virtual transitions of $0\nu\beta\beta$ decays as well as the value of the particle-particle interaction parameter g_{pp} of the proton-neutron quasiparticle random-phase approximation (pnQRPA) [4–6], or the in-medium renormalization of the axial-vector coupling constant g_A [7–12]. Thanks to the large momentum exchange in the OMC, the process activates also the induced weak currents, including the weak magnetism and pseudoscalar contributions, quite like in the case of the $0\nu\beta\beta$ decay [13]. The magnitude of the induced pseudoscalar term is mostly unknown in atomic nuclei [7,8,14–21]. Additional OMC experiments and calculations concerning nuclei involved in $0\nu\beta\beta$ decays could help theories better understand the possible connections between OMC and $0\nu\beta\beta$ NMEs as well as the effective values of the weak couplings [22].

There have been early attempts to compare the OMC rates against the $2\nu\beta\beta$ (two-neutrino double beta decay) NMEs for light nuclei using the nuclear shell model [6]. In the work of Kortelainen *et al.* [6] it was found that there was a clear correlation between the energy distributions of the OMC rates to 1^+ states and the energy decomposition of the $2\nu\beta\beta$ NMEs for the $2\nu\beta\beta$ decays of the *sd*-shell nuclei ^{36}Ar, ^{46}Ca, and ^{48}Ca. In this study we extend these studies to $0\nu\beta\beta$ decays of medium-heavy and heavy nuclei by computing the average OMC matrix elements in the intermediate nuclei of $0\nu\beta\beta$ decays up to some 50 MeV

using the pnQRPA formalism and compare them with the energy-multipole decompositions of the NMEs of $0\nu\beta\beta$ decays computed using the same formalism and model spaces. We compute the average OMC matrix elements instead of OMC rates in order to reduce the phase-space effects. We decompose the average OMC ME to J^π multipole states within MeV energy bins while for the $0\nu\beta\beta$ decay the energy-multipole decomposition entails division of the NMEs into multipoles and their energy distributions binned by MeV energy intervals. In [23] we computed the strength functions for the OMC on ^{76}Se, ^{82}Kr, ^{96}Mo, ^{100}Ru, ^{116}Sn, ^{128}Xe, ^{130}Xe, and ^{136}Ba, leading to states in $0\nu\beta\beta$ intermediate nuclei ^{76}As, ^{82}Br, ^{96}Nb, ^{100}Tc, ^{116}In, ^{128}I, ^{130}I, and ^{136}Cs. In this study we extend those calculations by comparing the average OMC matrix elements with the corresponding energy-multipole decompositions of $0\nu\beta\beta$ NMEs.

Since we are interested in wide excitation-energy regions of medium-heavy or heavy open-shell nuclei, the shell-model framework is infeasible for our calculations due to the enormous computational burden and the very restricted single-particle model spaces allowed by the shell-model treatment. The pnQRPA formalism allows us to study the OMC and $0\nu\beta\beta$ decay NMEs at high excitation energies, since it allows the use of large no-core single-particle bases. Even though the pnQRPA often fails to predict the properties of individual states accurately, it can reproduce the gross features of a distribution of nuclear states quite reasonably. In our earlier studies, it has been shown that the pnQRPA reliably reproduces the locations of the isovector spin-dipole giant resonances [24], as well as the location of the newly discovered OMC giant resonance in the case of ^{100}Mo [25,26], and the low-energy OMC rates in the case of ^{76}Se [1,23].

This article is organized as follows. In Sec. II we briefly introduce the pnQRPA formalism as well as the underlying formalism of the ordinary muon capture and $0\nu\beta\beta$ decay. In Sec. III we display and discuss the obtained results for the OMC rates and $0\nu\beta\beta$-decay matrix elements and examine possible connections between them. The final conclusions are drawn in Sec. IV.

II. COMPUTATIONAL SCHEME

In this section we introduce briefly our computational scheme. All the calculations are based on the pnQRPA theory. In the first subsection we outline the key points of the pnQRPA theory and introduce the parameters related to the corresponding Hamiltonian. In the second subsection we outline the theoretical aspects of the OMC rate, and in the last subsection we introduce the underlying theory of the $0\nu\beta\beta$-decay NMEs.

A. pnQRPA and its Hamiltonian parameters

For the present calculations we adopt the spherical version of the proton-neutron QRPA. The calculations use an even-even nucleus as a reference and then create proton-neutron excitations to reach the states of the adjacent odd-odd nucleus. We find the wave functions and excitation energies for the complete set of J^π excitations in the odd-odd nuclei by performing a pnQRPA diagonalization in the unperturbed basis

of quasiproton-quasineutron pairs coupled to J^π [27,28]. The resulting pnQRPA states in odd-odd nuclei are of the form

$$\left| J_k^\pi M \right\rangle = \sum_{pn} \left[X_{pn}^{J_k^\pi} A_{pn}^\dagger(JM) - Y_{pn}^{J_k^\pi} \tilde{A}_{pn}(JM) \right] |\text{pnQRPA}\rangle ,$$

$$(3)$$

where k labels the states of spin-parity J^π, the quantities X and Y are the forward- and backward-going pnQRPA-amplitudes, $A^\dagger$ and $\tilde{A}$ are the quasiproton-quasineutron creation and annihilation operators, M is the z projection of J and $|\text{pnQRPA}\rangle$ is the pnQRPA vacuum. The transition densities corresponding to transitions between the 0_{gs}^+ ground state of the even-even reference nucleus and a J_k^π excited state of the corresponding odd-odd nucleus, entering both the muon capture rates and the $0\nu\beta\beta$ NMEs, can then be written as

$$\left(0_{\text{gs}}^+ \left| \left| [c_p^\dagger \tilde{c}_n]_J \right| \right| J_k^\pi \right) = \sqrt{2J+1} \left[v_p u_n X_{pn}^{J_k^\pi} + u_p v_n Y_{pn}^{J_k^\pi} \right] , \quad (4)$$

$$\left(J_k^\pi \left| \left| [c_p^\dagger \tilde{c}_n]_J \right| \right| 0_{\text{gs}}^+ \right) = \sqrt{2J+1} \left[u_p v_n X_{pn}^{J_k^\pi} + v_p u_n Y_{pn}^{J_k^\pi} \right] , \quad (5)$$

where v (u) is the BCS occupation (vacancy) amplitude in the even-even nucleus. The formalism is explained in more detail in Refs. [27,28].

The X and Y amplitudes in Eq. (3) are calculated by diagonalizing the pnQRPA matrix separately for each multipole J^π. We adopt as the two-body interaction the one derived from the Bonn-A one-boson-exchange potential, introduced in [29]. We follow the partial isospin-restoration scheme introduced in [30], and multiply the isoscalar ($T = 0$) and isovector ($T = 1$) parts of the particle-particle G-matrix elements by factors $g_{\text{pp}}^{T=0}$ and $g_{\text{pp}}^{T=1}$, respectively. The isovector parameter $g_{\text{pp}}^{T=1}$ is adjusted such that the Fermi part of the corresponding two-neutrino double beta ($2\nu\beta\beta$) NME vanishes, leading to partial isospin-symmetry restoration. The isoscalar parameter $g_{\text{pp}}^{T=0}$ is subsequently varied to reproduce the $2\nu\beta\beta$-decay half-life. As for the particle-hole part, it was scaled by a common factor g_{ph}, fixed, as usual, by fitting the centroid of the Gamow-Teller giant resonance (GTGR) in the 1^+ channel of the calculations. These (particle-particle and particle-hole) renormalization factors are adopted from [24] except for the case $A = 82$, which was not included in there. For $A = 82$ we adopt the values from [23].

The quasiparticle spectra for protons and neutrons, needed in the pnQRPA diagonalization, are obtained by solving the BCS equations for protons and neutrons in the even-even reference nuclei. The calculated BCS pairing gaps are fitted to the phenomenological proton and neutron pairing gaps in a way described in detail in [31]. The values of the resulting pairing scaling factors are listed in [24,31].

For each even-even reference nucleus involved in the computations, we adopt the single-particle bases exploited successfully in our earlier calculations [23,24,31], i.e., we employ no-core bases with all the orbitals from the $N = 0$ oscillator major shell up to at least two oscillator major shells above the respective Fermi surfaces for both protons and neutrons. The single-particle energies were obtained by solving the radial Schrödinger equation for a Coulomb-corrected Woods-Saxon (WS) potential, optimized for nuclei close to the β-stability line [32]. As was mentioned in [24,31], this choice is justified since the $\beta\beta$-decaying nuclei are always situated rather close

to the bottom of the valley of beta stability. Both the bound and quasi-bound single-particle states are taken along in the calculations. The single-particle energies close to the Fermi surfaces were slightly modified in order to better reproduce the low-lying spectra of the neighboring odd-mass nuclei at the BCS-quasiparticle level.

B. Formalism of the ordinary muon capture

We compute the OMC nuclear matrix elements and rates using the formalism that was originally developed by Morita and Fujii in [33]. This formalism takes into account both the genuine and induced vector and axial-vector weak nucleon currents. The OMC rate from a J_i initial state to a J_f final state can be written as

$$W = 2\pi \langle |\text{M.E.}|^2 \rangle_{av} q^2 \frac{dq}{dE_f} \,, \tag{6}$$

where

$$\frac{dq}{dE_f} = \left[1 - \frac{q}{m_\mu + AM} \right] \tag{7}$$

and

$$\langle |\text{M.E.}|^2 \rangle_{av} = \frac{2J_f + 1}{(2j' + 1)(2J_i + 1)} \sum_{ij} \sum_{\kappa u} \\ \times \left[\sum_\nu C^{(i)} \mathcal{M}_{\nu u}^{(i)} \right]^* \left[\sum_{\nu'} C^{(j)} \mathcal{M}_{\nu' u}^{(j)} \right], \tag{8}$$

where j' is the angular momentum of the bound muon. The definitions of the matrix elements $\mathcal{M}_{\nu u}^{(i)}$ and the corresponding coefficients $C^{(i)}$ can be found in Table I of [33].

The Q value of the OMC process can be computed from

$$q = (m_\mu - W_0) \left(1 - \frac{m_\mu - W_0}{2(M_f + m_\mu)} \right), \tag{9}$$

where $W_0 = M_f - M_i + m_e + E_X$ [33]. Here, M_f (M_i) is the nuclear mass of the final (initial) nucleus, m_e the rest mass of an electron, and E_X the excitation energy of the final J^π state.

If we assume that the muon is initially bound on the K atomic orbit, and use Bethe-Salpeter point-like-nucleus approximation formula [34] for the bound muon wave function, the capture rate of Eq. (6) can be written as

$$W = 8P(\alpha Z m'_\mu)^3 \frac{2J_f + 1}{2J_i + 1} \left(1 - \frac{q}{m_\mu + AM} \right) q^2, \tag{10}$$

where A is the mass number of the initial and final nuclei, J_i (J_f) the angular momentum of the initial (final) nucleus, M the average nucleon rest mass, m_μ the mass of the bound muon, m'_μ the reduced mass of the muon in the parent μ-mesonic atom, Z the atomic number of the initial nucleus, α the fine-structure constant, and q the decay energy (Q value) of the OMC.

The term P in Eq. (10) has a complex form containing the nuclear matrix elements of the OMC, various geometric and kinematic factors, and weak coupling constants. The P term can be written explicitly for an nth forbidden transition. In [33] the authors derive explicit forms for the P term for different degrees of forbiddenness, assuming the muon being bound

on the atomic K orbit before capture, and approximating the bound-state muon wave function as the one of a point nucleus. All terms of the order of $1/M^2$ (except for terms containing the square of the weak pseudoscalar coupling, g_P, which is large compared with the other coupling constants) were omitted. We extend these explicit forms by including all the terms of the order of $1/M^2$ in our calculations, as given explicitly in [23].

The P term involves the usual weak vector and axial-vector couplings $g_V \equiv g_V(q)$ and $g_A \equiv g_A(q)$ at finite momentum transfer $q > 0$. The conserved vector current (CVC) and partially conserved axial-vector current (PCAC) hypotheses give the values $g_V(0) = 1.00$ and $g_A(0) = 1.27$ for a free nucleon at zero momentum transfer, and for finite momentum transfer we can use the dipole approximation [2]. For the induced pseudoscalar coupling g_P the Goldberger-Treiman PCAC relation [35] gives $g_P/g_A = 7.0$. However, deviations from the CVC and PCAC values have been recorded at zero momentum transfer [7,8,22,36].

Using the notation of Eq. (10) we can write Eq. (8) in the form

$$\langle |\text{M.E.}|^2 \rangle_{av} = \frac{8(2J_f + 1)}{2J_i + 1} (\alpha Z m'_\mu)^3 P \,. \tag{11}$$

Here, we define an average OMC matrix element as

$$|M^{(\mu)}|_{av} = \sqrt{\langle |\text{M.E.}|^2 \rangle_{av}} = \sqrt{\frac{8(2J_f + 1)}{2J_i + 1} (\alpha Z m'_\mu)^3 P} \,. \tag{12}$$

We compare this quantity, instead of OMC rate, with the $0\nu\beta\beta$ decay nuclear matrix element in order to reduce the phase-space effects.

In this work we choose the slightly quenched values of $g_A(0) = 0.8$ and $g_P(0) = 7.0$ and keep the CVC value $g_V(0) = 1.00$ for all the studied cases. These values were adopted also in our earlier works [23,26] but the (qualitative) results of the present study are not sensitive to the exact values of these couplings.

C. Outline of the $0\nu\beta\beta$-decay theory

We exploit the $0\nu\beta\beta$-decay formalism outlined, e.g., in [37] and further processed in [24,38], assuming that the $0\nu\beta\beta$ decay is dominated by the light-Majorana-neutrino-exchange mechanism. Here, we are only interested in the ground-state–to–ground-state transitions. The half-life for such a $0\nu\beta\beta$ transition can be written as

$$\left[t_{1/2}^{(0\nu)}(0_i^+ \to 0_f^+) \right]^{-1} = \left(g_A^{\text{eff}} \right)^4 G_{0\nu} |M^{(0\nu)}|^2 \left| \frac{\langle m_\nu \rangle}{m_e} \right|^2, \tag{13}$$

where $G_{0\nu}$ is a phase-space factor for the final-state leptons in units of inverse years (see [39]), defined here without including the axial-vector coupling g_A. The effective light-neutrino mass, $\langle m_\nu \rangle$, of Eq. (13) is defined as

$$\langle m_\nu \rangle = \sum_j (U_{ej})^2 m_j \tag{14}$$

with m_j being the mass eigenstates of light neutrinos. The amplitudes U_{ej} are the components of the electron row of the light-neutrino-mass mixing matrix.

The $0\nu\beta\beta$-decay NME $M^{(0\nu)}$ in Eq. (13) is defined as

$$M^{(0\nu)} = M_{\text{GT}}^{(0\nu)} - \left(\frac{g_{\text{V}}}{g_{\text{A}}^{\text{eff}}}\right)^2 M_{\text{F}}^{(0\nu)} + M_{\text{T}}^{(0\nu)}, \qquad (15)$$

where we adopt the CVC value $g_{\text{V}} = 1.0$ for the weak vector coupling strength. The double Fermi, Gamow-Teller, and tensor nuclear matrix elements for $0\nu\beta\beta$ decays are defined as

$$M_{\text{F}}^{(0\nu)} = \sum_k \left(0_f^+ \| \sum_{mn} h_{\text{F}}(r_{mn}, E_k) t_m^- t_n^- \| 0_i^+ \right), \qquad (16)$$

$$M_{\text{GT}}^{(0\nu)} = \sum_k \left(0_f^+ \| \sum_{mn} h_{\text{GT}}(r_{mn}, E_k)(\boldsymbol{\sigma}_m \cdot \boldsymbol{\sigma}_n) t_m^- t_n^- \| 0_i^+ \right), \quad (17)$$

$$M_{\text{T}}^{(0\nu)} = \sum_k \left(0_f^+ \| \sum_{mn} h_{\text{T}}(r_{mn}, E_k) S_{mn}^{\text{T}} t_m^- t_n^- \| 0_i^+ \right), \qquad (18)$$

where t_m^- is the isospin lowering operator (changing a neutron into a proton) for the nucleon m. The spin tensor operator S_{mn}^{T} is defined as

$$S_{mn}^{\text{T}} = 3[(\boldsymbol{\sigma}_m \cdot \hat{\mathbf{r}}_{mn})(\boldsymbol{\sigma}_n \cdot \hat{\mathbf{r}}_{mn})] - \boldsymbol{\sigma}_m \cdot \boldsymbol{\sigma}_n. \qquad (19)$$

The summation over k in Eqs. (16)–(18) runs over all the states of the intermediate odd-odd nucleus, and E_k is the excitation energy of a given state. Here, $r_{mn} = |\mathbf{r}_m - \mathbf{r}_n|$ is the relative distance between the two decaying neutrons, labeled m and n, and $\hat{\mathbf{r}}_{mn} = (\mathbf{r}_m - \mathbf{r}_n)/r_{mn}$. The ground state of the initial (final) even-even nucleus is denoted by 0_i^+ (0_f^+). The terms $h_K(r_{mn}, E_k)$, $K = \text{F, GT, T}$ are the neutrino potentials defined in [38].

In the pnQRPA framework the nuclear matrix elements can be written as

$$
\begin{aligned}
M_K^{(0\nu)} = &\sum_{J^\pi, k_1, k_2, J'} \sum_{pp'nn'} (-1)^{j_n + j_{p'} + J + J'} \sqrt{2J' + 1} \\
&\times \begin{Bmatrix} j_p & j_n & J \\ j_{n'} & j_{p'} & J' \end{Bmatrix} (pp'; J' \| \mathcal{O}_K \| nn'; J') \\
&\times \left(0_f^+ \| [c_{p'}^\dagger \tilde{c}_{n'}]_J \| J_{k_1}^\pi \right) \langle J_{k_1}^\pi | J_{k_2}^\pi \rangle \left(J_{k_2}^\pi \| [c_p^\dagger \tilde{c}_n]_J \| 0_i^+ \right),
\end{aligned}
\qquad (20)
$$

where the summation over k_1 and k_2 runs over the different pnQRPA solutions for a given multipole J^π. The operators $\mathcal{O}_K$ inside the two-particle matrix element refer to Eqs. (16)–(18), and they can be written as

$$\mathcal{O}_{\text{F}} = h_{\text{F}}(r, E_k)[f_{\text{CD}}(r)]^2, \qquad (21)$$

$$\mathcal{O}_{\text{GT}} = h_{\text{GT}}(r, E_k)[f_{\text{CD}}(r)]^2 \boldsymbol{\sigma}_1 \boldsymbol{\sigma}_2, \qquad (22)$$

$$\mathcal{O}_{\text{T}} = h_{\text{T}}(r, E_k)[f_{\text{CD}}(r)]^2 S_{12}^{\text{T}}, \qquad (23)$$

where S_{12}^{T} is the tensor operator of Eq. (19) and $r = |\mathbf{r}_1 - \mathbf{r}_2|$ is the distance between the participating nucleons. The energy E_k is the average of the kth pnQRPA-computed eigenvalues of the initial and final nuclei, corresponding to a given multipole J^π. The term $\langle J_{k_1}^\pi | J_{k_2}^\pi \rangle$ is the overlap between the two sets of
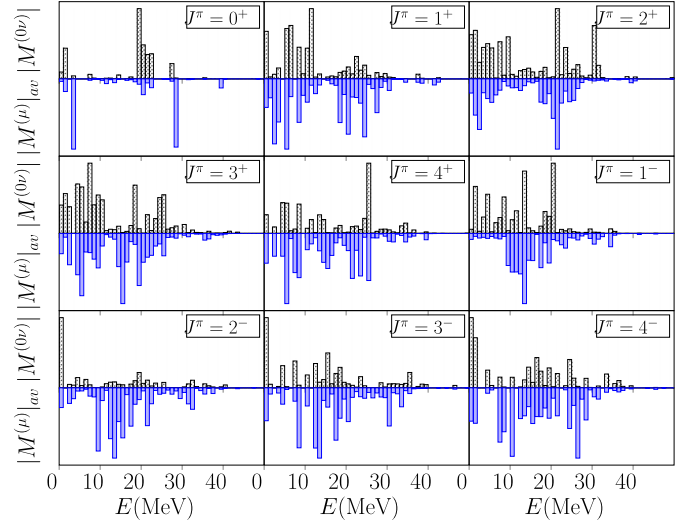

FIG. 1. Multipole decompositions in terms of relative $0\nu\beta\beta$ matrix elements (positive y axes) and average matrix elements of the OMC on ^{76}Se (negative y axes) as functions of the excitation energy E in the intermediate nucleus ^{76}As of the $0\nu\beta\beta$ decay of ^{76}Ge. Here, J^π refer to the angular momenta and parities of the virtual states in ^{76}As and all quantities have been summed within 1 MeV energy bins. The scale values of the y axes have been omitted, since they are not relevant for the current analysis. For more information see the text.

J^π states, and it can be written as

$$\langle J_{k_1}^\pi | J_{k_2}^\pi \rangle = \sum_{pn} \left[X_{pn}^{J_{k_1}^\pi} \bar{X}_{pn}^{J_{k_2}^\pi} - Y_{pn}^{J_{k_1}^\pi} \bar{Y}_{pn}^{J_{k_2}^\pi} \right], \qquad (24)$$

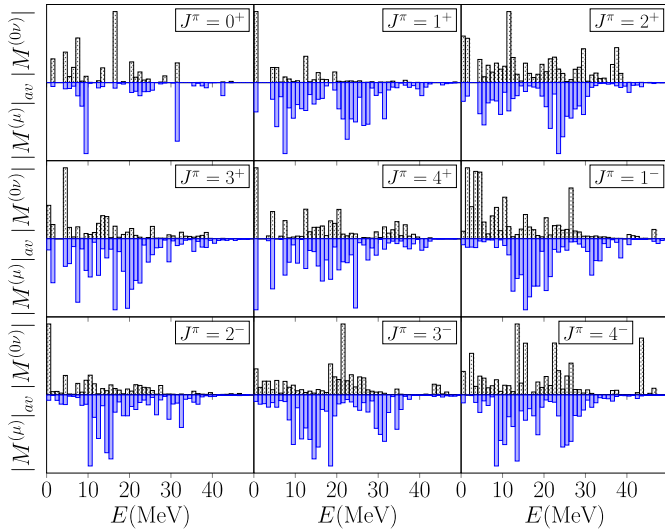where X and Y ($\bar{X}$ and $\bar{Y}$) are the pnQRPA amplitudes of the final (initial) nucleus.
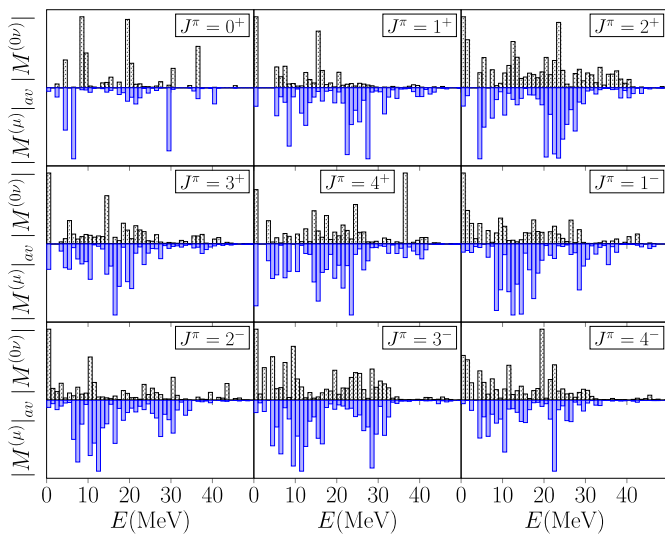
The factor $f_{\text{CD}}(r)$ in Eqs. (21)–(23) takes into account the nucleon-nucleon short-range correlations (SRC) [40,41]. We use the CD-Bonn form [42] with the parametrization

$$f_{\text{CD}}(r) = 1 - 0.46 e^{-(1.52/\text{fm}^2)r^2}[1 - (1.88/\text{fm}^2)r^2]. \qquad (25)$$

III. RESULTS AND DISCUSSION

In this section we present and discuss the results of our studies. We concentrate on the positive $J^\pi = 0^+, 1^+, 2^+, 3^+, 4^+$ and negative $J^\pi = 1^-, 2^-, 3^-, 4^-$ multipolarities of both the average OMC ME distributions and the $0\nu\beta\beta$ NME distributions. These multipoles are by far the most important ones for the OMC rates [23] and the leading ones for the $0\nu\beta\beta$ NMEs [24,43]. We discuss also the cumulative average OMC MEs and $0\nu\beta\beta$ NMEs.

We computed the average OMC MEs and the $0\nu\beta\beta$-decay NMEs using the formalism and parameters discussed in Sec. II A. For the values of the weak coupling constants, involved in both the $0\nu\beta\beta$ and OMC processes, we adopt the moderately quenched values $g_{\text{A}} = 0.8$ and $g_{\text{P}} = 7.0$, and the CVC value $g_{\text{V}} = 1.0$. This is in line with our earlier studies [23,26]. As stated at the end of Sec. II B, the results are not very sensitive to the values of these couplings.
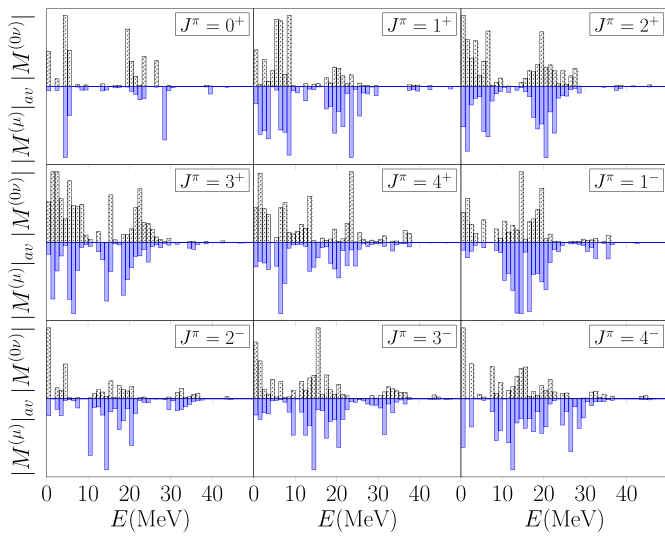
FIG. 2. The same as in Fig. 1 for the $A = 82$ system.

FIG. 3. The same as in Fig. 1 for the $A = 96$ system.

FIG. 4. The same as in Fig. 1 for the $A = 100$ system.
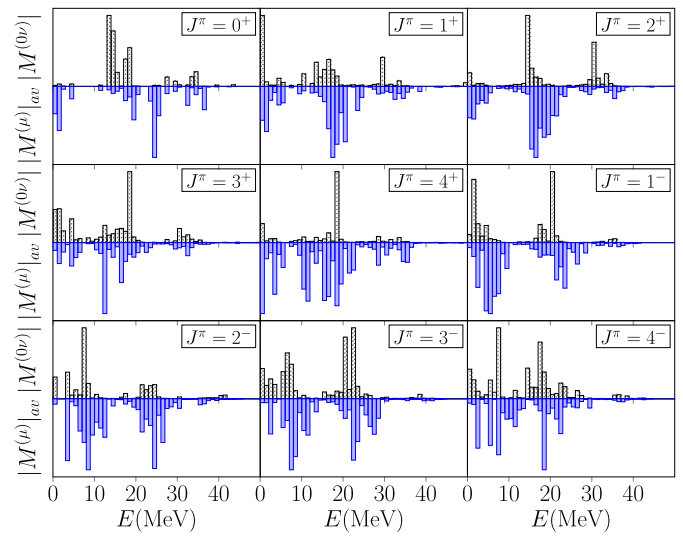
FIG. 5. The same as in Fig. 1 for the $A = 116$ system.
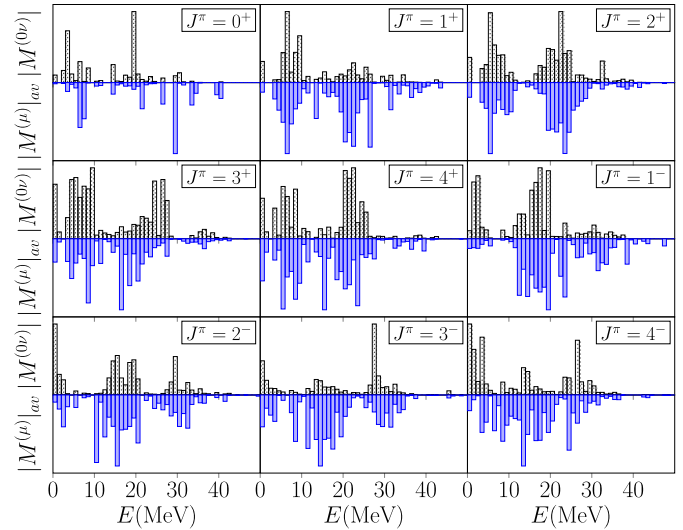
FIG. 6. The same as in Fig. 1 for the $A = 128$ system.
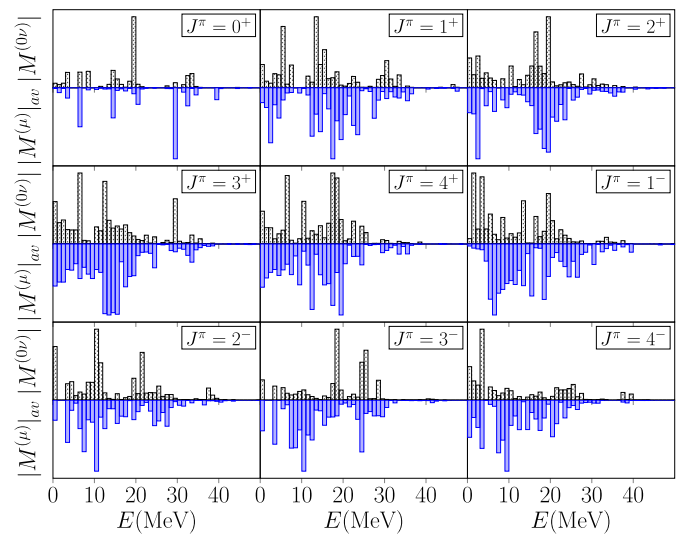
FIG. 7. The same as in Fig. 1 for the $A = 130$ system.
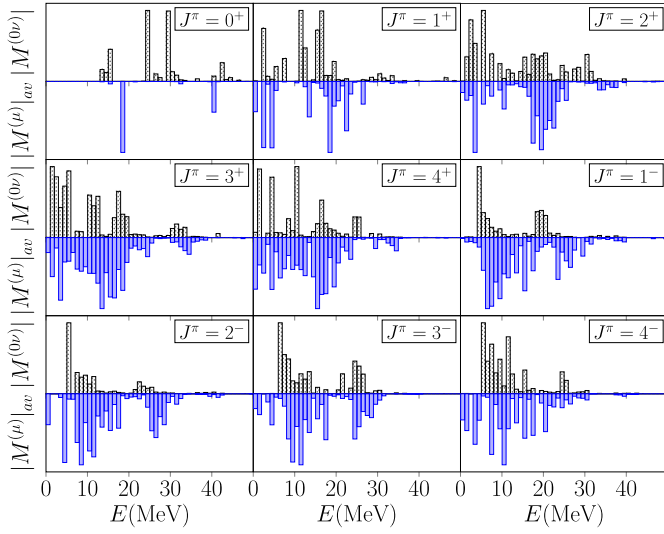
FIG. 8. The same as in Fig. 1 for the $A = 136$ system.

A. Distributions of the relative OMC MEs and $0\nu\beta\beta$ NMEs

In Figs. 1–8 we compare the computed relative OMC ME distributions

$$|M^{(\mu)}|_{av}(J^\pi)(E) \bigg/ \sum_E |M^{(\mu)}|_{av}(J^\pi)(E)$$

with the multipole decompositions $M^{(0\nu)}(J^\pi)$ of the $0\nu\beta\beta$-decay NMEs expressed in terms of relative contributions

$$|M^{(0\nu)}(J^\pi)|(E) \bigg/ \sum_E |M^{(0\nu)}(J^\pi)|(E) \,.$$

The analyses have been done for each multipole J^π separately, and for increasing excitation energy E in the OMC daughter (the same as $0\nu\beta\beta$-decay intermediate nucleus) using summed average OMC MEs and $0\nu\beta\beta$ NMEs within energy bins of 1 MeV. We have chosen to plot only absolute values of the matrix elements since they carry the essential information needed in the present comparison of the OMC and $0\nu\beta\beta$ decay. Only in the case of $A = 100$ the $J^\pi = 1^+$ contribution to the total $0\nu\beta\beta$ NME is negative. There are, however, negative contributions coming from individual energy bins in many cases (the same is of course true for the OMC matrix element). As such, the possible different relative signs of the contributions are not important in the context of our study, since we are interested in the multipoles and energy regions where notable (positive or negative) contributions appear in both the OMC matrix element and the $0\nu\beta\beta$ NME. This means that the nuclear states, with their wave functions, play an important role in both processes for these particular multipoles and energy regions. In order to make the comparison meaningful the excitation energy of the lowest J^π state of the pnQRPA set (for $0\nu\beta\beta$ decay the right-hand set) is fitted to the measured excitation energy. We display the relative $0\nu\beta\beta$ multipole NMEs on the positive and relative OMC MEs on the negative y axes. Since the comparison is qualitative and the quantities are relative we have omitted the scales of the y axes.

In the following we analyze the correspondences related to different multipoles arising from the Figs. 1–8. It should be noted that the number of 0^+ pnQRPA states is little, and hence the similarities between the two distributions are harder to conclude than for the other multipoles.

A = 76: The correspondence between relative OMC-rate and $0\nu\beta\beta$-NME distributions for the multipoles $J^\pi = 0^+$ is weak. However, for the rest of the multipoles one can see correspondences: in the cases of $J^\pi = 1^+, 2^+, 3^+$ one can see two bumps at similar energies. The $J^\pi = 1^-$ distributions both are peaked at ≈ 10 MeV, and the $J^\pi = 3^-, 4^-$ distributions at ≈ 15 MeV. On the other hand, in the case of $J^\pi = 2^-$ the $0\nu\beta\beta$ decays trough the 2^- ground state of ^{76}As seem to be enhanced.

A = 82: The $J^\pi = 1^+, 2^+, 3^+$ and $J^\pi = 1^-, 3^-$ distributions show nice correspondence. The $J^\pi = 0^+$ distributions both show a peak at $E \approx 5$ MeV, and the low-energy correspondences of $J^\pi = 4^\pm$ are also pretty good. In the case of $J^\pi = 2^-$ $0\nu\beta\beta$ seems to be more concentrated in low
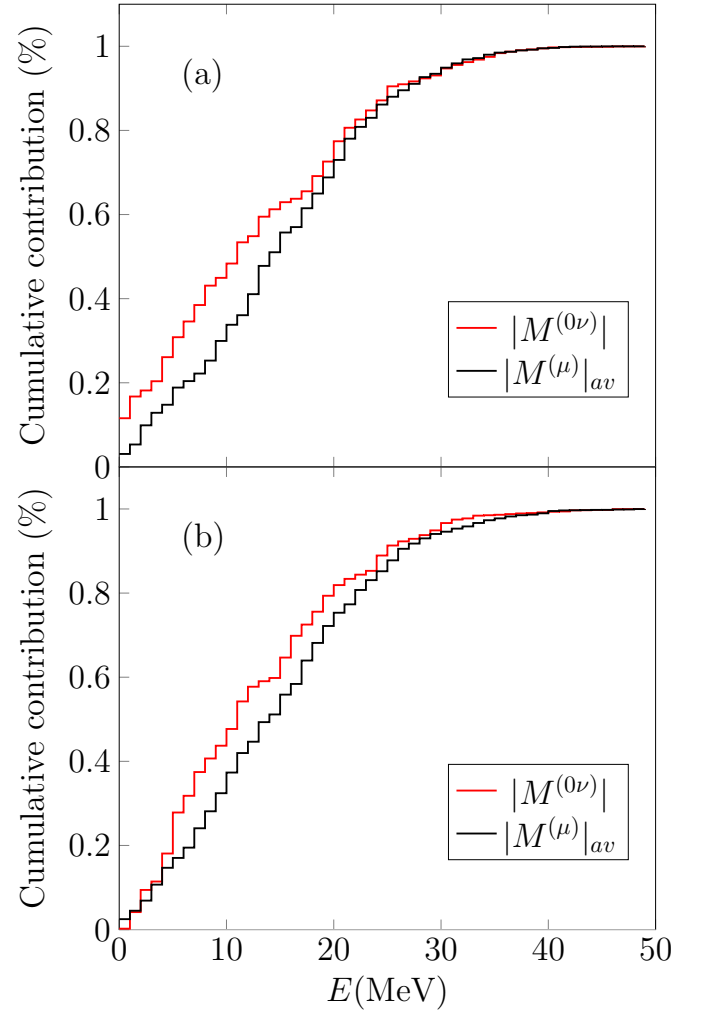

FIG. 9. Normalized cumulative average OMC MEs and normalized $0\nu\beta\beta$ NMEs as functions of energy in the intermediate nuclei ^{76}As (a) and ^{136}Cs (b) of the $A = 76$ and $A = 136$ $0\nu\beta\beta$ triplets. For more information, see the text.

TABLE I. Contributions (in percentages) from different multipoles to $0\nu\beta\beta$-decay NMEs and average OMC MEs for different $0\nu\beta\beta$-decay triplets. The presented values are normalized ratios $R(0\nu) = |M^{(0\nu)}|(J^\pi)/|M^{(0\nu)}|$ and $R(\mu) = |M^{(\mu)}|_{av}(J^\pi)/|M^{(\mu)}|_{av}$.

J^π \ Case	$A=76$		$A=82$		$A=96$		$A=100$		$A=116$		$A=128$		$A=130$		$A=136$	
	$R(0\nu)$	$R(\mu)$	$R(0\nu)$	$R(\mu)$	$R(0\nu)$	$R(\mu)$	$R(0\nu)$	$R(\mu)$	$R(0\nu)$	$R(\mu)$	$R(0\nu)$	$R(\mu)$	$R(0\nu)$	$R(\mu)$	$R(0\nu)$	$R(\mu)$
0^+	2	3	2	2	0	3	1	2	1	2	1	3	1	2	1	2
1^+	7	18	6	17	6	17	6	17	9	16	2	16	2	14	7	14
1^-	16	21	16	21	18	18	20	19	23	18	13	17	13	17	9	17
2^+	13	16	14	17	13	16	12	16	9	16	12	17	12	15	14	15
2^-	10	18	9	17	7	17	3	17	7	17	5	16	5	17	6	16
3^+	5	11	5	11	6	12	5	12	6	11	6	12	6	12	7	12
3^-	11	6	11	6	10	7	9	8	9	8	10	8	10	9	9	9
4^+	7	2	7	2	8	2	8	2	7	3	9	3	9	4	9	4
4^-	5	5	5	5	4	5	4	5	4	5	5	5	5	6	5	6
$\sum$	76	10	75	98	72	97	68	98	75	96	63	97	63	96	67	95

energies, but both distributions show three clear bumps at similar energies.

$A = 96$: The $J^\pi = 0^+$ distributions show three bumps at energies $E \approx 10, 20, 30$ MeV, but there is a strong peak in the $0\nu\beta\beta$ distribution at $E \approx 15$ MeV, that is missing from the OMC distribution. In the cases of $J^\pi = 1^+$ and $J^\pi = 2^-$ the $0\nu\beta\beta$ distributions are clearly more concentrated on lower energies than OMC. The correspondence of $J^\pi = 2^+, 3^+, 1^-$, and 3^- is not too good, either. However, the $J^\pi = 4^+$ distributions show three clear bumps at similar energies.

$A = 100$: In this case, the situation in the cases of $J^\pi = 1^\pm$ and 2^- is similar as in Figs. 3(b) and 3(g): $0\nu\beta\beta$ is more concentrated on lower energies. However, the $J^\pi = 2^+$ distributions both show a clear bump at $E \approx 25$ MeV, and $J^\pi = 3^+$ at $E \approx 15$ MeV. The $J^\pi = 4^+$ distributions show good correspondence at $E < 30$ MeV, but there is an extra peak at $E \approx 35$ MeV in the $0\nu\beta\beta$ distribution. The $J^\pi = 3^-, 4^-$, on the other hand, show two clear bumps at similar energies.

$A = 116$: In this case, the correspondence is best for the $J^\pi = 1^+, 2^+, 3^+$ multipoles, which show three clear bumps in both distributions. In the case of $J^\pi = 4^+$ there is some concentration in both distributions at around 20 MeV. There are similarities also in the cases of the $J^\pi = 1^-, 2^-, 3^-, 4^-$: there are two clear bumps at similar energies in both spectra. On the other hand, the $J^\pi = 0^+$ distributions show no clear correspondence.

$A = 128$: In this case, the correspondence is best for the $J^\pi = 1^+, 2^+, 3^+, 4^+$ and 4^- multipoles, which show two clear bumps at $E \approx 8$ MeV and at $E \approx 20$ MeV, and for $J^\pi = 1^-, 2^-, 3^-$, which show three bumps. The $J^\pi = 0^+$ distributions also have two peaks at $E \approx 5$ and 20 MeV.

$A = 130$: In this case, the low-energy correspondence for $J^\pi = 2^-, 4^-$ multipoles is great. The $J^\pi = 0^+, 1^+$ distributions both show three peaks, and the $J^\pi = 2^+, 3^+, 4^+$ three bumps at similar energies. The $J^\pi = 3^-$ distributions also show two bumps at $E \approx 10$ and 25 MeV, but there is an extra peak in the $0\nu\beta\beta$ distribution that is absent in the OMC distribution. In the case of $J^\pi = 1^-$ the $0\nu\beta\beta$ decay is more concentrated on lower energies.

$A = 136$: In this case, the correspondence is clearest for the $J^\pi = 1^+, 2^+$ distributions, which show two bumps at around $E \approx 3$ MeV and at $E \approx 20$ MeV. The $J^\pi = 3^-$ distributions also show two bumps at around $E \approx 10$ MeV and $E \approx 25$ MeV. As for the $J^\pi = 1^-, 2^-$ multipoles, there are two bumps in both distributions, but the second bump is situated at slightly lower energy for in the $0\nu\beta\beta$ distribution. In the case of $J^\pi = 4^-$ the OMC distribution is more spread compared to the $0\nu\beta\beta$ distribution, but both distributions show a bump at around $E \approx 10$ MeV.

All in all, the correspondence between the $J^\pi = 0^+$ $0\nu\beta\beta$-NME and OMC-ME distributions seems to be not too good, and the overall correspondence seems to be best for the $J^\pi = 3^\pm$ and $4^\pm$ multipoles. Also for other multipoles there seems to be a more or less clear correspondence for all the discussed $0\nu\beta\beta$ triplets. The distributions and their correspondences vary quite much between the different $0\nu\beta\beta$ triplets indicating that nuclear structure varies strongly with nuclear mass owing to different mean-field properties (single-particle energies, Fermi surfaces) and two-nucleon correlations.

B. Cumulative average OMC MEs and $0\nu\beta\beta$ NMEs

Cumulative average OMC MEs and $0\nu\beta\beta$ NMEs nicely illustrate the build-up of these quantities as functions of the excitation energy in the intermediate nuclei of the discussed $0\nu\beta\beta$ triplets. We choose the $A = 76$ and $A = 136$ triplets as representative cases and plot the corresponding cumulative matrix elements

$$\sum_{J^\pi} |M^{(0\nu)}(J^\pi)|(E) \Big/ \sum_{J^\pi, E} |M^{(0\nu)}(J^\pi)|(E)$$

and

$$\sum_{J^\pi} |M^{(\mu)}|_{av}(J^\pi)(E) \Big/ \sum_{J^\pi, E} |M^{(\mu)}|_{av}(J^\pi)(E)$$

in Fig. 9. Thus, Fig. 9 is just an other way to present the results of Figs. 1–8. We can see that the running sums for the average OMC MEs and $0\nu\beta\beta$ NMEs, for both triplets, are quite similar, but in the $A = 76$ case [panel (a)] the $0\nu\beta\beta$
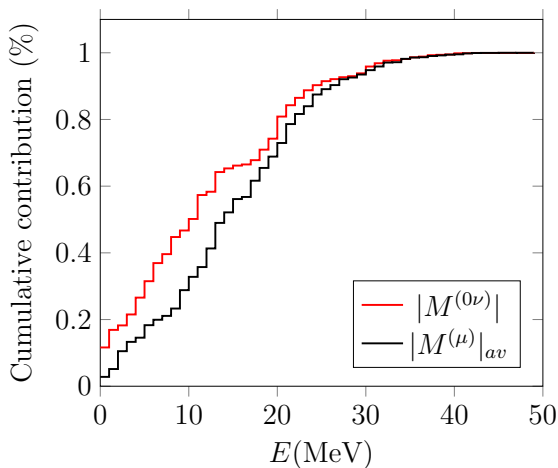
FIG. 10. The same as in Fig. 9, but only for the $A = 76$ $0\nu\beta\beta$-decay triplet and containing contributions from only the leading multipoles $J^\pi = 1^+, 1^-, 2^+, 2^-$.

NME starts at a higher value and has thus a smaller inclination of the cumulative curve. Both cases show that $0\nu\beta\beta$ decay is slightly more concentrated on lower energies than OMC.

In Table I we show for the discussed $0\nu\beta\beta$-decay triplets the relative multipole contributions to the $0\nu\beta\beta$ NMEs and average OMC MEs for J^π ($J \leqslant 4$), which are the leading multipoles for both the $0\nu\beta\beta$ decay and OMC (see Figs. 1 and 3 of [38], and the results of [23]). The multipole $J^\pi = 0^-$ is omitted from the table, since its contribution to both $|M^{(0\nu)}|$ and $|M^{(\mu)}|_{av}$ is negligible. First of all, one can see that basically all of the OMC strength is coming from the multipoles with $J \leqslant 4$, while the $0\nu\beta\beta$ strength is more distributed to higher multipoles, and only about $60 - 75\%$ comes from the multipoles with $J \leqslant 4$. Having a closer look at the table one notices that the multipoles $J^\pi = 1^+, 1^-, 2^+, 2^-$ are among the leading multipoles for both the $0\nu\beta\beta$ decay and OMC for all the nuclei. Also multipoles $J^\pi = 3^-, 4^+$ are important for the $0\nu\beta\beta$ NMEs, but less important for the OMC. On the other hand, $J^\pi = 3^+$ is rather important for OMC but not so important for $0\nu\beta\beta$ decay. The $J^\pi = 2^+$ and 1^- contributions are practically the same for both quantities. On the other hand, a considerable part of the OMC strength is coming from the multipoles $J^\pi = 1^+, 2^-$, but they are less important for the $0\nu\beta\beta$-decay NMEs. These features of the $0\nu\beta\beta$-decay NMEs were also recorded in [38], the small quantitative deviations from our results stemming from the much smaller single-particle bases employed there.

The multipoles $J^\pi = 1^+, 1^-, 2^+, 2^-$ are, according to Table I, the leading multipoles for both the average OMC MEs and $0\nu\beta\beta$ NMEs in our example case of $A = 76$. In Fig. 10 we plot for the $A = 76$ case the cumulative sums of the OMC rate ($|M^{(\mu)}|_{av}$) and $0\nu\beta\beta$ NME ($|M^{(0\nu)}|$) stemming only from these multipoles. We notice that the $0\nu\beta\beta$ decay strength is coming from lower energies than the OMC strength, as is also the case for the total multipole contributions in Fig. 9. Comparing Figs. 9 and 10 implies that the multipoles

$J^\pi = 1^\pm, 2^\pm$ not only constitute most of the $0\nu\beta\beta$ decay and OMC strength, but also define the energy distributions of the processes.

IV. SUMMARY AND CONCLUSIONS

In this work we computed the average matrix elements corresponding to the ordinary muon capture on the 0^+ ground states of ^{76}Se, ^{82}Kr, ^{96}Mo, ^{100}Ru, ^{116}Sn, ^{128}Xe, ^{130}Xe, and ^{136}Ba, which are the daughter nuclei of the eight $0\nu\beta\beta$-decaying parent nuclei ^{76}Ge, ^{82}Se, ^{96}Zr, ^{100}Mo, ^{116}Cd, ^{128}Te, ^{130}Te, and ^{136}Xe. We compared these matrix elements with the corresponding $0\nu\beta\beta$-decay nuclear matrix elements. The calculations were performed using the proton-neutron quasiparticle RPA with realistic two-body interactions and slightly modified no-core Woods-Saxon single-particle bases. We studied the cumulative behavior of the average OMC MEs and $0\nu\beta\beta$ NMEs and also presented multipole decompositions of the average OMC MEs and $0\nu\beta\beta$-decay NMEs.

We found that there are correspondences especially between the $J^\pi = 3^\pm, 4^\pm$ $0\nu\beta\beta$ NMEs and average OMC MEs, and also for other multipoles there can be seen correspondences for all the studied $0\nu\beta\beta$-decay triplets. Furthermore, we noticed that overall the cumulative behavior of the $0\nu\beta\beta$ NMEs and average OMC MEs is quite similar, but for $A \leqslant 128$ the $0\nu\beta\beta$ NME is more evenly distributed within the energy region of $E = 0$–50 MeV than the OMC ME. This difference is related to the different behavior of these two quantities at low excitation energies in the $0\nu\beta\beta$-decay intermediate nuclei.

When studying the multipole decompositions of the $0\nu\beta\beta$-decay NMEs and average OMC MEs we found that basically all of the OMC strength is coming from the multipoles with $J \leqslant 4$, while the $0\nu\beta\beta$ strength is more distributed to higher multipoles, only approximately 60–75% coming from the multipoles with $J \leqslant 4$. We also found that the multipoles $J^\pi = 1^+, 2^+, 1^-, 2^-$ are among the leading multipoles for both the $0\nu\beta\beta$ decay and average OMC MEs for all the studied $0\nu\beta\beta$-decay triplets.

According to this study, the overall behavior of the OMC and $0\nu\beta\beta$ matrix elements is pretty similar. Therefore, measurements of the OMC strength functions for the daughter nuclei of $0\nu\beta\beta$ decays could enable a systematic study of the involved nuclear wave functions and the sensitivity of the OMC strength functions to the effective values of the weak axial couplings, and hence help improve the accuracy of calculations of the NMEs of the $0\nu\beta\beta$ decay. Experimental studies are in progress, e.g., at RCNP Osaka for nuclei of interest in studies of nuclear double beta decay and astroneutrino interactions.

[1] D. Zinatulina, V. Brudanin, V. Egorov, C. Petitjean, M. Shirchenko, J. Suhonen, and I. Yutlandov, Phys. Rev. C **99**, 024327 (2019).

[2] H. Ejiri, J. Suhonen, and K. Zuber, Phys. Rep. **797**, 1 (2019).

[3] D. F. Measday, Phys. Rep. **354**, 243 (2001).

[4] M. Kortelainen and J. Suhonen, Europhys. Lett. **58**, 666 (2002).

[5] M. Kortelainen and J. Suhonen, Nucl. Phys. A **713**, 501 (2003).

[6] M. Kortelainen and J. Suhonen, J. Phys. G: Nucl. Part. Phys. **30**, 2003 (2004).

[7] E. Kolbe, K. Langanke, and P. Vogel, Phys. Rev. C **50**, 2576 (1994).

[8] B. L. Johnson *et al.*, Phys. Rev. C **54**, 2714 (1996).

[9] T. P. Gorringe *et al.*, Phys. Rev. C **60**, 055501 (1999).

[10] T. Siiskonen, J. Suhonen, and M. Hjorth-Jensen, J. Phys. G: Nucl. Part. Phys. **25**, L55 (1999).

[11] T. Siiskonen, M. Hjorth-Jensen, and J. Suhonen, Phys. Rev. C **63**, 055501 (2001).

[12] N. Auerbach and B. A. Brown, Phys. Rev. C **65**, 024322 (2002).

[13] F. Šimkovic, G. Pantis, J. D. Vergados, and A. Faessler, Phys. Rev. C **60**, 055502 (1999).

[14] T. P. Gorringe *et al.*, Phys. Rev. Lett. **72**, 3472 (1994).

[15] G. Jonkmans, S. Ahmad, D. S. Armstrong, G. Azuelos, W. Bertl, M. Blecher *et al.*, Phys. Rev. Lett. **77**, 4512 (1996).

[16] D. Gazit, Phys. Lett. B **666**, 472 (2008).

[17] L. E. Marcucci, A. Kievsky, S. Rosati, R. Schiavilla, and M. Viviani, Phys. Rev. Lett. **108**, 052502 (2012).

[18] V. Brudanin *et al.*, Nucl. Phys. A **587**, 577 (1995).

[19] T. Siiskonen, J. Suhonen, V. A. Kuz'min, and T. V. Tetereva, Nucl. Phys. A **635**, 446 (1998); **651**, 437(E) (1999).

[20] T. Siiskonen, J. Suhonen, and M. Hjorth-Jensen, Phys. Rev. C **59**, R1839(R) (1999).

[21] T. Gorringe and H. W. Fearing, Rev. Mod. Phys. **76**, 31 (2004).

[22] J. Suhonen, Front. Phys. **5**, 55 (2017).

[23] L. Jokiniemi and J. Suhonen, Phys. Rev. C **100**, 014619 (2019).

[24] L. Jokiniemi, H. Ejiri, D. Frekers, and J. Suhonen, Phys. Rev. C **98**, 024608 (2018).

[25] I. H. Hashim, H. Ejiri, T. Shima, K. Takahisa, A. Sato, Y. Kuno, K. Ninomiya, N. Kawamura, and Y. Miyake, Phys. Rev. C **97**, 014617 (2018).

[26] L. Jokiniemi, J. Suhonen, H. Ejiri, and I. H. Hashim, Phys. Lett. B **794**, 143 (2019).

[27] J. Suhonen, *From Nucleons to Nucleus: Concepts of Microscopic Nuclear Theory* (Springer, Berlin, 2007).

[28] J. Suhonen, T. Taigel, and A. Faessler, Nucl. Phys A **486**, 91 (1988).

[29] K. Holinde, Phys. Rep. **68**, 121 (1981).

[30] F. Šimkovic, V. Rodin, A. Faessler, and P. Vogel, Phys. Rev. C **87**, 045501 (2013).

[31] L. Jokiniemi and J. Suhonen, Phys. Rev. C **96**, 034308 (2017).

[32] A. Bohr and B. R. Mottelson, *Nuclear Structure, Vol. I* (Benjamin, New York, 1969).

[33] M. Morita and A. Fujii, Phys. Rev. **118**, 606 (1960).

[34] H. A. Bethe and E. E. Salpeter, *Quantum Mechanics of One- and Two-Electron Atoms* (Academic Press, New York, 1959).

[35] M. L. Goldberger and S. B. Treiman, Phys. Rev. **111**, 354 (1958).

[36] H. Ejiri, Front. Phys. **7**, 30 (2019).

[37] J. Suhonen and O. Civitarese, Phys. Rep. **300**, 123 (1998).

[38] J. Hyvärinen and J. Suhonen, Phys. Rev. C **91**, 024613 (2015).

[39] J. Kotila and F. Iachello, Phys. Rev. C **85**, 034316 (2012).

[40] G. A. Miller and J. E. Spencer, Ann. Phys. (NY) **100**, 562 (1976).

[41] M. Kortelainen, O. Civitarese, J. Suhonen, and J. Toivanen, Phys. Lett. B **647**, 128 (2007).

[42] F. Šimkovic, A. Faessler, H. Müther, V. Rodin, and M. Stauf, Phys. Rev. C **79**, 055501 (2009).

[43] J. Hyvärinen and J. Suhonen, Adv. High Energy Phys. **2016**, 4714829 (2016).